Universidad de Alcalá

COMISIÓN DE ESTUDIOS OFICIALES
DE POSGRADO Y DOCTORADO

ACTA DE EVALUACIÓN DE LA TESIS DOCTORAL
(FOR EVALUATION OF THE ACT DOCTORAL THESIS)

Año académico *(academic year)*: 2017/18

DOCTORANDO *(candidate PHD)*: **RIZZELLI MARTELLA, GIUSEPPE**
D.N.I./PASAPORTE *(Id.Passport)*: ******2355B**
PROGRAMA DE DOCTORADO *(Academic Committee of the Programme)*: **D441-ELECTRÓNICA: SISTEMAS ELECTRÓNICOS AVANZADOS. SISTEMAS INTELIGENTES**
DPTO. COORDINADOR DEL PROGRAMA *(Department)*: **ELECTRÓNICA**
TITULACIÓN DE DOCTOR EN *(Phd title)*: **DOCTOR/A POR LA UNIVERSIDAD DE ALCALÁ**

En el día de hoy 16/04/18, reunido el tribunal de evaluación, constituido por los miembros que suscriben el presente Acta, el aspirante defendió su Tesis Doctoral **con Mención Internacional** *(In today assessment met the court, consisting of the members who signed this Act, the candidate defended his doctoral thesis with mention as International Doctorate)*, elaborada bajo la dirección de *(prepared under the direction of)* JUAN DIEGO ANIA CASTAÑÓN.

Sobre el siguiente tema *(Title of the doctoral thesis)*: *TRANSMISSION IMPAIRMENTS MITIGATION AND POLARIZATION CONTROL IN ULTRALONG RAMAN FIBER LASERS AND AMPLIFIERS*

Finalizada la defensa y discusión de la tesis, el tribunal acordó otorgar la CALIFICACIÓN GLOBAL[1] de (**no apto, aprobado, notable y sobresaliente**) *(After the defense and defense of the thesis, the court agreed to grant the GLOBAL RATING (fail, pass, good and excellent)*: _____ SOBRESALIENTE _____

Alcalá de Henares, a 16 de ABRIL de 2018

Fdo. *(Signed)*: José Mª Soto (rjo)   Fdo. *(Signed)*:   Fdo. *(Signed)*: SONIA MARTÍN LÓPEZ

FIRMA DEL ALUMNO (candidate's signature),

GIUSEPPE RIZZELLI MARTELLA

Fdo. *(Signed)*:

Con fecha 7 de mayo de 2018 la Comisión Delegada de la Comisión de Estudios Oficiales de Posgrado, a la vista de los votos emitidos de manera anónima por el tribunal que ha juzgado la tesis, resuelve:

☒ Conceder la Mención de "Cum Laude"
☐ No conceder la Mención de "Cum Laude"

La Secretaria de la Comisión Delegada

[1] La calificación podrá ser **"no apto" "aprobado" "notable"** y **"sobresaliente"**. El tribunal podrá otorgar la mención de "cum laude" si la calificación global es de sobresaliente y se emite en tal sentido el voto secreto positivo por unanimidad. *(The grade may be "**fail**" "**pass**" "**good**" or "**excellent**". The panel may confer the distinction of "cum laude" if the overall grade is "Excellent" and has been awarded unanimously as such after secret voting.).*

INCIDENCIAS / OBSERVACIONES: SIN INCIDENCIAS.
(Incidents / Comments)

En aplicación del art. 14.7 del RD. 99/2011 y el art. 14 del Reglamento de Elaboración, Autorización y Defensa de la Tesis Doctoral, la Comisión Delegada de la Comisión de Estudios Oficiales de Posgrado y Doctorado, en sesión pública de fecha 7 de mayo, procedió al escrutinio de los votos emitidos por los miembros del tribunal de la tesis defendida por *RIZZELLI MARTELLA, GIUSEPPE*, el día 16 de abril de 2018, titulada *TRANSMISSION IMPAIRMENTS MITIGATION AND POLARIZATION CONTROL IN ULTRALONG RAMAN FIBER LASERS AND AMPLIFIERS*, para determinar, si a la misma, se le concede la mención "cum laude", arrojando como resultado el voto favorable de todos los miembros del tribunal.

Por lo tanto, la Comisión de Estudios Oficiales de Posgrado **resuelve otorgar** a dicha tesis la

MENCIÓN "CUM LAUDE"

Alcalá de Henares, 8 de mayo de 2018
EL VICERRECTOR DE INVESTIGACIÓN Y TRANSFERENCIA

F. Javier de la Mata de la Mata

Copia por e-mail a:
Doctorando: RIZZELLI MARTELLA, GIUSEPPE
Secretario del Tribunal: SONIA MARTÍN LÓPEZ
Director/a de Tesis: JUAN DIEGO ANIA CASTAÑÓN

DILIGENCIA DE DEPÓSITO DE TESIS.

Comprobado que el expediente académico de D./Dª _____

reúne los requisitos exigidos para la presentación de la Tesis, de acuerdo a la normativa vigente, y habiendo presentado la misma en formato: ☐ soporte electrónico ☐ impreso en papel, para el depósito de la misma, en el Servicio de Estudios Oficiales de Posgrado, con el nº de páginas: _____ se procede, con fecha de hoy a registrar el depósito de la tesis.

Alcalá de Henares a _____ de _____ de 20_____

Fdo. El Funcionario

ESCUELA POLITÉCNICA SUPERIOR

DEPARTAMENTO DE ELECTRÓNICA

Universidad de Alcalá

Programa de Doctorado en
Electrónica: Sistemas Electrónicos Avanzados. Sistemas Inteligentes

Transmission Impairments Mitigation and Polarization Control in Ultralong Raman Fiber Lasers and Amplifiers

Tesis Doctoral presentada por
Giuseppe Rizzelli Martella

Director
Juan Diego Ania Castañón
Doctor en Física

Tutor
Miguel González Herráez
Doctor en Ingeniería de Telecomunicación

Alcalá de Henares, 2018

D. Juan Diego Ania Castañón, Investigador Científico del Instituto de Óptica "Daza de Valdés" (CSIC)

INFORMA que la Tesis Doctoral titulada **"Transmission impairment mitigation and polarization control in ultralong Raman fiber lasers and amplifiers"**, presentada por D. Giuseppe Rizzelli, y realizada bajo mi dirección, reúne los requisitos científicos de originalidad y rigor metodológicos para ser defendida ante un tribunal.

Para que así conste y surta los efectos oportunos, se firma el presente informe en Alcalá de Henares a 8 de enero de 2018.
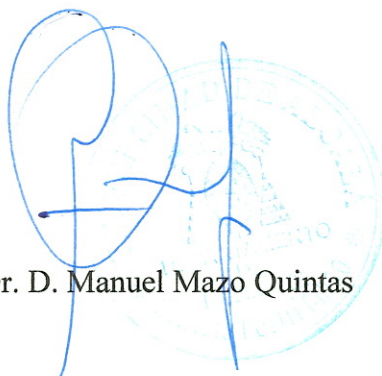
Fdo.: Juan Diego Ania Castañón

Universidad de Alcalá

Dr. D. Manuel Mazo Quintas, coordinador del Programa de Doctorado "ELECTRÓNICA: Sistemas Electrónicos Avanzados. Sistemas Inteligentes".

INFORMA: Que la Tesis Doctoral titulada **"Transmission Impairments Mitigation and Polarization Control in Ultralong Raman Fiber Lasers and Amplifiers"** presentada por D. Giuseppe Rizzelli, y dirigida por el doctor D. Juan Diego Ania Castañón, cumple con todos los requisitos científicos y metodológicos, para ser defendida ante un Tribunal para optar al Grado de Doctor, según lo indicado por la Comisión Académica del Programa de Doctorado.

Alcalá de Henares, 31 de Enero de 2018

Fdo. Dr. D. Manuel Mazo Quintas

To my family.

Abstract

Although the introduction of fiber cables for data transmission over long distances, about 50 years ago, was thought to provide an endless supply of information capacity in comparison to the copper ones, nowadays, the scientific community is facing significant challenges in trying to cope with the ever growing demand for higher data rates. With 99% of the data traffic being carried over optical cables, and a 40% increase in the amount of data being exchanged on the world's network every year, we are looking to the fast approach of the so-called "capacity crunch", which has been widely predicted to happen in 2020.

Over the past 30 years several key technological discoveries, e.g. the invention of the erbium doped fiber amplifier and the development of wavelength division multiplexing, have paved the way to the rise of novel, bandwidth-eager services such as cloud computing, high-definition video streaming, social networking, etc. As of the early 2000s, a renewed interest in coherent optical communications coupled with digital signal post-processing, has considerably contributed to defer the capacity shortage. There is, though, a universally shared opinion in the scientific community that, short of other breakthroughs in the physical network infrastructure in order to overcome the constraint imposed by the nonlinear Shannon limit on the capacity of a single optical fiber, it will become harder and harder to keep optical communications technology ahead of the projected growth in demand for bandwidth.

Some of the solutions under investigation across the world include the use of space division multiplexing through a multicore fiber or multimode fiber, the development of wide-bandwidth amplifiers, the reduction of fiber attenuation and the mitigation of optical nonlinearity. In this scenario, distributed amplification

based on stimulated Raman scattering has attracted a great deal of attention, as it is able to provide quasi-lossless transmission over a broader bandwidth and a greatly improved balance between noise and nonlinear effects than the traditional lumped amplifiers can offer. Furthermore, Raman amplifiers in combination with digital or optical nonlinearity mitigation techniques have already proven suitable options towards faster, more spectrally efficient and farther reaching optical communications. However, Raman amplification is not entirely free of downsides: eye safety, optical damage, pumping efficiency and noise are some of the concerns that partly prevent its widespread implementation.

This study aims at the numerical modeling, experimental characterization and performance measurement of different Raman architectures for long-haul and unrepeatered optical communication applications, with a special focus on the impairments due to nonlinear effects, amplified spontaneous emission noise, relative intensity noise transfer from the fiber laser pumps to the signal and on how to minimize them. A number of configurations are analyzed that bring along various pros and cons and the best trade-off among main parameters found under different operational conditions.

In the first section of this manuscript a numerical optimization technique based on a multi-level approach that allows to remarkably reduce the computation time in the simulation of Raman amplifiers is presented, followed by the characterization of three amplification schemes: a 1st-order Raman amplifier, a closed cavity 2nd-order ultralong Raman fiber laser (URFL) and a half open cavity 2nd-order random distributed feedback (rDFB) amplifier. Afterwards, the importance of the average signal power distribution symmetry in data transmission based on optical phase conjugation for all-optical nonlinearity compensation is investigated, and asymmetry minimized for an rDFB architecture. Transmission experiment results are also presented, for both long-haul and unrepeatered optical systems employing a wide variety of cavity configurations, ranging from half open (rDFB) to fully closed (URFL).

The final section of this thesis deals with the experimental evaluation of the performance of a Raman polarizer based on low polarization mode dispersion (PMD) spun fiber and rDFB design. Raman polarizers take advantage of the intrinsic polarization-dependent gain of a Raman amplifier to concurrently amplify and re-polarize the signal thanks to the "polarization pulling" phenomenon. A highly polarized pump combined with a sufficiently long span of low-PMD fiber allows to achieve efficient polarization control with high gain. Thus, the impact of PMD is also analyzed by comparing the performance of several 1st-order Raman polarizer configurations with standard single mode fiber and different PMD values.

Resumen

Hace 50 años, cuando se introdujeron los cables de fibra para transmisión de datos a larga distancia, se pensaba que la capacidad de transmisión de información de los mismos, en comparación con los cables de cobre era ilimitada. A pesar de este pensamiento, hoy en día, la comunidad científica se está enfrentando a retos relevantes para hacer frente a la creciente demanda de datos. Con el 99 % de tráfico de datos que, a día de hoy, se transmiten a través de fibra óptica, y el 40 % de incremento de la cantidad de datos que, a nivel mundial, se intercambian cada año, estamos presenciando el acercamiento del así llamado fenómeno del "capacity crunch", que está previsto sucederá en el año 2020.

A lo largo de los últimos 30 años muchos descubrimientos tecnológicos, como por ejemplo la invención del amplificador de fibra dopada con Erbio y el desarrollo de la multiplexación por división de longitud de onda, han establecido el camino para el nacimiento de servicios novedosos y que requieren mucho ancho de banda como por ejemplo cloud computing, reproducción de videos online en alta definición, redes sociales, etc. A partir de los primeros años del nuevo milenio un renovado interés en las comunicaciones ópticas coherentes junto con el post-procesado digital de las señales, ha contribuido considerablemente a diferir la escasez de capacidad. Sin embargo, según un pensamiento compartido globalmente entre la comunidad científica, a menos que se logren otros avances en la estructura física de la red, para poder superar las restricciones impuestas por el limite no lineal de Shannon sobre la capacidad de una sola fibra óptica, se volverá cada vez más difícil mantener la tecnología de comunicaciones ópticas al frente de la creciente demanda de banda ancha.

Algunas de las soluciones que se están investigando en el mundo incluyen el uso de la multiplexación por división de espacio a través de fibras multinucleo o multimodo, el desarrollo de amplificadores de banda ancha, la reducción de la atenuación de la fibra y la mitigación de las no linealidades ópticas. En este escenario, la amplificación distribuida basada en scattering Raman estimulado ha atraído gran atención, siendo capaz de posibilitar transmisión casi sin perdidas en una banda más ancha, además de una mejora en el balance entre los efectos no lineales y el ruido que pueden ofrecer los amplificadores tradicionales. Asimismo, los amplificadores Raman en combinación con técnicas ópticas y digitales de mitigación de no linealidades han demostrado ser opciones apropiadas para alcanzar comunicaciones ópticas de mayor rapidez, eficiencia espectral y distancia de transmisión. Sin embargo, la amplificación Raman no está enteramente libre de inconvenientes: seguridad ocular, danos ópticos, eficiencia de bombeo y ruido son algunas de las preocupaciones que en parte impiden su amplia difusión.

Este estudio apunta al modelado numérico, la caracterización experimental y la medida de rendimiento de distintas arquitecturas Raman para aplicaciones a la comunicación óptica ultra-larga y sin repetición. Su enfoque particular consiste en evaluar las deficiencias relacionadas con los efectos no lineales, el ruido de emisión espontánea amplificada y el ruido de intensidad relativa transferido de los láseres de bombeo de fibra a la señal, y cómo minimizarlos. Además, a lo largo de este trabajo de investigación, han sido analizadas un gran número de configuraciones que conllevan varios pros y contras, y la mejor solución intermedia entre los principales parámetros ha sido encontrada bajo diferentes condiciones operacionales.

El primer apartado de este manuscrito presenta una técnica de optimización numérica basada en una estrategia multi-nivel, la cual permite reducir notablemente el tiempo de computación en la simulación de amplificadores Raman, seguida por la caracterización de tres esquemas de amplificación: un amplificador Raman de primer orden, un láser Raman de fibra ultralargo (URFL) de cavidad

cerrada de segundo orden y un amplificador de retroalimentación aleatoria distribuida (rDFB) de cavidad entreabierta de segundo orden. A continuación, se investiga la importancia de la simetría de la distribución de la potencia media de la señal en la transmisión de datos basada en la conjugación óptica de fase para la compensación óptica de las no linealidades, y se minimiza la asimetría en una arquitectura rDFB. Asimismo, se presentan los resultados de los experimentos de transmisión, tanto para los sistemas ópticos de larga distancia como para los sistemas sin repetición, que abarcan una amplia variedad de configuraciones entre las entreabiertas (rDFB) y enteramente cerradas (URFL).

El apartado final de esta tesis trata de la evaluación experimental de los rendimientos de un polarizador Raman basado en una fibra spun de baja dispersión por polarización de modos (PMD) además de en el diseño rDFB. Los polarizadores Raman se benefician de la ganancia, intrínsecamente dependiente de la polarización, de un amplificador Raman para amplificar y simultáneamente repolarizar la señal gracias al fenómeno de "atracción de polarización". Un bombeo altamente polarizado, combinado con un segmento de fibra de baja PMD suficientemente largo permite lograr un control de polarización eficiente con alta ganancia. Por consiguiente, también se analiza el impacto de la PMD comparando el rendimiento de varios polarizadores de primer orden con fibra monomodo estándar y distintos valores de PMD.

Acknowledgements

Many people have contributed in various capacities to the successful completion of this research, and to all of them goes my deepest appreciation. I wish to extend my immense gratitude and respect to my Supervisor and Director of this thesis, Dr. Juan Diego Ania-Castañón of the Instituto de Óptica "Daza de Valdés" at the Consejo Superior de Investigaciones Científicas, for his constant help and meticulous guidance. All along, at various phases of my thesis, he has filled all my efforts with constant inspiration and support transcending well above the academic level.

I would like to express my most sincere gratefulness also to Dr. Pedro Corredera. His infectious passion and enthusiasm for science as well as his assistance and advice have had a decisive influence on my ability to perform even the most arduous tasks in the lab.

During my relatively young research career I have been fortunate enough to meet and work side by side with many brilliant scientists, who are above all exquisite persons that tremendously helped me shape my attitude towards science and my professional life as a whole. Thus, I would like to take the opportunity to show my deeply felt appreciation to Prof. Roberto Gaudino of the Politecnico di Torino, Dr. Antonino Nespola of the Istituto Superiore Mario Boella, Dr. Russel Wilcox of the Lawrence Berkeley National Laboratory and Prof. Paul Harper of the Aston Institute of Photonics Technologies.

I wish also to thank all those people, friends, who have played a role to a different, but by no means less important, extent. Parts of this thesis could not have been completed without the technical and human support by Dr. Pawel Rosa, Dr.

Contents

List of Figures

xxiii

List of Tables

Acronyms

ASE   Amplified Spontaneous Emission

ASK   Amplitude Shift Keying

AWG   Arbitrary Waveform Generator

BER   Bit Error Rate

BPP   Backward Pump Power

BPSK   Binary Phase Shift Keying

BW   Backward

CW   Continuous Wave

DBP   Digital Back-Propagation

DCF   Dispersion Compensating Fiber

DD   Direct Detection

DFB   Distributed Feedback

DFG   Difference Frequency Generation

DML   Directly Modulated Laser

DOP   Degree Of Polarization

ACRONYMS

DP   Dual Polarization

DRA   Distributed Raman Amplifier

DRB   Double Rayleigh Backscattering

DSF   Dispersion Shifted Fiber

DSO   Digital Storage Oscilloscope

DSP   Digital Signal Processing

DWDM   Dense Wavelength-Division Multiplexing

EAM   Electroabsorption Modulator

ECL   External Cavity Laser

EDFA   Erbium Doped Fiber Amplifier

EVM   Error Vector Magnitude

F-BPS Filtered Blind Phase Search

FBG   Fiber Bragg Grating

FEC   Forward Error Correction

FOPA   Fiber Optical Parametric Amplifier

FPP   Forward Pump Power

FPR   Forward Pump Ratio

FSK   Frequency Shift Keying

FW   Forward

FWM   Four-Wave Mixing

GFF   Gain Flattening Filter

GVD   Group Velocity Dispersion

HNLF   Highly Nonlinear Fiber

IM   Intensity Modulation

ITU   International Telecommunication Union

LO   Local Oscillator

LW   Linewidth

MLSI   Mid-Link Spectral Inversion

MMA   Multi Modulus Algorithm

MMF   Multi-Mode Fiber

MSSI   Mid-Span Spectral Inversion

MZM   Mach-Zender Modulator

NA   Numerical Aperture

NF   Noise Figure

NISI   Nonlinear Inter-Symbol Interference

NLC   Nonlinear Compensation

NLPP   Non-Linear Polarization Pulling

NLSE   Nonlinear Schrödinger equation

NPS   Nonlinear Phase Shift

NRZ   Non-Return-to-Zero

NSNI   Nonlinear Signal-Noise Interaction

OBP   Optical Back Propagation

ACRONYMS

OOK   On-Off Keying

OPC   Optical Phase Conjugation

OSNR   Optical Signal-to-Noise Ratio

PC   Polarization Controller

PCTW   Phase-Conjugated Twin Waves

PDG   Polarization Dependent Gain

PM   Polarization Multiplexing

PMD   Polarization Mode Dispersion

PRBS   Pseudo Random Bit Sequence

PSA   Phase-Sensitive Amplification

PSK   Phase Shift Keying

QAM   Quadrature Amplitude Modulation

rDFB   random Distributed Feedback

RIN   Relative Intensity Noise

ROPA   Remote Optically Pumped Amplifier

RZ   Return-to-Zero

SBS   Stimulated Brillouin Scattering

SDM   Space-Division Multiplexing

SLA   Super Large Area

SMF   Single Mode Fiber

SOA   Semiconductor Optical Amplifier

SOP   State Of Polarization

SPM   Self-Phase Modulation

SPV   Signal Power Variation

SRS   Stimulated Raman Scattering

SSFM Split-Step Fourier Method

TOD   Third Order Dispersion

ULA   Ultra Large Area

ULL   Ultra Low Loss

URFL Ultra-long Raman Fiber Laser

VOA   Variable Optical Attenuator

VRM   Variable Reflectivity Module

WDM   Wavelength-Division Multiplexing

XPM   Cross-Phase Modulation

1

Introduction

Ever since the installation of the first telegraph for transatlantic exchange of information in 1866, telecommunication technology has undergone a tremendous transformation both in terms of speed and network extension. It wasn't until the second half of the twentieth century, though, with the advent of light-based transmission, that the slope of the capacity curve depicted in Fig. 1.1 took a decisive hike, showing an unprecedented increase in the bitrate-distance product of about eight orders of magnitude in less than 30 years.

In the late 1970s, after coherent optical sources [1] and low-loss optical fibers [2] became available, optical communication systems started being commercially deployed. As the operating wavelength was gradually shifted from the initial $0.8\,\mu m$ [3] first to a spectral region with lower loss and minimum dispersion around $1.3\,\mu m$ and, later, to the currently employed C-band around $1.55\,\mu m$ [4] where the dispersion issue was resolved by means of dispersion shifted fibers, bitrates of up to 10 Gb/s were achieved and the research efforts moved towards the replacement of optoelectronic regenerators, the real bottlenecks of the early generations of optical transmission systems. The breakthrough invention of optical amplifiers in the late 1980s allowed for all-optical, long-distance transmission over a few tens of thousands of km [5] and, soon thereafter, the wavelength-division multiplexing (WDM) technique [6] enabled

a further improvement of the bitrate by simultaneously propagating several channels through the same medium.
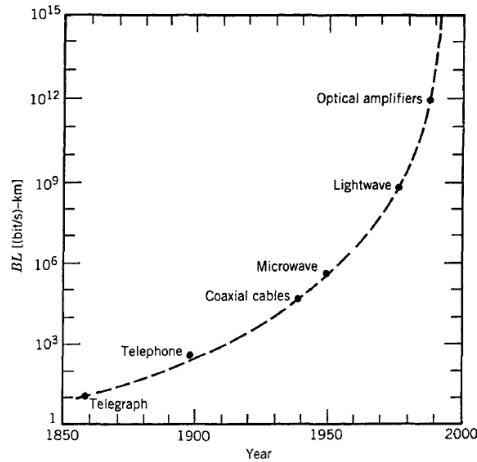
Figure 1.1: Evolution of the bitrate-distance product BL [7].

As of the end of the twentieth century WDM systems in combination with lumped Erbium Doped Fiber Amplifiers (EDFAs) have been installed worldwide. Although they still represent the core and backbone of the global network, new research trends have emerged, driven by the need to overcome the limitations related to the spectral efficiency of these systems. Thus, advanced modulation formats [8] for coherent detection techniques and novel amplification schemes [9] have been developed, respectively, to increase the amount of data encoded onto the optical carrier and improve the overall noise performance over an extended amplification bandwidth.

This thesis aims at improving the use of distributed amplification based on Raman scattering in optical fibers as a key tool to unlock the capacity of future optical fiber transmission systems. To do so, several Raman amplifier architectures are simulated, experimentally characterized and tested in the attempt to optimize their typical parameters, minimize impairments and enhance their benefits with respect to traditional EDFAs. A special focus is placed on the Relative Intensity Noise (RIN) transfer from the pump to the signal occurring in ultra-long Raman fiber laser (URFL) amplifiers and on the use of 2nd order Raman amplification under

different transmission conditions. Raman polarizers are also studied as a promising solution for simultaneous amplification and polarization of an optical signal, which can be potentially very useful in polarization-sensitive applications.

1.1 Motivation

Over the last four decades since the introduction of optical communication systems in the late 1970s, the capacity per fiber has been growing exponentially at a rate of 100 every 10 years, reaching several Tbits/s. Likewise, the bandwidth demand has also been swelling at an exponential rate, pushed by emerging new digital services and the overall ever-expanding centrality of telecommunications that permeates our society. Many technological advances, such as third-window semiconductor lasers, erbium doped fiber amplifiers, wavelength-division multiplexing, dispersion management, forward error correction and Raman amplification, have empowered this growth. However, it is now a fact that what was once seen as a limitless, profitable business opportunity, is now coming to a standstill as fiber capacity is limited [10], and the current network architectures and transmission technologies will not be capable of keeping up with the customer bandwidth demand in the medium term.
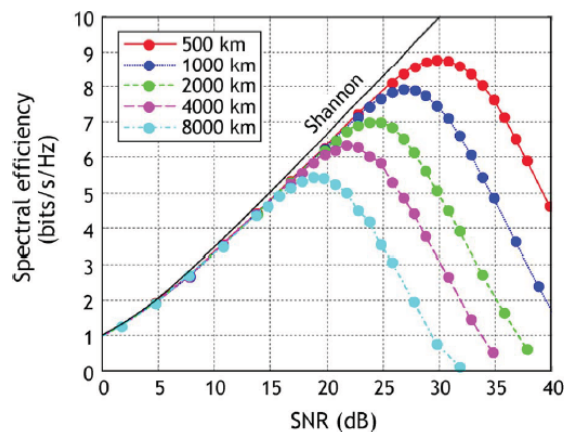
Figure 1.2: Spectral efficiency of an optical system as a function of the signal-to-noise ratio for various transmission distances [11].

The Shannon-Hartley theorem states that the maximum rate at which information can be

transmitted over a linear noisy communication channel of a specified bandwidth is given by the equation

$$C = B \cdot log_2 \left(1 + \frac{S}{N} \right) \tag{1.1}$$

where C is the channel capacity, B is the channel bandwidth, S is the average received signal power over the bandwidth, N is the average power of the noise in the bandwidth and S/N represents the signal-to-noise ratio at the receiver.

Assuming, without lack of realism, that the data traffic will continue growing in the future, according to Eq. (1.1), there exist a number of solutions to increase the amount of information supported by current single mode fibers: i) increase the launch power into the fiber to achieve better signal-to-noise-ratio at the receiver; ii) enhance the spectral efficiency (rate of information transmitted over a given bandwidth); iii) increase the bandwidth to accommodate additional channels. Although the first might appear straightforward and easy to implement, constraints imposed by safety concerns about fiber breakage and the nonlinear Kerr effects generated at high power levels, make it unpractical. In fact, as shown by Fig. 1.2, the linear capacity limit theorized by Shannon [12] in 1948 only sets an upper bound to the maximum achievable spectral density for an inherently nonlinear medium such as a standard fiber. Regardless of the transmission distance, efficiency increases with signal strength at low power, reaches a maximum value, then declines at higher signal powers as the increasing degradation from nonlinear effects more than offsets other benefits of higher signal power. This is called the "nonlinear Shannon limit" and it represents the main reason for the ongoing rush of research activity to avert the upcoming "capacity crunch".

While it is widely accepted that radical technological advancements (i.e. space-division multiplexing) will be required to simultaneously address the fiber capacity, fiber damage and power consumption issues, there is still room for improving the technology we are currently relying upon. Fig. 1.3 presents the evolution of the transmission capacity in optical fibers and highlights the closing gap between modern communication systems performance and the estimated maximum capacity per fiber of 100-200 Tbits/s. As the space-division multiplexing (SDM) technique seems unlikely to become mature enough for commercial deployment in
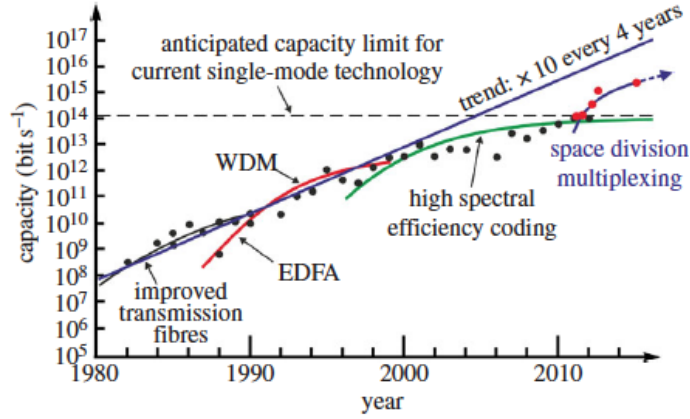
Figure 1.3: Evolution of transmission capacity in optical fibers [13].

the near future, researchers' efforts are focusing on the improvement of the spectral density by reducing fiber nonlinearities and enhancing the optical bandwidth.

Raman amplification can, thus, play a leading role as it is capable of providing high gain over an extended bandwidth centered around any wavelength where suitable pump sources are available, thanks to the spectral transparency of the Raman scattering effect, as well as a much better trade-off between nonlinear effects and generated amplified spontaneous emission (ASE) noise [14]. Despite some concerns related to laser safety, pumping efficiency and other sources of noise in the distributed amplification process, Raman amplifiers are becoming more and more common in optical communications, and record transmission performance have been achieved by combining them with novel methods for nonlinear impairments mitigation (i.e. optical phase conjugation, digital back propagation) in coherent detection systems using high-order modulation formats (i.e. PSK, QAM) and advanced digital signal processing (DSP) techniques.

1.2 Objectives of this work

In consideration of the suitability of distributed Raman amplification in a wide variety of applications to optical communications, ranging from long-haul to unrepeatered transmission

1. INTRODUCTION

and including polarization control techniques and distributed sensing, this work has been devised to improve our understanding of the physics that govern distributed amplifiers functioning through detailed characterization of some of the most popular architectures, to ameliorate current Raman-based optical communication systems performance in different transmission scenarios by mitigating some of the most adverse impairments they are affected by and, ultimately, to produce guidelines for the effective identification of the best configuration given the set of constraints for a specific application.

In more detail, the main objectives of this work are:

i. A detailed numerical comparison of different distributed amplification schemes, from the most simple and widely adopted 1st order Raman amplifier to more advanced and promising 2nd order solutions such as the Ultralong Raman Fiber Laser (URFL) and the random Distributed Feedback (rDFB) amplifier, in order to learn how key figures of merit such as achievable optical signal-to-noise ratio (OSNR), generated nonlinearities and average signal power variation (SPV) evolve according to a variation of the main amplifier parameters.

ii. An accurate experimental characterization of the mechanisms regulating the relative intensity noise transfer from the pumps to the signal in 2nd order schemes, in order to identify the operational conditions that can lead to the most efficient data transmission and enable the use of these amplifiers in a bidirectionally pumped configuration, so as to take advantage of the simultaneous reduction of RIN and ASE noise.

iii. An experimental optimization of the constitutive components of a 2nd order Raman amplifier, i.e. fiber length, fiber Bragg grating (FBG) reflectivity and pump laser power, in order to determine under what circumstances the best compromise can be found that maximizes benefits in terms of tolerance to RIN, maximum output OSNR and pumping efficiency in long-distance communications as well as in unrepeatered optical systems.

iv. The measurement of the transmission performance of the most favorable 2nd order architectures in order to demonstrate how coherent optical communication systems, either with or without the aid of nonlinear mitigation techniques, can benefit from the

6

aforementioned amplifier parameters optimization and the resulting optimal balance between noise and nonlinear impairments.

v. The experimental validation of some of the latest theoretical works on Raman polarizers, in order to achieve polarization control combined with an improved conversion efficiency in rDFB amplifiers and to confirm the dependence of the output degree of polarization (DOP) of the signal on the polarization mode dispersion (PMD) of the fiber.

1.3 **Structure of the thesis**

This thesis has been arranged to include 7 chapters. Chapter 1 has laid out the historical framework, the motivation and the main objectives of this work, highlighting the when, why and how this research was designed and developed.

In chapter 2 the theoretical background is presented. Fundamental notions of optical communications are explained, including optical fibers physical properties, the basics of light propagation in both linear and nonlinear regimes, a detailed description of the main nonlinear effects occurring in fiber-optic transmission and the distinction between discrete and distributed optical amplification. The final part of the chapter introduces essential concepts of optical transmission networks such as modulation techniques, detection methods and system configurations.

Chapter 3 is entirely dedicated to Raman amplification. The main advantages and drawbacks of the most common schemes are discussed. Sources of distortion in 1st order as well as higher order Raman amplifiers are theoretically reviewed and analyzed through a numerical model that describes the propagation of signals and the noise build-up in distributed amplifiers. In the last section of the chapter the first novel results of these work are also introduced: a multilevel numerical optimization of the main amplifier parameters based on the aforementioned model is presented and applied to the characterization of unrepeatered and long-haul transmission systems.

Chapter 4 to 6 report on the most important findings obtained during the course of this investigation. They all provide an initial theoretical introduction of the specific topic, followed

by a detailed account of the results and of the adopted methods.

The relative intensity noise issue in Raman amplification is at the core of this study and represents the main topic of chapter 4. It deals with the extensive examination of the RIN-affected amplified signal, performed both numerically and experimentally, for Raman amplifiers in various configurations and under different pumping conditions. Here, the search for the optimal amplifier design and the transmission performance of URFLs and rDFBs with variable RIN impact in long-haul, coherent telecommunications systems with phase modulation are presented.

In chapter 5, two of the latest techniques for nonlinear impairments reduction are reviewed. Optical Phase Conjugation (OPC) for all-optical mitigation and Digital Back Propagation (DBP) for DSP-based post compensation of nonlinear distortions have been separately examined in different transmission scenarios. The former has been evaluated through simulations, focusing on the SPV asymmetry impact on long-haul, coherent communications; the latter has been tested experimentally in unrepeatered systems under different RIN-induced stress levels.

In chapter 6 the novel concept of Raman polarizer is introduced and the results of the analysis of the generated Stokes lasing polarization properties are shown. The effects of fiber characteristics such as PMD, dispersion and Raman gain are examined in half-open and fully-closed cavities with polarized pump. The evolution of the signal state of polarization and DOP with the pump power, as well as the lasing threshold for each polarizer configuration are reported for four different types of optical fiber. It is worth mentioning here that these results are mostly preliminary, nevertheless they represent a solid advance in the study of Raman polarizers and, therefore, have been included in this dissertation.

Finally, conclusions are drawn in chapter 7, where a brief summary of the thesis and some possible future developments of the presented study are also included.

2

Fiber-Optic Communications

Fiber-optic communication is a particular type of optical communication in which information is transmitted between two far apart places by sending pulses of light through an optical fiber. To achieve so, every fiber-based optical system has to envisage a way to carry out the following steps: i) generation of an optical signal; ii) modulation of the optical carrier according to the information to be sent; iii) undistorted transmission of the signal along the fiber; iv) conversion of the received optical signal in the electrical domain.

The first generation of fiber-optic communication was developed in the late 1970s, when the first compact GaAs semiconductor lasers became available. The evolution of these early systems into the most recent fifth-generation ones was empowered by the concurrent advances in fiber components. The introduction of low-loss single mode fibers, followed by dispersion-shifted fibers for dispersion management and, ultimately, the invention of optical amplification, have allowed for an increasingly reliable transmission of data over optical fibers, and for the introduction of multi-channel, high-capacity transmission solutions such as WDM, where several different communication channels can be established simultaneously in the same link by allocating a separate wavelength to each one of them. Thus, today nearly

all of global long-distance telecommunications travel on fiber (see Fig. 2.1), and even local access networks are becoming increasingly fiber-oriented [15].

As communication systems become more and more complex in order to break the barrier set by the capacity constraint, new optical and digital technologies are being developed to cope with the distortion compensation issue. In this chapter the sources of the main impairments occurring during light propagation in optical fibers are discussed, together with a review of the concepts that are at the foundation of any fiber-optic transmission system.
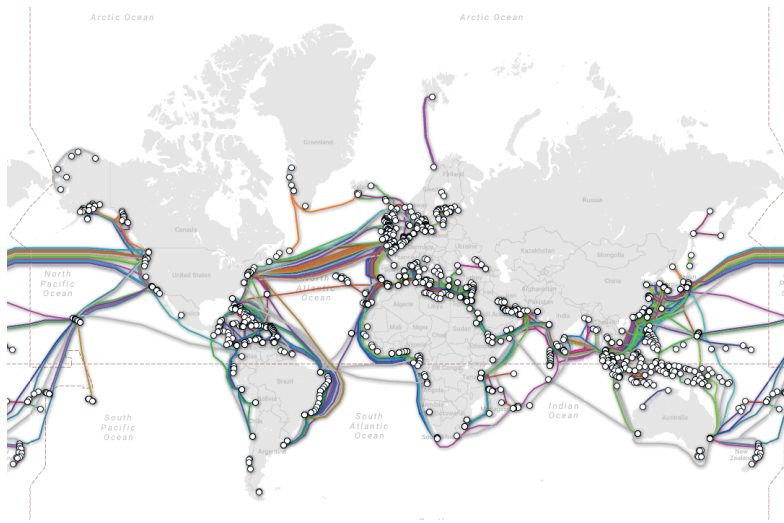
Figure 2.1: Submarine fiber links across the globe [16].

2.1 Optical Fibers

The possibility to manufacture low-loss dielectric optical waveguides was first theorized by Kao and Hockham in 1966 [17], who identified the dielectric material impurity as the main cause for the massive attenuation experienced by the lightwave, which at that time was in the order of 1000 dB/Km. The first high-purity optical waveguide based on fused silica, later referred to as optical fiber, was developed in 1972 by Maurer et al. [18]. It was a multi-mode fiber (MMF) with 17 dB/Km attenuation, capable of carrying 65000 times more information than copper wire. Today, optical fibers can be engineered to achieve extremely low losses

below 0.2 dB/Km, and many types of fibers can be manufactured thanks to the exceptional control over their physical parameters that modern production processes enable. A detailed exposition of optical fibers physics and technology can be found in [19]. Here, the discussion will focus on the most widespread form of optical fiber, the single mode fiber (SMF).

Optical fibers are circular dielectric wave-guides that consist of a cylindrical core of silica glass surrounded by a concentric cladding with slightly lower (by $\approx 1\%$) refractive index n_2, as shown in Fig. 2.2a. When the index change at the core-cladding interface is sharp the fiber is called step-index, as opposed to the graded-index fiber, where the refractive index profile within the core is a function of the radius d. This refractive index difference allows for a tight confinement of light into the core through the total internal reflection phenomenon depicted in Fig. 2.2b for a step-index fiber.
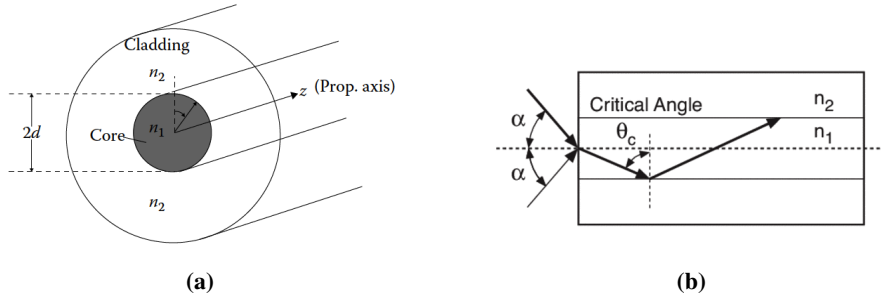
Figure 2.2: Optical fiber cross section (a) and light confinement through total internal reflection in step-index fibers (b).

Any light ray incident on the fiber-air interface at an angle α with the fiber axis z, bends inside the core because of refraction and hits the cladding at an angle θ with the perpendicular to the propagation axis. Total reflection occurs for angles larger than the critical angle θ_c defined as [20]

$$\theta_c = sin^{-1}\left(\frac{n_2}{n_1}\right) \tag{2.1}$$

where n_1 is the core index of refraction. If we define the numerical aperture (NA) of the fiber as the sine of $\alpha_{\max}$, the largest angle an incident ray can have for total internal reflectance in the core, we can use Eq. (2.1) combined with the Snell's law $n_0 sin(\alpha) = n_1 cos(\theta)$, where

$n_0 = 1$ is the air refractive index, to obtain

$$NA = sin(\alpha_{max}) = n_1 cos(\theta_c) = \sqrt{n_1^2 - n_2^2} \tag{2.2}$$

Thus, the larger the refractive index difference, the higher the NA of the fiber. A large-NA fiber can accept a higher guided optical power, therefore α_{max} is also called acceptance angle. However, a large acceptance angle results in a wider range of possible optical paths inside the core that leads to the distortion of the lightwave due to modal dispersion, a phenomenon caused by different modes reaching the output end of the fiber dispersed in time because they traveled along paths of different lengths.

The number of modes that can be propagated through a fiber depends on the core radius, the numerical aperture and the wavelength λ of the light being transmitted. These may be combined into the normalized frequency parameter or V number

$$V = \frac{2\pi d}{\lambda} NA \tag{2.3}$$

If $V \leq 2.405$ only the fundamental zero-order mode is transmitted. The light beam travels straight through the fiber, with no reflections from the core-cladding sidewalls at all, the fiber operates in single mode conditions and no intermodal dispersion is present. The core diameters of multi-mode fibers are much larger than single mode fibers. As a result, higher-order modes are also propagated. The International Telecommunication Union (ITU) standards G651.1 and G.652 set to $50\,\mu$m and $9\,\mu$m the core diameter for MMF and SMF respectively.

2.2 Pulse Propagation in Optical Fibers

The electromagnetic field propagation in optical fibers can be described by solving the following Maxwell's equations

$$\bigtriangledown \times \mathbf{E} = -\frac{\partial \mathbf{B}}{\partial t} \tag{2.4}$$

$$\bigtriangledown \times \mathbf{H} = \mathbf{J} + \frac{\partial \mathbf{D}}{\partial t} \tag{2.5}$$

$$\bigtriangledown \cdot \mathbf{D} = \rho \tag{2.6}$$

$$\bigtriangledown \cdot \mathbf{B} = 0 \tag{2.7}$$

where $\mathbf{E}$ and $\mathbf{B}$ are the electric and magnetic field vectors, respectively, and $\mathbf{D}$ and $\mathbf{B}$ are the corresponding flux densities. $\mathbf{J}$ is the current density vector and ρ is the charge density through which the electromagnetic field is generated. For a non conductive material such as the optical fiber, in absence of free charges, these two quantities can be set to 0. From Eqs. (2.4) and (2.5), we see that a time-changing magnetic field produces an electric field and a time-changing electric field or current density produces a magnetic field. The charge distribution ρ and current density $\mathbf{J}$ are the sources for generation of electric and magnetic fields. For the given charge and current distribution, Eqs. (2.4)-(2.7) may be solved to obtain the electric and magnetic field distributions. The terms on the right-hand sides of Eqs. (2.4) and (2.5) may be viewed as the sources for generation of field intensities appearing on the left-hand sides. The field vectors are related to the flux densities through the following equations

$$\mathbf{D} = \epsilon_0 \mathbf{E} + \mathbf{P} \tag{2.8}$$

$$\mathbf{B} = \mu_0 \mathbf{H} + \mathbf{M} \tag{2.9}$$

where ϵ_0 is the vacuum permittivity, μ_0 is the vacuum permeability, $\mathbf{P}$ is the induced electric polarization and $\mathbf{M}$ is the induced magnetic polarization, which is 0 in a nonmagnetic medium such as the optical fiber.

By applying the curl operator to Eq. (2.4) and using Eqs. (2.5), (2.8), (2.9) and the relation $\mu_0 \epsilon_0 = 1/c^2$, we can obtain the wave equation that describes light propagation in optical fibers

$$\bigtriangledown \times \bigtriangledown \times \mathbf{E} = -\frac{1}{c^2} \frac{\partial^2 \mathbf{E}}{\partial t^2} - \mu_0 \frac{\partial^2 \mathbf{P}}{\partial t^2} \tag{2.10}$$

where c is the speed of light in vacuum.

Any dielectric, including optical fibers, becomes a nonlinear medium when intense electromagnetic fields propagate through it. As a result, the relationship between the total induced polarization $\mathbf{P}$ and the electric field $\mathbf{E}$ is nonlinear and satisfies the relation

$$\mathbf{P} = \epsilon_0 \left(\chi^{(1)} \cdot \mathbf{E} + \chi^{(2)} : \mathbf{EE} + \chi^{(3)} \vdots \mathbf{EEE} + \cdots \right) \tag{2.11}$$

13

where $\chi^{(n)}$ is the n-th order susceptibility, and is a tensor of rank $n+1$. The linear susceptibility $\chi^{(1)}$ is the dominant contribution to **P** and includes effects such as fiber loss and material dispersion. The second-order susceptibility $\chi^{(2)}$ is responsible for nonlinear effects like second harmonic generation and sum-frequency generation and is negligible for symmetric molecules such as SiO_2. The third-order susceptibility $\chi^{(3)}$ represents nonlinear phenomena such as third-harmonic generation, four-wave mixing and nonlinear refraction. The contributions of susceptibilities higher than the 3rd order are in general small in transmission systems and can be neglected. Consequently, the induced polarization consist of the sum of a linear term $\mathbf{P}_L$ and a nonlinear term $\mathbf{P}_{NL}$, defined as

$$\mathbf{P_L}\left(\mathbf{r}, t\right) = \epsilon_0 \int_{-\infty}^{t} \chi^{(1)}\left(t - t'\right) \cdot \mathbf{E}\left(\mathbf{r}, t'\right) dt' \tag{2.12}$$

$$\mathbf{P_{NL}}\left(\mathbf{r}, t\right) = \epsilon_0 \int_{-\infty}^{t} \int_{-\infty}^{t} \int_{-\infty}^{t} \chi^{(3)}\left(t - t_1, t - t_2, t - t_3\right)$$
$$\vdots \mathbf{E}\left(\mathbf{r}, t_1\right) \mathbf{E}\left(\mathbf{r}, t_2\right) \mathbf{E}\left(\mathbf{r}, t_3\right) dt_1 dt_2 dt_3 \tag{2.13}$$

Under some assumptions and after several mathematical steps detailed in [21], Eq. (2.10) can be written in the form

$$\nabla^2 \mathbf{E} - \frac{1}{c^2}\frac{\partial^2 \mathbf{E}}{\partial t^2} = \mu_0 \frac{\partial^2 \mathbf{P}_L}{\partial t^2} + \mu_0 \frac{\partial^2 \mathbf{P}_{NL}}{\partial t^2} \tag{2.14}$$

and solved to obtain the following propagation equation

$$\frac{\partial A}{\partial z} = -\frac{\alpha}{2}A - \frac{j}{2}\beta_2 \frac{\partial^2 A}{\partial t^2} + \frac{1}{6}\beta_3 \frac{\partial^3 A}{\partial t^3} + j\gamma \left|A\right|^2 A \tag{2.15}$$

where β is the propagation constant that will be discussed in section 2.3.2 and γ is the nonlinear coefficient defined as

$$\gamma = \frac{n_2 \omega_0}{c A_{eff}} \tag{2.16}$$

where n_2 is the nonlinear refractive index and A_{eff} is the fiber effective mode area. Eq. (2.15) is often referred to as the nonlinear Schrödinger equation (NLSE) because it can be reduced to that form under certain conditions. It describes the evolution of the slowly varying amplitude of the pulse envelope $A\left(z, t\right)$ in a single mode fiber, where t is measured in a frame of reference moving with the pulse at the group velocity v_g. The four terms on the

right-hand side govern respectively, the effects of fiber loss ($\alpha > 0$), group velocity dispersion (β_2), dispersion slope (β_3) and fiber nonlinearity ($\gamma > 0$) on pulses propagating inside optical fibers. Depending on the initial width T_0 and the peak power P_0 of the incident pulse, either dispersive or nonlinear effects dominate along the fiber.

If we introduce a time scale τ normalized to the input pulse width and a normalized amplitude U defined respectively as

$$\tau = \frac{t}{T_0} \tag{2.17}$$

$$U(z,\tau) = \frac{A(z,\tau)}{\sqrt{P_0} exp(-\alpha z/2)} \tag{2.18}$$

$U(z,\tau)$ satisfies Eq. (2.15) in the form

$$j\frac{\partial U}{\partial z} = \frac{sgn(\beta_2)}{2L_D}\frac{\partial^2 U}{\partial \tau^2} - \frac{exp(-\alpha z)}{L_{NL}}|U|^2 U \tag{2.19}$$

where $sgn(\beta_2) = \pm 1$ depending on the sign of the group velocity dispersion (GVD) parameter β_2 and

$$L_D = \frac{T_0}{|\beta_2|}, \qquad L_{NL} = \frac{1}{\gamma P_0} \tag{2.20}$$

are called dispersion length and nonlinear length respectively.

Different propagation regimes can be defined depending on the relative magnitudes of L_D, L_{NL} and the fiber length L:

- $L \ll L_{NL}$ and $L \ll L_D$ - Both terms on the right-hand side of Eq. (2.19) are negligible and neither dispersive nor nonlinear effects are generated. The pulse shape is not affected and the fiber can be considered passive.

- $L \ll L_{NL}$ and $L \sim L_D$ - The predominant effect is that of GVD and nonlinearities can be neglected. This regime occurs when

$$\frac{L_D}{L_{NL}} = \frac{\gamma P_0 T_0^2}{|\beta_2|} \ll 1 \tag{2.21}$$

- $L \ll L_D$ and $L \sim L_{NL}$ - Nonlinear effects prevail over dispersion and changes in the pulse temporal profile and spectrum are likely. This regime occurs when

$$\frac{L_D}{L_{NL}} = \frac{\gamma P_0 T_0^2}{|\beta_2|} \gg 1 \tag{2.22}$$

15

- $L>L_D$ and $L>L_{NL}$ - When L is longer or comparable to both L_D and L_{NL}, dispersion and nonlinearity combine and new qualitative features arise in the temporal and spectral shape of the pulse from an interplay between GVD and nonlinear effects.

2.3 Linear Impairments

As it can be seen from Eq. (2.15), in the linear regime ($\gamma=0$ or $L \ll L_{NL}$) the only terms that play a role in pulse propagation are those related to signal attenuation and dispersion. The former has two main causes, material absorption and Rayleigh scattering, whereas the latter is primarily associated with chromatic dispersion and polarization mode dispersion. Fig. 2.3 summarizes the linear effects in an optical fiber.
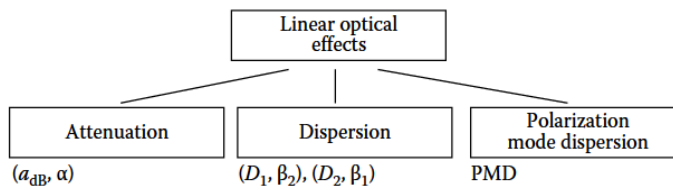
Figure 2.3: Linear effects in an optical fiber [22].

2.3.1 Fiber Loss

Before the advent of optical amplifiers, the maximum transmission distance of a fiber-optic system was determined by the fiber loss, as the optical receivers need a certain amount of optical power to detect the transmitted signal reliably. Now optical amplifiers are widely used and yet the maximum reach is affected by the fiber loss. This is because the optical amplifiers add noise whose power spectral density is proportional to the amplifier gain, which in turn is proportional to the fiber loss (see section 2.5). In other words, the amount of noise in a long-haul communication systems is directly related to fiber loss. In addition, if the fiber loss is small, the amplifier spacing can be increased, which reduces the system cost. So, it is important to design a fiber with the lowest possible loss.

If P_{in} is the optical power at the input end of a fiber, the optical power $P(z)$ at a point z along the fiber is

$$P(z) = P_{in} \cdot exp(-\alpha z) \qquad (2.23)$$

where α is the attenuation coefficient, commonly expressed in dB/km as

$$\alpha_{dB} = \frac{10}{ln(10)}\alpha \approx 4.343\alpha \qquad (2.24)$$

Eq. (2.23) shows that due to fiber loss the signal power decreases exponentially along the transmission line.

Fig. 2.4 shows the typical loss of a single mode fiber as a function of the wavelength. The minimum loss for most silica fibers is obtained at a wavelength around $1550\,\mathrm{nm}$. The theoretical lower limit to the achievable loss was found to be $0.114\,\mathrm{dB/km}$ [19] but, in practice, the lowest reported attenuation was $0.1484\,\mathrm{dB/km}$ [23]. Two fundamental loss mechanism govern the loss profile of an optical fiber:
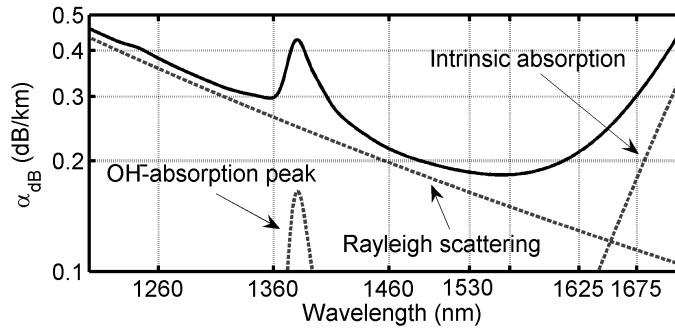
Figure 2.4: Fiber attenuation as a function of the optical wavelength.

i. **Rayleigh Scattering** - A light wave incident on a crystal causes the electrons in the atoms to oscillate and, consequently, emit light waves of the same frequency as the incident light in all directions. In a perfect crystal with uniformly spaced atoms, the secondary light waves add up coherently in the direction of the incident wave and destructively in any other direction, therefore no scattering takes place. However, any

perturbation in the crystal structure may break its homogeneity in such a way that emitted waves combine constructively over a range of directions, leading to scattering.

Rayleigh scattering arises from local microscopic fluctuations in density and compositional variations that result in the incident light being scattered over a range of angles. If the angle of scattering is less than the critical angle, it will escape to the cladding, otherwise part of the optical field is reflected and propagates in backward direction. These effects lead to loss of power in the forward-propagating signal. The loss coefficient due to Rayleigh scattering α_r is proportional to $1/\lambda^4$. Owing to this λ^{-4} dependance short wavelengths are scattered more than long wavelengths and, as a result, fiber-optic communication systems are operated in the infrared region instead of the visible region.

ii. **Material Absorption** - From the λ^{-4} dependance one may think that fiber loss can be almost entirely avoided by transmitting on longer wavelength ranges extending beyond the infrared portion of the spectrum. Unfortunately, pure silica is affected by resonance phenomena occurring on either side of the infrared region, that represent the intrinsic absorption of the material: the tails of electronic resonances in the ultraviolet region ($\lambda<0.4\,\mu$m) and vibrational resonances in the far-infrared region ($\lambda>7\,\mu$m) limit in practice the useful bandwidth to approximately the 1.3-1.6 μm spectral region.

Within this portion of the spectrum one of the major sources of extrinsic absorption also occurs: the OH ion of the water vapor is bonded into the glass structure and has a fundamental vibrational resonance at $2.73\,\mu$m. Its overtones and combination tones with the fundamental silica vibrational resonances lead to strong absorption at 1.38, 1.24, 0.95, and 0.88 μm wavelengths. In modern fibers the absorption peak around 1.4 μm has been reduced to less than about $0.35\,\mathrm{dB/km}$ by controlling the water content in the glass during the fabrication process [24].

2.3.2 Chromatic Dispersion

In general, the refractive index n of a fiber is dependent on the optical frequency ω. If v_p is the phase velocity of an optical signal in a fiber, the speed of light in the fiber is lower than

that in vacuum and given by

$$c = n\left(\omega\right) \cdot v_p \tag{2.25}$$

that is, different frequency components of a pulse travel at different speeds in glass, leading to pulse spreading. This phenomenon is called material dispersion. Its effect on a modulated signal can be described by considering the propagation constant β expanded in a Taylor series about the central frequency ω_0 of the pulse spectrum

$$\beta\left(\omega\right) = n\left(\omega\right)\frac{\omega}{c} = \beta_0 + \beta_1\left(\omega - \omega_0\right) + \frac{1}{2}\beta_2\left(\omega - \omega_0\right)^2 + \frac{1}{6}\beta_3\left(\omega - \omega_0\right)^3 + \cdots \tag{2.26}$$

where $\omega = 2\pi f$, f is the optical frequency of the signal and

$$\beta_m = \left.\frac{\mathrm{d}^m\beta}{\mathrm{d}\omega^m}\right|_{\omega=\omega_0} \qquad \left(for \quad m = 0, 1, 2, ...\right) \tag{2.27}$$

In Eq. (2.26) β_0 represents a constant phase shift and β_1 is associated with the group velocity as $\beta_1 = 1/v_g$. The second-order dispersion β_2 and the third-order dispersion β_3 represent the group velocity dispersion and the dispersion slope and are usually expressed in terms of the dispersion parameter D and the dispersion slope parameter S, respectively

$$D = -\frac{2\pi c}{\lambda^2}\beta_2 \tag{2.28}$$

$$S = \frac{4\pi c}{\lambda^3}\beta_2 + \left(\frac{2\pi c}{\lambda^2}\right)^2\beta_3 \tag{2.29}$$

Chromatic dispersion results from the combined effect of material dispersion and waveguide dispersion. Waveguide dispersion refers to the contribution arising from the difference in refractive index between the core and the cladding, which carries part of the propagating optical field. Generally, the waveguide contribution to β_2 is relatively small except near the zero-dispersion wavelength λ_0 where the two become comparable (see Fig. 2.5).

Interestingly, the waveguide contribution to D depends on the physical parameters of the fiber. Therefore, specialty fibers can be manufactured to have a displaced λ_0 by acting, for instance, on the core radius or on the core-cladding index difference. A specific example of such dispersion-shifted fiber (DSF) is called dispersion compensating fiber (DCF) [26] as the zero-dispersion wavelength is shifted to wavelengths beyond 1.6 μm in order to have
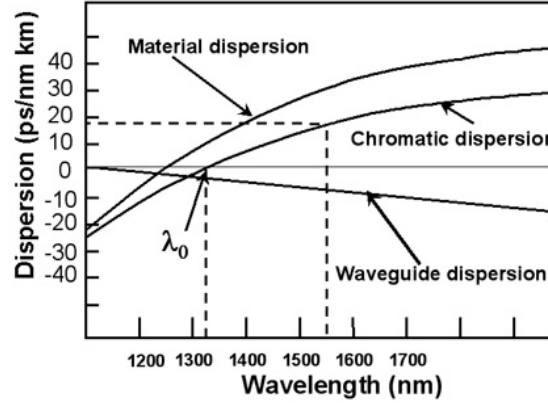
Figure 2.5: Fiber dispersion as a function of wavelength [25].

negative chromatic dispersion in the telecom transmission band. Thus, the overall positive dispersion accumulated during propagation in an SMF can be compensated for, in the optical domain, through propagation in a short section of high-negative-dispersion DCF. When $\beta_2 < 0$ an optical pulse experiences anomalous dispersion, where high-frequency components of the pulse travel faster than the low-frequency components, as opposed to the normal dispersion regime ($\beta_2 > 0$) where the opposite occurs.

2.3.3 Polarization Mode Dispersion

In reality, two orthogonally polarized modes propagate in a single mode fiber, one with propagation constant β_{x} along the x polarization and one with propagation constant β_{y} along the y polarization. In an ideal fiber with isotropic material and circular symmetry, these two modes are degenerate, i.e. $\beta_{\mathrm{x}} = \beta_{\mathrm{y}}$. However, an ideal manufacturing process free of imperfections is impracticable and some degree of asymmetry is introduced along the fiber core, which leads to birefringence and, in general, to $\beta_{\mathrm{x}} \neq \beta_{\mathrm{y}}$.

The birefringence B is defined as [27]

$$B = \frac{|\beta_{1x} - \beta_{1y}|}{k_0} = |n_x - n_y| \tag{2.30}$$

where $k_0 = 2\pi/\lambda$ and n_x and n_y are the refractive indices of the two orthogonal modes. The polarization axis with the smaller mode index is referred to as "fast axis", whereas the

polarization axis with the larger mode index is the "slow axis". Due to birefringence, the state of polarization of the light beam changes during transmission. The beat length L_b is defined as the propagation distance for which a 2π phase rotation is introduced between the two components. The beat length is wavelength dependent and is related to the birefringence by the following equation

$$L_b = \frac{2\pi}{\Delta\beta} = \frac{\lambda}{B} \tag{2.31}$$

As a result of fiber birefringence, components traveling in the two polarizations with different group velocities $1/\beta_{1x}$ and $1/\beta_{1y}$, arrive at the fiber output at different times, leading to pulse broadening when a polarization insensitive receiver is used. This phenomenon is known as polarization mode dispersion [28, 29]. Furthermore, for real transmission fibers, the birefringence changes randomly over time due to environmental changes such as stress induced fluctuations of the shape of the core, temperature changes, etc. Therefore, the pulse broadening due to PMD is stochastic in nature.

When two pulses travel a distance L, one pulse along the fast axis and one pulse along the slow axis of the transmission fiber, the arrival time difference $\Delta\tau$ of the two pulses at the output of the fiber is the differential group delay (DGD)

$$\Delta\tau = \left| \frac{L}{v_{gx}} - \frac{L}{v_{gy}} \right| = |\beta_{1x} - \beta_{1y}| L = (\Delta\beta_1) L = \frac{\omega B}{c} \tag{2.32}$$

Thus, the DGD also changes randomly with B, and the PMD cannot be estimated directly through Eq. (2.32) but rather by the root-mean-square value of $\Delta\tau$

$$\sigma_\tau^2 = \left\langle (\Delta\tau)^2 \right\rangle = 2 (\Delta\beta_1 L_c)^2 \left[exp\left(-L/L_c\right) + L/L_c - 1 \right] \tag{2.33}$$

where $\Delta\beta_1 \equiv \Delta\tau/L$ and L_c is the correlation length defined as the length over which two polarization components remain correlated. If $L_c \ll L$ Eq. (2.34) can be simplified to

$$\sigma_\tau \approx \Delta\beta_1 \sqrt{2L_c L} \equiv D_p \sqrt{L} \tag{2.34}$$

where D_p is the PMD parameter. Although a typical value of $0.1\,\mathrm{ps}/\sqrt{\mathrm{km}}$ for standard fibers appears unimportant, polarization mode dispersion is now the largest obstacle to further increase of the data-carrying capacity of fibers.

2.4 Nonlinear Impairments

As discussed in section 2.2, the lowest order nonlinear effects in optical fibers stem from the third order susceptibility. Due to $\chi^{(3)}$, the refractive index n of an optical fiber is dependent on the optical power $|A|^2$ of the transmitted signal and can be expressed as

$$n\left(\omega, |A|^2\right) = n_0\left(\omega\right) + n_2 \frac{|A|^2}{A_{eff}} \tag{2.35}$$

where $n_0\left(\omega\right)$ is the linear refractive index, n_2 is the nonlinear refractive index, A_{eff} is the effective mode area of the fiber and A is the amplitude of the optical field. This intensity-dependent phenomenon is known as the Kerr effect and is the cause of most of the fiber nonlinear effects.

The nonlinear effects in an optical fiber are presented in Fig. 2.6. They can have elastic or nonelastic nature: elastic nonlinear effects are associated with the power dependence of the refractive index (Kerr effect) and do not involve any energy exchange between the electromagnetic field and the dielectric medium. On the other hand, inelastic nonlinear effects are due to electronic vibrations in which the optical field transfers part of its energy to the nonlinear medium.
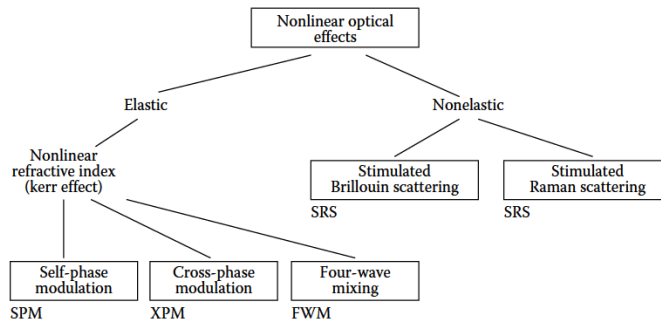
Figure 2.6: Classification of nonlinear effects in an optical fiber [22].

The Kerr nonlinearity can lead to self-phase modulation (SPM), cross-phase modulation (XPM) and four-wave mixing (FWM), whereas the inelastic scattering phenomenon can induce stimulated effects such as stimulated Brillouin scattering (SBS) and stimulated Raman scattering (SRS). When the incident power exceeds a certain threshold value the intensity of

scattered light grows exponentially. Brillouin generated phonons (acoustic) are coherent and give rise to a macroscopic acoustic wave in the fiber, in contrast to Raman scattering, where the phonons (optical) are incoherent and no macroscopic wave is generated.

Except for SPM and XPM, all nonlinear effects provide gain to some channel at the expense of depleting power from other channels. SPM and XPM affect only the phase of signals and can cause spectral broadening, which leads to increased dispersion.

2.4.1 Self-Phase Modulation

The dependence of the refractive index on the intensity, causes an intensity dependent phase shift to the signal. The impact of this phase variation can be studied by neglecting the effects of chromatic dispersion ($\beta_2=\beta_3=0$) in the NLSE equation (2.15)

$$\frac{\partial A}{\partial z} = -\frac{\alpha}{2}A + j\gamma \left|A\right|^2 A \tag{2.36}$$

where, again $A = A\left(z,t\right)$. The solution to this equation is given by

$$A\left(z,t\right) = A\left(0,t\right) \cdot exp\left(-\alpha z/2\right) \cdot exp\left(j\phi_{NL}\left(z,t\right)\right) \tag{2.37}$$

where $A\left(0,t\right)$ represent the field amplitude at $z=0$ and the induced phase modulation ϕ_{NL}, commonly called nonlinear phase shift (NPS), is defined as

$$\phi_{NL}\left(z,t\right) = \gamma \left|A\left(0,t\right)\right|^2 L_{eff} = \gamma P_{in}\left(t\right) L_{eff} \tag{2.38}$$

where L_{eff} is the effective length of a fiber with length L, defined as

$$L_{eff} = \frac{1 - exp\left(-\alpha L\right)}{\alpha} \tag{2.39}$$

that is, the section of the fiber where the influence of the Kerr effect is strongest.

The time dependence of P_{in} makes also ϕ_{NL} to vary in time. In other words, the optical phase changes with time in exactly the same way as the optical signal, and since this nonlinear phase modulation is self-induced, the nonlinear phenomenon responsible for it is called self-phase modulation. Usually, SPM is the dominant nonlinear effect for systems employing transmission fiber with high local dispersions, such as SSMF and DCF. The temporal variation of the nonlinear phase ϕ_{NL} results in the generation of new spectral components

far apart from the light wave carrier ω_0, indicating the broadening of the signal spectrum. In fact, SPM may also be interpreted as self-frequency modulation since phase and frequency modulation are closely related. The frequency deviation due to nonlinearity is given by

$$\Delta\omega = \frac{\mathrm{d}\phi_{NL}}{\mathrm{d}t} = \gamma L_{eff}\frac{\mathrm{d}P_{in}}{\mathrm{d}t} \tag{2.40}$$

It's worth mentioning that, in the anomalous dispersion regime ($\beta_2 < 0$) the GVD of SMF is negative and the GVD induced chirp is the inverse of the SPM induced chirp. As a result, GVD can compensate for the effect of SPM and, in principle, lead to distortion-free propagation of optical solitons [30]. Conversely, in the normal dispersion regime ($\beta_2 > 0$), the GVD effect adds to the SPM effect and often leads to additional pulse broadening.

2.4.2 Cross-Phase Modulation

When two or more optical channels are transmitted simultaneously inside an optical fiber using the WDM technique, the nonlinear phase shift for a specific channel depends not only on the power of that channel but also on the power of other channels. This phenomenon is called cross-phase modulation. Due to the intensity dependent refractive index, power fluctuations in a WDM channel are converted into phase fluctuations in other neighboring WDM channels. The phase shift for the *j*th channel becomes

$$\phi_j^{NL} = \gamma L_{eff}\left(P_j + 2\sum_{m \neq j}P_m\right) \tag{2.41}$$

where the sum is calculated over the number of channels. The XPM-induced phase shift can occur only when two pulses overlap in time. In practice, due to dispersive effects, pulses in different channels travel at different speeds and, therefore, overlap only for a limited propagation distance. The walk-off length L_w between two channels located at λ_1 and λ_2 represents this distance and is defined as the propagation length for which a faster moving pulse is shifted by one bit with respect to a slower moving pulse of a co-propagating channel

$$L_w = \frac{T_b}{|d_{12}|} \tag{2.42}$$

where T_b is the bit period and d_{12} is the walk-off parameter defined as

$$d_{12} = \frac{1}{v_{g1}} - \frac{1}{v_{g2}} = D\Delta\lambda \qquad (2.43)$$

where v_{g1} and v_{g2} are the group velocities of the two channels and $\Delta\lambda = |\lambda_1 - \lambda_2|$. Thus, the XPM impact is inversely proportional to the GVD, the channel spacing and the data rate.

2.4.3 Four-Wave Mixing

When three optical waves with carrier frequencies ω_1, ω_2 and ω_3 co-propagate simultaneously inside a fiber, a fourth wave is generated by $\chi^{(3)}$ at a frequency resulting from any of the following combinations

$$\omega_{FWM} = \omega_1 \pm \omega_2 \pm \omega_3 \qquad (2.44)$$

This nonlinear phenomenon is known as four-wave mixing [31]. For it to efficiently produce new frequency components, the momentum conservation imposes that a phase matching requirement be satisfied [21]. The most efficient process corresponds to the case in which two photons at frequencies ω_1 and ω_2 are destroyed and their energy transferred to two new photons at frequencies ω_3 and ω_4, such that $\omega_1 + \omega_2 = \omega_3 + \omega_4$. The phase-matching requirement for this process is $\Delta k = 0$, where

$$\Delta k = \beta\left(\omega_3\right) + \beta\left(\omega_4\right) - \beta\left(\omega_1\right) - \beta\left(\omega_2\right) \qquad (2.45)$$

and $\beta\left(\omega\right)$ is the propagation constant for an optical field with frequency ω.

Due to chromatic dispersion, the phase-velocity is not the same for all interacting signals. The smaller the difference in phase-velocity, the better the phase matching between different WDM channels and, consequently, the stronger the FWM generation. Thus, FWM is mostly a problem for transmission systems with low dispersive fibers (e.g. DSF) and with narrow channel spacing. For fibers with a high dispersion in the C-band such as SSMF, in general FWM does not limit the transmission performance and can be neglected.

From a different perspective, the FWM process can be harnessed e.g. to produce parametric amplification of a pre-existing wave at frequency ω_3 or ω_4 [32], or can take the form of a modulation instability (MI) process, which leads to the phase conjugation phenomenon discussed in section 5.1.

2.4.4 **Stimulated Raman Scattering**

Scattering processes occur when the photons of an optical signal interact with the molecular structure of the transmission medium. Rayleigh scattering (see section 2.3.1) is a form of elastic scattering in which the frequency of the scattered light does not change. Inelastic scattering phenomena, such as Raman scattering or Brillouin scattering discussed in section 2.4.5, involve a certain energy difference between the incident and scattered photons, that results in a frequency downshift.

When a pump wave propagates inside an optical fiber, a portion of the light is scattered by the material in such a way that part of the energy of the pump photons is absorbed by the silica molecules, which move from the ground state to an excited vibrational state (see Fig. 2.7b). As a result, the scattered photons have reduced energy and lower frequency. When the pump power exceeds a threshold value, this spontaneous process becomes stimulated and therefore is known as stimulated Raman scattering. SRS is an isotropic process that occurs in all directions and produces a Raman frequency shift $\Omega_R = \omega_p - \omega_s$ dependent on the vibrational energy levels of silica. ω_p and ω_s are, respectively, the optical frequencies of the pump and of the scattered signal, also called Stokes wave. If the molecule makes transition from a high-energy vibrational state to a low-energy vibrational state in the presence of an incident pump of energy $\hbar\omega_p$, the difference in energy is added to the incident photon, leading to a photon of higher energy $\hbar\omega_a$. This is known as anti-Stokes Raman scattering.

SRS is the underlying process that makes Raman amplification possible and will be discussed in detail in chapter 3.
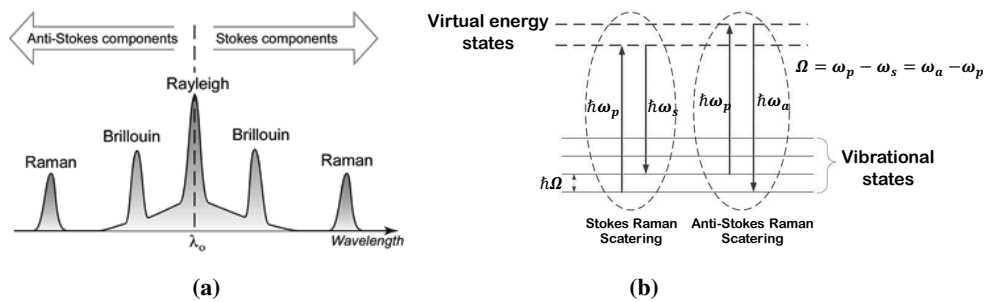
Figure 2.7: Spectrum of the scattering phenomena in an optical fiber [33] (a) and energy-level diagram of the stimulated Raman scattering process (b).

2.4.5 **Stimulated Brillouin Scattering**

An oscillating electric field at the pump frequency ω_p generates an acoustic wave through a phenomenon known as electrostriction [34]. The scattering of the pump wave from the acoustic wave with frequency Ω produces a Stokes wave at frequency ω_s. This form of scattering generated by the interaction of an optical signal with an acoustic wave is called Stimulated Brillouin Scattering. Both energy and momentum must be conserved in the scattering process, which yield respectively

$$\Omega = \omega_p - \omega_s, \qquad \mathbf{k}_A = \mathbf{k}_p - \mathbf{k}_s \tag{2.46}$$

where $\mathbf{k}$ is the wave vector for each wave. Using the dispersion relation $\Omega = |k_A| \, v_A$, where v_A is the acoustic velocity, the acoustic frequency is given by

$$\Omega = |k_A| \, v_A = 2 v_A \, |k_p| \, sin \, (\theta/2) \tag{2.47}$$

where $|k_p| \approx |k_s|$ was used and θ is the angle between the pump and the scattered waves. Eq. (2.47) shows that Ω is maximum in the backward direction ($\theta = \pi$) and null in the forward direction ($\theta = 0$), therefore in an optical fiber SBS can only propagate backward. This is one of the fundamental differences between SBS and SRS, that derive from different dispersion relations for acoustic and optical phonons. For instance, the backward propagating Stokes shift amounts to approximately $10\,\mathrm{GHz}$, as opposed to the $\sim 13\,\mathrm{THz}$ Stokes shift generated by SRS (see Fig. 2.7a), and it is extremely narrow ($<100\,\mathrm{MHz}$) compared to the Raman Stokes bandwidth that amounts to $\sim$20-30 THz.

2.5 **Optical Amplification**

Before the commercialization of optical amplifiers, it was necessary to electronically regenerate the optical signals every $80 - 100\,\mathrm{km}$ in order to achieve transmission over long distances by ensuring that the signal can be retrieved intelligibly at the receiving end. The optical signal was first converted to an electrical signal using a photodetector and then converted back to the optical domain after amplification in the electrical domain. This type of amplification, was a viable option in early fiber-optic systems where a single low-capacity channel was transmitted, but it quickly became unpractical when new generations of WDM-based communication

systems started to be designed. Such a regeneration technique used today, in modern systems, would result in highly expensive, power-hungry and bulky ad-hoc stations, and would ultimately represent the main bottleneck to the data rates that can be transmitted over an optical fiber. The theoretically available bandwidth of the fiber of tens of THz would be reduced to the few tens of GHz that the electronics can process.

In contrast, optical amplifiers can amplify the optical signals directly without requiring its conversion to the electric domain. They can amplify all WDM channels together, and are generally transparent to the number of channels, their bit-rate, protocol, and modulation format, which translates into a more easily upgradable optical link. Depending on the amplification scheme used, amplifiers can be divided into two categories known as lumped (or discrete) and distributed amplifiers. Most of the currently installed systems rely on EDFA-based lumped amplification, where a short length of erbium-doped fiber ($\sim 10\,\text{m}$), placed in a specific location, usually at the end of the transmission link, is used to compensate for losses accumulated over $60 - 80\,\text{km}$. Other rare-earth elements that can be used to manufacture doped-fiber discrete amplifiers include ytterbium (Yb^{3+}), neodymium (Nd^{3+}), thulium (Tm^{3+}) and holmium (Ho^{3+}) [35, 36]. The operational wavelength and tuning range of the amplifier change with the chosen dopant and are depicted in Fig. 2.8, where erbium is indicated as Er^{3+}.
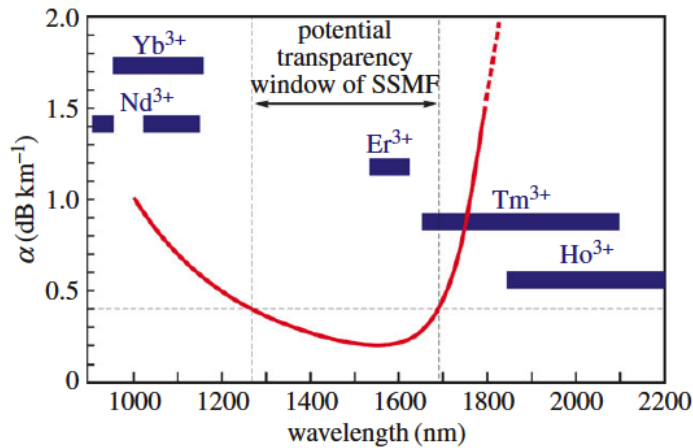
Figure 2.8: Amplification bands associated with rare-earth elements superimposed on the SMF transmission bandwidth [13].

Another class of optical devices for lumped amplification are the semiconductor optical amplifiers (SOAs). SOAs are amplifiers that use a semiconductor to provide the gain medium [37] and, unlike other optical amplifiers, are pumped electronically, via an applied current. Despite their small size and potentially low cost thanks to mass production, major drawbacks such as relatively low gain ($<15\,\mathrm{dB}$), low saturated output power ($<15\,\mathrm{dBm}$) and relatively high noise figure, make them unsuitable for multichannel WDM applications [38].

In contrast to lumped amplification, distributed amplification takes advantage of the non-linear scattering phenomena (SBS, SRS) that occur during propagation of an optical signal inside a dielectric medium, to achieve optical amplification over the entire fiber link. Distributed Raman amplifiers (DRAs) based on SRS are by far the most commonly used distributed amplifiers as stimulated Brillouin scattering can only provide a narrow bandwidth of about $100\,\mathrm{MHz}$, that severely limits its application in WDM systems.

DRAs are often used to enhance the performance of fiber optical parametric amplifiers (FOPAs) [39], a novel amplification technology based on FWM associated with the third-order Kerr nonlinearity of optical fibers [40, 41]. In FOPAs the shape of the optical gain spectrum is determined primarily by the fiber dispersion properties and, in addition to optical transparency they can, in principle, provide adjustable gain spectra, adjustable operating wavelength range, phase conjugation, pulsed operation for signal processing and a $0\,\mathrm{dB}$ noise figure when operated in phase-sensitive mode. However, to date FOPAs still do not offer an economically competitive alternative for telecom applications. In addition, the very same nonlinearity that provides the gain mechanism in FOPAs can also cause deleterious nonlinear crosstalk between multiple channels during amplification [42].

Today, EDFAs and DRAs remain the two families of amplifiers deployed in communication systems, hence they will be discussed in detail in section 2.5.2 and chapter 3 respectively.

2.5.1 Noise in Optical Amplification

An optical amplifier can be thought of as a laser without feedback. Defining P_{in} as the signal power at the amplifier input and P_{out} as the signal power after the amplification process, a simple amplifier model can be described by the following relation

$$P_{out} = GP_{in} \tag{2.48}$$

where G is the amplifier gain, a magnification factor produced by the gain medium (a doped silica fiber in the case of fiber amplifiers) of the amplifier.

The ability of an optical amplifier to produce gain is enabled by the population inversion mechanism of the ions within the gain medium: by applying an external energy source, the pump, the dopant ions are forced to move from the initial ground state to an excited state at a higher energy level. After some time the excited ions may decay into a lower energy level, releasing energy in the form of a photon. When this process takes place spontaneously, the generated photons are emitted in random spatial directions and the phenomenon is called spontaneous emission. However, when light propagates through the inverted medium at an adequate frequency, the photons can either be absorbed by the remaining atoms in the ground state, leading to attenuation, or stimulate the excited atoms to emit additional photons of the same frequency, phase and direction, producing amplification. This two processes are called absorption and stimulated emission, respectively. Population inversion, thus, ensures that a larger number of ions are in the excited state than in the ground state, so that amplification has a higher probability than absorption. On the other hand, when reinforced by the amplification process, spontaneous emission, which is also more likely to occur in an inverted medium, leads to amplified spontaneous emission (ASE), the main noise source in optical amplifiers.

Considering the noise contribution $n(t)$ introduced by the amplifier Eq. (2.48) becomes

$$P_{out} = GP_{in} + P_n \tag{2.49}$$

where P_n is the mean noise power. The noise added by the amplifier can be characterized by either the OSNR or the noise figure (NF). The OSNR is defined as

$$OSNR = \frac{\text{mean signal power}}{\text{mean noise power in a bandwidth of x nm}} = \frac{P_{out}}{P_n} \tag{2.50}$$

where the noise bandwidth is usually $0.1\,\text{nm}$, whereas the noise figure F of an amplifier is defined as the ratio of the electrical input SNR to the electrical SNR at the amplifier output [43]

$$F = \frac{SNR_{in}}{SNR_{out}} \tag{2.51}$$

Assuming an ideal photodetector affected by shot noise only, the SNR before amplification is given by [44]

$$SNR_{in} = \frac{I^2}{\sigma_s^2} = \frac{P_{in}}{2h\nu\Delta f} \tag{2.52}$$

where h is the Plank's constant, ν is the optical frequency, Δf is the detector bandwidth, $I = R_d P_{in}$ is the average photocurrent and σ_s^2 is the contribution of shot noise given by

$$\sigma_s^2 = 2q R_d P_{in} \Delta f \tag{2.53}$$

where q is the electron charge and $R_d = q/h\nu$ is the responsivity of an ideal photodetector.

The amplification process adds a gain factor to the shot noise contribution to the photocurrent and a component σ_{sp} resulting from the beating of spontaneous emission with the signal. Thus the total variance of the photocurrent is [44]

$$\sigma^2 = \sigma_s^2 + \sigma_{sp}^2 = 2q R_d G P_{in} \Delta f + 4 \left(R_d G P_{in} \right) \left(R_d S_{sp} \right) \Delta f \tag{2.54}$$

where S_{sp} is the spectral density of spontaneous emission noise given by [45]

$$S_{sp} = (G - 1) n_{sp} h\nu \tag{2.55}$$

where n_{sp} is the spontaneous emission factor defined as

$$n_{sp} = \frac{N_2}{N_2 - N_1} \tag{2.56}$$

with N_1 and N_2 being the population densities in the ground and excited state respectively.

The SNR of the amplified signal is thus given by

$$SNR_{out} = \frac{I^2}{\sigma^2} = \frac{R_d G P_{in}}{\sigma^2} \approx \frac{G P_{in}}{\left(4 S_{sp} + 2h\nu \right) \Delta f} \tag{2.57}$$

and substituting Eq. (2.52) and Eq. (2.57) in Eq. (2.51) yields the amplifier noise figure expressed as

$$F = 2 n_{sp} \left(1 - \frac{1}{G} \right) + \frac{1}{G} \tag{2.58}$$

From Eq. (2.58) it can be noted that the amplification mechanism entails a worsening of the output SNR by a factor of 2 even for an ideal amplifier with $G \gg 1$ and $n_{sp} = 1$.

Moreover, combining Eqs. (2.50), (2.55) and (2.58), the OSNR at the amplifier output is given by

$$OSNR = \frac{P_{out}}{(FG - 1)\,h\nu\Delta f} = \frac{GP_{in}}{(FG - 1)\,h\nu\Delta f} \tag{2.59}$$

For a constant output power P_{out}, Eq. (2.59) shows that the OSNR decreases with the amplifier gain. The higher the required gain is, the more ASE is added during the amplification process and thus the output OSNR reduces. Therefore, it can be concluded that a lower input power results in a higher OSNR degradation.

2.5.2 Erbium Doped Fiber Amplifier

At the heart of the EDFA amplification technology lies a short length of optical fiber whose core has been doped with around 0.1% Erbium ions. The other components shown in Fig. 2.9a are two laser diode pumps to generate population inversion, two WDM couplers to insert the pump light into the signal path and two isolators to block backward propagating components such as ASE and Brillouin scattering.
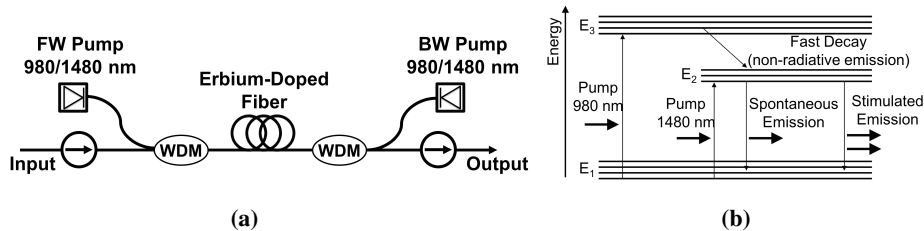
Figure 2.9: Block diagram of an EDFA (a) and energy-level diagram of the stimulated emission process (b).

As the signal propagates through the erbium-doped fiber, it stimulates emission of light from the excited ions, thereby amplifying the signal. The pumping configuration can be forward (FW) or backward (BW), but usually a combination of the two is chosen to achieve the best trade-off between the lower gain produced by FW only pumping, and the higher ASE noise generated through BW only pumping. As the Erbium ions can transition to several energy states when pumped at the appropriate wavelength, many different pumps can be used. However, effective EDFA pumping is usually obtained using more efficient semiconductor

lasers operating near $980\,\text{nm}$ or $1480\,\text{nm}$. As depicted in Fig. 2.9b the pumping process can be described by either a two-level or three-level energy scheme. In either case, directly or after a certain relaxation time ($\sim 1\,\mu\text{s}$), the excited photons reach a metastable state with energy E_2. From there, they can revert to the fundamental energy state either spontaneously (spontaneous emission) or stimulated to do so by some incident photon of exactly the same energy corresponding to the drop to a lower state (stimulated emission).

Owing to the presence of other co-dopants such as germania and alumina being integrated with Erbium ions into the glass of optical fibers, the level E_2 is a collection of sublevels. Hence, emitted photons can acquire slightly different energies, leading to a broad gain spectrum. The absorption and emission spectra of an EDFA are presented in Fig. 2.10.
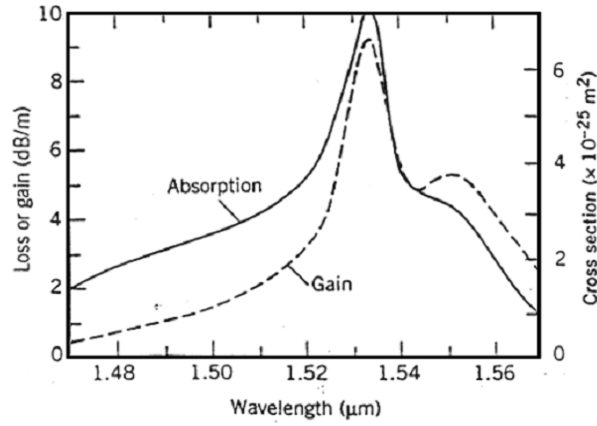
Figure 2.10: Absorption and emission spectra of an EDFA.

EDFAs are of particular interest in telecommunications because their emission spectrum shows a gain of more than $20\,\text{dB}$ over the range of 1530 - $1560\,\text{nm}$, which is the C-band in optical communication. In an EDFA the two population densities N_1 and N_2 vary along the fiber. Eq. (2.56) becomes

$$n_{sp} = \frac{\sigma_e N_2}{\sigma_e N_2 - \sigma_a N_1} \tag{2.60}$$

where σ_e and σ_a are the emission and absorption cross-sections of the erbium-doped fiber respectively. Eq. (2.60) can be inserted in Eq. (2.55) to obtain the spectral density of spontaneous emission in an EDFA amplifier. In a long-haul transmission system, many EDFAs

are cascaded to compensate for the fiber loss at the end of each span. Thus, the ASE noise accumulates and after transmission over N_{spans} identical spans, we have

$$P_{ASE}^{tot} = N_{spans} \cdot P_{ASE}^0 \qquad (2.61)$$

where P_{ASE}^0 is the contribution of a single amplifier to the total ASE noise P_{ASE}^{tot}. By combining Eq. (2.61) and Eq. (2.59), the OSNR at the output of an EDFA-based transmission system composed of several chained spans can be calculated as

$$OSNR^{tot} = \left[\frac{P_{out}}{N_{spans} \left(FG - 1 \right) h f_0 \Delta f} \right] \qquad (2.62)$$

The uneven gain spectrum shown in Fig. 2.10 can lead to slightly different gain levels being experienced by spaced apart channels in WDM transmission. When several cascaded EDFAs are used in long-haul communications, these gain discrepancies can propagate down the amplification chain and accumulate in large variations among channel powers that greatly affect the system performance. Filters with customized spectral responses are usually employed to compensate for this effect and flat gain bandwidths up to $35\,\mathrm{nm}$ can be achieved. Nevertheless, fully loaded WDM systems may require gain flatness over bandwidths as large as $50\,\mathrm{nm}$. For this reason, complex EDFA architectures have been developed [46, 47] to obtain uniform gain over up to $80\,\mathrm{nm}$, but wider bandwidths ($> 100\,\mathrm{nm}$) and lower noise figures can be achieved through multi-pump Raman amplifiers [48, 49, 50].

2.6 Optical Transmission Systems

A simplified schematic diagram of an optical communication system is depicted in Fig. 2.11. This model is quite general and applies to practically all existing optical systems. A fiber-optic transmission system, therefore, also consists of three main components: a transmitter, an optical channel and a receiver. An information source provides an electrical signal to the transmitter comprising an electrical stage, which drives an optical source to give modulation of the lightwave carrier produced by the laser. The optical source used for electrical-optical conversion may be either a semiconductor laser or a light-emitting diode (LED). The transmission channel consists of an optical fiber cable alone (unrepeatered transmission) or several

amplified fiber sections (long-haul transmission) and, in general, comprises all the in-line active or passive devices needed to convey a quality signal to the final user. The receiver includes an optical detector which drives a further electrical stage to provide demodulation of the optical carrier. The optical carrier may be modulated using either an analog or digital information signal. Analog modulation is often simpler to implement, but less efficient in fiber-optic communications, as it requires a much higher signal-to-noise ratio at the receiver than digital modulation. Hence, analog optical fiber communication links are generally limited to shorter distances and lower bandwidth operation than digital links.
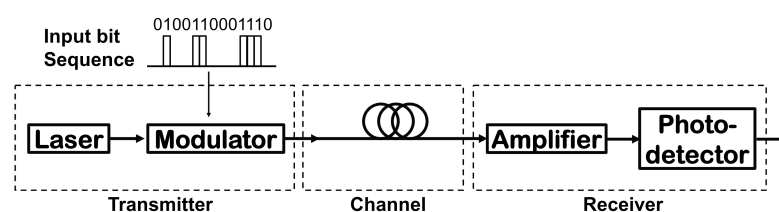
Figure 2.11: Simplified block diagram of an optical communication system.

The performance of a digital transmission system is measured in terms of bit error rate (BER), defined as the percentage of erroneous bits relative to the total number of bits received in a transmission. For example, a BER of 10^{-6} corresponds to one error per million bits.

As the main concepts and technologies related to the transmission channel have been presented throughout this chapter, in the following sections the discussion will focus on the most relevant elements of the transmission and detection stages of an optical telecom system.

2.6.1 The Transmitter

The main task of a transmitter is to map encoded information from the electrical domain to the optical domain. An optical source, usually a semiconductor laser, provides an optical signal that can either be directly or externally modulated. Semiconductor lasers, often in the distributed feedback (DFB) configuration, are used as optical source because of the advantages they can provide in terms of compact size, high efficiency, reliability and wavelength.

In its simplest form, modulation consists in turning on and off the light emitted by the laser, in accordance with the bit sequence to be transmitted. Direct modulation is achieved through direct control over the laser drive current: the optical source emits light to transmit 1s and no light when 0s are being transmitted. External modulation, on the other hand, relies on an additional device, the modulator, to switch on and off the continuous wave (CW) optical signal generated by the laser. External modulation is commonly preferred in high-speed optical communications thanks to its improved speed, extinction ratio and chirp-free operation. Directly modulated lasers (DMLs) performance, in fact, is limited by the population inversion delay and the inherent frequency chirp due to the refractive index variation with the carrier density.

Two types of external modulators are commonly used in optical communication systems. One relies on the modification of the absorption of a semiconductor material when an external electric field is applied (electroabsorption modulator, EAM), whereas the second type is based on the change of the refractive index observed for some crystals under an external electric field (electro-optic modulator). A change in refractive index itself does not permit modulation of the intensity of a lightwave. However, using an interferometric structure, such as the Mach-Zehnder structure, enables to convert the induced phase modulation into the desired intensity modulation. In most transmission systems, external modulation is realized through a modulator of the second type, called Mach-Zender modulator (MZM), that offers significant features in terms of bandwidth and extinction ratio, defined as the difference in intensity between the 1 level and the 0 level.

So far, we have implicitly assumed that modulation is carried out in the digital domain. In practice, the original electrical signal can be in analog form, but digital modulation is extremely more robust than the analog one, thus, in modern telecommunications the analog signal is always converted into a digital bit stream consisting of a pseudorandom sequence of 0 and 1 bits.

There are three basic types of digital modulation techniques: amplitude shift keying (ASK), frequency shift keying (FSK), and phase shift keying (PSK), in which the parameter that is varied is the amplitude, frequency, or phase of the carrier, respectively. Let the laser

output be

$$c\left(t\right) = A \cdot cos\left(2\pi f_c t + \theta\right) \tag{2.63}$$

where A, f_c and θ are the constant amplitude, frequency and phase of the signal. Basic features of the modulation formats most relevant to this work can be described as:

i. **Amplitude shift keying** - When the amplitude A is varied in accordance with a message signal $m(t)$ while keeping f_c and θ constant, amplitude modulation is performed. Thus, the modulated signal is given by

$$s\left(t\right) = k_a m\left(t\right) \cdot cos\left(2\pi f_c t + \theta\right) \tag{2.64}$$

where k_a is called amplitude sensitivity.
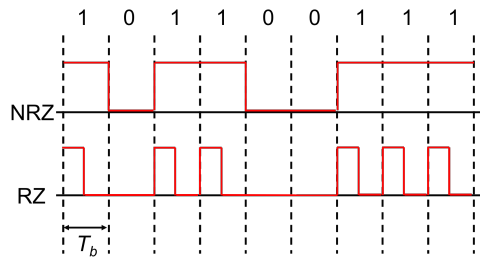
Figure 2.12: NRZ (top) and RZ (bottom) coding.

Sometimes referred to as on-off keying (OOK), is the standard modulation format in commercially deployed optical transmission systems and transmits logical 1 when intensity of the pulse is high and logical 0 when it's low. Its two main variants are non-return-to-zero OOK (NRZ-OOK) and return-to-zero OOK (RZ-OOK), depending on the technique used to encode the message signal. In the RZ format the amplitude of the optical pulse returns to zero before the bit duration is over, according to a certain duty-cycle, whereas in the NRZ format pulse width T_p is equal to the bit duration T_b, as shown in Fig. 2.12. As a result, NRZ provides a narrower (depending on the duty-cycle) bandwidth occupation than RZ, but RZ is more robust to interfering effects due to pulse broadening [51], which makes it the preferred choice in high-speed communications above $40\,\text{GBps}$ [52, 53].

ii. **Phase shift keying** - When the phase θ is varied in accordance with a message signal *m(t)* while keeping *A* and f_c constant, phase modulation is performed, and the modulated signal can be written as

$$s(t) = A \cdot cos\left[2\pi f_c t + k_p m(t)\right] \tag{2.65}$$

where k_p is called phase sensitivity. When $m(t)$ is a digital signal and the phase θ admits two possible values θ_1 and θ_2, with a $180°$ phase jump between them, the modulation scheme is known as binary phase-shift keying (BPSK). Generally speaking, BPSK has the same bandwidth requirement as ASK, but yields a $3\,\mathrm{dB}$ receiver sensitivity improvement [54, 55] and is one of the most robust modulation techniques. Like OOK, PSK can be implemented in RZ and NRZ format.

iii. **Quadrature Amplitude Modulation** - The combination of the two previous modulation schemes, where both amplitude and phase are varied simultaneously, is known as quadrature amplitude modulation (QAM). A QAM signal may be interpreted as a signal obtained by simultaneous amplitude modulation of in-phase and quadrature carriers. In fact, the modulated signal is given by

$$s(t) = m_I(t) cos(2\pi f_c t) + m_Q(t) sin(2\pi f_c t) \tag{2.66}$$

where the amplitude of the in-phase carrier $cos(2\pi f_c t)$ is modulated by $m_I(t)$ and that of the quadrature carrier $sin(2\pi f_c t)$ is modulated by $m_Q(t)$. Also QAM can be implemented in RZ and NRZ format.

So far the use of binary coding has been assumed, in which the bits 0 and 1 satisfy a one-to-one correspondence with the signal levels. Digital communication devices, however, allow for a much more efficient utilization of the available bandwidth via the implementation of multilevel signaling. With this strategy, the bit-stream is segmented in consecutive groups of *M* bits that are associated with one of the 2^M possible signaling values (symbols). As a consequence, high-order versions of the previously discussed modulation formats can be defined. As an example, Quadrature phase shift keying (QPSK) with $M = 2$, transmits two bits per symbol. In other words, a QPSK symbol doesn't represent 0 or 1, it represents 00,

01, 10, or 11. Multilevel signaling is used as a means of compressing the bandwidth required to transmit data at a given bit rate. Each symbol can represent more than one bit of data, thus, the number of symbols that needs to be transmitted is less than the number of bits (that is, the symbol rate is less than the bit rate), and hence the bandwidth is compressed. The main drawback of the multilevel scheme is that symbols are separated by a smaller voltage than in the binary scheme. This means that when noise is added to the data signal, the probability of the noise changing one symbol to another is increased.

It is often convenient to represent a modulated signal using a phasor or constellation diagram. Using this scheme, the phase of the signal is represented by the angle, and the amplitude by the distance from the origin or centre of a unit circle, so that the symbols can be displayed as points whose location is identified by their in-phase and quadrature components. Some of the most popular constellations are sketched in Fig. 2.13. It can be noted that 4-QAM
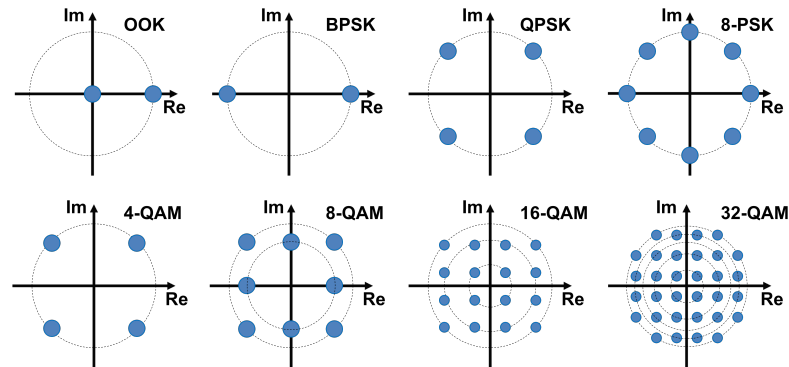
Figure 2.13: Constellation diagrams for various modulation formats.

uses the same signaling scheme as QPSK; the aforementioned $3\,\mathrm{dB}$ sensitivity improvement of BPSK with respect to OOK can be explained with the separation between constellation symbols, which is doubled in BPSK; as the number of amplitude levels increases, the distance between adjacent symbols shortens drastically, resulting in higher required OSNR at the receiver to reduce the probability of error in the decision process.

In recent times, another degree of freedom is being actively exploited to improve the capacity of the optical channel: polarization. Polarization multiplexing (PM), or dual polar-

ization (DP) transmission schemes can increase spectral efficiency, either by transmitting two different signals at the same wavelength but in two orthogonal polarizations, or by transmitting adjacent WDM channels in alternating polarizations to reduce coherent WDM crosstalk or nonlinear interactions between the channels (polarization-interleaving).

All things considered, advanced modulation of signal parameters such as frequency, phase and polarization, often combined with classic amplitude modulation, can greatly enhance our capability to transmit data efficiently. However, this comes at the cost of an increased receiver complexity. The traditional direct detector, in fact, operates on a square law principle, in which the output of the detector is proportional to the intensity (i.e. the square of the input signal magnitude). Thus, a direct detection (DD) receiver is not able to track frequency or phase changes, but only amplitude variations, and to fully benefit from an advanced modulation technique coherent detection must be employed.

2.6.2 The Receiver

The receiver is the device appointed to convert the optical signal received at the output end of the optical fiber back into the original electrical signal. In its simplest form, an optical receiver can be seen as composed by two stages: photodetection and demodulation. The photodetector converts light into electricity through the photoelectric effect. The main requirements for efficient photodetection (high sensitivity, fast response, low noise, low cost and high reliability) are effectively met by semiconductor photodetector such as *p-n*, *p-i-n* or avalanche photodiodes. These are usually followed by electrical amplification, filtering and a decision circuit. The demodulator design depends on the specific modulation format and its complexity ranges from rather simple direct detection schemes, when intensity modulation (IM) is used at the transmitter, to advanced coherent demodulation setups, when information is coded into phase of the optical carrier.

One of the key parameters of any receiver is the sensitivity. It is defined as the minimum average power required to obtain a certain BER and it is directly affected by the numerous noise sources at the different stages of transmission, propagation and detection. Shot noise introduced by the photodetection process and intrinsic thermal noise are two of the noise contributions of the receiver itself, but sensitivity is also limited by phase noise and relative

intensity noise of the laser and the electronic noise at the transmitter side, as well as by backreflections of the Fresnel type, scattering phenomena and ASE occurring in the optical channel. The cumulative effect of all these noise sources degrades the SNR at the decision circuit and, therefore, reduces the receiver sensitivity.

In an optical communication system, the photodetector can be configured either as a direct or incoherent detector, or as a coherent detector:

i. **Direct detection** - The detector converts the incident radiation into an electrical signal (sometimes called the photo-signal) that is proportional to the power of the incident light. There is no phase or frequency information and the photo-signal is then processed electronically using a low-noise preamplifier followed by signal processing circuits. As depicted in Fig. 2.14, in between these two stages a high-gain amplifier (Amp) followed by a low-pass filter (LPF) are used to further increase the electric SNR and, thus, diminish the probability of error in the decision. The data-recovery section consists of a decision circuit and a clock-recovery circuit. At the sampling time (usually in the middle of the bit interval), the decision circuit interprets the received photocurrent as 1 if it is above a certain threshold, otherwise the received bit is 0. The sampling time for the decision is provided by a clock which is extracted from the received signal using a clock-recovery circuit.
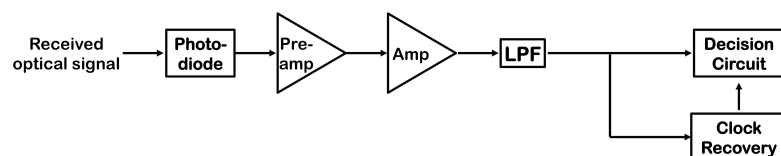
Figure 2.14: Schematic diagram of a direct detection receiver.

ii. **Coherent detection** - A coherent detector converts phase variation in amplitude variation, therefore the output electrical signal is related to the phase of the input as well as the input power. The coherent detection technique combines the incoming optical signal coherently with a CW optical field (local oscillator, LO) before detection. Let

the optical signal incoming from the transmitter be

$$E_s\left(t\right) = A_s cos\left[2\pi f_0 t + \phi_s\left(t\right)\right] \tag{2.67}$$

where A_s is the amplitude, f_0 is the carrier frequency and $\phi_s(t)$ is the phase. Likewise, the optical field associated with the local oscillator is given by

$$E_{LO}\left(t\right) = A_{LO} cos\left[2\pi f_{LO} t + \phi_{LO}\left(t\right)\right] \tag{2.68}$$

where A_{LO}, f_{LO} and $\phi_{LO}(t)$ are the amplitude, frequency and phase of the LO, respectively. The optical power reaching the photodetector when signal and LO are on the same polarization is

$$P\left(t\right) = \left|E\left(t\right) + E_{LO}\left(t\right)\right|^2 = P_s + P_{LO}$$
$$+2\sqrt{P_s P_{LO}} \cdot cos\left[2\pi f_{IF} t + \phi_s\left(t\right) - \phi_{LO}\right] \tag{2.69}$$

where $P_s = A_s^2$, $P_{LO} = A_{LO}^2$ and $f_{IF} = f_0 - f_{LO}$ is called intermediate frequency. This detection technique is known as heterodyne, as opposed to homodyne detection where $f_{IF} = 0$. In either case, Eq. (2.69) shows that the amplitude and phase modulations imprinted on the received optical signal are transferred unaltered to the radio-frequency signal resulting from the beating of the received signal with the LO, which can be electronically processed to recover the bit stream.
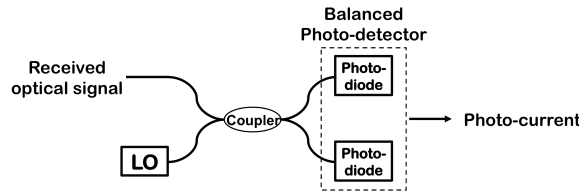
Figure 2.15: Schematic diagram of a coherent detection receiver.

The block diagram of a coherent receiver is shown in Fig. 2.15. A $3\,\mathrm{dB}$ optical coupler is used to mix the received signal and the LO and concurrently add a π phase shift to either one of the two signals. Balanced detection is used in order to suppress the DC

component and maximize the signal photocurrent $I(t)$ at the balanced detector output given by

$$I\left(t\right) = RP\left(t\right) = R\left(P_s + P_{LO}\right) + 2R\sqrt{P_s P_{LO}}$$
$$\cdot cos\left[2\pi f_{IF}t + \phi_s\left(t\right) - \phi_{LO}\right] \tag{2.70}$$

where R is the detector responsivity.

Coherent detection main advantages with respect to direct detection are:

- It can extract amplitude, frequency, and phase information from an optical carrier, and consequently can achieve much higher capacity in the same bandwidth.

- Usually $P_{LO} \gg P_s$, thus the local oscillator acts as a sort of optical preamplifier, reinforcing the received low-power signal and de facto improving the sensitivity. The generated electric current has a much higher intensity than in DD and is much more robust to the noise generated in the receiver.

- In a WDM environment, coherent detection allows the filtering of a desired channel to reside entirely in the electrical domain, taking advantage of the sharp cutoff characteristics of electrical filters.

- It is habitually used in combination with DSP techniques that can compensate for very large chromatic and polarization mode dispersion due to optical fibers, and eliminate the need for optical dispersion compensators and the associated optical amplifiers.

3

Distributed Raman Amplification

Raman amplifiers are a particular class of optical amplifiers based on the stimulated Raman scattering process presented in section 2.4.4. When research on Raman amplification started in the 1970s, high power pumps at the appropriate wavelength, needed to generate meaningful gain levels, had not been developed yet. The commercialization of EDFAs in the early 1990s further contributed to the fading interest in the Raman technology for telecommunications. In the late 1990s, when high power pump lasers became available, Raman amplification started to yield significant improvements over the established EDFA technology in terms of transmission reach and broadband operations, and is now one of the preferred solutions in optical transmission systems.

Stimulated Raman scattering is a fundamental nonlinear process that turns optical fibers into broadband amplifiers. First predicted by Adolf Smekal in 1923 it was then reported by G. Landsberg and L. Mandelstam and, a few days later, by C. V. Raman who was ultimately awarded the Nobel Prize for his work on the scattering of light in 1930. Although Raman amplification in optical fibers was observed as early as 1972, until recently SRS was mainly viewed as a harmful nonlinear effect because it can also severely limit the performance of

multichannel lightwave systems. Three important features are: (i) SRS can occur in any fiber; (ii) because the pump photon is excited to a virtual level, Raman gain can occur at any signal wavelength by proper choice of the pump wavelength; (iii) the Raman gain process is very fast (order of fs).

The main advantages and disadvantages of Raman and EDFA amplification schemes are summarized in Fig. 3.1. As a general guideline, Raman amplifiers can provide improved bandwidth, noise figure and gain flatness, without the need to resort to specialty optical fiber. However, additional issues arise in Raman amplification that are not present in EDFA. These include a reduction in pump efficiency and additional noise contributions, such as the one related to the relative intensity noise of the pump lasers. Other advantages in terms of signal power variation and signal power asymmetry are related to the distributed nature of the amplification process and will become clear in the following chapters.

	SMF-Based	Bandwidth	Gain Flatness	Noise Figure	Gain	Pump Efficiency	Signal Power Variation	Signal Power Symmetry	RIN Transfer
Raman	☺	☺	☺	☺	☹	☹	☺	☺	☹
EDFA	☹	☹	☹	☹	☺	☺	☹	☹	☺

Figure 3.1: Pros and cons of Raman amplification with respect to EDFA technology.

A schematic example of a Raman amplifier is depicted in Fig. 3.2. It comprises one or more CW pumps at either end of a standard single mode fiber. Light emitted by the laser at the transmitter side travels with the signal towards the output end and is called forward (FW), or co-propagating pump. Conversely, the backward (BW) or counter-propagating pump travels in opposite direction to the signal. WDM couplers are used to combine into the same SMF the signal and the pump, which need to have different wavelengths for Raman amplification to take place.

During the SRS process, part of the energy of the pump photons is lost to molecular vibrations of the dielectric material, hence the generated photons have a lower energy or, equivalently, a lower frequency. In standard transmission fibers made of silica with some Germanium doping in the core, the frequency (or Stokes) shift resulting from the energy difference between the pump and the signal photon, has its peak at about $13.2\,\mathrm{THz}$. As
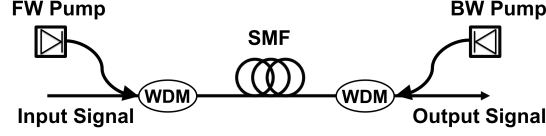
Figure 3.2: Schematic diagram of a Raman amplifier.

many vibrational states at slightly different energies are possible, the gain provided by SRS is rather broad and is shown in Fig. 3.3 for two relative states of polarization between the pump and the signal. The Raman gain is maximum when pump and signal are co-polarized (solid curve), and minimum when pump and signal are orthogonally polarized (dotted curve). In practice, the polarization dependence is reduced by combining two orthogonally polarized pumps to create a circularly polarized pump, or by depolarizing the pumps.
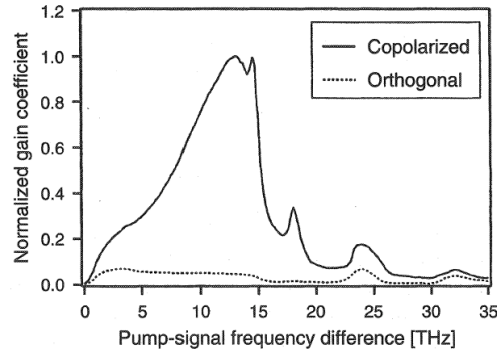
Figure 3.3: Normalized Raman gain profile for co-polarized (solid curve) and orthogonally polarized (dotted curve) pump and signal in silica fibers.

The coupled differential equations that govern the Raman amplification process under the assumption of depolarized pumps are [56]

$$\frac{\mathrm{d}P_s}{\mathrm{d}z} = g_R P_p P_s - \alpha_s P_s \tag{3.1}$$

$$\pm\frac{\mathrm{d}P_p}{\mathrm{d}z} = -\frac{\omega_p}{\omega_s} g_R P_p P_s - \alpha_p P_p \tag{3.2}$$

where the $\pm$ sign is associated with a co-propagating or counter-propagating pump wave respectively, P_p is the pump power, P_s is the signal power and α_s and α_p are the attenuation of

the fiber at the signal and pump frequency respectively, ω_p and ω_s are the angular frequencies of the pump and the signal and g_R is the Raman gain coefficient normalized by the effective area of the fiber. By integrating Eq. (3.1), the signal gain in a DRA can be obtained

$$G\left(z\right) = \frac{P_s(z)}{P_s(0)} = exp\left[g_R \int_0^z P_p\left(z\right)dz - \alpha_s z\right] \tag{3.3}$$

and the corresponding nonlinear phase shift due to self-phase modulation accumulated over a fiber of length L is [21]

$$\phi_{NL} = \gamma \int_0^L P_s\left(z\right)dz = \gamma P_s\left(0\right)\int_0^L G\left(z\right)dz \tag{3.4}$$

If the SMF employed as the transmission medium coincides with the gain medium, the amplifier is a distributed Raman amplifier and the SMF length is of the order of a few tens of km. A variant of the DRA makes use of shorter lengths (order of a few km) of high-Raman-gain fibers, such as DCF or highly nonlinear fiber (HNLF), to generate the same levels of gain in a more compact device that can be enclosed in a box. This is called discrete Raman amplifier and it is used to act as a lumped amplifier.

3.1 **Distributed Raman Amplifier Configurations**

Depending on the selected pumping scheme and cavity configuraton, several DRA architectures can be obtained. The term pumping scheme refers to the number, wavelength and direction of propagation of the pumps.

The most basic Raman amplifier is designed according to a 1st-order pumping scheme, where the pumps and the signal are one Stokes shift apart. Consequently, higher order Raman amplification is accomplished through one or more pumps that are two or more Stokes shifts away from the signal. As an example, assuming that amplification in the telecom C-band (1530 nm-1565 nm) is to be achieved, a 2nd-order Raman amplifier can be set up according to either one of the configurations depicted in Fig. 3.4.

Fig. 3.4a represents the so called dual-order Raman amplifier: 2nd-order pumps emitting at 1365 nm are used to amplify the 1st-order pumps at 1455 nm, which are then responsible for the amplification of the signal around 1550 nm. The seeds at 1455 nm are removed in the scheme shown in Fig. 3.4b and replaced by two high-reflectivity fiber Bragg gratings centered
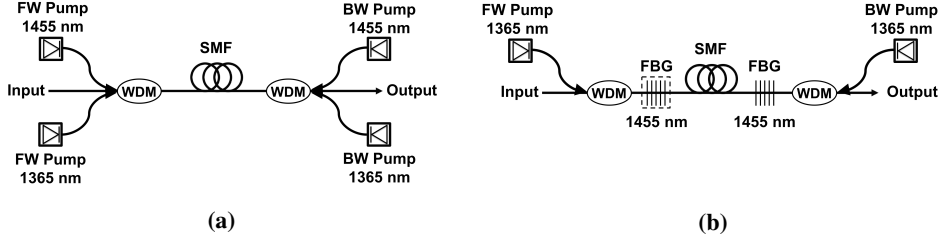
Figure 3.4: Schematic diagram of a dual-order Raman amplifier (a) and a 2nd-order Raman amplifier (b).

at the same wavelength, which help the formation of the 1st-order pumps by creating a closed Fabry-Perot-like cavity. This architecture is known as ultra-long Raman fiber laser [57] and will be examined in detail in the following sections. The URFL architecture can be further modified by removing the FBG at the input side. Due to absence of a mirror, in this half-open cavity, the feedback is partially provided by randomly distributed Rayleigh backscattering. This scheme is therefore one of the possible implementations of the architecture known as random distributed feedback Raman laser amplifier [58]. It will be hereafter called rDFB and, as it will be shown, it can be advantageous in addressing some of the drawbacks of the URFL scheme.

Higher-order versions of these two amplification schemes can be obtained by cascading multiple pumps progressively displaced by one Stokes shift, or by forming several cavities confined between pairs of FBGs centered at the appropriate wavelengths.

Regardless of the amplification order, the pumping scheme can also take different forms depending on the propagation direction of the pumps relative to that of the signal. Assuming bidirectional pumping, in which co-propagating and counter-propagating pumps co-exist and act jointly to amplify the signal, the contribution of the generated FW and BW 1st-order pumps can be conveniently adjusted to favor amplification at the beginning or end of the fiber span, respectively. The parameter that describes this contribution is the pump ratio, defined as the ratio of the power of one of the pumps to the total pump power. Alternatively, the pumps can be removed from either side of the amplifier resulting in FW only or BW only pumping, when the counter-propagating pump or the co-propagating pump is turned off, respectively.
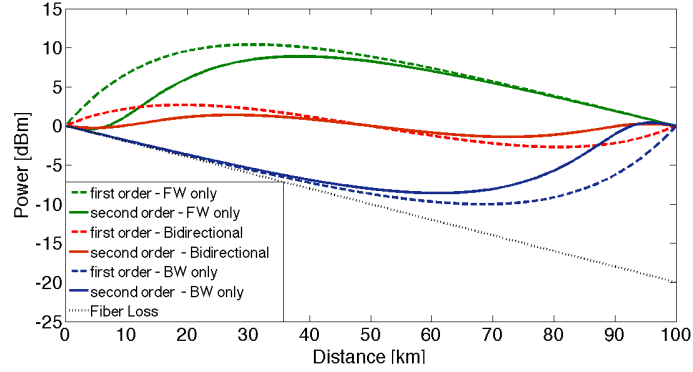
Figure 3.5: Average signal power evolution in a $100 \, \mathrm{km}$ long DRA for different pumping schemes (color curves), in 1st-order (dashed) and 2nd-order (solid) configurations. The fiber loss experienced by the signal in an EDFA-amplified span (dashed black curve) is included for comparison.

Some of the benefits provided by distributed amplification in various configurations can be qualitatively understood by observing the average signal power evolution inside the amplifier in each case, as shown in Fig. 3.5 for a $100 \, \mathrm{km}$ long amplifier:

i. Distributed amplification prevents the excessive drop of the signal average power. For instance, an EDFA would amplify the signal at the end of the span, when the signal power has decreased by about $20 \, \mathrm{dB}$ (dashed black curve). Raman amplifiers, on the other hand, push the amplification process further into the optical fiber and, as a result, even in the worst case scenario of 1st-order, BW only amplification, the optical power loss does not exceed $10 \, \mathrm{dB}$, which translates in reduced generated ASE noise.

ii. FW only pumping (green curves) allows for amplification of the signal in the first few tens of km. Therefore, ASE-related impairments are strongly reduced, at the cost of enhanced nonlinear effects generation due to high signal power.

iii. Bidirectional pumping offers intermediate propagation conditions between FW only and BW only and, thus, provides the best possible trade-off between ASE noise and nonlinearity.

iv. The signal power evolution in higher-order Raman amplification (solid color curves) experiences a lower excursion along the fiber link. The result is an improved robustness to both ASE and nonlinearity with respect to 1st-order amplification. The downside is the decreased pumping efficiency as more power is required at the nth-order pump output to excite the 1st-order pump through cascaded effects.

v. High-order Raman amplification with bidirectional pumping provides quasi-lossless transmission [57, 59, 60, 61] with extremely low signal power variation when the total pump power is equally divided between the FW and BW pumps (symmetrical pumping).

3.2 Theoretical Model of a DRA

The average power evolution of the signal in a distributed Raman amplifier can be expressed analytically through the following set of ordinary differential equations (ODEs) [57]. It takes into account all major effects including pump depletion, ASE, double Rayleigh backscattering and thermal noise and includes two equations for each nth-order pump, one for FW and one for BW propagation, one equation for the signal, and two equations for the noise. A 2nd-order configuration can be described as follows:

$$\frac{\mathrm{d}P_{P1}^{\pm}}{\mathrm{d}z} = \mp \alpha_1 P_{P1}^{\pm} \mp \frac{g_1}{A_{eff}} \frac{\nu_1}{\nu_2} P_{P1}^{\pm}$$
$$\left[P_{P2}^+ + P_{P2}^- + 4h\nu_2\Delta\nu_2 \left(1 + \frac{1}{e^{\frac{h(\nu_1-\nu_2)}{K_BT}} - 1} \right) \right] \pm \varepsilon_1 P_{P1}^{\mp} \tag{3.5}$$

$$\frac{\mathrm{d}P_{P2}^{\pm}}{\mathrm{d}z} = \mp \alpha_2 P_{P2}^{\pm} \mp \frac{g_1}{A_{eff}} \left[P_{P2}^+ + 2h\nu_2\Delta\nu_2 \left(1 + \frac{1}{e^{\frac{h(\nu_1-\nu_2)}{K_BT}} - 1} \right) \right] \left(P_{P1}^+ + P_{P1}^- \right)$$
$$\mp \frac{g_2}{A_{eff}} \frac{\nu_2}{\nu_2} P_{P2}^{\pm} \left[P_s + N_s^+ + N_s^- + 4h\nu_s\Delta\nu_s \left(1 + \frac{1}{e^{\frac{h(\nu_2-\nu_s)}{K_BT}} - 1} \right) \right]$$
$$\pm \varepsilon_2 P_{P2}^{\mp} \tag{3.6}$$

$$\frac{\mathrm{d}P_s}{\mathrm{d}z} = -\alpha_s P_s + \frac{g_2}{A_{eff}} P_s \left(P_{P2}^+ + P_{P2}^- \right) \tag{3.7}$$

$$\frac{\mathrm{d}N_s^+}{\mathrm{d}z} = -\alpha_s N_s^+ + \frac{g_2}{A_{eff}} \left[N_s^+ + 2h\nu_s\Delta\nu_s \left(1 + \frac{1}{e^{\frac{h(\nu_2-\nu_s)}{K_B T}} - 1} \right) \right] \left(P_{P2}^+ + P_{P2}^- \right)$$
$$+ \varepsilon_s N_s^- \tag{3.8}$$

$$\frac{\mathrm{d}N_s^-}{\mathrm{d}z} = \alpha_s N_s^- - \frac{g_2}{A_{eff}} \left[N_s^- + 2h\nu_s\Delta\nu_s \left(1 + \frac{1}{e^{\frac{h(\nu_2-\nu_s)}{K_B T}} - 1} \right) \right] \left(P_{P2}^+ + P_{P2}^- \right)$$
$$- \varepsilon_s \left(P_s + N_s^+ \right) \tag{3.9}$$

where subscripts 1, 2 and s refer to primary pump at $1365\,\mathrm{nm}$, secondary pump at $1455\,\mathrm{nm}$ and signal at $1550\,\mathrm{nm}$ respectively, superscripts + and - represent FW and BW propagating components respectively, z is the location along the fiber, P_{Pi} are the pump powers, P_s is the signal power, N_s are the noise powers at the signal frequency, ν_i are the corresponding frequencies of the pumps and the signal, $\Delta\nu_i$ are the effective bandwidths of the secondary pumps and the signal, g_i are the Raman gain coefficients for each of the Raman transitions, A_{eff} is the effective area of the fiber, α_i are the fiber attenuation values at each respective frequency, h is Plank's constant, K_B is Boltzmann's constant, T is the absolute temperature of the fiber and ε_i are the double Rayleigh scattering coefficients of the fiber at each particular frequency.

The cavity design is described through a corresponding set of boundary conditions which, in the case under consideration of URFL-based amplification, are:

$$P_{P1}^+ (0) = P_{P1}^- (L) = P_0 \tag{3.10}$$

$$P_{P2}^+ (0) = R_1 P_{P2}^- (0) \tag{3.11}$$

$$P_{P2}^- (L) = R_2 P_{P2}^+ (L) \tag{3.12}$$

$$N_s^+ (0) = N_0 \tag{3.13}$$

$$N_s^- (L) = 0 \tag{3.14}$$

$$P_s (0) = P_{in} \tag{3.15}$$

where R_1 and R_2 are the reflectivities of the input FBG and output FBG respectively, and L is the length of the SMF span. $R_1 = 0$ for an rDFB.

The above mathematical model was used to generate Fig. 3.5 and throughout this research work to simulate signal propagation in numerous different cavity designs. It was implemented

in Matlab® and numerically solved through the built-in boundary value problem solver bvp5c [62].

3.3 Noise in Distributed Raman Amplifiers

There are three major noise sources in distributed amplification: the fundamental quantum noise, usually expressed in terms of ASE noise, the double Rayleigh backscattering (DRB) and the pump-to-signal relative intensity noise transfer.

Noise-induced performance degradation in Raman amplification can be described through the equivalent noise figure F_{eq}, defined as the noise figure a discrete amplifier needs to have to be able to provide the same OSNR as that of a DRA used to amplify the same fiber link. The total noise figure for an amplifier chain is given by [63]

$$F_{tot} = F_1 + \frac{F_2 - 1}{G_1} + \frac{F_3 - 1}{G_1 G_2} + \cdots \qquad (3.16)$$

where F_n and G_n are the noise figure and the gain of the n_{th} amplifier respectively. In the equivalent system composed of a passive span (G_1, F_1) and a lumped amplification stage at the receiver side (G_2, F_2), the overall loss is $\alpha_s L$, hence $G_1 = (\alpha_s L)^{-1}$, and the noise figure of the unpumped span (no noise added) is $\alpha_s L$. Thus, the setup based on discrete amplification, under the assumption of perfect loss compensation and using Eq. (2.49) with no noise contribution, can be described by the following equations,

$$G_1 = \frac{1}{\alpha_s L}, \qquad F_1 = \frac{P_{in}}{P_{out}} = \alpha_s L \qquad (3.17)$$

$$G_2 = \alpha_s L, \qquad F_2 = F_{eq} \qquad (3.18)$$

and, from Eq. (3.16) the total noise figure is

$$F_{tot} = F_{eq} \alpha_s L \qquad (3.19)$$

The noise figure F_R of the Raman-based system has to be equal to the noise figure F_{tot} of the equivalent system. As a result,

$$F_{eq} = \frac{F_R}{\alpha_s L} \qquad (3.20)$$

Hence, in principle the equivalent noise figure can be less than 1 (or 0 in dB units). This is not achievable in practice, but can be explained by thinking of a Raman amplifier as a series of tiny amplifiers placed throughout the fiber with very short amplifier spacing, so that the gain each of these amplifiers has to provide is very small and less ASE is generated at each step along the fiber. Because of the distributed nature of the amplification, the OSNR of the distributed Raman amplifiers is higher than that of lumped amplifiers such as EDFA.

As the main concepts associated with ASE generation have already been presented in section 2.5.1 here the discussion will focus on the other two noise types.

3.3.1 **Double Rayleigh Backscattering**

Rayleigh backscattering occurs in all fibers and is their fundamental loss mechanism [64]. Usually, most of the scattered light escapes through the cladding and only a negligible part of it, about $40\,\mathrm{dB}$ lower than the signal power, remains into the core and propagates in backward direction. Regrettably, this very weak lightwave can be amplified over long lengths of fibers with distributed Raman gain, resulting in additional in-band cross talk.
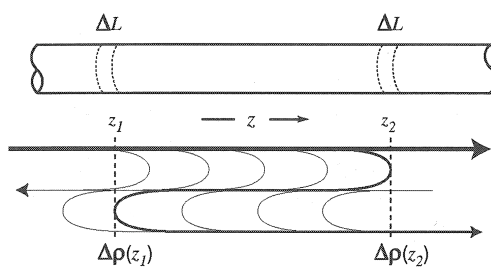
Figure 3.6: The double Rayleigh backscattering phenomenon in distributed Raman amplifiers.

Fig. 3.6 shows the double Rayleigh backscattering mechanism inside an optical fiber. Part of the FW propagating signal is backscattered due to density fluctuations $\Delta\rho$ in the medium at the location z_2. A fraction of this BW propagating light is then backscattered again in the FW direction by density fluctuations at z_1. z_1 and z_2 are random locations along the fiber and the total noise is obtained by summing over all possible contributions.

Double Rayleigh backscattering of the signal creates many FW propagating interfering components with the same spectral features as the signal. This Rayleigh-induced noise, often referred to as multiple path interference (MPI), is amplified by the distributed Raman gain and is the major source of power penalty in Raman-amplified lightwave systems [65].

3.3.2 **Pump-to-Signal Noise Transfer**

All lasers exhibit some intensity fluctuations caused by a number of factors such as small variations in the gain medium or cavity length of the pump laser, or the dependence of gain on a randomly varying polarization [66, 67, 68]. Eq. (3.3) highlights the exponential dependence of the Raman gain on the pump power. Any fluctuation in the pump intensity translates into fluctuations of the gain experienced by the signal. This pump intensity fluctuations are magnified during amplification and result in even larger fluctuations of the amplified signal power.

Power fluctuations of a laser are quantified through a frequency-dependent quantity called the relative intensity noise. It represents the spectrum of intensity or power fluctuations and is defined as [56]

$$\frac{\sigma_p}{\langle P_0 \rangle^2} = \int_0^\infty RIN_p\left(f\right) df \tag{3.21}$$

where σ_p^2 is the variance of the pump power fluctuations and $\langle P_0 \rangle$ is the average pump power. The amplified signal also exhibits fluctuations, thus its RIN is

$$\frac{\sigma_s}{\langle P_s\left(L\right) \rangle^2} = \int_0^\infty RIN_s\left(f\right) df \tag{3.22}$$

The pump noise transfer function represents the enhancement in the signal noise at a specific frequency f and is defined as

$$H\left(f\right) = \frac{RIN_s\left(f\right)}{RIN_p\left(f\right)} \tag{3.23}$$

The pump and the signal have different propagation speeds due to the dispersion experienced at different wavelengths. For this reason, the pump-to-signal noise transfer process depends on the pumping scheme, the amplifier length and the dispersion parameter D of the fiber.
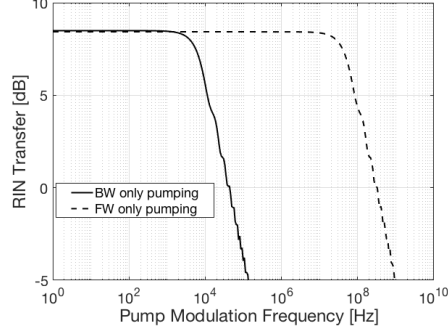
Figure 3.7: Simulated RIN transfer function for BW only (solid) and FW only (dashed) pumping scheme in a $100\,\mathrm{km}$ 1st-order DRA.

As seen from Fig. 3.7 for a $100\,\mathrm{km}$ 1st-order DRA, the RIN transfer function has a low-pass profile with a cut-off frequency dependent on the propagation direction of the pump, given by [66]

$$f_c^{BW} = \frac{\alpha_p v_{gs}}{4\pi}, \qquad f_c^{FW} = \frac{\alpha_p}{2\pi S \left(\lambda_s - \lambda_p\right) \left|\frac{\lambda_s + \lambda_p}{2} - \lambda_0\right|} \tag{3.24}$$

respectively for BW only and FW only pumping, where v_{gs} is the signal group velocity, α_p is the fiber attenuation at the pump wavelength, λ_s and λ_p are the signal and pump wavelengths, S is the dispersion slope and λ_0 is the zero-dispersion wavelength.

In general, the noise increase is relatively small in the backward-pumping configuration and for large values of D. Let us define the walk-off parameter as

$$d^{\pm} = \frac{1}{v_{gs}} \pm \frac{1}{v_{gp}} \tag{3.25}$$

where v_{gs} and v_{gp} are the group velocities of the signal and the pump respectively, d^+ is used for the co-propagating pump and d^- for the counter-propagating pump. Then we can distinguish three different cases:

i. **FW pumping and low dispersion** - The walk-off parameter is small and pump and signal travel at nearly the same speed. They overlap for a longer length during propagation and thus interact for a longer time. This is the worst case scenario in the RIN transfer mechanism.

ii. **FW pumping and high dispersion** - The walk-off parameter is large, the pump and the signal quickly move apart from each other and have less time to interact. As a result the signal sees a somewhat averaged gain.

iii. **BW pumping** - The averaging is much stronger as pump and signal propagate in opposite direction and the walk-off parameter is much larger than in the other cases. This configuration features almost negligible RIN increase and is often used in practice.

3.4 Analysis of Distributed Raman Amplifiers

As qualitatively exposed in the previous sections, each one of the Raman amplifier architectures discussed so far has its own unique advantages. 1st-order amplifiers have a better pumping efficiency as they involve only one Stokes generation and, in general a much simpler configuration, which has made them the preferred choice in early commercial Raman-based systems. On the other hand, 2nd-order amplification can effectively address the challenge related to a more even distribution of the gain along the transmission line. They enable propagation with improved signal power evolution flatness that eventually leads to the minimization of ASE generation and an enhanced tolerance to nonlinear effects.

From a system design perspective, a quantitative analysis of the benefits associated with the possible implementations of distributed amplification is crucial in the decision as to which specific amplification scheme is more convenient for achieving a given goal. Such a thorough investigation needs to take into account a wide variety of parameters and has to rely on a multi-faceted approach that includes modeling, full numerical transmission simulation and experimental characterization of the parameters impact on the system. As a consequence, the process can easily become extremely costly, time-consuming and ultimately inefficient.

In this section a numerical characterization of the three aforementioned Raman amplification schemes (1st-order, URFL and rDFB) performance as a function of some of the main parameters is presented and, afterwards used as the starting point of the multilevel optimization technique devised to minimize the computational time devoted to a full propagation analysis.

The theoretical model presented in Eqs. (3.5)-(3.9), with the appropriate boundary conditions, provides a powerful tool to visualize propagation of all the components involved in a Raman amplifier under any configuration, and extract useful information. Two examples of what can be obtained are displayed in Fig. 3.8 for $100\,\text{km}$ URFL and rDFB schemes, with bidirectional symmetric pumping and zero net gain (perfect loss compensation). Solid and dashed lines represent co-propagating and counter-propagating components respectively.
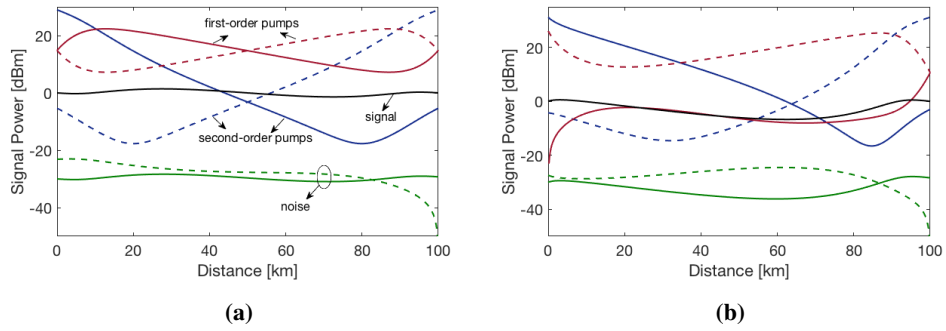
Figure 3.8: Evolution of FW (solid) and BW (dashed) propagating components in $100\,\text{km}$ URFL (a) and rDFB (b) with symmetrical bidirectional pumping.

Focusing on FW propagation in a URFL (Fig. 3.8a), it can be noted that the second-order pump is attenuated along the direction of propagation due to fiber loss and pump depletion. Similarly, the first-order pump (Stokes lasing) arises thanks to the energy transferred from the second-order pump in the first $\sim 20\,\text{km}$, and then drops until amplification from the BW first-order pump occurs in the final section of the fiber. Similar considerations can be made for the BW propagating pumps. As a consequence, the signal undergoes different propagation regimes in which the gain-loss coefficient varies according to the first-order pumps evolution, which results in a flat average power distribution with a $2.8\,\text{dB}$ excursion between the lowest and highest point along the link. The input OSNR over a $1\,\text{nm}$ bandwidth is set to $30\,\text{dB}$, and the output OSNR can be calculated from the difference between the signal and the FW noise (solid green curve) at the fiber output.

In the rDFB case, due to the absence of the input side reflector, the FW lasing is much weaker than in URFL. Thus, the signal receives less gain from the co-propagating pump, and when amplification from the counter-propagating pump starts, it has already dropped about

7 dB. This results in a higher required pump power to produce enough gain to recover from fiber loss and, therefore, a reduced OSNR by $\sim$1 dB in this specific case.

3.4.1 Performance Comparison of DRAs

Several indicators such as signal power variation, nonlinear phase shift, OSNR, on-off gain, net gain and so forth, can be extrapolated from the average signal propagation model. All of them are dependent on design parameters such as fiber type, fiber length, attenuation, pump power, input signal power, number of transmitted channels, FBGs reflectivity and many more. Although some of these parameters are constrained by the characteristics of the system to be designed and cannot be modified, cavity parameters can, in general, be tweaked conveniently to meet the design specifications. Thus, it is useful to compare the behavior of different Raman amplifiers under the same constraints.

Table 3.1 includes a list of the main parameters used in the simulation of 1st-order, URFL and rDFB architectures. In some cases, the behavior of DRAs based on a super large area (SLA) fiber has been investigated in order to provide insights on how to harness the specific properties of this type of fiber, especially in an unrepeated scenario, where the choice of the fiber to be used is an additional degree of freedom that does not have to conform to pre-installed SMF fiber. SLA fibers have a larger effective mode area that allows for higher optical intensities in their core and, therefore, higher damage threshold and lower nonlinearitites.

Table 3.1: Simulation Parameters

Parameter	Fiber	Wavelength	Notation	Value	Unit
Secondary Pump Bandwidth	-	1455 nm	$\Delta\nu_p$	125	GHz
Signal Bandwidth	-	1550 nm	$\Delta\nu_s$	125	GHz
Effective Area	SMF	-	A_{eff}	85	μm^2
Primary Pump Attenuation	SMF	1365 nm	α_1	0.36	dB/km
Secondary Pump Attenuation	SMF	1455 nm	α_2	0.23	dB/km
Signal Attenuation	SMF	1550 nm	α_s	0.2	dB/km
Raman Gain Coefficient	SMF	1365 nm	g_1	0.52	W^{-1}km^{-1}
Raman Gain Coefficient	SMF	1455 nm	g_2	0.42	W^{-1}km^{-1}
DRB Coefficient	SMF	1365 nm	ε_1	$1 \cdot 10^{-7}$	m^{-1}
DRB Coefficient	SMF	1455 nm	ε_2	$6 \cdot 10^{-8}$	m^{-1}
DRB Coefficient	SMF	1550 nm	ε_s	$4.3 \cdot 10^{-8}$	m^{-1}
Effective Area	-	A_{eff}	106	μm^2	SLA

Primary Pump Attenuation	SLA	1365 nm	α_1	0.38	dB/km
Secondary Pump Attenuation	SLA	1455 nm	α_2	0.234	dB/km
Signal Attenuation	SLA	1550 nm	α_s	0.19	dB/km
Raman Gain Coefficient	SLA	1365 nm	g_1	0.36	$W^{-1}km^{-1}$
Raman Gain Coefficient	SLA	1455 nm	g_2	0.29	$W^{-1}km^{-1}$
DRB Coefficient	SLA	1365 nm	ε_1	$1 \cdot 10^{-7}$	m^{-1}
DRB Coefficient	SLA	1455 nm	ε_2	$5 \cdot 10^{-8}$	m^{-1}
DRB Coefficient	SLA	1550 nm	ε_s	$4 \cdot 10^{-8}$	m^{-1}
Plank's Constant	-	-	h	$6.626 \cdot 10^{-34}$	J s
Boltzmann's Constant	-	-	K_B	$1.381 \cdot 10^{-23}$	J/K
Absolute Temperature	-	-	T	298	K

The Matlab® function bvp5c uses a collocation formula, the numerical solution is based on a mesh of points at which the collocation equations are satisfied. Mesh selection and error control are based on the residual of this solution: on each subinterval of the mesh, a norm of the residual for each component of the solution is estimated and is required to be less than or equal to a tolerance. This tolerance is a function of the relative and absolute tolerances which were set to 10^{-6}, and the points spacing within the mesh was set to 500 m.

The three schemes have been analyzed in quasi-lossless conditions (perfect compensation of fiber loss) for the best case with a 50% pump power ratio, to ensure the best achievable balance between ASE noise generation and nonlinear effects. The signal output power has an accuracy exceeding 10^{-4} with respect to the input power and most of the fiber parameters used in the model were previously experimentally characterized to guarantee realistic and verifiable results.

Fig. 3.9 shows the characterization results for a 1st-order Raman amplifier as a function of SMF fiber length and signal input power, when a single-channel at 1550 nm is transmitted. Fiber length was varied from 30 km to 250 km with a 1 km step and input power from -10 dBm to 10 dBm with 2 dBm step. The first parameter directly affects the attenuation endured by the signal during propagation and results in a higher required pump power and a larger power excursion along the link when the transmission distance is extended. A higher SPV, in turn, translates into enhanced excitation of nonlinear effects, due to increased signal power at the beginning of the span, and in a decreasing OSNR due to a higher required gain for full recovery of the signal power after attenuation.
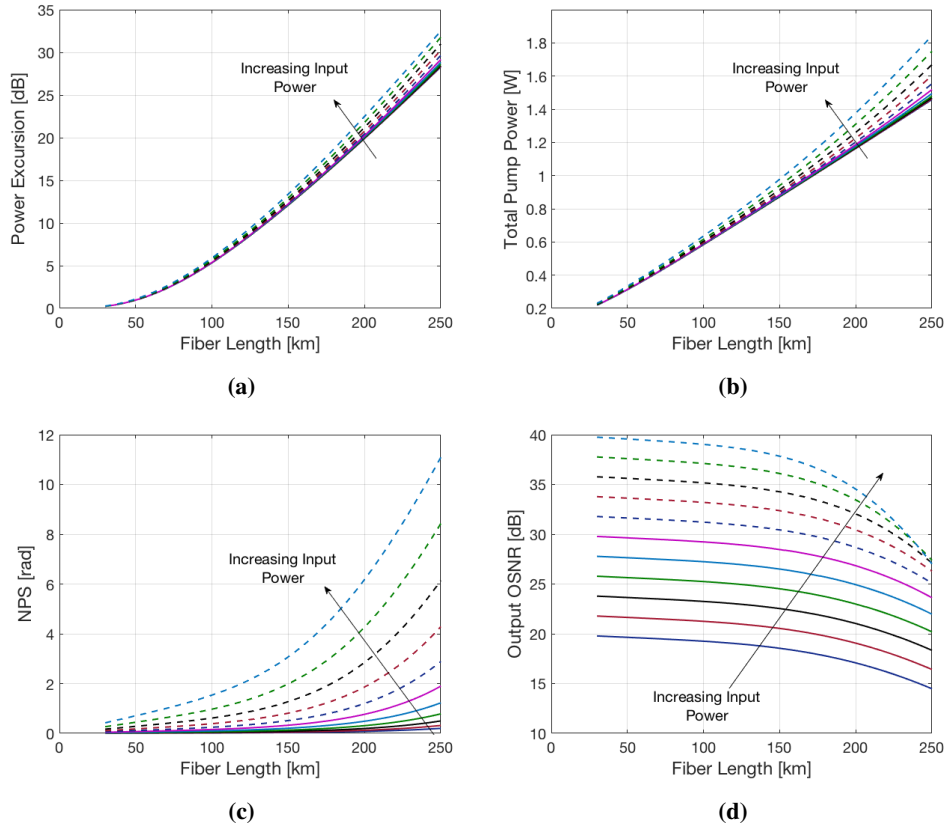
Figure 3.9: Numerical characterization of signal power variation (a), required pump power for perfect loss compensation (b), nonlinear phase shift (c) and output OSNR in a 1 nm bandwidth (d) for a single-channel, SMF-based, 1st-order DRA with symmetrical bidirectional pumping and signal input power ranging from $-10\,\mathrm{dBm}$ to $10\,\mathrm{dBm}$.

Moreover, the signal input power, intended as the sum of the power per channel in a multi-channel system, can drastically influence the pump depletion factor. Propagation of a single channel with a high input power or, equivalently, multiple low-power channels, alters the slope of the curves in Figs. 3.9a and 3.9b, thereby causing an ever increasing separation between them as length and input power are increased. As a result, NPS and OSNR evolve according to different regimes: for low input powers up to $0\,\mathrm{dBm}$ the NPS increases slowly with the fiber length and the OSNR reduces by nearly the same quantity ($\sim 6\,\mathrm{dB}$) in the considered distances range. For high signal input powers, on the other hand, nonlinear effects

dramatically raise, as expected during propagation of high optical intensities, and can be quantified in about $135\,\mathrm{km}$ reduction of the maximum transmission distance for a given value of accumulated NPS, when input power is increased form $0\,\mathrm{dBm}$ to $10\,\mathrm{dBm}$. In addition, the output OSNR experiences a much more abrupt drop that leads to a conspicuous constriction of the benefits implied by a higher launch power.
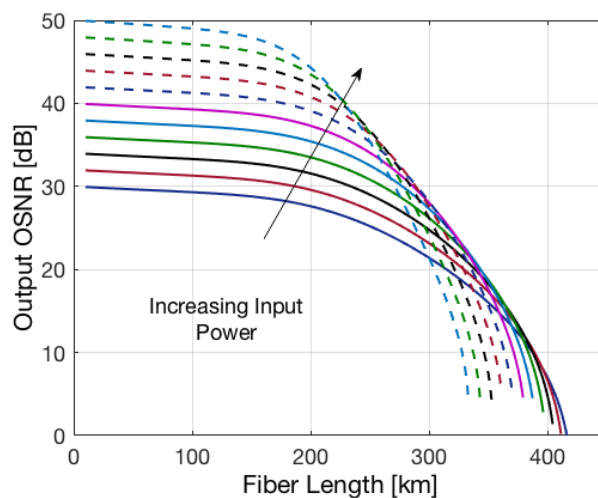
Figure 3.10: Simulated OSNR in a 0.1 nm bandwidth of a 2nd-order URFL as a function of the transmission distance and the signal input power.

This can be better understood by looking at Fig. 3.10, where the OSNR in a $0.1\,\mathrm{nm}$ bandwidth of a URFL scheme is shown for fiber lengths beyond $400\,\mathrm{km}$: increasing the launch power entails an OSNR enhancement for distances up to $\sim 200\,\mathrm{km}$. Afterwards, pump depletion becomes so strong as to establish the opposite regime where, for a given OSNR level a lower input power allows for an extended reach.

The same numerical characterization was performed for the two 2nd-order schemes (URFL and rDFB). For the sake of clarity, Fig. 3.11 only presents a comparison of the amplifiers for three different input powers ($-10\,\mathrm{dBm}$, $0\,\mathrm{dBm}$ and $10\,\mathrm{dBm}$) corresponding to undepleted, mild depletion and strong depletion regimes respectively.

Fig. 3.11a shows that URFL provides the flattest signal power distribution along the link, for every considered transmission distance and input power level. This results in an output

OSNR comparable to that of a 1st-order amplifier, and considerably higher than that of the rDFB scheme, where the absence of a strong FW Stokes component leads to higher power excursion and drastically reduced OSNR.
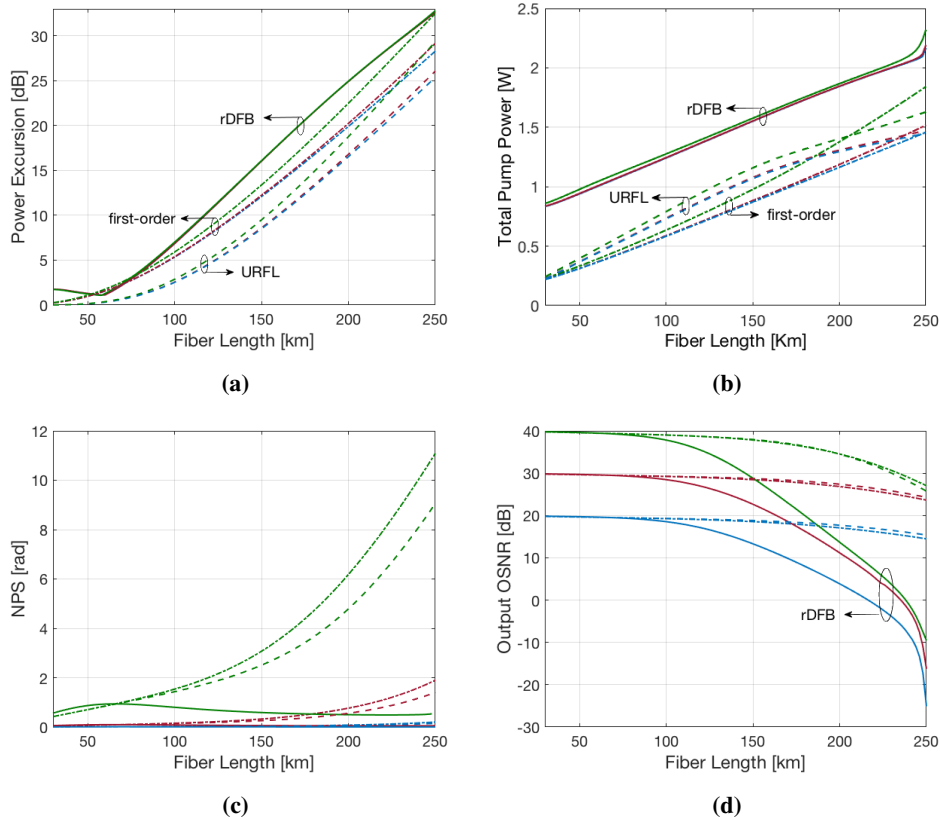
Figure 3.11: Comparison of signal power variation (a), required pump power for perfect loss compensation (b), nonlinear phase shift (c) and output OSNR in a 1 nm bandwidth (d) for single-channel, SMF-based, 1st-order (dash-dot), URFL (dashed) and rDFB (solid) configurations with symmetrical bidirectional pumping. Signal input power is $-10\,\mathrm{dBm}$ (light blue), $0\,\mathrm{dBm}$ (red) and $10\,\mathrm{dBm}$ (green).

Where the ultimate benefit of the rDFB architecture resides, is in the amount of excited nonlinearity: extremely low NPS across the whole fiber length range and in any depletion regime can be achieved at the cost of an increase of the required pump power, with respect to the other schemes. In fact, although rDFBs produce the highest SPV, most of it is due to fiber

loss and only a small part to amplification above the initial power. Thus, the signal power mainly evolves within the low power regime and nonlinear effects are minimal.

In general, most of the gain in rDFBs is provided by the BW pump in the final section of the span, when the signal power has already been reduced by fiber attenuation, therefore they are the least affected by pump depletion, as the almost perfectly overlapping curves in Figs. 3.11a and 3.11b show. Moreover, URFLs represent an extremely beneficial alternative to 1st-order amplification, especially in long-haul systems, where the advantages in terms of NPS and OSNR, although may seem exiguous in a single link, can result in a dramatic improvement over several transmission spans.

3.4.2 Multilevel Optimization

Unrepeatered wavelength-division-multiplexed transmission links, operating without active in-line elements between transmitter and receiver terminals, present a number of advantages in terms of reduced maintenance costs and increased reliability. These kinds of systems have proven to be ideal for communication with or between islands, as well as with offshore infrastructures such as oil platforms or wind farms. As such, they have garnered much interest in recent years, as continuous technological improvements have allowed for longer spans (up to 90 dB loss) and higher capacities (up to the 10s of Tb/s) [69].

This section presents a new, general, simplified approach to the optimization of unrepeatered systems using distributed amplification. It is based on the procedure first presented in [70, 71] for long-distance transmission systems, extended and adapted to the particular constraints of modern unrepeatered transmission, in which full recovery of signal power at the end of the span is not a requirement, allowing for an extra degree of freedom. The method helps study the impact of spectral density on performance and optimal amplifier configuration and is equally applicable to ASK and PSK formats, as well as to any form of WDM configuration. It employs a multi-level approach to greatly reduce the time devoted to full NLSE simulations, by searching for sets of parameters satisfying optimal trajectories in the system configuration space, that fulfill a conditional minimization of nonlinear impairments for given values of the optical signal-to-noise ratio (OSNR).

Different transmission formats present a different ideal balance between noise and nonlinearities, but the optimal performance will correspond in any case to a given point in the defined optimal trajectory. Moreover, the defined optimal trajectories in the parameter space are fully compatible with the solutions obtained by solving the same problem through NLSE simulations [71].

The multilevel optimization technique comprises the following four steps:

   i. **Parameter Space Identification** - The first phase consists in determining the parameters that affect the system. Transmission requirements as well as physical layer specifications and impairment mitigation, all contribute to the definition of the set of parameters that have an impact on the system.

   ii. **Elementary Dependence Assessment** - The effect that each parameter has on the system is individually analyzed at this stage, and the optimization targets identified. Depending on the objective of the optimization (i.e. OSNR maximization, NPS minimization, bandwidth enhancement, transmission distance extension, etc.) some of the system variables may have a greater impact than others.

   iii. **Optimal Trajectory Determination** - Step 3 is where the impact of multiple variables is simultaneously examined and optimal trajectories in the parameter space identified. Optimal trajectories represent the points where a specific combination of parameters satisfies the optimization targets

   iv. **Optimal Impairment Mitigation** - Once the optimal conditions are found, the selected impairment mitigation technique can be applied only to the corresponding subset of configurations defined by the optimal parameters combinations, thus avoiding lengthy full numerical transmission simulations.

To illustrate the application of multilevel optimization to realistic systems, let us consider the design of a DRA-based unrepeatered transmission link, where dispersion precompensation is to be performed for impairments reduction and where conditional optimization is required to minimize the NPS at a fixed OSNR or, vice versa, to maximize the OSNR at a fixed NPS. The parameter space of the system is identified by the following variables:

- Cavity Configuration
- Pumping Scheme
- Transmission Length
- Type of Fiber

- Input Power
- Pump RIN
- Spectral Window
- Number of Channels

- Channel Spacing
- Modulation Format
- FBG Reflectivity

Many of them are interdependent, but a thorough analysis of the isolated effect of each variable can be carried out in step 2. Figs. 3.9 and 3.11 are good examples of what can be accomplished at this stage. The individual contribution of transmission distance, launch power, fiber type and amplification scheme on NPS, OSNR and pumping efficiency can be extracted and used to deduce which parameters have the strongest impact on the system and require tight control, or which ones can offer a better leeway.

Step 3 is where the appropriate conditional minimization is carried out by assessing the influence of several parameters at once. In this example, the amplification scheme of choice is a typical URFL cavity based on superchannel transmission.

Superchannel transmission is an improved version of WDM for spectral efficiency enhancement [72, 73]. A more efficient use of the optical fiber spectrum is obtained by allocating a large number of compact wavelength channels, spaced at the symbol rate, known as Nyquist spacing [74, 75]. From a distributed amplifier design standpoint, the first immediate consequence of the improved spectral efficiency offered by superchannel transmission is an equivalent increase in signal power spectral density, and consequently in amplifier pump depletion, which affects the total power budget and affects the optimal trajectories in the amplifier configuration space. This is particularly important in the case of unrepeatered transmission, as becomes evident in Fig. 3.12, corresponding to the optimal trajectories for a $250\,\text{km}$ long URFL projected in the channel power vs. pump ratio plane for a given percentage of loss compensation. Hereafter, the pump ratio (or pump split) is defined as the ratio of the FW pump power to the total pump power. Fig. 3.12 shows the contour plots of NPS (dashed red curves) and OSNR (solid black curves), along with the optimal trajectories (solid blue curves) obtained from the tangency points of NPS and OSNR curves.

Fig. 3.12a shows the trajectories for the close-to-ideal situation of transmission of a single

DP-QPSK channel, in which optimal pump power split is always close to 50%. Fig. 3.12b illustrates the impact of adding just 4 more DP-QPSK channels with a $50\,\text{GHz}$ spacing, which immediately modifies the optimal pump power split for channel powers above $-10\,\text{dBm}$, requiring a larger proportion of forward pump power to improve OSNR.
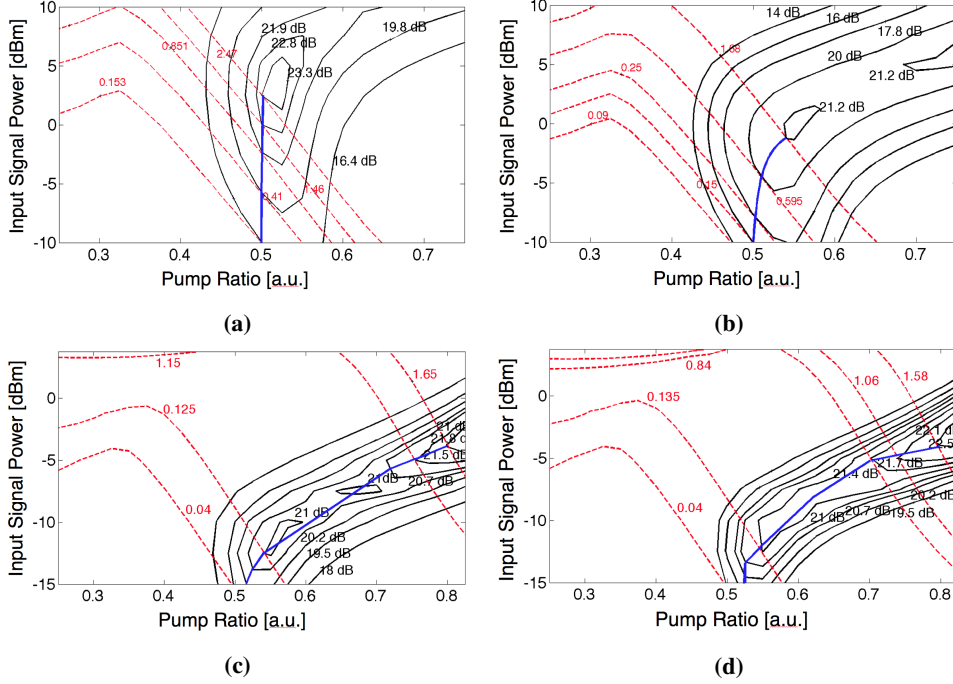
Figure 3.12: Optimal trajectories in the amplification scheme configuration space for URFL amplification in single-channel DP-QPSK (a), 5-channel DP-QPSK, $50\,\text{GHz}$ spacing (b), 70-carrier Nyquist-PDM-16QAM (c), 70-carrier Nyquist-PDM-16QAM with 20% undercompensation (d).

In comparison, Fig. 3.12c displays the optimal trajectories for a 70-carrier Nyquist PDM-16QAM over a $700\,\text{GHz}$ spectral bandwidth. Optimal power per sub-channel can be expected to be close to $-5\,\text{dBm}$ [76], which would shift optimal pump split towards 80% forward pumping. This would be entirely unpractical both in terms of available pumping technology (due to the higher amounts of RIN transfer to be expected from forward pumping at such gain levels) and from a system reliability viewpoint, as would require forward pump powers in excess of $9\,\text{W}$ for standard ITU G.652 fiber. However, full attenuation compensation is rarely convenient in unrepeated transmission, so Fig. 3.12d illustrates the optimal

trajectories for the same 70-carrier Nyquist system of Fig. 3.12c with a 20% power penalty. Unfortunately, optimal trajectories are barely modified. This suggests that purely distributed multi-wavelength Raman pumped amplification solutions for unrepeatered superchannel transmission encompassing the C or the C+L windows might prove to be both unable to deal with low-cost scalability, and unpractical in terms of reliable operation due to the high pump power requirements.

Switching to long-haul transmission, the picture is rather different. Here, span length becomes one more parameter in the configuration space, which provides some more room for minimizing the impact of the increased spectral density. As an example, Fig. 3.13a displays the optimal trajectory for an $80\,\mathrm{km}$ SSMF span. Here optimal operation is achieved for a pump split close to 50%, in which power excursion (Fig. 3.13b) is minimized and optimal balance between noise and nonlinearities achieved, as corresponds to a quasi-lossless transmission scheme. Moreover, the system seems scalable in terms of pump power, with a required combined pump power of about $5\,\mathrm{W}$ if the system is to be scaled to a 700 carriers ($7\,\mathrm{THz}$ bandwidth) with powers below $0\,\mathrm{dBm}$ per sub-channel. Still, extending this kind of amplification through multi-wavelength 2nd-order Raman amplification over the complete C+L bands seems unrealistic in terms of system reliability due to the high pump powers required.
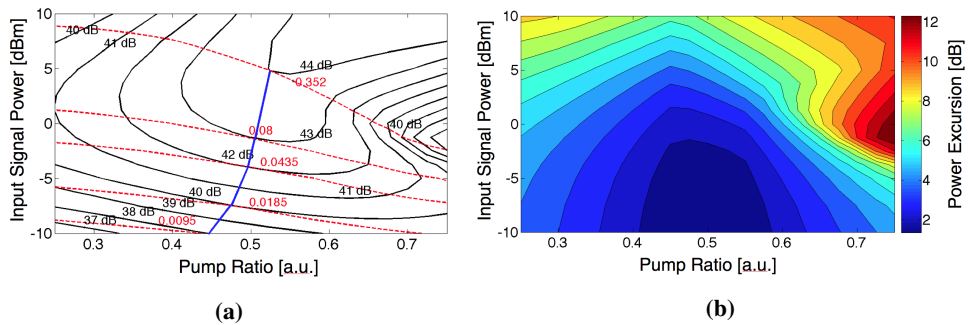
Figure 3.13: Optimal trajectories in the amplification scheme configuration space for a URFL-amplified 70-carrier Nyquist-PDM-16QAM transmission system with an $80\,\mathrm{km}$ ITU G.652 fiber span (a). Signal power excursion in the same parameter space (b).

After locating the points along the optimal trajectory, step 4 is dedicated to the imple-

mentation of the preferred impairment reduction technique. As it will be discussed in chapter 5, intra-channel and inter-channel distortions are of utmost concern in the design of transmission systems. Many mitigation and compensation techniques are being investigated, both at an optical and digital level, to combat the interaction between nonlinear effects and chromatic dispersion that leads to transmission degradation through phase-to-intensity conversion [77]. As a simple example, dispersion pre-compensation is used here to minimize both the pulse overlap within the nonlinear length of the fiber and the distortion resulting from the nonlinear phase shift converted into power fluctuations by the dispersion experienced in the remaining part of the link. To this end, Fig. 3.14 shows in a combined plot the OSNR and average signal power evolution, as well as the corresponding NPS barycentrics [78], for the central $(1552\,\text{nm})$ channel of a 16-channel WDM, $40\,\text{Gbps}$, $250\,\text{km}$ URFL system, using two different launch powers ($-4\,\text{dBm}$ and $10\,\text{dBm}$ per channel). The NPS barycentric z' is the point where the accumulated NPS reaches half of its total value, and is used to determine the optimal dispersion pre-compensation in each case ($D_{pre} = -D_{SMF} \cdot z'$) and can be found by numerically solving the following equation [79] for each of the points in the desired parameter space trajectory

$$\int_0^{z'} P_s\left(z\right) dz = \int_{z'}^{L} P_s\left(z\right) dz \tag{3.26}$$

where L is the total span length.
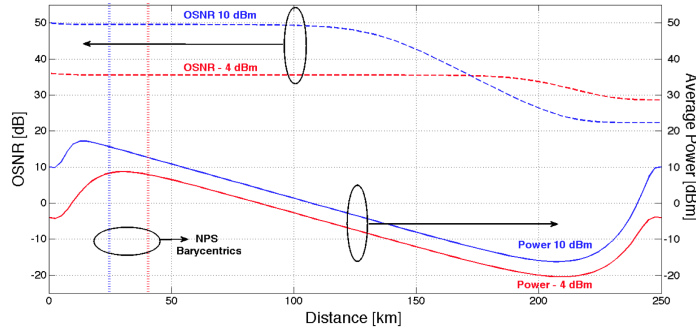
Figure 3.14: Combined plot of OSNR and power evolution, for a 16-channel WDM $250\,\text{km}$ URFL system, for $-4\,\text{dBm}$ and $10\,\text{dBm}$ per channel. Vertical lines signal the positions of the NPS barycentrics.
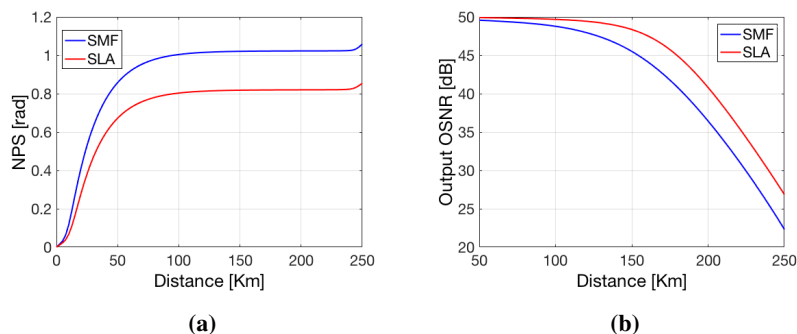
Figure 3.15: Accumulated nonlinearity (a) and OSNR (b) in two identical 16-channel $250\,\mathrm{km}$ URFL-amplified systems using legacy and SLA fiber bases.

Fig. 3.15, on the other hand, illustrates the advantages of modern fibers, comparing the noise and accumulated nonlinearities, again in the central channel of 16, with an input average power of $10\,\mathrm{dBm}$, in the same URFL-amplified $250\,\mathrm{km}$ spans with identical gain and pump ratio, one based on SMF and the other on SLA fiber. The extra margins of SLA in both noise and nonlinearities provide system designers with the possibility of achieving higher capacities by extending the parameter space into regions that can provide a more convenient OSNR/NPS balance for their format of choice.

4

RIN Transfer in Distributed Raman Amplifiers

In fused silica, the Raman response time has been demonstrated to be less than $100\,\mathrm{fs}$ [80, 81]. This implies that any phenomenon occurring on a slower time scale can be "seen" and reinforced by the Raman mechanism. In this regard, fluctuations of the pump power, primarily those at low frequencies, can cause almost instantaneous gain variations, and thus can be easily transferred to the signal instantaneous power, especially when pump-signal cross talk is allowed to build-up over large time and space intervals, namely in co-pumped distributed Raman amplification.

The propagation direction of the pump is typically chosen to be opposite to that of the signal, in order to profit from the averaging of the gain fluctuations and thus limit the effect of the cross talk. However, FW pumping offers an improved noise performance and is often desirable to utilize it in alternative pumping configurations that can convey the combined benefits of purely FW and purely BW pumping.

In addition, 2nd-order URFL amplifiers have consistently proved to be an excellent option in terms of maximum reach for both unrepeatered and long-haul multichannel coherent transmission systems [82, 83, 84] using advanced modulation formats in combination with nonlinearity compensation techniques such as digital back propagation or optical phase conjugation [76, 85]. However, extended reach comes at the cost of an increase in required pump power and, more importantly, is limited by the RIN transferred from the FW pump to the signal. In fact, assuming that the SPV is sufficiently low and that deterministic fiber nonlinear effects generated during the transmission can be entirely compensated for, the RIN transferred from fiber pump lasers to the signal becomes the most problematic effect when the use of symmetric bidirectional pumping is needed (i.e. in an OPC-based system [86]) or, in wider terms, whenever a certain amount of FW pump power can be beneficial to reduce SPV and improve OSNR [66, 87]. Nevertheless, recent works [88, 89] have shown that rDFB amplifiers can be suitable for overcoming RIN impairments enabling transmission distances up to 7915 km for a 10 x 116 Gbps DP-QPSK long-haul system by removing the FBG at the input side of an URFL, thus essentially transforming a Fabry-Perot-like closed cavity into an half-open cavity, at the expense of an additional reduction of the FW pumping efficiency.

Bearing all this in mind, this chapter first presents a numerical characterization of the RIN transfer function for 1st-order, URFL and rDFB amplifiers as a function of transmission distance, input power and pump ratio. As 2nd-order amplification schemes can tangibly ameliorate performance in DRA-based communication systems, in the other sections the spotlight is pointed towards the RIN transfer mechanism dependence on the 2nd-order cavity design and to how RIN-induced impairments in URFLs can be made less severe in realistic transmission systems employing low-front-reflectivity URFL architectures. To this purpose, a thorough experimental characterization of a wide spectrum of amplifier configurations is presented, followed by the results of the optimization of cavity structures in terms of output signal RIN, OSNR and pump efficiency, and of the laboratory testing for several of them.

The numerical analysis of RIN transfer in DRAs was performed with the aid of the model presented in section 3.2. The set of coupled differential equations (3.5)-(3.9) was properly extended through additional equations that account for the evolution of the spectral density of the amplitude noise associate with all the propagating components in a DRA. In the

illustrative example of a 2nd-order amplifier, these equations are:

$$\frac{\mathrm{d}n_1^{\pm}}{\mathrm{d}z} + id_1^{\pm}\omega n_1^{\pm} = \mp \alpha_1 n_1^{\pm} \mp g_1 \frac{\nu_1}{\nu_2} P_{P1}^{\pm}\left(n_2^+ + n_2^-\right)$$
$$\mp g_1 \frac{\nu_1}{\nu_2}\left(P_{P2}^+ + P_{P2}^-\right)n_1^{\pm} \pm \varepsilon_1 n_1^{\mp} \tag{4.1}$$

$$\frac{\mathrm{d}n_2^{\pm}}{\mathrm{d}z} + id_2^{\pm}\omega n_2^{\pm} = \mp \alpha_2 n_2^{\pm} \pm g_1 P_{P2}^{\pm}\left(n_1^+ + n_1^-\right) \pm g_1\left(P_{P1}^+ + P_{P1}^-\right)n_2^{\pm}$$
$$\mp g_2 \frac{\nu_2}{\nu_s} P_{P2}^{\pm} n_s^{\pm} \mp g_2 \frac{\nu_2}{\nu_s} n_2^{\pm} P_s \pm \varepsilon_2 n_2^{\mp} \tag{4.2}$$

$$\frac{\mathrm{d}n_s^+}{\mathrm{d}z} = -\alpha_s n_s^+ + g_2 P_s\left(n_2^+ + n_2^-\right) + g_2\left(P_{P2}^+ + P_{P2}^-\right)n_s^+ + \varepsilon_s n_s^- \tag{4.3}$$

$$\frac{\mathrm{d}n_s^-}{\mathrm{d}z} = \alpha_s n_s^- + g_2\left(P_{P2}^+ + P_{P2}^-\right)n_s^- - \varepsilon_s n_s^+ \tag{4.4}$$

where subscripts 1, 2 and s refer to primary pump at $1365\,\mathrm{nm}$, secondary pump at $1455\,\mathrm{nm}$ and signal at $1550\,\mathrm{nm}$ respectively, superscripts + and - represent FW and BW propagating components respectively, n_i represent the spectral density of the amplitude noise, z is the location along the fiber, v_i are the group velocities for each spectral component, d_i are the walk-off parameters defined in Eq. (3.25), P_{Pi} are the pump powers, P_s is the signal power, ν_i are the corresponding optical frequencies of the pumps and the signal, g_i are the Raman gain coefficients for each of the Raman transitions, α_i are the fiber attenuation values at each respective frequency, ε_i are the double Rayleigh scattering coefficients of the fiber at each particular frequency, and ω represent the modulation frequency of the pump intensity.

The walk-off parameters d_i in the two propagating conditions can be simplified by considering the average group velocity $\bar{v}$ between two wavelengths [67], and by using the relation $\bar{v} = c/\bar{n}$ to obtain

$$d^+ = \frac{1}{v_p} - \frac{1}{v_s} = \frac{\Delta v}{\bar{v}^2} = c\frac{\Delta n}{\bar{n}^2}\frac{1}{\bar{v}^2} = \frac{c^2 D\Delta\lambda}{\bar{n}^2 c^2}\bar{n}^2 = D\Delta\lambda \tag{4.5}$$

$$d^- = \frac{1}{v_p} + \frac{1}{v_s} = \frac{2}{\bar{v}} = \frac{2}{c}\bar{n} \tag{4.6}$$

where $\bar{n}$ is the average group index, $\Delta v = c \cdot \Delta n/\bar{n}^2$ is the group velocity difference, $\Delta n = c \cdot D \cdot \Delta\lambda$ is the index difference, $\Delta\lambda$ is the pump-signal wavelength separation, c is the speed of light and D is the fiber dispersion.

As customary, any boundary value problem is associated with a set of boundary conditions which, in this case, can be written as

$$n_1^+ (0) = n_{10} \tag{4.7}$$

$$n_1^- (L) = n_{20} \tag{4.8}$$

$$n_2^+ (0) = R_1 n_2^- (0) \tag{4.9}$$

$$n_2^- (L) = R_2 n_2^+ (L) \tag{4.10}$$

$$n_s^+ (0) = 0 \tag{4.11}$$

$$n_s^- (L) = 0 \tag{4.12}$$

where R_1 and R_2 are the reflectivities of the input FBG and output FBG respectively, L is the length of the SMF span and n_{10} and n_{20} are the initial RIN values for the co-propagating and counter-propagating pump respectively. $R_1 = 0$ for an rDFB, $n_{10} = 0$ for BW only pumping and $n_{20} = 0$ for FW only pumping.

4.1 Numerical Study of RIN Transfer

It is convenient to use the definition of the pump noise transfer function in Eq. (3.23) to specify the 1st-order and 2nd-order transfer functions as

$$H^{1st} (f) = \frac{RIN_s (f)}{RIN_p^{1st} (f)}, \qquad H^{2nd} (f) = \frac{RIN_s (f)}{RIN_p^{2nd} (f)} \tag{4.13}$$

where RIN_s is the output signal RIN, and RIN_p^{1st} and RIN_p^{2nd} represent the RIN of the co-propagating 1st-order $1455\,\text{nm}$ pump and 2nd-order $1366\,\text{nm}$ pump respectively. All these three terms are calculated as the ratio of the time-averaged mean squared value of the power fluctuations to the squared averaged power of the particular spectral component [66, 67, 87, 90]

$$RIN_s = \frac{|n_s (L)|^2}{P_s (L)^2}, \qquad RIN_p^{1st} = \frac{|n_1 (0)|^2}{P_p^{1st} (0)^2}, \qquad RIN_p^{2nd} = \frac{|n_1 (0)|^2}{P_p^{2nd} (0)^2} \tag{4.14}$$

where L is the fiber length and the spectral density of amplitude noise $n_1(0) = n_{10}$ has been considered constant in frequency and identical in the two cases of 1st-order and 2nd-order

amplification, and equals to $-120\,\mathrm{dB/Hz}$. Thus, Eqs. (4.13) describe how RIN is conveyed from the FW propagating pump to the signal.
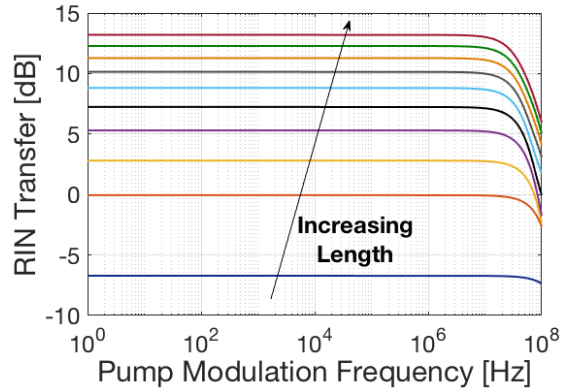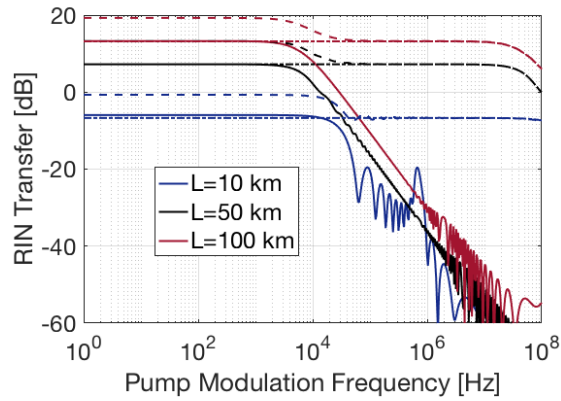
Figure 4.1: Simulated RIN transfer function up to $100\,\mathrm{MHz}$ in 1st-order Raman amplification as a function of the SMF fiber length ranging from $10\,\mathrm{km}$ to $100\,\mathrm{km}$ with FW only pumping (a) and for three different SMF lengths with BW only (solid), symmetrical bidirectional (dashed) and FW only (dash-dot) pumping (b). The channel launch power is $-10\,\mathrm{dBm}$.

Fig. 4.1a shows the simulated RIN transfer function for a single-channel 1st-order DRA as a function of the SMF length, when only the FW pump is employed for full recovery of the span loss and the channel launch power is $-10\,\mathrm{dBm}$. For each of the considered amplifier lengths ranging from $10\,\mathrm{km}$ to $100\,\mathrm{km}$ with a $10\,\mathrm{km}$ step, a low-pass-like outline is clearly

visible, with a $-3\,\mathrm{dB}$ corner frequency around $100\,\mathrm{MHz}$ slightly decreasing down to about $48\,\mathrm{MHz}$ with increasing transmission distance. On the contrary, the maximum RIN transfer value grows with length, confirming that, for a given dispersion, the longer the amplifier is the more RIN the signal acquires, as it overlaps with the pump for a longer time.

Fig. 4.1b, on the other hand, highlights the change in noise transfer with the pump propagation direction, for three amplifier lengths of $10\,\mathrm{km}$, $50\,\mathrm{km}$ and $100\,\mathrm{km}$ in the same configuration as Fig. 4.1a. In purely counter-propagating pumping (solid curves) the corner frequency is dramatically lower than in the purely co-propagating pumping (dash-dot curves). As in the FW pumping case, the shortest amplifier exhibits the highest $-3\,\mathrm{dB}$ frequency of about $27\,\mathrm{kHz}$, which further reduces to about $6.5\,\mathrm{kHz}$ in a $100\,\mathrm{km}$ span. This can be explained by noting that the corner frequency scales with the walk-off length divided by the effective length of the pump $L_{eff} = [1 - exp(\alpha_p L)]/\alpha_p$ [56]. Since the fiber dispersion is constant, so is the walk-off length, whereas the effective length increases asymptotically with fiber length up to the upper bound value $1/\alpha_p$, and the corner frequency lowers accordingly.

The symmetrical bidirectional scheme (50% FPR) appears as a combination of the other two pumping configurations in as much as it displays both corner frequencies. The first one arises from the aggregated effect of the two pumps, which forms a higher initial plateau in the low frequency range. At higher frequencies, the effect of the BW pump ceases and the transfer function follows the purely co-propagating profile. With the exclusion of the corner frequency variation, no other significant differences can be seen as an effect of the amplifier length in this conditions.

Fig. 4.2 presents the same analysis just discussed for a 1st-order DRA, when the selected amplification method is URFL-based. Similarities can be observed in the way the maximum RIN transfer value increases with the fiber length, but the corner frequency in a URFL has a somewhat counterintuitive behavior. Both its absolute value and its evolution with the transmission distance widely differ from the previous results. For short FW pumped fiber lengths, the transfer function displays a $3\,\mathrm{dB}$ drop in the kHz range and some very peculiar features in the high frequency regime. Fluctuations appear in a portion of the frequency spectrum that broadens as the fiber length increases (Fig. 4.2a).

(a)

(b)
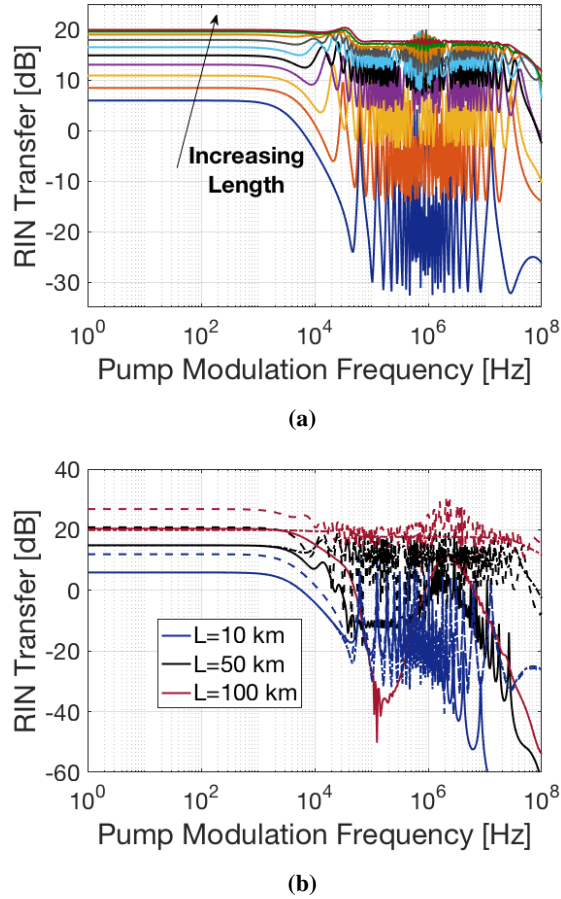
Figure 4.2: Simulated 2nd-order RIN transfer function up to $100\,\mathrm{MHz}$ in URFL amplification as a function of the SMF fiber length ranging from $10\,\mathrm{km}$ to $100\,\mathrm{km}$ with FW only pumping (a) and for three different SMF lengths with BW only (solid), symmetrical bidirectional (dashed) and FW only (dash-dot) pumping (b). The channel launch power is $-10\,\mathrm{dBm}$.

In long URFL amplifiers these oscillations are stronger, their amplitude variation is reduced and they are so widespread in frequency that the corner frequency becomes affected by them and is, eventually, pushed beyond the $100\,\mathrm{MHz}$ limit used in the simulations, leaving a nearly flat transfer function. These fluctuations have already been reported in the literature [90, 91], they are caused by the interaction between the generated counter-propagating signals and have a separation given by the cavity resonance frequency in traditional lasers.

From Fig. 4.2b it can be noted that the RIN transfer for BW pumping also exhibits fluctuations regardless of the SMF length, and that, as expected, symmetric pumping shows common features in the three pumping schemes, resulting in a higher response at low frequencies.

(a)

(b)
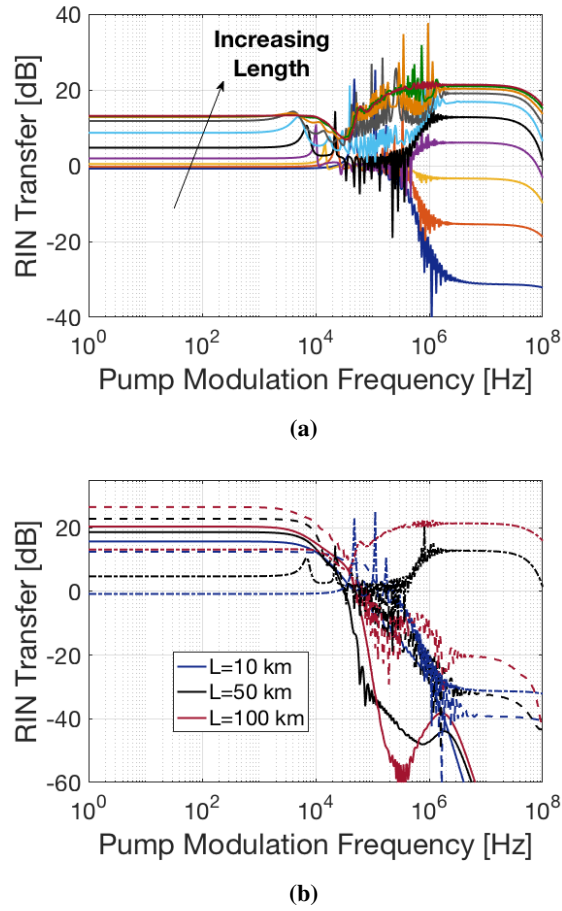
Figure 4.3: Simulated 2nd-order RIN transfer function up to $100\,\mathrm{MHz}$ in rDFB amplification as a function of the SMF fiber length ranging from $10\,\mathrm{km}$ to $100\,\mathrm{km}$ with FW only pumping (a) and for three different SMF lengths with BW only (solid), symmetrical bidirectional (dashed) and FW only (dash-dot) pumping (b). The channel launch power is $-10\,\mathrm{dBm}$.

The simulated RIN transfer function for a single-channel rDFB as a function of the SMF length, in the purely co-pumping configuration is depicted in Fig. 4.3a. As the span length

increases, so does the the RIN transfer, especially in the high frequency range, where a second floor arises and, eventually, provides the largest contribution to the transfer of noise to the signal. Interestingly, this high frequency noise becomes predominant only in purely FW pumping. Fig. 4.3b shows that the frequency response in BW only pumping (solid curves) has a single corner frequency in the kHz range, as expected. The whole frequency response grows for a 50% FPR (dashed curves) and the second floor at high frequency starts to rise. In the FW only configuration (dash-dot curves), this high frequency contribution overtakes the low and mid frequency portion of the spectrum, at least in amplifiers longer than $100\,\mathrm{km}$. It is worth mentioning that in the rDFB case, the purely co-propagating pumping scheme is merely descriptive, as it requires powers in excess of $7\,\mathrm{W}$ to pump a $50\,\mathrm{km}$ cavity, which would be highly unpractical in a realistic system.

In general, the URFL and rDFB amplifiers seem to have similar performance in terms of intensity noise, with maximum RIN transfer function values reaching $\sim 26\,\mathrm{dB}$ in a symmetrically pumped $100\,\mathrm{km}$ cavity. However, the URFL cavity produces strong fluctuations in the high frequency regime that enhance the overall amount of RIN that can be transferred to the signal. Contrarily, 1st-order amplifiers exhibit a lower maximum RIN transfer as well as a negligible high frequency contribution.

Lastly, Fig. 4.4 highlights the impact of pump depletion on the RIN transfer for 1st-order (Fig. 4.4a), URFL (Fig. 4.4b) and rDFB (Fig. 4.4c) amplifiers, in FW only pumping configuration and for three different SMF lengths. As the signal launch power is increased from $-10\,\mathrm{dBm}$ (solid curves) to $0\,\mathrm{dBm}$ (dashed curves) and $10\,\mathrm{dBm}$ (dash-dot curves) the transfer function remains nearly unchanged for cavity lengths up to $50\,\mathrm{km}$ and no effect of pump depletion can be appreciated in all of the considered amplification schemes. For longer cavities, on the other hand, a high signal input power translates into a mitigated RIN transfer in the investigated pump modulation frequency range. Nevertheless, the transfer function in the pump depletion regime does not display a definite corner frequency within the first $100\,\mathrm{MHz}$ RF spectrum. Thus, as already discussed in literature [56, 67], the combined effect of increased corner frequency and reduced low frequency response do not alter significantly the overall integrated noise level.

Figure 4.4: Simulated RIN transfer function up to $100\,\text{MHz}$ in 1st-order (a), URFL (b) and rDFB (c) amplification with FW-only pumping, for $10\,\text{km}$ (blue curves), $50\,\text{km}$ (black curves) and $100\,\text{km}$ (red curves) SMF length. The channel launch power is $-10\,\text{dBm}$ (solid), $0\,\text{dBm}$ (dashed) and $10\,\text{dBm}$ (dash-dot).

4.2 **RIN Characterization for 2nd-order DRAs**

This section presents a detailed experimental investigation of the RIN transfer from the pumps to the signal when the backreflections level (FBG effective reflectivity) at the input side of a 2nd-order Raman amplifier is varied from 0% (half-open cavity rDFB) to 95% (high-efficiency URFL) and the FW pump power is gradually increased from 0% (BW only pumping) to 100% (FW only pumping) of the total pump power. To do so, several configurations are characterized in terms of output signal RIN and mode structure of the first Stokes component at $1455\,\text{nm}$.
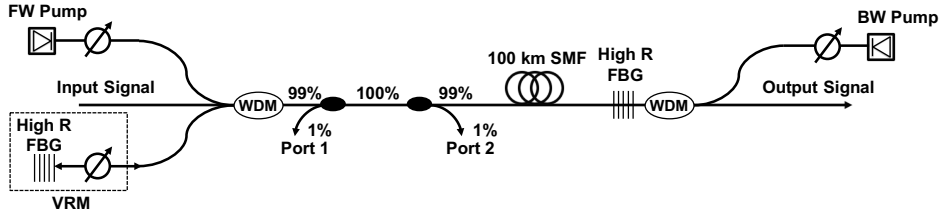
Figure 4.5: Experimental setup of a 2nd-order Raman laser amplifier with variable input-side reflectivity.

The schematic diagram of the 2nd-order Raman laser amplifier used to carry out the analysis is shown in Fig. 4.5. Two fully depolarized, virtually identical fiber lasers emitting at $1366\,\text{nm}$ bidirectionally pump $100\,\text{km}$ of standard ITU G.652 single mode fiber. A wavelength division multiplexer (WDM) is used at each end of the fiber to couple/split three signals: the pump, the generated first Stokes component at the 1455 nm central wavelength of the high reflectivity FBG at the output side and an injected $-10\,\text{dBm}$ CW signal at $1550\,\text{nm}$. The $1455\,\text{nm}$ nm port of the WDM at the input is connected to a variable reflectivity module (VRM) that provides an adjustable amount of backreflections. The VRM is composed of a variable optical attenuator (VOA) and a high reflectivity (>95%) FBG centered at 1455 nm. The VRM can reflect up to 40% of the incident light back into the cavity. The VRM effective reflectivity, which is limited by the losses of connectors and the WDM itself, is constantly monitored by means of two 99/1 splitters used to tap out part of the incident and reflected Stokes wave. Lastly, two VOAs placed at the output of both pump lasers are used to regulate the injected FW and BW pump powers while maintaining their output power and, therefore, keeping the output RIN fixed. Avoiding direct manipulation of the pump lasers current ensures that signal RIN is exclusively affected by the combined effect of the reflectivity and pump power ratio. Another possible uncertainty factor that can have an impact on RIN transfer to the signal is the variation of the FBG central wavelength with the incident power [92]. An increase in the pump power incident on the FBG causes spectral broadening of the 1455 nm lasing and a deviation of the central wavelength from the nominal value due to thermal expansion. Fig. 4.6a displays the spectrum of the lasing incident on the front FBG for several values of the pump split, whereas Fig. 4.6b shows the reflectivity provided by
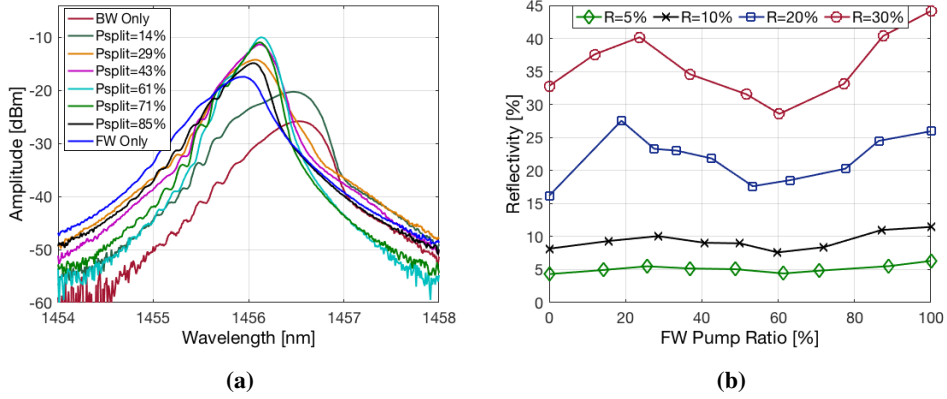
Figure 4.6: Lasing spectrum for different FW pump ratios (a) and input-side reflectivity as a function of the FW pump ratio (b).

the VRM as a function of the FW pump ratio (FPR) for four different attenuation settings of the VOA inside the VRM, corresponding to 5%, 10%, 20% and 30% reflectivity. Effective reflectivity was measured as the ratio of the reflected power at port 2 to the incident power at port 1, whereas the FW pump ratio is the percentage of total pump power provided by the FW pump. Total pump power is adjusted to obtain zero net gain for the signal at the amplifier output. As expected the reflectivity excursion is greater when the VOA attenuation is lower, as more light is let through to the FBG, but all of the four curves exhibit the same trend with a local maximum at about 20% FW pump power ratio, a minimum around 60% where the first Stokes power is highest, and an absolute maximum at 100% when the total pump power injected into the cavity is lowest. Nevertheless, large excursions of over 10% when the initial reflectivity value is set to 20% or 30% do not have any impact on the measured signal RIN.

RIN was measured using a low noise photodetector with a $125\,\mathrm{MHz}$ bandwidth and integrated over the first $1\,\mathrm{MHz}$. The VRM VOA attenuation was adjusted to obtain 20% reflectivity for BW only pumping and then, following two different approaches, kept fixed, as the FW pump ratio was increased, in order to produce the variable reflectivity depicted in Fig. 4.6b or carefully adjusted to achieve full compensation of the backreflections variation. The comparison shown in Fig. 4.7 presents no appreciable difference: RIN evolves nearly identically in both cases according to the typical S-shaped trend.
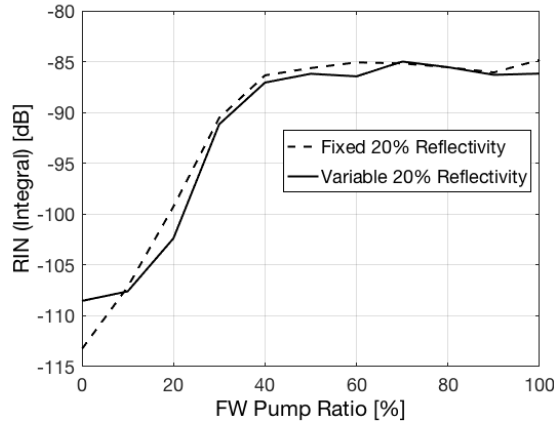
Figure 4.7: Signal RIN integrated over $1\,\mathrm{MHz}$ for a 20% variable (solid) and fixed (dashed) input FBG reflectivity.

Fig. 4.8 shows that the fiber pump lasers, two Keopsys with $8\,\mathrm{W}$ maximum output power and $-120\,\mathrm{dBc/Hz}$ nominal RIN level, exhibit a RIN level dependent on their drive current. Fig. 4.8a shows what the RIN looks like for one of the pumps as we vary the laser current. If we integrate these curves up to $1\,\mathrm{MHz}$ a better indication of the overall RIN provided to the cavity by the pumps can be obtained. From Fig. 4.8b, it turns out both lasers have a high integrated RIN for low powers, then it stabilizes to a value in between $-95\,\mathrm{dB}$ and $-110\,\mathrm{dB}$ and then starts increasing again for high powers above $32.5\,\mathrm{dBm}$.
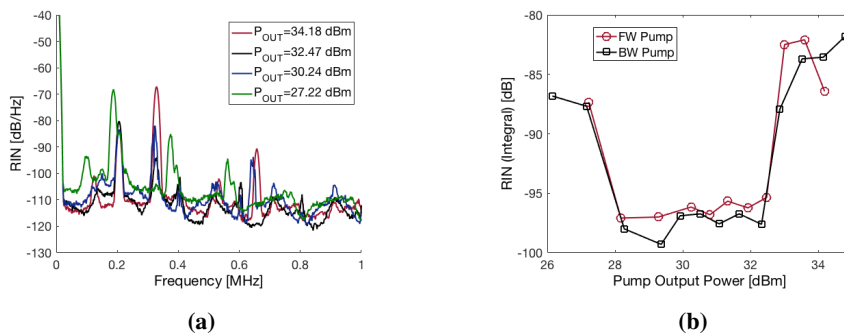
Figure 4.8: Measured pump RIN for different pump output powers (a) and integrated RIN over $1\,\mathrm{MHz}$ as a function of the output power for both pump lasers (b).

To avoid the dependence of the RIN from the pump output power and study how a fixed amount of RIN is transferred to the signal, the output power of both lasers was set to approximately $34\,\mathrm{dBm}$, a power level high enough for each laser to single-handedly pump the $100\,\mathrm{km}$ cavity.

Fig. 4.9 shows how the output signal RIN varies when the RIN of the pumps is allowed to vary with the pump power, as opposed to the adopted fixed RIN solution accomplished through external attenuation of the pumps output powers. The integrated RIN is presented as a function of the FPR for cavity configurations with the highest (40%) and the lowest (1.5%) achievable backreflections. The latter was obtained by replacing the VRM with a straight FC/PC connector.
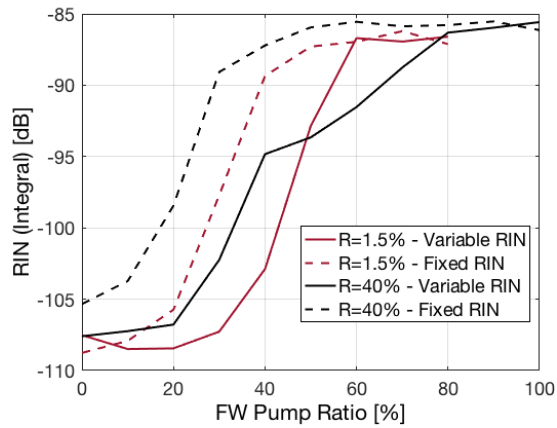
Figure 4.9: Signal RIN integrated over $1\,\mathrm{MHz}$ for variable (solid) and fixed (dashed) pump RIN in the 1.5% and 40% reflectivity cases.

The RIN level is comparable in all four cavity designs when only the BW pump is used to amplify the signal to the initial power. As the FW pump power contribution is increased, the pump-to-signal RIN transfer functions follow a dissimilar growth. The cavity most resilient to the effect of the FW pump is the one with the lowest input-side reflections and variable RIN. A FPR as high as 30% is admissible in this case with negligible penalty in terms of output signal RIN. On the other hand, feeding a fixed amount of pump RIN into the same cavity results in 10 dB integrated RIN penalty for the same 30% FPR. Furthermore, if we consider

$-100\,\mathrm{dB}$ as a reference point on the rising slope of the integrated RIN curves, the effect of the reflectivity on the maximum admissible FW pump ratio becomes clear. Regardless of the pump RIN being variable or fixed, the reduction in FPR amounts to about 10% when the input-side reflectivity is increased from 1.5% to 40%.

One way the RIN transfer principle can be explained, is by examining the mode structure of the Stokes component at $1455\,\mathrm{nm}$. A longitudinal mode structure arising in the cavity is one of the most important characteristics of a laser and manifests itself through periodic peaks in the RF spectrum of the lasing, spaced by $\Delta = c/2nL$ Hz [93].
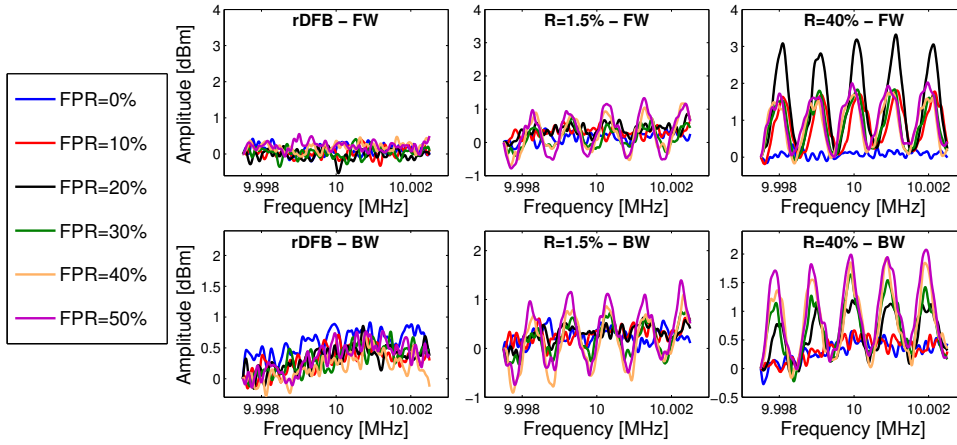
Figure 4.10: FW (upper row) and BW (lower row) propagating Stokes mode structure for rDFB, 1.5% reflectivity and 40% reflectivity configurations.

Fig. 4.10 shows the Stokes lasing component mode structure measured in FW and BW direction for FPR up to 50%. It can be noticed that for a half-open cavity with no reflections at the input side (rDFB) the $1455\,\mathrm{nm}$ wave does not present any sign of structure thus confirming the dominance of random lasing with Rayleigh backscattering feedback in both directions. The lack of a seeded forward Stokes component is also visible in the low-reflectivity (1.5%) cavity and in the high-reflectivity (40%) one with a fundamental difference: beyond a certain limit of the FW pump ratio these two partially-closed cavities do show fairly well defined modes with a $1\,\mathrm{kHz}$ peak spacing, as cavity lasing begins to dominate. In the 1.5% reflectivity configuration the FPR threshold is 30% both in the FW and BW direction, whereas in the

40% reflectivity cavity it is 10% and 20% in the FW and BW direction respectively.

These values reflect remarkably well the evolution depicted in Fig. 4.9 and confirm that it is the presence of the FW-propagating $1455\,\text{nm}$ seed that mediates in the RIN transfer between the high-order pump and the signal. As a result, 1.5% reflectivity allows for a 20% FPR, with low-RIN operation whereas, with a 20% FPR, a high reflectivity in the order of 40% causes the RIN to get more easily transferred and leads to a $7\,\text{dB}$ RIN penalty.

A more comprehensive cavity characterization for different reflectivity values is presented in Fig. 4.11a. All of the cavities, including the half-open rDFB, suffer from higher RIN transfer with increasing FW pump power. The higher the front-end reflectivity, the lower the FW pump power can be before the signal RIN starts to increase and the steeper the integrated signal RIN growth is. Interestingly, RIN transfer seems to saturate for FW pump ratios above 50%, so further increasing FW pump power does not greatly affect performance.
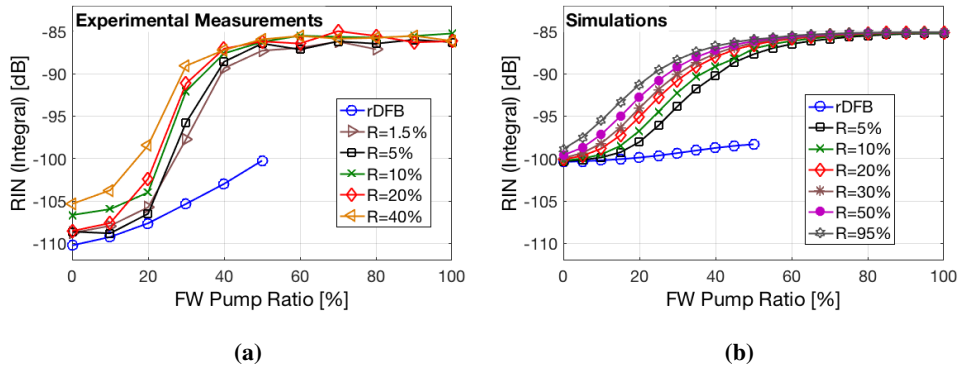
Figure 4.11: Experimental (a) and simulated (b) signal RIN integrated over $1\,\text{MHz}$ as a function of the pump power split and front-end reflectivity for a $100\,\text{km}$ 2nd-order ultra-long Raman laser amplifier.

Numerical simulations based on the ODE model were used to investigate this behavior for FW pump ratios above 40%. The results produced using the actual measured output RIN of the pump lasers, are presented in Fig. 4.11b. These show good agreement with experimental RIN trends, with the minor differences in absolute values attributable to small deviations from the stock fiber characteristics used in the simulation.

4.3 **Transmission Span Optimization**

Over the past few years, various ultralong Raman laser-based amplifier configurations have been proposed [57, 58, 59] which have unlocked record performances in a variety of applications. Discrete broadband Raman amplification [94] and distributed amplification, both unrepeatered and long-haul [76, 82, 83, 84, 89, 95], provide tangible improvements but are usually limited by two main drawbacks: low pumping efficiency and RIN transfer from the pumps to the signal [66, 90, 91, 96]. For a given number of channels and transmission format, the required pump power mainly depends on the medium properties and, therefore there is little room for improvement if standard single mode fibers are to be used. Conversely, there exist a number of ways to mitigate RIN through system design while preserving the improved balance between ASE noise and nonlinearity typically provided by Raman amplifiers. For some low-gain applications, semiconductor pump lasers can be used that are inherently less noisy than fiber lasers, but these can only supply powers up to a few hundreds of mW. In more power-consuming applications, fiber pump lasers are usually deployed in conjunction with different cavity setups, pumping schemes and nonlinearity compensation techniques [85, 86, 97].

Optimal design of a Raman-amplified periodic cell depends strongly on the constraints set by overall system requirements. The best possible trade-off in terms of costeffectiveness, nonlinearity, pumping efficiency, OSNR and tolerance to relative intensity noise transfer varies depending on characteristics such as total transmission length, desirable number of spans or power budget requirements. In the previous section it has been shown that in 2nd-order amplification the maximum admissible forward pump contribution before RIN buildup depends on the amount of backreflected light at the front end of the cavity. Here, a thorough experimental and theoretical study of the best performing configurations for 2nd-order amplification over a broad range of applications is presented. Cavity parameters such as length, FW pump ratio and front-end FBG reflectivity are optimized through careful experimental characterization of the input RIN of the laser pumps, the signal output RIN, the optical signal-to-noise ratio (OSNR) and the pump power requirements for full signal power recovery after the transmission span.

The bench-top implementation of the 2nd-order URFL under investigation is the one presented in Fig. 4.5 where, this time, the SMF length is not fixed, but ranges form very short (10 km) to quite long (150 km). Although short lengths are commonly used in practice for discrete amplification only, and due to their generally lower power requirements might in some applications rely on low-RIN semiconductor laser pumps instead of noisier fiber pump lasers, they have been included in the analysis in order to have a full picture of the evolution of system response. Also, short length URFL schemes have been demonstrated to provide simultaneous spectral and spatial transparency [60], and thus have interest on their own as a potential framework for the study of nonlinear transmission systems.

Signal input power is fixed at -10 dBm to minimize the impact of pump depletion or nonlinear effects in the evaluation of the relative contribution of the different noise sources, but is nevertheless a realistic input power value for a broad range of applications, as the optimal launch power has been shown to be in between -10 dBm and -4 dBm in most of the experimental setups studied to date with this kind of amplification schemes [83, 84, 97, 98].

Since the amount of gain provided by forward pump power is key to the performance of a Raman amplifier [76, 83, 84], as it is responsible for most of the RIN transfer to the signal, this analysis, as the previous, aims at showing the evolution of system parameters as a function of the ratio of the FW pump power to the total pump power, while the latter is adjusted to fully compensate for span losses at the amplifier output.

The primary (second-order) pumps are two Keopsys high-RIN fiber lasers, whose RIN characteristics are depicted in Fig. 4.8. The RIN is measured with a 125 MHz bandwidth low-noise photodetector in the [9 kHz, 1 MHz] RF frequency range which, simulations show, is where most of the RIN transfer to the signal takes place. The FW and BW pump powers were set to 34.2 dBm and 34.8 dBm respectively in order to span all of the possible FPRs while keeping the pumps RIN fixed.

Fig. 4.12 shows how the sum of FW and BW pump powers evolves due to an increase of the VRM reflectivity as we gradually change the pumping scheme from purely counter-propagating (FPR=0) to co-propagating (FPR=1). The drop in pumping efficiency due to the absence of a reflector that helps the creation of the 1455 nm lasing is very clear for short cells up to 50 km (Fig. 4.12a): a reflectivity as low as 5% at the input side is sufficient to lower the

amount of required pump power by $2\,\mathrm{dB}$ and $1.5\,\mathrm{dB}$ for a $25\,\mathrm{km}$ and $50\,\mathrm{km}$ cell respectively, when compared to the rDFB configuration at a 50% FPR. In the longer cells the pumps experience a higher attenuation, hence the backward pump power reaching the input side is too low to have any meaningful effect on FW Stokes generation and the 5% reflectivity cavity behaves similarly to the rDFB in configurations with low FW pumping. However, as the FW pump contribution grows, the FW $1455\,\mathrm{nm}$ Stokes is more efficiently generated thanks to the feedback provided by the front FBG and the overall pumping efficiency improves.

(a) **(b)**
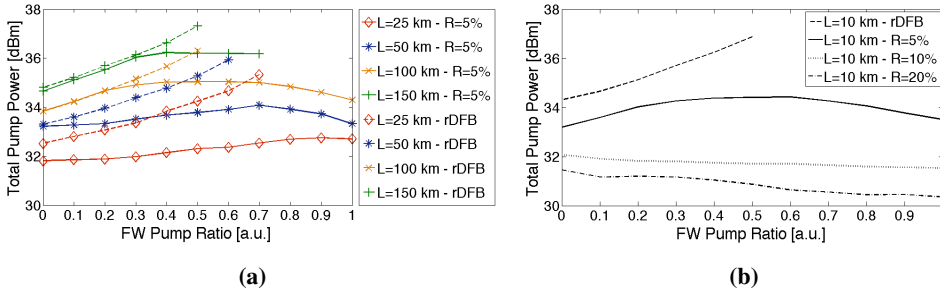
Figure 4.12: Total pump power required to achieve zero net gain as a function of the FPR for four different cavity lengths in the rDFB and 5% reflectivity cases (a) and for a $10\,\mathrm{km}$ cavity and front reflectivity ranging from 0% to 20% (b).

The special case of an extremely short $10\,\mathrm{km}$ cavity is depicted as an example in Fig. 4.12b. The SMF length in this case is too short to be able to generate enough Raman gain inside the cavity and it results in a higher required pump power, comparable to the power necessary to pump $150\,\mathrm{km}$ in an rDFB design. The power efficiency improvement yielded by a higher front reflectivity is remarkable: about $6\,\mathrm{dB}$ can be saved at a 50% FPR using a 20% FBG, nevertheless such a short cavity is still less efficient than the $25\,\mathrm{km}$ one and, in some cases, than the $50\,\mathrm{km}$ one.

Pumping efficiency is a crucial design parameter due to the energy consumption and the safety concerns it brings about in certain scenarios. If we assume that these aspects of the system design are addressed properly, Raman amplifiers are ultimately limited by ASE noise and RIN. Fig. 4.13 shows the output signal integrated RIN for the five investigated cavity lengths as a function of the FW pump ratio. Please note that the RIN has been normalized to

the cavity length L according to the formula below, in order to have a better estimation of the best-performing configuration independently of the required number of spans.

$$RIN_{dB}^{norm} = 10 \cdot log_{10} \left[\frac{1km}{L_{km}} \int_{9kHz}^{1MHz} RIN_{lin}(f) \, df \right] \qquad (4.15)$$
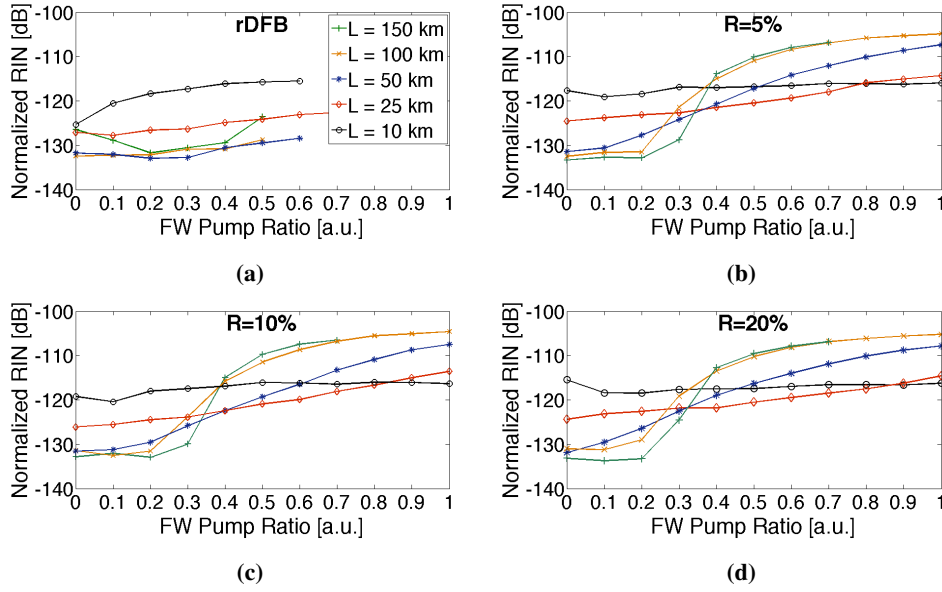
Figure 4.13: Output normalized signal RIN integrated over the [9 kHz, 1 MHz] RF frequency range for different cavity lengths in the rDFB (a), 5% (b), 10% (c) and 20% (d) front reflectivity cavity cases. The legend shown in (a) applies to (b), (c) and (d) as well.

In the rDFB case with no front-FBG the RIN evolution is essentially flat up to 50% FPR in all of the cases except for the 10 km cavity, where the required pump power is substantially higher than in most of the other designs. A higher reflectivity produces a stronger FW propagating Stokes component and, therefore, a greater amount of RIN is transferred from the FW pump to the signal, as shown in section 4.2. RIN transfer in short cavities is only marginally affected by an increase of the front reflectivity, whereas cavities longer than 50 km show a clear inflection point in between 20% and 30% FPR. Interestingly, the 150 km long cavity can tolerate a slightly higher FPR than the 100 km cavity before the signal RIN starts to increase. This behavior can be ascribed to the reduced impact of the BW pump: the

BW propagating first Stokes component generated by the BW pump travels a longer length and therefore experiences a higher attenuation. Thus, the portion reflected back in the FW direction by the front FBG is weaker and provides a smaller contribution to the RIN transfer.

Furthermore, in longer cavities, where the interaction length between the FW lasing and the signal is enough for the RIN provided by the pump to be fully transferred to the signal, a clear saturation effect occurs, with the upper bound to the signal RIN being the FW pump RIN. Some of the curves in Fig. 4.13 couldn't be completed owing to the limited available pump power.

The OSNR measured at the amplifiers output over a $0.1\,\mathrm{nm}$ bandwidth as a function of the FPR is presented in Fig. 4.14. The partially closed low-reflectivity cavity configurations exhibit somewhat similar performance: as the FW pump contribution increases the output OSNR grows as expected. Longer spans display the larger variation across the FPR range due to the higher attenuation experienced by the signal when the pumping scheme is BW biased, before the amplification from the BW pump takes place. As in the case of the RIN transfer above, the OSNR has been normalized in each case dividing the linear accumulated noise by the total length of the span, in order to compare the relative performance of the amplifier spans with independence of the total transmission length.

The beneficial effect of the FW pumping contribution is barely visible in short cavities up to $50\,\mathrm{km}$ long: the improvement is nearly negligible for FPRs up to 50% and the overall OSNR enhancement is below $1.5\,\mathrm{dB}$. On the other hand, the half-open rDFB structure seems to perform rather differently depending on the cavity length: the two shortest amplifiers perform best when purely counterpumped as the SMF length is short enough for the BW pump to amplify the signal at the beginning of the span, acting for all practical purposes as a FW pump (see Fig. 4.15, depicting signal power evolution). An increase in the FW pump contribution only adds noise and therefore reduces the OSNR. For longer lengths, the BW pump reaching the front-end is not strong enough and the signal drops significantly in the first tens of km. As a consequence, FW pumping does have a role in counteracting the fiber loss and the OSNR improves when the FPR increases as shown in Fig. 4.14c, 4.14d and 4.14e.
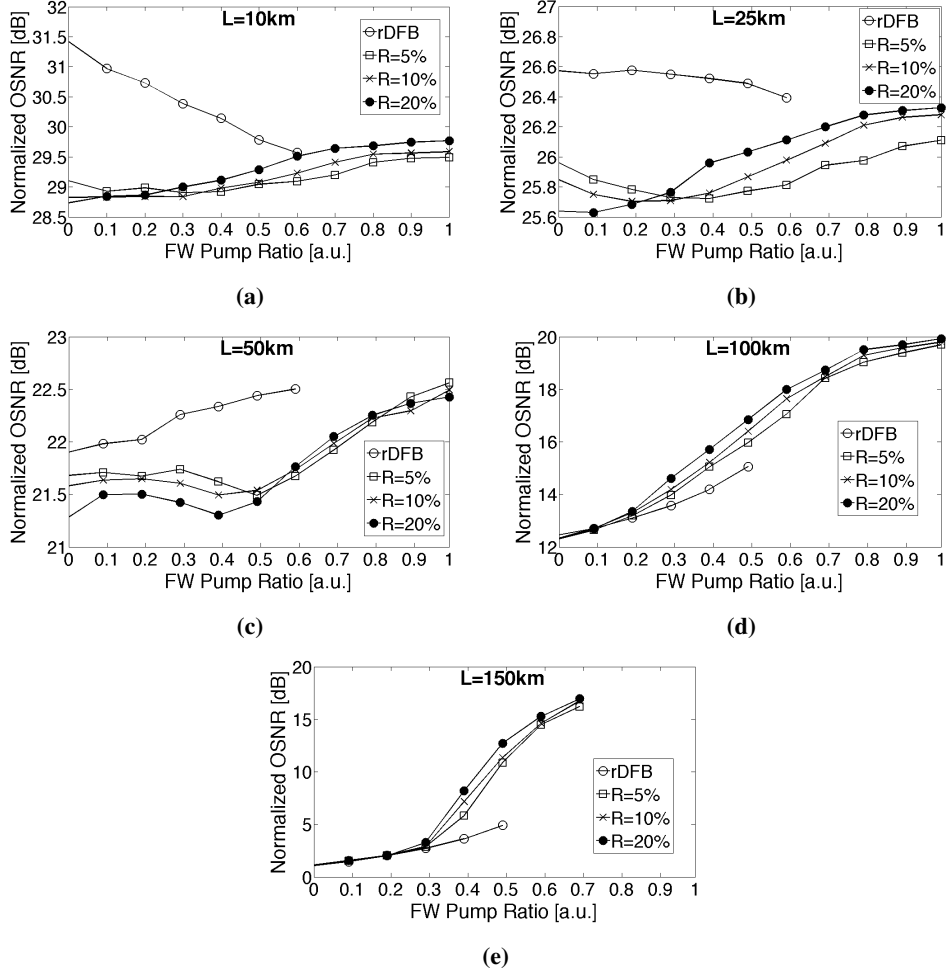
Figure 4.14: Output normalized OSNR for different front-end reflectivities in the $10\,\mathrm{km}$ (a), $25\,\mathrm{km}$ (b), $50\,\mathrm{km}$ (c), $100\,\mathrm{km}$ (d) and $150\,\mathrm{km}$ (e) cavities.

Please note that an unrestricted improvement of the ASE-based OSNR obtained increasing FPR would, as shown in Fig. 4.13, bring with it a very large increase of the RIN transfer for all spans longer than $50\,\mathrm{km}$. Moreover, after a certain value of FPR, the improvement in OSNR would also be counterbalanced by nonlinearities. Although a close-to-symmetrical scheme approaching the lowest power excursion would provide the best balance between noise and nonlinearities [99], and the gained OSNR margin would up to that point translate

into a reduced optimal launch power and better overall performance, pushing the FPR beyond this optimal point (typically above 50%) would only increase nonlinear penalties. Nevertheless, RIN transfer becomes a major limitation at even lower FPRs of 20% to 30%, hence being the latter the more restrictive effect on forward pump ratio.

Generally speaking, the rDFB scheme provides better OSNR than the low-reflectivity closed cavity URFLs in shorter cells, thanks to a higher contribution of the FW gain (see Fig. 4.15). On the other hand, in longer cells, where the attenuation experienced by the signal in the initial section of the span is quite high, the favorable effect of a low reflectivity front-end FBG becomes evident.

Fig. 4.15 shows the simulated signal power evolution for the three BW pumped rDFB configurations and for the BW pumped, $10\,\mathrm{km}$, 20% reflectivity one.
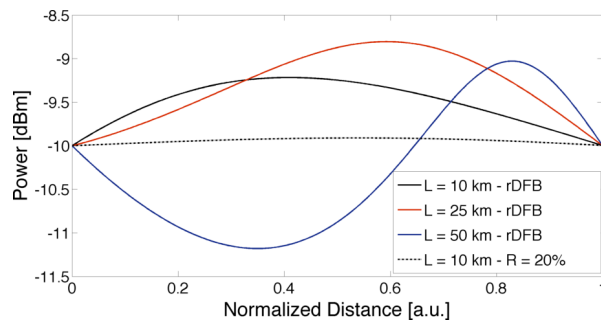
Figure 4.15: Simulated signal power evolution for three different cavity lengths in the rDFB configuration with BW-only pumping, and for a 20% reflectivity, $10\,\mathrm{km}$ cavity (dashed curve).

In conclusion, these findings offer insight on the optimal design for cavity based configurations, showing the best options to take full advantage of the benefits of Raman amplification without incurring in potentially disruptive effects for the specific applications considered. The rDFB architecture can offer advantages in terms of both OSNR and tolerance to RIN transfer only when the cavity length can be chosen to be shorter than $100\,\mathrm{km}$ as it is the case in [89] and [84], and paying a non-negligible price in pump power requirements. The specific case of unrepeatered transmission demands that the cell be as long as possible. Therefore, additional care has to be taken, as the configurations that maximize OSNR require increased front-end reflectivity and strong FW pumping that, in turn, produce the highest RIN transfer

from the pumps to the signal. In this scenario, an accurate selection of the design parameters can help improve the performance and efficiency of previously presented unrepeatered systems as in [76, 82, 95]. These results fully support the conclusions on RIN transfer reported in the previous section, and extend them to other cavity configurations, showcasing different optimal operational conditions depending on the preferred span length.

4.4 Transmission Experiment

Building upon the previously exposed results on RIN characterization, here the direct impact of RIN on transmission performance is evaluated. A 2nd-order DRA was inserted in a $30\,\mathrm{GBaud}$ dual polarization quadrature phase shift keying (DP-QPSK) system and used as the primary cell for long-haul communication. Fig. 4.16 shows the entire system, including the recirculating loop used for long-haul transmission emulation. This architecture was used to perform transmission of a single channel in a $83\,\mathrm{km}$ Raman cell, as well as of 10 WDM channels in a $100\,\mathrm{km}$ span.
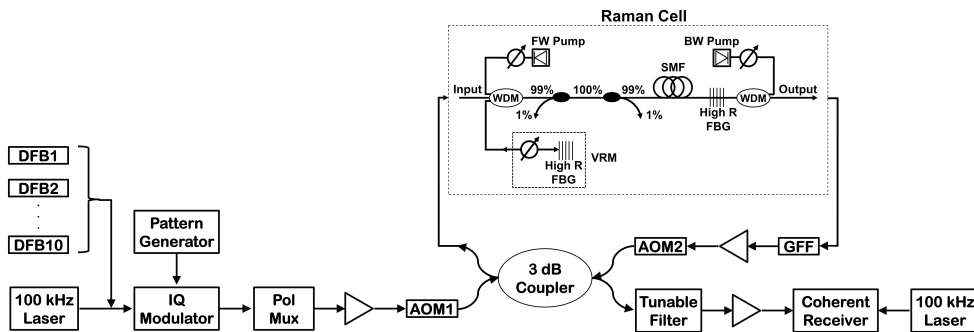
Figure 4.16: Setup of the 10x30 GBaud DP-QPSK transmission system based on a recirculating loop for long-haul transmission emulation. DFB: distributed feedback laser; AOM: amplitude optical modulator; GFF: gain flattening filter; Pol Mux: polarization multiplexer.

In the multi-channel configuration the transmitter comprises ten $100\,\mathrm{GHz}$ spaced distributed feedback (DFB) lasers located between $1542.94\,\mathrm{nm}$ and $1550.12\,\mathrm{nm}$. In order to test each available channel, the grid is combined with a $100\,\mathrm{kHz}$ linewidth tunable laser that replaces the corresponding DFB laser during the measurement cycle. No temporal decorrelation is applied to the data transmitted at each wavelength, but fiber dispersion effect-

ively decorrelates the 10 WDM channels temporally. The modulated DP-QPSK signals are launched into the Raman amplified span in the recirculating loop. The output spectrum is equalized by a gain flattening filter (GFF) and an EDFA compensates for the losses of the loop before the coherent receiver. The receiver is a standard polarization diverse coherent detection setup using an $80\,\mathrm{GSa/s}$, $25\,\mathrm{GHz}$ bandwidth real time oscilloscope for analogue to digital conversion. Digital signal processing was used offline with standard algorithms for signal recovery and linear transmission impairments compensation. A detailed description of a similar system is available in [83].

4.4.1 Single-Channel Transmission

For single-channel transmission, the three different schemes outlined in Fig. 4.17 were deployed individually as Raman cell, each providing different amounts of front reflectivity. An angled FC/APC connector at the $1455\,\mathrm{nm}$ output of the input WDM ensures that the portion of light reflected back towards the transmission fiber is close to 0%, forming a nearly perfect half-open cavity in Fig. 4.17a. The scheme sketched in Fig. 4.17b includes a flat straight PC connector at the same port (hence the name "Flat") which reflects back about 1.5% of the incident light, thus partially closing the cavity. Lastly, Fig. 4.17c shows the final stage of the transition towards a closed cavity where the input FBG reflectivity has been varied from 7% to >95%. This last structure is named after the FBG reflectivity adopted.
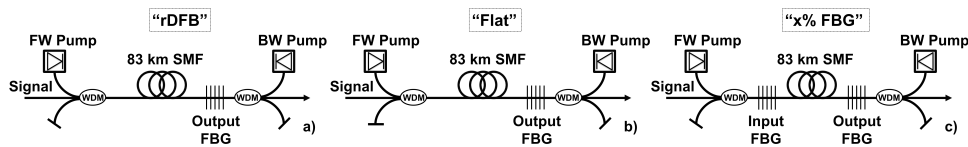
Figure 4.17: Schematic diagrams of the investigated schemes: rDFB (a), "Flat" (b) and "x% FBG" (c).

In this case, the power supplied by the two pumps was varied internally by acting on the pump lasers current, therefore the input RIN level to the cavity would change accordingly.

The test-bed performance of each scheme was evaluated by measuring the Q factor and the OSNR for a single $30\,\mathrm{GBaud}$ DP-QPSK channel propagating in a recirculating loop. Fig.

4.18a shows the Q penalty calculated as the difference between Q values at the optimal launch power for each forward pump power (FPP) after $2007\,\mathrm{km}$.
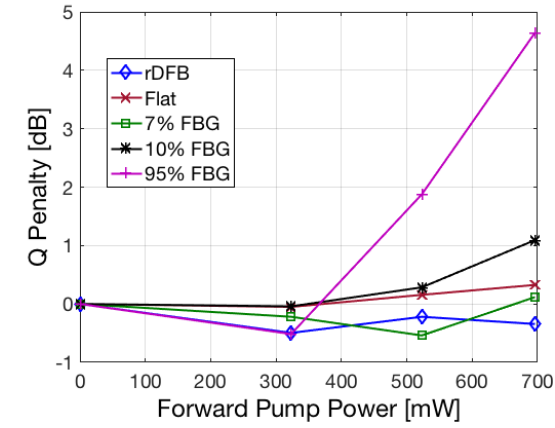
(a)
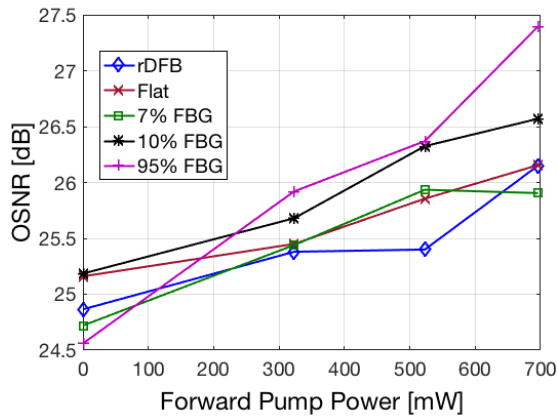
(b)

Figure 4.18: Measured Q penalty (a) and OSNR (b) for different configurations as functions of the forward pump power.

The impact of RIN translates into a penalty greater than $1\,\mathrm{dB}$ for reflectivities above 10% and $700\,\mathrm{mW}$ FPP (corresponding to $\sim$40% FPR). On the other hand low back reflections allow for the use of higher FPP at nearly no cost in terms of performance deterioration. This has the twofold benefit of improving the SPV (and therefore OSNR and transmission

performance as a whole) and reducing the total pump power requirement of a rDFB by about 10% when the cavity is partially closed with a PC connector or a 7% FBG. The OSNR variation as a function of the FPP is displayed in Fig. 4.18b for a launch power of $-10\,\mathrm{dBm}$: it grows as expected with the FPP and the FBG reflectivity thanks to the improved SPV nevertheless at high FPP the RIN contribution has the greatest influence on the system leading to the worsening of the Q penalty in Fig. 4.18a.

4.4.2 Multi-Channel Transmission

For multi-channel transmission, the Raman cell was arranged according to the variable front-reflectivity configuration of Fig. 4.5. In this case, RIN was fixed and the 1.5% reflectivity was still given by an FC/PC connector at the front WDM $1455\,\mathrm{nm}$ port.

Fig. 4.19a shows how the Q factor evolves with the launch power of the middle WDM channel at $194\,\mathrm{THz}$ for an illustrative reflectivity of 20% and FW pump ratios ranging from 0% to 40%. The optimal launch power is approximately $-4\,\mathrm{dBm}$ for up to 20% FPR and reduces to approximately $-9.5\,\mathrm{dBm}$ for 40% FPR. The Q penalty due to the FW pump power is selfevident and it becomes clear by looking at Fig. 4.19b where it is plotted against the FPR for different reflectivity levels. The launch power per single channel is the optimal for each cavity configuration and the transmission distance is $2159\,\mathrm{km}$. Cavities with front-reflectivity below 5% can tolerate pump ratios up to 40% paying a penalty of about $0.6\,\mathrm{dB}$ to the BW only pumping configuration. Backreflections of 10% and 20% lead to a non-negligible drop in the Q factor by $1.6\,\mathrm{dB}$ and $2.9\,\mathrm{dB}$ respectively for a 40% FPR.

The results for a 10% front reflectivity cavity in a multi-channel system, reflect quite accurately the Q penalty measured in a single-channel system (Fig. 4.18a), with an additional $0.6\,\mathrm{dB}$ worsening due to a slightly longer transmission distance and to the detrimental effect caused by the "fixed RIN" condition (see Fig. 4.9).

Fig. 4.20 shows the achievable Q-factors of the central channel at $1545.32\,\mathrm{nm}$ as a function of transmission distance for the different cavity configurations. A maximum reach of $5399\,\mathrm{km}$ is achievable for the 1.5% front reflectivity (Fig. 4.20a) with 10% and 20% FW pump ratios (the second one giving the best results), but RIN transfer at 40% FW ratio

quickly degrades performance despite the improved OSNR offered by the URFL configuration. The flat connector configuration offers, in any case, worse performance than any of the FBG-based configurations tested, possibly due to its extended reflection bandwidth.
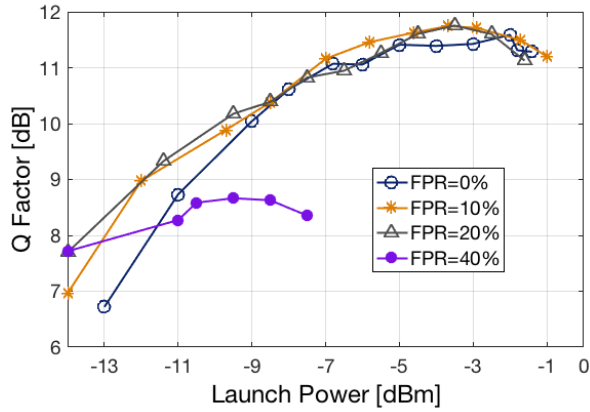
(a)
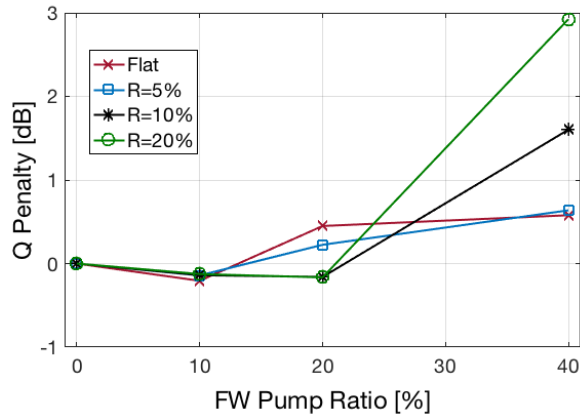
(b)

Figure 4.19: Q factor vs launch power for a 20% front reflectivity cavity (a) and Q penalty as a function of the FPR for four different cavities (b) measured in a 2159 km long 10 x 30GBaud DP-QPSK coherent transmission system.

For a 10% reflectivity front-FBG (Fig. 4.20b), reach is extended to 6479 km for a 20% FW pump ratio, which offers the best trade-off between OSNR and RIN performance. The

20% reflectivity front-FBG (Fig. 4.20c) case can offer a similar reach of $6479\,\mathrm{km}$ (with better pump conversion efficiency) for a 10% FW pump ratio, but the performance is degraded for higher FW pump ratios due to RIN transfer, as well as for the backward-only pump case, in which ASE dominates. Regarding the results obtained with 40% FW pump ratio, it is clear that, besides allowing for shorter reaches (down to only $2159\,\mathrm{km}$ for 20% front-end reflectivity), the starting performance itself is worse than in the cases with lower FW pump ratios (which allow for Q-factors close to or over $11\,\mathrm{dB}$ at a $2159\,\mathrm{km}$ distance) and decreasing for higher front-FBG reflectivities.

(a)

(b)

(c)
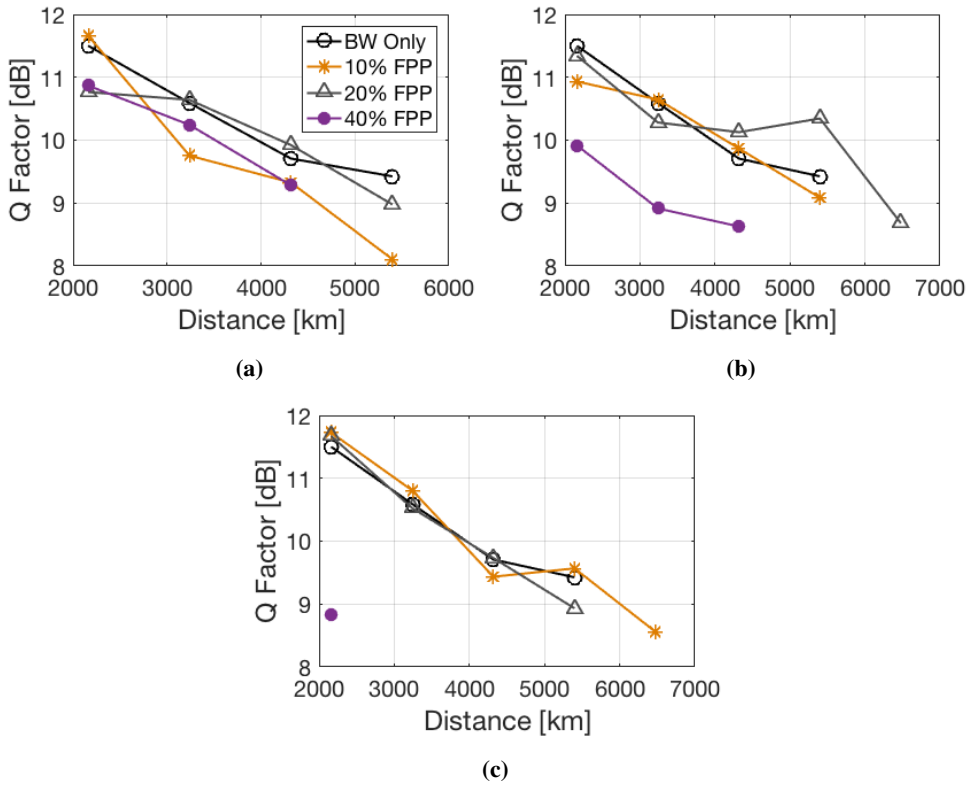
Figure 4.20: Transmission distance versus Q-factors measured at $1545.32\,\mathrm{nm}$ for 1.5% (a), 10% (b) and 20% (c) front-end reflectivity. Legend in (a) holds for (b) and (c) as well.

5

Impairment Mitigation Techniques

The performance of lightwave systems is fundamentally limited by fiber nonlinearity and its interplay with chromatic dispersion and noise. Due to nonlinearity, the signal propagating through the fiber interacts with itself and with the noise generated from the inline amplifiers. This process results in deterministic nonlinear inter-symbol interference (NISI) and stochastic nonlinear signal-noise interaction (NSNI).

One realistic and cost effective way to scale up the performance of an optical transmission system is, therefore, by mitigating (or compensating for) the effects of fiber nonlinearity. Nonlinear compensation (NLC) represents a key technology for data rate enhancement in modern telecom systems that can be implemented in the optical or digital domain. Some NLC techniques are applied at the transmitter side, others are done in the optical link and the majority is digitally implemented at the receiver side. In fact, due to the introduction of coherent detection, DSP algorithms have been employed to combat fiber impairments and in particular nonlinear distortion. Thus, nonlinear compensation techniques can be broadly classified into two categories: electronic compensation through DSP and optical compensation.

5. IMPAIRMENT MITIGATION TECHNIQUES

Optical NLC techniques can be further categorized into the use of solitons, optical phase conjugation, optical backpropagataion (OBP), phase-conjugated twin waves (PCTW) [100], and phase-sensitive amplifiers (PSAs) [101]. The use of optical solitons is the first method suggested to mitigate the nonlinear distortions due to Kerr effect [102, 103]. A soliton is an optical pulse that is formed when the phase shift induced by the self-phase modulation exactly counterbalances the phase shift induced by the CD, leading to a pulse propagation unaltered in the fiber. However, solitons were limited to low-order modulation formats such as on-off keying and suffer from pulse interactions. Communication based on solitons is regaining attention in the context of eigenvalue communication and nonlinear Fourier transform [104, 105, 106, 107].

The idea behind OPC is to reverse the nonlinear distortions generated in the first half of the link by performing a phase conjugation in the optical domain on the signal at the mid-point of a fiber-optic link. Even before coherent detection was possible, the use of phase conjugation was suggested as a way to compensate for the dispersion in optical fibers [108]. Based on this work, it was demonstrated that an OPC can also cancel out the influence of the nonlinear Kerr effect [109]. In order for this approach to work efficiently, nonlinearity, dispersion, and power profiles need to be symmetric with respect to the OPC location. Recently, OPC has regained attention as a promising candidate for reducing the impact of NSNI [110, 111, 112, 113] and will be discussed in more detail in the next section.

In the digital domain, NLC techniques can be broadly categorized into predistortion [114, 115, 116, 117], DBP either at the transmitter or at the receiver or a combination of both [118, 119, 120, 121], techniques based on Volterra kernels [122, 123, 124], and techniques based on maximum a posteriori criteria [125, 126]. One of the first studies was carried out in early 1990s where dispersion compensation was suggested using electronic signal processing at the transmitter [114]. With the advancements in DSP, dispersion was compensated using electronic precompensation at the transmitter or using a coherent or intradyne detection with coherent DSP equalization at the receiver [115, 116, 127]. Starting 2005, many studies have been focused on nonlinearity mitigation mainly using predistortion at the transmitter [117]. In these approaches, predistorted signals are calculated by backward propagating the

desired signal from the receiver to the transmitter. The idea is that the pre-distortions in the transmitted signal cancel the distortions accumulated in the real fiber propagation.

In [112], a comparison of DBP and OPC was performed and the study concluded that ideal OPC provides $1.5\,\mathrm{dB}$ SNR improvement compared to DBP. Nevertheless, DBP has been shown to yield over $4\,\mathrm{dB}$ improved SNR when combined with Raman amplification with respect to systems employing lumped amplification, at the price of a 25% increase in the number of steps used in the algorithm [128]. A combination of OPC and DBP has been suggested as an alternative to complement the shortcomings in each approach and thereby reaping the benefits of both optical and digital worlds [111].

In this chapter, the basic concepts associated with these two NLC techniques will be presented, with particular emphasis on the signal power asymmetry issue in OPC-based communications, and on the application of DBP to a Raman amplified unrepeated system.

5.1 Optical Phase Conjugation

The concept of OPC is adopted from electric communication systems and radar applications [129]. Yariv et al. introduced OPC for optical communication systems in 1979 for the compensation of chromatic dispersion [108]. In this work it was theoretically shown that the chromatic dispersion impairments in a fiber section before phase conjugation can be compensated for by the chromatic dispersion in the second fiber section. Optical phase conjugation for the purpose of mitigating nonlinear distortion due to the Kerr effect was first suggested by Fisher et al. in [109]. In that paper it was shown with a theoretical and numerical analysis that the combined effect of GVD and SPM on a pulse propagating in a dispersive nonlinear medium, e.g. an optical fiber, could be reversed by performing optical phase conjugation. The first experimental verifications of optical transmission with OPC were reported in 1993 [130, 131].

OPC is also referred to as mid-span spectral inversion (MSSI) or mid-link spectral inversion (MLSI), depending on wether a single-span or a multi-span link configuration is used. As this names suggest, the OPC NLC technique is based on the all-optical conjugation of the propagating signal when it is halfway through the transmission distance, so that distortions accumulated before the midpoint can be accumulated again, with the opposite sign, after the

101

OPC, thus effectively canceling each other out. Conjugation is usually accomplished through FWM or difference-frequency generation (DFG), two nonlinear effects based on third-order $\chi^{(3)}$ and second-order $\chi^{(2)}$ susceptibility respectively. Although DFG is a convenient instantaneous phase sensitive process, unaffected by third order nonlinear impairments, to produce conversion in the telecom C-band it requires strong pumping at $\sim 775\,\mathrm{nm}$ according to the relation $\omega_{conj} = \omega_{pump} - \omega_{signal}$. In this wavelength region it is not straightforward to provide a strong enough pump due to the unavailability of suitable amplification and, moreover, the multi-mode operations of most waveguide hinders the efficient coupling of the pump. Thus, despite the additional $\chi^{(3)}$ nonlinear distortions generated during the conversion process, FWM is often preferred and the conjugated signal frequency is given by $\omega_{conj} = \omega_{pump} + \omega_{pump} - \omega_{signal}$.

From an analytical perspective, the OPC concept can be expressed in terms of the nonlinear Schrödinger equation (2.15) to describe the evolution of a signal in a nonlinear, dispersive and lossy medium, in the first half of the transmission link, up to the midpoint z_0 where the OPC is located

$$\frac{\partial A}{\partial z} = -\frac{\alpha}{2}A - \frac{j}{2}\beta_2 \frac{\partial^2 A}{\partial t^2} + \frac{1}{6}\beta_3 \frac{\partial^3 A}{\partial t^3} + j\gamma \left| A \right|^2 A$$

Through phase conjugation the signal is complex conjugated and the pulse envelope A becomes

$$A\left(z_0 + \delta\right) = A^*\left(z_0 - \delta\right) \tag{5.1}$$

where δ is an infinitesimal transmission distance. As a consequence, the complex conjugate of Eq. (2.15) can be written as [132]

$$\frac{\partial A^*}{\partial z} = -\frac{\alpha}{2}A^* + \frac{j}{2}\beta_2 \frac{\partial^2 A^*}{\partial t^2} + \frac{1}{6}\beta_3 \frac{\partial^3 A^*}{\partial t^3} - j\gamma \left| A^* \right|^2 A^* \tag{5.2}$$

which describes the propagation of the conjugated waveform in the second half of the link. By comparing Eqs. (2.15) and (5.2) it can be noted that the conjugated signal A^* propagates with the sign reversed for the GVD and nonlinear parameters. This suggests that if the optical field is phase conjugated in the middle of the link, second-order dispersion (GVD) and the SPM-induced phase distortions acquired along the first part of the link will be exactly compensated in the second part. As the attenuation and β_3 terms do not change sign on phase

conjugation, OPC cannot compensate for fiber loss and third order dispersion (TOD). In fact, OPC compensates for all even-order dispersion terms, while leaving the odd-order terms unaffected. Interestingly, A^* also satisfies Eq. (2.15) when z is changed to $-z$. This suggests that propagation of A^* in forward direction is equivalent to sending the signal backwards, undoing distortions induced by GVD and Kerr effects simultaneously.

A method for the exact compensation of GVD and SPM using OPC has been proposed [133] in which the ratio of dispersion to the strength of the optical Kerr effect is designed to be the same at two corresponding positions, $-z_1$ and z_2, with respect to OPC as follows

$$\frac{\beta_2\left(-z_1\right)}{\gamma_1\left(-z_1\right)P_1\left(-z_1\right)} = \frac{\beta_2\left(z_2\right)}{\gamma_2\left(z_2\right)P_2\left(z_2\right)} \tag{5.3}$$

As a result total compensation of chromatic dispersion and the Kerr-effect can only be realized in a perfectly symmetric transmission link with respect to $\beta_2(z)$, $\gamma(z)$ and $P(z)$. Due to the attenuation of the optical fiber, the power envelope along the transmission line is non-constant. However, a more symmetric power envelope along the transmission line can be created by using Raman amplification and thereby obtain a significantly better compensation of nonlinear impairments [134]. In conclusion, a sufficient condition for perfect distortions compensation requires:

  i. Negligible third order dispersion

 ii. Negligible attenuation

iii. Symmetrical distribution of dispersion and Kerr effects

Although the dispersion slope issue cannot be addressed through Raman amplification and demands for a separate approach (i.e. slope compensators [135]), distributed amplifiers, especially in high-order configurations, can be highly beneficial in dealing with the other two requirements, as they allow for quasi-lossless transmission with enhanced signal power evolution symmetry.

The next section presents a numerical analysis of signal power symmetry in DRAs and shows the benefits of a reduced asymmetry in data transmission.

5.2 Signal Power Symmetry Optimization for OPC

As previously discussed, to combat fiber nonlinear effects, the use of mid-link [136] or transmitter-based [137] optical phase conjugation enables real time compensation of all deterministic (signal-signal) nonlinear impairments. However, the degree of nonlinear compensation using mid-link OPC is related to the asymmetry match of the conjugated and transmitted signal power evolution in the fiber. Meaningful performance improvement has only been demonstrated in Raman-based amplification optical links [85], thanks to the better control over signal asymmetry provided by distributed amplification, as well as its improved noise performance. The key to maximize performance in OPC-assisted systems lies in reducing signal power asymmetry within the periodic spans while ensuring a low impact of noise and non-deterministic nonlinear impairments in the overall transmission link.

In the search for an optimal setup for OPC the three previously introduced distributed Raman amplification schemes have been considered: a conventional 1st-order Raman amplifier, a 2nd-order URFL and a 2nd-order rDFB. To compare signal power asymmetry in the proposed configurations, transmission of a single channel in the middle of the C-band at $1545\,\mathrm{nm}$ with fixed launch power ($0\,\mathrm{dBm}$) was simulated. For each forward pump power ($100\,\mathrm{mW}$ step), the backward pump was simulated to give $0\,\mathrm{dB}$ net gain for the span lengths from 10 to $100\,\mathrm{km}$. Signal power asymmetry within the span was determined as [86]

$$Asymmetry = \frac{\int_0^{L/2} |P(z) - P(L-z)|\,dz}{\int_0^{L/2} P(z)\,dz} \times 100 \tag{5.4}$$

where L is the span length and P represents the average signal power.

Fig. 5.1 summarizes some of the most relevant span optimization results. The lowest asymmetry values and highest signal OSNRs for all span lengths above $58\,\mathrm{km}$ were achieved with random DFB Raman amplification. Note that optimal asymmetry in 1st-order Raman amplification is found for backward only pumping. For URFL, optimal forward pump ratios are very close to 50% for spans of up to $50\,\mathrm{km}$, but the optimal contribution of backward pumping grows for longer span lengths (FPR of $\sim$20% at $100\,\mathrm{km}$), whereas the random DFB configuration favors backward pumping at short lengths up to $30\,\mathrm{km}$, but ratios close to 50%

for longer spans. Fig. 5.1c shows accumulated residual phase shift (the product of optimal asymmetry at a given distance and corresponding nonlinear phase shift).
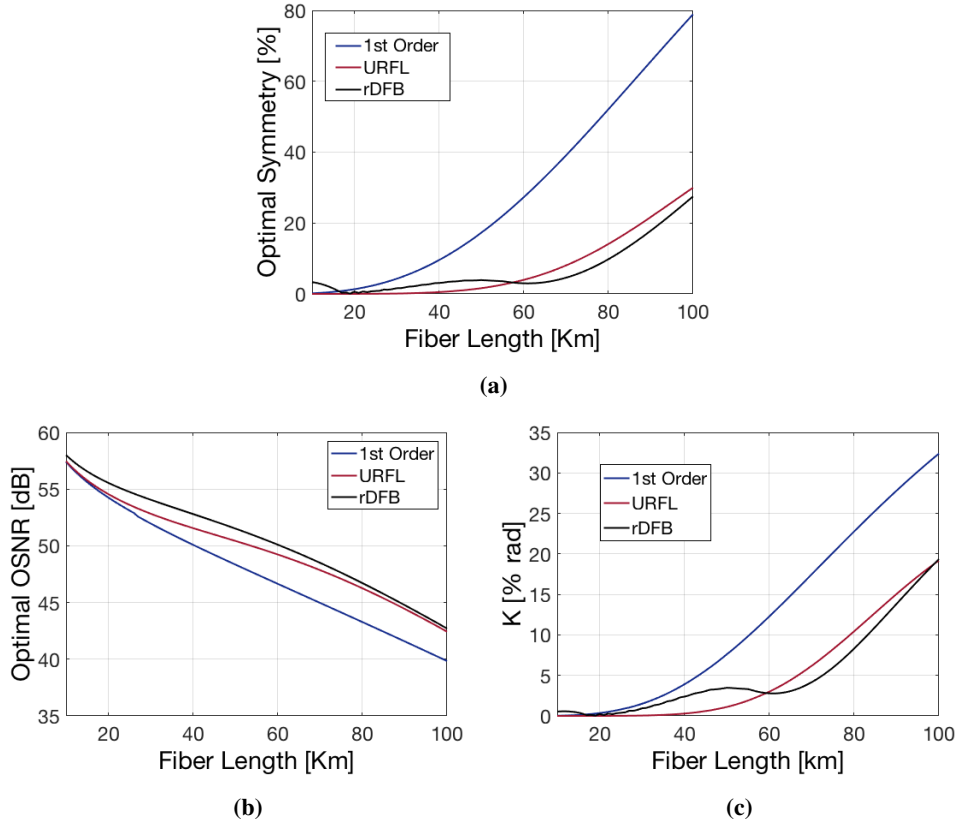
Figure 5.1: Lowest in-span signal power asymmetry for a given length and amplification setup (a), corresponding optimal OSNR (b) and accumulated residual phase shift (c).

5.2.1 Characterization of Random DFB Raman Laser Amplifier

Results for optimal asymmetry (Fig. 5.1a), corresponding OSNR (Fig. 5.1b) and residual phase shift (Fig. 5.1c), and its better resilience to forward-pumping RIN in coherent transmission applications, shows that bi-directionally pumped random DFB laser with a single grating seems to be the best option, performance-wise, for amplification in long spans with OPC. Considering these results, random DFB Raman laser amplifier was chosen for a further characterization study.
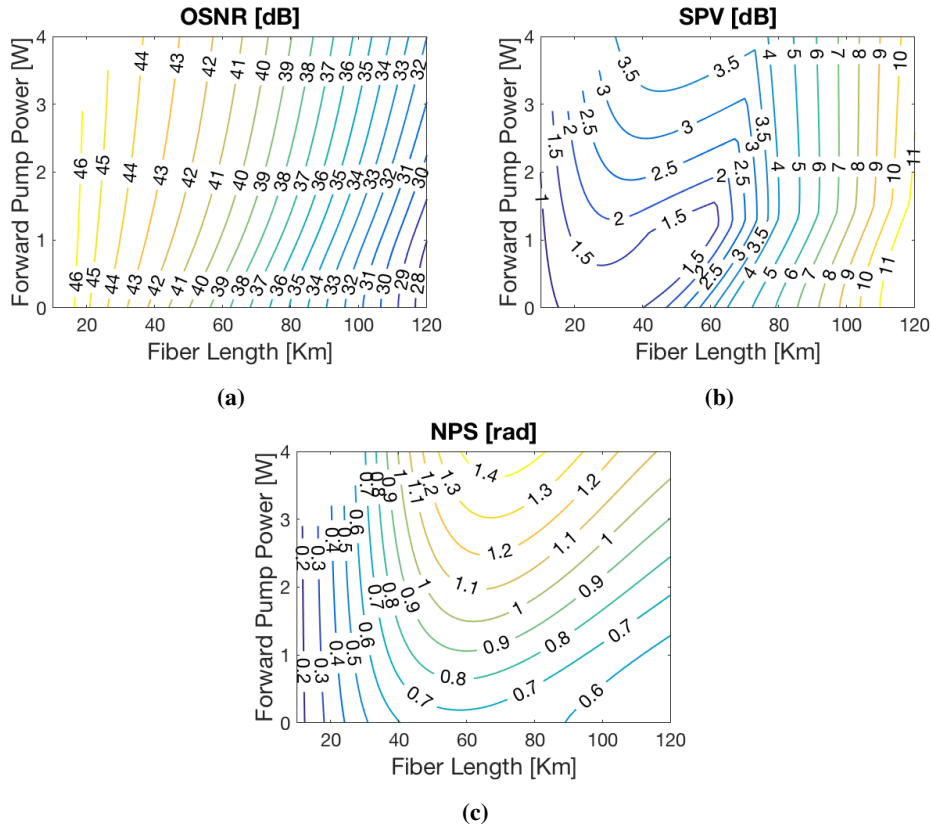
Figure 5.2: Contour plots of received OSNR [dB] (a), SPV [dB] (b) and NPS [rad] (c) for forward pump powers up to $4\,\mathrm{W}$ in the links from $10\,\mathrm{km}$ to $120\,\mathrm{km}$. Backward pump power was simulated to give $0\,\mathrm{dB}$ net gain at the end of the span.

The contour plots of the received OSNR in a $0.1\,\mathrm{nm}$ bandwidth, total signal power variation and nonlinear phase shift in the links from $10\,\mathrm{km}$ to $120\,\mathrm{km}$ are shown in Fig. 5.2 for a single channel transmission. The high forward pump power prevents the signal power from dropping at the beginning of the fiber, therefore the received OSNR will increase as expected (Fig. 5.2a), however, most of the signal gain comes from the backward-amplified $1455\,\mathrm{nm}$ component, hence not much RIN is transferred from the forward $1366\,\mathrm{nm}$ pump to the signal. A "sweet spot" for the SPV (Fig. 5.2b) can be found for the forward pump fixed just below $1.5\,\mathrm{W}$. In the simulated fiber length above $90\,\mathrm{km}$, further forward pump power increase gives negligible improvement in the SPV, while increasing the NPS (Fig. 5.2c) significantly,

therefore a reasonable trade-off must be applied in the real system design.

To evaluate the impact of the reflectivity of the FBG at the end of the transmission span, a comparison was performed between received OSNR and NPS measured at the lowest SPV that gives a reasonable trade-off between the nonlinearity induced degradation due to high forward pumping and accumulated ASE. As Fig. 5.2b shows, there is very little improvement in SPV for forward pump powers above $1.5\,\mathrm{W}$, therefore the best SPV was chosen below that level for all distances. This results in a lower total pump power consumption and more acceptable NPS in the data transmission system.

Results for FBGs reflectivities of 50%, 70% and 99% are shown in Fig. 5. The received OSNR (Fig. 5.3a) remains the same for all FBGs, however, an improvement in NPS with the higher FBG reflectivity (Fig. 5.3b) can be noticed. Increased reflectivity also results in better pump power efficiency conversion (reducing the random laser threshold and required pump power).
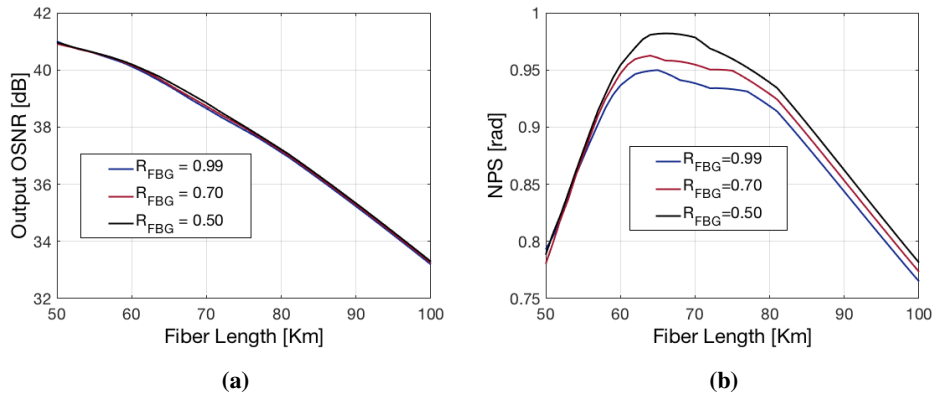
Figure 5.3: Impact of the reflectivity of the FBGs on received OSNR (a) and NPS (b), simulated for the pump power configuration that gives the lowest SPV at a given distance, with a realistic forward pump power below $1.5\,\mathrm{W}$.

The effect of power transfer from the pump to the signal is an important consideration when designing real WDM transmission systems. Due to pump depletion, the increased number of WDM channels will require higher pump powers. To simulate the impact of the pump depletion on the received OSNR, NPS, SPV and On-Off gain in dense WDM (DWDM)
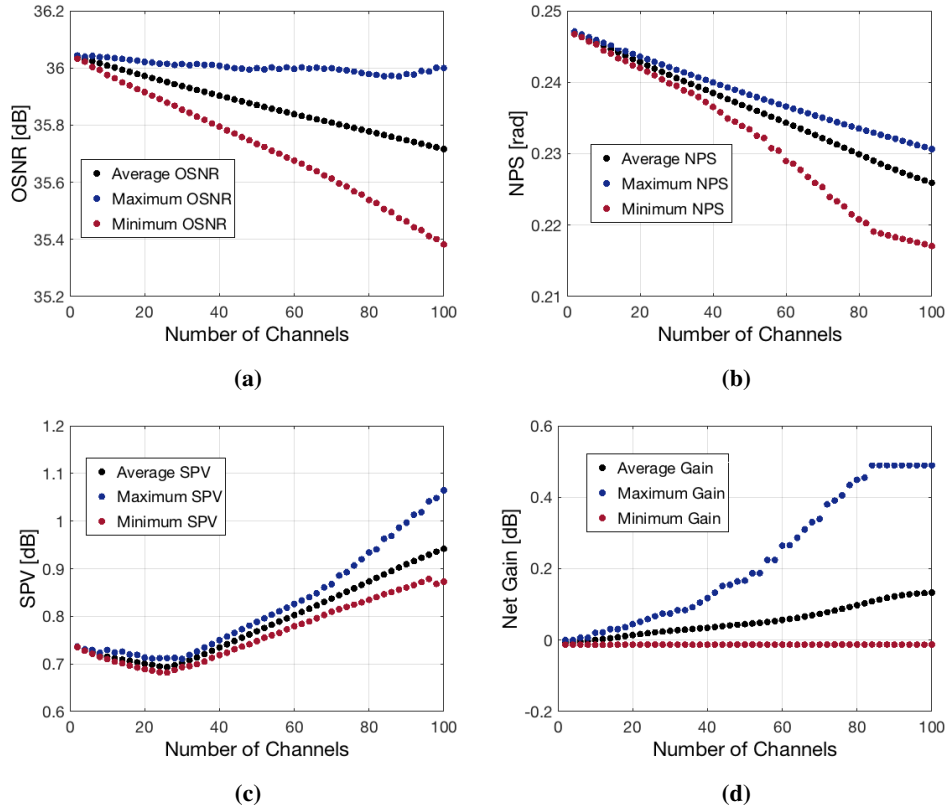
Figure 5.4: The performance of the 25 GHz spaced DWDM transmission with up to 100 channels using random DFB Raman laser amplifier. The received OSNR (a), NPS (b), SPV (c) and net gain (d) are shown for the best (blue) and the worst (red) performing channels. The span length was 50 km and the launch power per channel was set to -5 dBm.

transmission, the forward pump power was fixed to 1 W (a reasonable trade-off between OSNR, SPV and NPS shown in Fig. 5.2) and the backward pump power was optimized for a central channel at 1545 nm to give 0 dB net gain. The number of 25 GHz spaced WDM channels was incremented by 2. The DWDM channel provisioning started in the centre of the C-band at 1545 nm, with subsequent channels being added in pairs at either side of the band centre, building out towards both ends of the band. The results for the DWDM transmission covering the 1535 nm - 1555 nm band (up to 100 channels) are shown in Fig. 5.4.

The variation in OSNR results from different net gain and SPV (a result of attenuation and

Raman gain at a given wavelength). Thanks to combined gain provided by the $1366\,\mathrm{nm}$ and $1455\,\mathrm{nm}$ pumps, the maximum OSNR difference between the best and the worst performing channels is only about $0.5\,\mathrm{dB}$ ($0.3\,\mathrm{dB}$ on average) in the most loaded case of 100 channels transmission.

These results show the convenience of using high-reflectivity gratings in this kind of amplifying setup to maximize efficiency without negative impact on performance. The use of high forward pump power ratios improves OSNR performance at lengths above $30\,\mathrm{km}$, but optimal signal power variation is optimized for forward pump powers just below $1.5\,\mathrm{W}$, which could result on a more convenient balance between noise and nonlinearities for systems not limited by ASE. The results also show the excellent capacity for DWDM transmission with total gain variation across the simulated band of less than $0.2\,\mathrm{dB}$ on average.
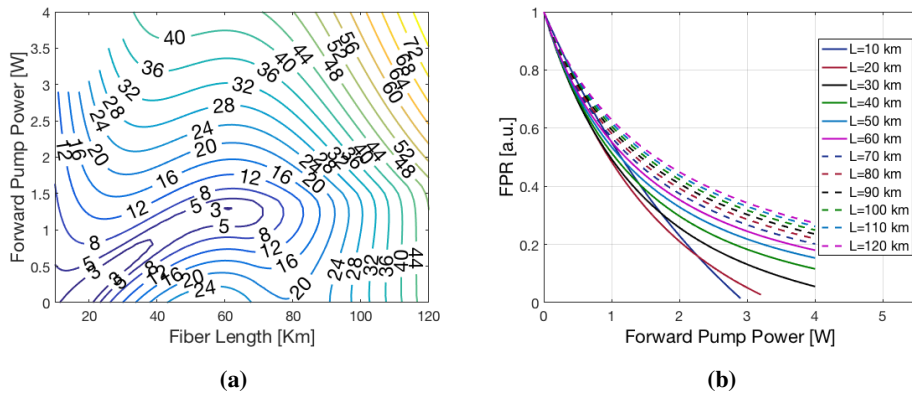
Figure 5.5: In-span signal power asymmetry in an rDFB amplifier as a function of forward pump power for different span lengths (a) and optimal forward pump ratio as a function of forward pump power (b).

The asymmetry of the signal power evolution in the transmission fiber using random DFB Raman laser amplifier with span lengths up to $120\,\mathrm{km}$, as a function of FPP with optimal backward pumping is shown in Fig. 5.5a. A "sweet spot" is found again at $62\,\mathrm{km}$ with a signal power asymmetry just below 3%, for a symmetrical forward/backward pump power split. In this scheme, the same asymmetry level can be achieved using two different values of the FPP, which allows us to further study the design principle considering both ASE noise

and nonlinearity compensation. The optimal FPR in each case as a function of forward pump power values is shown in Fig. 5.5b. To visualize the signal power distribution at different lengths, examples of power evolution profiles for $62\,\mathrm{km}$ and $100\,\mathrm{km}$ spans are shown in Fig. 5.6.
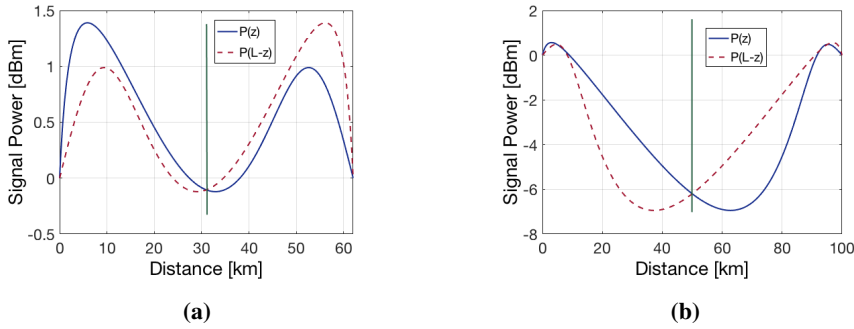
Figure 5.6: Signal power evolution profiles for $62\,\mathrm{km}$ rDFB configuration with minimal in-span power asymmetry (a) and $100\,\mathrm{km}$ rDFB (b).
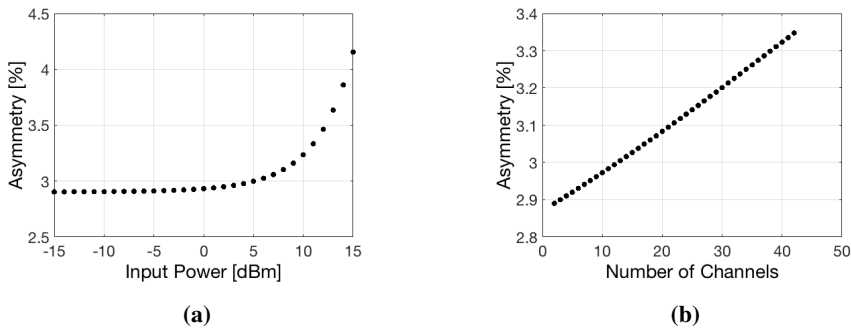
Figure 5.7: Signal power asymmetry as a function of the launch power per channel (a) and the number of the WDM channels (b) in a $62\,\mathrm{km}$ rDFB.

Signal power asymmetry as a function of a single channel launch power is shown in Fig. 5.7a. The asymmetry is rather constant for launch powers up to $5\,\mathrm{dBm}$ and increases steadily for higher power levels. To simulate the impact of the pump depletion on the signals asymmetry in dense WDM (DWDM) transmission, the pump powers were optimized for a central channel at $1545\,\mathrm{nm}$ to give $0\,\mathrm{dB}$ net gain and the number of $25\,\mathrm{GHz}$ spaced WDM chan-

nels ($0\,\mathrm{dBm}$ per channel) was incremented on both sides of the central channel. The results for the asymmetry in DWDM transmission up to 42 channels assisted with the random DFB fiber laser amplifier are shown in Fig. 5.7b. The results in Fig. 5.7 shows great asymmetry tolerance to increased launch power and pump depletion using random DFB Raman laser amplifier in OPC assisted DWDM transmission.

5.2.2 Simulation of OPC-Assisted Transmission

To investigate the impact of signal power asymmetry on the performance of system employ- ing mid-link OPC (Fig. 5.8), transmission of $7\times15\,\mathrm{GBaud}$ 16-QAM Nyquist spaced WDM polarization multiplexed signals, based on random DFB amplification in a $62\,\mathrm{km}$ Raman cell was simulated. For each channel and polarization, a random binary sequence of length 218 was first mapped into the complex plane using 16-QAM, oversampled by a factor of 20 and then passed through a Nyquist filter to generate a Nyquist-shaped signal. The filter length was 128 and the baudrate was $15\,\mathrm{GBaud}$. After polarization combining, the WDM channels were multiplexed with a channel spacing equal to the baudrate. The transmission link consisted of 40 Raman loops and an OPC placed in the middle, after the 20th loop. The propagation of signal in the fiber was simulated using a well-known split-step Fourier method, with a step size of $1\,\mathrm{km}$ considering the simulated gain and noise profiles. At the receiver, the channel under test (central) was coherently detected, the received signal was resampled and then the Q^2 factor was estimated through the error vector magnitude (EVM).
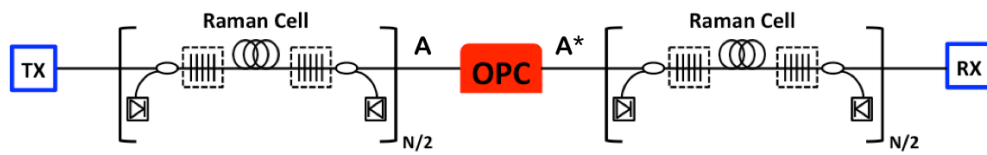
Figure 5.8: Schematic design of an OPC system.

To show the true impact of the asymmetry on the OPC system the case with fixed noise power (the worst OSNR case, that is backward pumping only, Fig. 5.9a) as well as the actual noise power in each configuration (Fig. 5.9b) were investigated. There is a perfect match of the pump powers ratio requirement for the optimum signal power asymmetry in $62\,\mathrm{km}$

link (Fig. 5.5b) and the Q-factor performance of the investigated OPC-assisted system that is $1.2\,\mathrm{W}$ for the forward and the backward pump. The optimum Q factor as a function of FPP (BPP was simulated to give $0\,\mathrm{dB}$ net gain) is shown in Fig. 5.10. It can be noticed that when the noise is fixed, the optimum Q-factor varies by $5\,\mathrm{dB}$, clearly showing that the asymmetry of the signal power evaluation has a significant impact on the performance of an OPC-assisted system. In the case of actual noise power, the optimum asymmetry level offers an additional $3\,\mathrm{dB}$ performance gain in comparison with the backward pumping only case, indicating the importance of the optimization task performed in this work.

(a) **(b)**
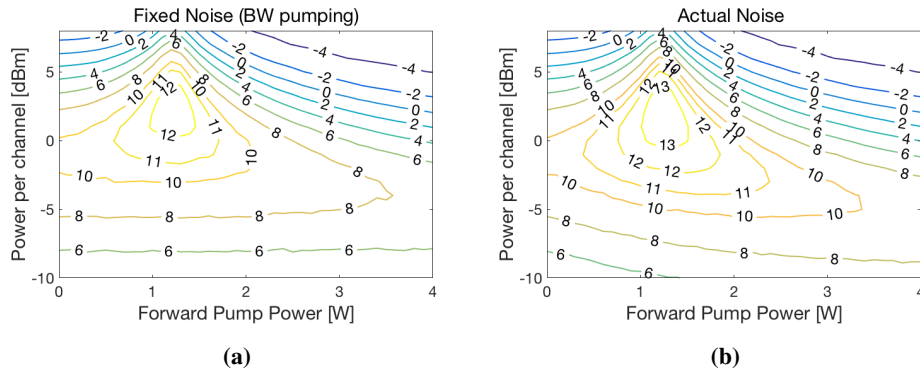
Figure 5.9: Simulated Q-Factor vs. launch power with fixed noise based on backward pumping only configuration (a) and the actual noise (b). The backward pump power was simulated to give $0\,\mathrm{dB}$ net gain.
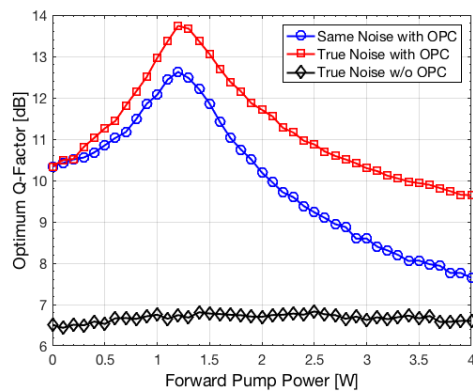
Figure 5.10: Optimum Q-factor at different forward pump powers in an rDFB-based $62\,\mathrm{km}$ link.

In conclusion, random DFB Raman laser amplifier is the most suitable solution for OPC-assisted WDM systems using span lengths between $60\,$km and $100\,$km. This setup allows to potentially reduce signal power evolution asymmetry inside the span with respect to its middle point to a mere 3% over a realistic span length of $62\,$km SMF, which constitutes the lowest asymmetry level achieved up to date on such a long span. Moreover, through simulations it has been verified, using 7x15 GBaud 16-QAM Nyquist spaced WDM signals, that the minimization of asymmetry up to a 3% over a $62\,$km span leads to greatly improved transmission performance, improving Q-factor by $5\,$dB.

5.2.3 Link Optimization for DWDM Transmission with OPC

In the previous sections it has been demonstrated that half-open cavity random distributed feedback Raman laser amplifier with bidirectional 2nd-order pumping can reduce signal power evolution asymmetry inside the span with respect to its middle point and shows the highest level of symmetry achieved up to date.

In this section the optimization of the single channel in-span signal power asymmetry variation due to wavelength dependent Raman gain and attenuation at different frequencies and span lengths is performed and, in order to investigate the best practical rDFB-based link design and the potential impact of the reduced mid-link asymmetry between transmitted and conjugated channels, two DWDM grids (original and conjugated) of 20 channels with a $25\,$GHz spacing are simulated independently across the C-band with frequency range from $192\,$THz to $195.775\,$THz.

To show wavelength dependent in-span asymmetry a single channel across the $30\,$nm C-band ($1531\,$nm - $1561\,$nm) with a $25\,$GHz step was simulated. The span length ranged from $50\,$km to $70\,$km and the pump powers were optimized to give $0\,$dB net gain and the lowest in-span asymmetry at each distance.

The forward and backward pump power split for an optimized asymmetry within the span can vary with distance. Fig. 5.11 shows the asymmetry extracted from experimental measurements and the simulated fit as a function of the pump power split at the central $1545\,$nm wavelength in a $60\,$km rDFB span.
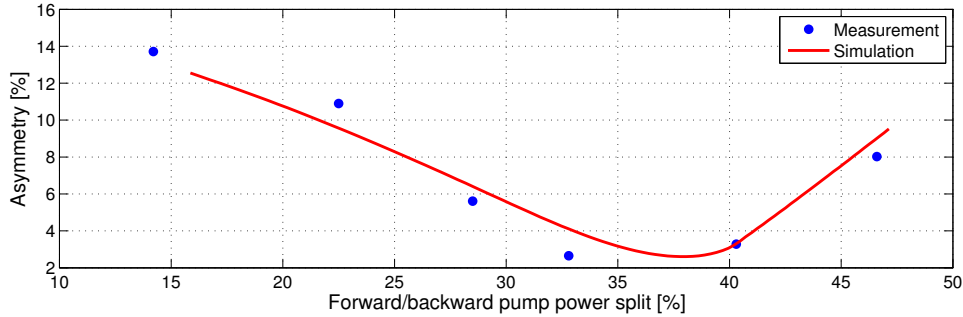
Figure 5.11: Asymmetry excursion dependence on the forward and backward pump power split measured at the central wavelength at $1545\,\mathrm{nm}$ in a $60\,\mathrm{km}$ rDFB span.

The lowest asymmetry calculated as in Eq. (5.5), and the corresponding OSNR at a given frequency for each distance are shown in Fig. 5.12. With the higher span length the asymmetry variation across the residual grid is more pronounced, hence the optimization of the link for wideband DWDM transmission is important as the performance of an OPC is directly related to the symmetry of the transmitted and conjugated channel. The flattest and the lowest overall asymmetry excursion across the simulated band was found at 58 km (Fig. 5.13).

(a)   (b)
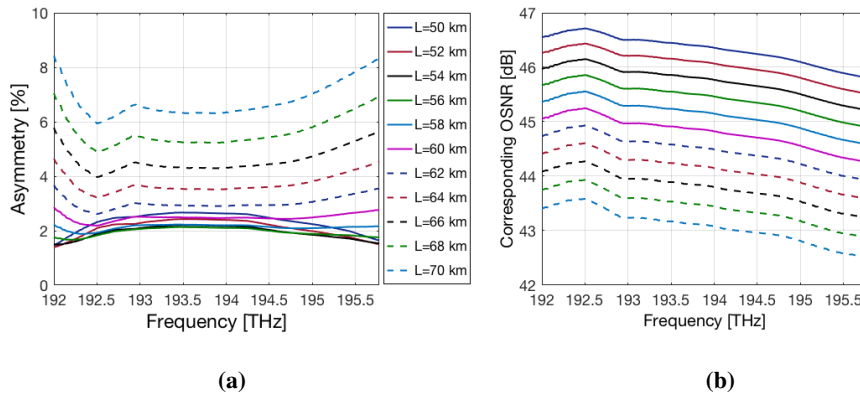
Figure 5.12: Signal power asymmetry at given frequency for different span lengths (a) and the corresponding OSNR (b).

The lowest asymmetry as well as asymmetry excursion across the measured band is found

to be for span lengths shorter than $62\,\mathrm{km}$ (solid curves in Fig. 5.12a), hence further optimization for WDM transmission has been performed in that region.
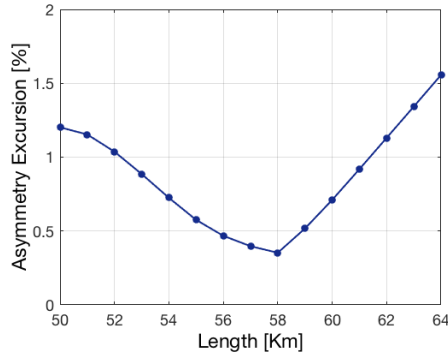
Figure 5.13: Asymmetry excursion of a single channel across C band ($1531\,\mathrm{nm}$ - $1561\,\mathrm{nm}$).

In DWDM transmission with a mid-link OPC the power evolution of the original channels and of their conjugated copies shifted in frequency was independently simulated. The channel count was set to 20, with a $25\,\mathrm{GHz}$ spacing. A $300\,\mathrm{GHz}$ spacing caused by the optical phase conjugator between the transmitted and the conjugated sets of channels was assumed. The grid was then downshifted in wavelength by $500\,\mathrm{GHz}$ until the $30\,\mathrm{nm}$ band ($1531\,\mathrm{nm}$ - $1561\,\mathrm{nm}$) was fully covered. A diagram depicting the simulated frequency sections is shown in Fig. 5.14, where original and conjugated channels are indicated with C_i and C_i^* respectively.
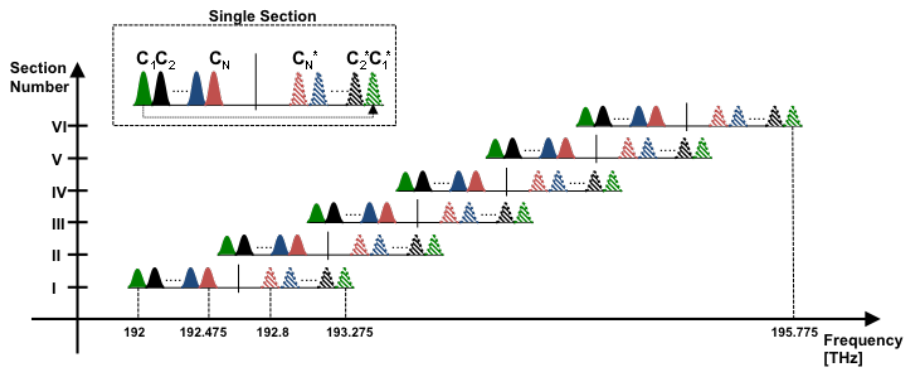
Figure 5.14: Frequency sections of transmitted and conjugated channels.

The inter-span asymmetry between transmitted and conjugated channels was calculated using the formula:

$$Asymmetry = \frac{\int_0^L |P_1(z) - P_2(L-z)|\,dz}{\int_0^L P_1(z)} \times 100 \qquad (5.5)$$

where L is the span length and P_1 and P_2 represents the average signal power of the transmitted and conjugated channel, respectively.

Each section of the band was optimized to the channel that gave the best overall asymmetry performance: the entire grid was first simulated using the pump power needed to obtain $0\,\mathrm{dB}$ net gain for the first channel, then for the second channel and so on. The same logic was applied to the conjugated copy and finally the asymmetry between original and conjugated channels with all possible combinations was calculated. The optimized results with the lowest achievable asymmetry in each section for distances from $50\,\mathrm{km}$ to $62\,\mathrm{km}$ is shown in Fig. 5.15.
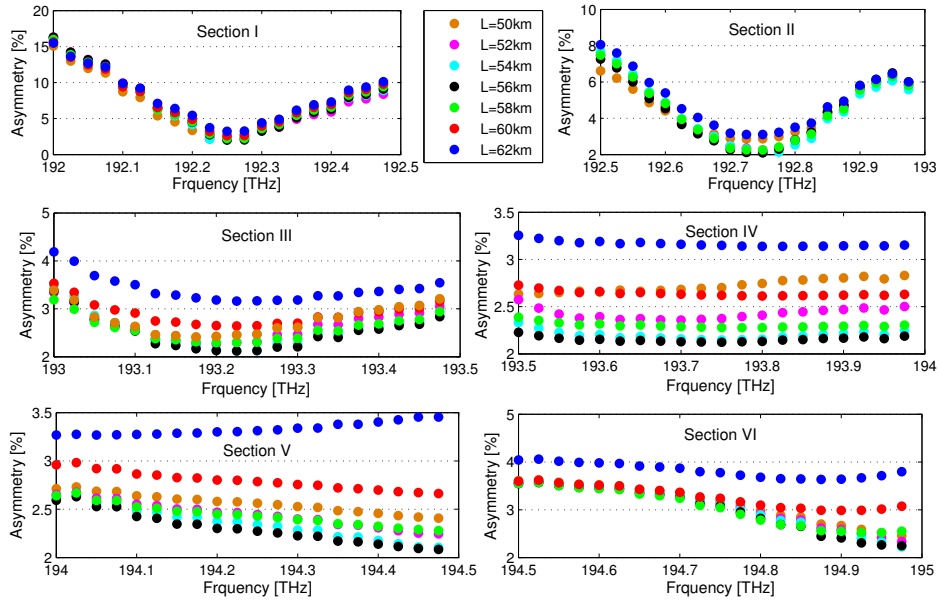
Figure 5.15: Optimized asymmetry between transmitted and conjugated WDM channels in different frequency sections and rDFB lengths from $50\,\mathrm{km}$ to $62\,\mathrm{km}$.

Due to the frequency dependence of the attenuation and Raman gain coefficient profiles, the asymmetry in the residual windows (I and II) is most pronounced. This is also valid for single channel in-span asymmetry as shown in Fig. 5.12a. As a result, the symmetry between transmitted and conjugated channels is greatest for the sections with the best in-span symmetry. Asymmetries below 4% are found to be achievable for all frequency sections from 193 THz to 195.775 THz (window III, IV, V and VI) at all span lengths considered.

The results in Fig. 5.15 highlight the importance of span length optimization for OPC-assisted wide band WDM transmission. A span length difference of only $4\,\mathrm{km}$ can lead to a strong performance degradation in nonlinear compensation using OPC due to the associated increase in asymmetry.

5.3 **Digital Back Propagation**

The DBP approach was proposed to deal with fiber nonlinearity in the digital domain. This technique can be implemented either at the transmitter [138], or at the receiver side [139], or can be split between transmitter and receiver to improve performance [140]. DBP is based on the split-step Fourier method (SSFM) [141], which represents an efficient and widely used technique to solve the Manakov equation (NLSE Eq. 2.15 in case of single-polarization transmission) given by:

$$\frac{\partial \mathbf{A}}{\partial z} = -\frac{\alpha}{2}\mathbf{A} - i\frac{\beta_2}{2}\frac{\partial^2 \mathbf{A}}{\partial t^2} + i\gamma \left\|\mathbf{A}\right\|^2 \mathbf{A} \tag{5.6}$$

where $\mathbf{A} \triangleq [A_x \ A_y]^T$ is the complex envelope of the two polarization components of the optical field, γ is the nonlinear coefficient, $\left\|\mathbf{A}\right\|^2$ represents the optical power, β_2 is the group velocity dispersion coefficient, α is the fiber attenuation factor, z is the distance of propagation and t is the time coordinate in a reference frame moving with the signal group velocity.

The solution of the Manakov equation is known analytically for particular cases, such as zero dispersion transmission, however in most situations it has to be solved numerically. The Manakov equation (5.6) can be re-written as

$$\frac{\partial \mathbf{A}}{\partial z} = \left(\hat{D} + \hat{N}\right)\mathbf{A} \tag{5.7}$$

where $\hat{D}$ is a linear differential operator accounting for dispersion and losses in the fiber and $\hat{N}$ is a nonlinear operator. In fibers, dispersion and nonlinearity act simultaneously, but they can be roughly treated as being independent in a very small distance. Thus, the SSFM can be applied following an iterative approach to describe propagation form $z = 0$ to $z = L$ with step h:

i. $\hat{D} = 0$ - The Manakov equation is analytically solved from the known initial field $\mathbf{A}\left(0,t\right)$ to obtain a nonlinear solution $\mathbf{A^{NL}}\left(h,t\right)$.

ii. $\hat{N} = 0$ - The linear solution $\mathbf{A}\left(h,t\right)$ can be calculated in the Fourier domain [21].

iii. The output from (i) and (ii) is used as initial condition for computing the solution at the next step $z + h$.

In its general form, the approximated solution to the Manakov equation in an asymmetric SSFM is

$$\mathbf{A}\left(z + h,t\right) \approx exp\left(h\hat{D}\right) exp\left(h\hat{N}\right) \mathbf{A}\left(z,t\right) \tag{5.8}$$

This equation is then applied repeatedly over the length of the fiber L, divided into N segments each of length h, so that $L = Nh$. The step size h should be chosen sufficiently small so that the absolute value of the nonlinear phase shift accumulated over a distance h should be much smaller than π. On the other hand, the smaller the step size the more complex the algorithm [142].

The main idea of the DBP approach is to find a solution of the inverse Manakov equation with inverse optical link parameters $(-\beta_2, -\gamma, -\alpha)$ so that, much as in the OPC technique, accumulated inverse distortions cancel out nonlinearities and dispersion experienced during propagation. To backpropagate the signal through a section of fiber which extends from $z + h$ to z, methods such as noniterative asymmetric SSFM [143] and iterative symmetric SSFM [144, 145] have been used. In spite of the high computational complexity, DBP has been proposed as a universal technique for jointly compensating the linear and nonlinear impairments, although DBP does not account for the NSNI, and hence is optimal when noise from the optical amplifiers of the fiber-optic channels is ignored [146].

Some new approaches have been proposed to reduce the complexity of DBP based on SSFM, such as weighted DBP [147] and correlated DBP [148]; however, they are still far from addressing efficient real-time implementation.

A detailed exposition of the numerous DBP algorithm and their performance is out of the scope of this thesis. In the next section a specific realization of the DBP technique, coupled with DRA will be employed to perform experimental unrepeatered transmission, and to assess to what extent DBP performance can be improved by feeding the DSP algorithm with simulated signal power profiles.

5.4 Unrepeatered Transmission Using DRA and DBP

In recent years, a wide variety of experiments have been carried out, that have proven unrepeatered transmission based on high order modulation formats feasible. After record repeaterless transmission distances were achieved in Raman-assisted DPSK direct detection systems [82, 149], research focus shifted towards new methods for capacity enhancement, usually achieved at the cost of a dramatic increase in system complexity. In fact, as unrepeatered systems do not normally have to abide by the backward compatibility rule, but can be designed from scratch to meet the performance requirements imposed by the specific application, within the recent past they have been equipped with all kinds of complex and costly novel technologies: advanced modulation formats (i.e. QPSK and QAM), specialty fibers such as ultra low loss (ULL) fibers [150] or ultra large effective area (ULA) fibers [151], remote optically pumped amplifiers (ROPAs), 3rd-order Raman amplification [151, 152] are examples of radical solutions that, combined with coherent detection, impairments mitigation techniques and enhanced forward error correction (FEC), have enabled the continuous growth of unrepeatered communications.

Focusing on the recently developed QAM-based solutions, transmission over distances as long as $370 \, \text{km}$ [153] and with spectral efficiencies up to $7.99 \, \text{b/s/Hz}$ [76, 150] has been achieved using 16-QAM modulation, usually in combination with polarization multiplexing, Raman amplification, ROPAs and DBP.

In fiber optic communications, quadrature amplitude modulation with coherent detection is widely deployed due to its good balance between robustness against OSNR degradation

and spectral efficiency. To maximize the transmission distance, it is necessary to maintain an acceptable OSNR through the system, which is critical when using high order modulation formats. In fact, when considering higher cardinality QAM, spectral efficiency can be improved up to $8.95\,\mathrm{b/s/Hz}$ with 64-QAM [154] or $10.31\,\mathrm{b/s/Hz}$ with 128-QAM [155] at the price of a reduction in communication distance down to $160\,\mathrm{km}$ and $120\,\mathrm{km}$ respectively. Furthermore, distributed Raman amplification reduces signal decay in the fiber span leading to a higher OSNR, and is therefore the preferred amplification method in unrepeatered systems [82, 95, 97, 149, 151, 153, 154, 155, 156, 157].

This section presents the experimental results obtained for Raman-based, DBP-assisted single-channel unrepeatered transmission with 64-QAM modulation over up to $240\,\mathrm{km}$, without the aid of any specialty fiber or remote pumping scheme.
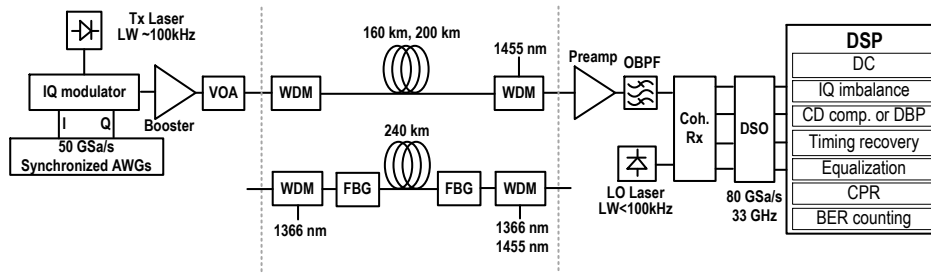
Figure 5.16: Schematic design of 64 QAM experiment setup with distributed Raman amplifiers.

Fig. 5.16 depicts the experimental setup for the $28\,\mathrm{GBaud}$ Nyquist-shaped optical 64-QAM unrepeatered system. The transmitter consists of two synchronized $550\,\mathrm{GSa/s}$ arbitrary waveform generators (AWGs), optical IQ modulator and an external cavity laser (ECL) laser having less than $100\,\mathrm{kHz}$ linewidth (LW). A pseudo-random bit sequence with a word length of $2^{15} - 1$ (PRBS15) is generated and Gray mapped to generate a $28\,\mathrm{GBaud}$ 64-QAM signal followed by Nyquist pulse shaping with a 0.15 roll off factor. The sequence is then resampled to match the sampling rate of the AWGs. At the output of the IQ modulator, the optical signal is amplified using an EDFA. The signal is then fed into a preamplifier, bandpass filtered and detected by a coherent receiver with an integrated local oscillator laser with

less than $100\,\text{kHz}$ LW. A digital storage oscilloscope (DSO, $80\,\text{GSa/s}$, $33\,\text{GHz}$) is used to convert the signal into the digital domain with offline demodulation.

The transmission fiber used in the experiment was standard SMF-28 with approximately $0.2\,\text{dB/km}$ loss. The measured loss in $160\,\text{km}$, $200\,\text{km}$ and $240\,\text{km}$ links, including splices, was $33.6\,\text{dB}$, $41\,\text{dB}$ and $52.7\,\text{dB}$, respectively. The loss from forward and backward WDM was $0.6\,\text{dB}$ and $0.8\,\text{dB}$, respectively. In unrepeated $160\,\text{km}$ and $200\,\text{km}$ transmissions, a first-order distributed backward pumped Raman laser based amplification with pump centered at $1455\,\text{nm}$ was sufficient to achieve a BER below the soft FEC limit. However, given the strong OSNR constraints of the system at longer distances, in the $240\,\text{km}$ experiment 2nd-order hybrid dual/URFL bidirectional pumping scheme was used, with the highly depolarized forward and backward pumps centered at $1366\,\text{nm}$. Note that, although the amplifier configuration is itself similar to that of an ultralong cavity laser, due to the span length, two independent random DFB fiber laser amplifiers are formed at the beginning and at the end of the transmission fiber [58]. The random distributed feedback lasing in the forward direction was formed due to reflected Stokes-shifted light by a high reflectivity (95%) FBG centered at $1455\,\text{nm}$ with a $0.5\,\text{nm}$ bandwidth. The backward pumping was formed by two Raman pumps at $1366\,\text{nm}$ and $1455\,\text{nm}$. To combine and demultiplex Raman pumps and the signal, two 1x3 WDM couplers were inserted in the beginning and at the end of the span. In all setups, an EDFA stage was implemented before and after the transmission line.

Digital post-processing includes DBP realized by fixed step algorithm [141] followed by resampling to 1 samples per symbol. A multi-modulus algorithm (MMA) equalizer is applied to compensate for linear polarization effects and finally a filtered blind phase search (F-BPS) [158] for carrier frequency and carrier phase recovery (CPR) is performed, followed by error counting.

The back-to-back performance of the system implemented in the RISE/Acreo laboratory in Stockholm (Sweden) is presented in Fig. 5.17. Due to hardware limitations, only OSNRs in excess of $22\,\text{dB}$ allow for BER below the soft-FEC threshold of $2 \cdot 10^{-2}$.
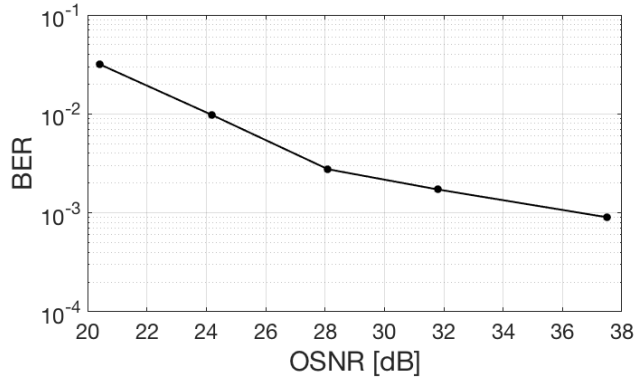
Figure 5.17: BER back to back performance of the 64-QAM system as a function of the received OSNR.

Generally speaking, the DBP algorithm requires as an accurate simulated power profile as possible in order to properly compensate for deterministic nonlinear effects occurring during transmission. Different evolutions of the signal average power, in fact, lead to different nonlinear interactions along the span. When used in combination with Raman amplification, especially 2nd-order bidirectionally pumped Raman schemes, DBP complexity increases due to the nonlinear effects being distributed along the whole transmission link. On the contrary, in EDFA-based systems, the nonlinear phase shifts experienced by the signal are condensed in the first few km of the span, where the signal power is highest.

For each of the two chosen pumping configurations, the DBP stage within the DSP was fed with the simulated power profiles shown in Fig. 5.18 for the specific case of $0\,\mathrm{dBm}$ launch power. Fig. 5.18b, in particular, shows that in order to reduce the SPV, and consequently improve the OSNR, in the $240\,\mathrm{km}$ bidirectionally pumped hybrid dual/URFL amplifier, high FPRs above 50% are required. Although in unrepeatered single span communications the signal travels along the transmission link only once and, thus, the RIN-induced penalty is remarkably lower than in long-haul transmission where it accumulates in each span, RIN associated with such high FPRs can still frustrate the benefits of the increased OSNR.
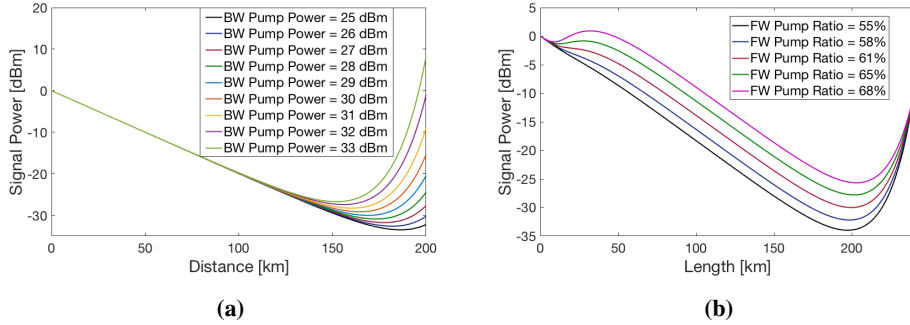
Figure 5.18: Simulated signal power profiles for a $200\,\mathrm{km}$ purely counter-pumped system (a) and a $240\,\mathrm{km}$ hybrid dual/URFL bidirectional pumping scheme (b).

On the other hand, in purely BW pumped $160\,\mathrm{km}$ and $200\,\mathrm{km}$ links, where the signal average power evolves as in Fig. 5.18a, an increase in the BW pump power only affects propagation in the last few tens of km, when the signal power is so low that nonlinear effects are hardly intensified. As a result, DBP performance is negligibly affected by the power profile.
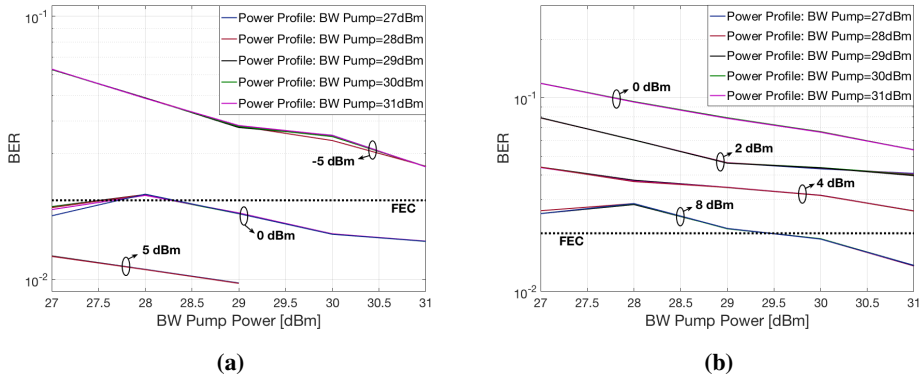
Figure 5.19: Measured BER for the $160\,\mathrm{km}$ (a) and the $200\,\mathrm{km}$ (b) BW only pumped link as a function of the BW pump power for different launch power levels and power profiles fed to the DBP algorithm. The dotted black line represents the soft-FEC threshold.

As shown in Fig. 5.19, at each experimental launch power level, the BER curves as a function of the experimental BW pump power evolve identically, regardless of the simulated

power profile used in the DBP algorithm. As the backward pump power is increased, so does the OSNR and the BER shows some improvement. The effect of the DBP in the $1^{st} - order$ purely counter-pumped systems is presented in Fig. 5.20, where the best achieved BER (averaged over 10 consecutive measurements) curves are compared to those obtained when no DBP was used to compensate for impairments in the $160\,\mathrm{km}$ and $200\,\mathrm{km}$ links.

In both cases the best BER improvement occurs for the highest input powers due to higher nonlinear effects at the beginning of the span that the DBP is able to compensate for. It can be noticed that without DBP below FEC, 64-QAM transmission over $200\,\mathrm{km}$ could not be accomplished at any launch power level. DBP makes it feasible to reliably transmit a $28\,\mathrm{GBaud}$ 64-QAM modulated channel over $200\,\mathrm{km}$ with $6\,\mathrm{dBm}$ launch power and $30\,\mathrm{dBm}$ BW pump power or, alternatively, with $8\,\mathrm{dBm}$ launch power and a relatively low BW pump power of $27.5\,\mathrm{dBm}$.

(a)   **(b)**
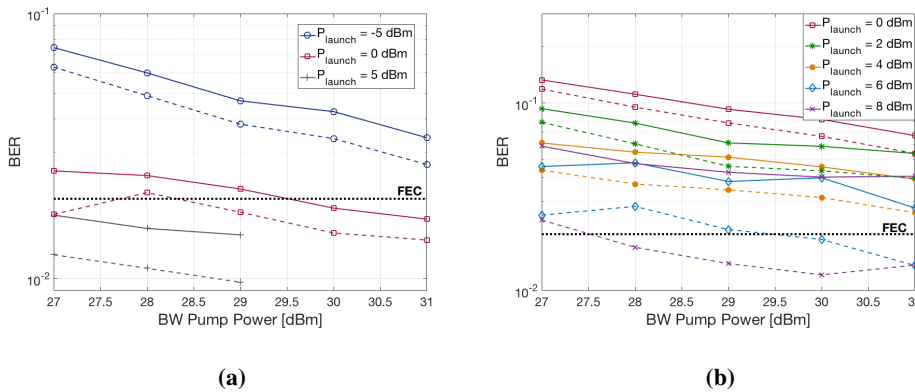
Figure 5.20: Comparison between measured BER for the $160\,\mathrm{km}$ (a) and the $200\,\mathrm{km}$ (b) BW only pumped link as a function of the BW pump power for different launch power levels, with (dashed) and without (solid) DBP. The dotted black line represents the soft-FEC threshold.

Although higher order amplification has proven [82, 83, 95] to be superior in long-haul and unrepeatered communications, transmission over $240\,\mathrm{km}$ using 2nd-order bidirectional Raman pumping could not be achieved. The results of transmission with and without DBP for different launch and total pump powers are shown in Fig. 5.21. The FPR in this configuration was about 50% throughout the experiment.

Similarly to previous transmission experiments, the highest BER improvement employing DBP is for the signal with the highest launch power (light blue and purple curves). DBP successfully compensates for nonlinear effects up to a certain total pump power level, beyond which a combination of different factors leads to performance degradation. ASE noise, RIN, hardware limitations and the limits of the specific DBP implementation result in BERs well above the FEC limit for every considered launch power and total pump power.

Dashed curves in Fig. 5.21 represents the minimum achievable BER at each total pump power level. In fact, a thorough optimization of the DSP parameters (i.e. equalizer taps, number of SSFM iterations, SSFM step size, number of test phases in the CPR) as well as of the simulated signal power profiles used by the DBP was carried out. An example is shown in Fig. 5.22 for a single acquired waveform with $8\,\mathrm{dBm}$ launch power and $3.8\,\mathrm{W}$ total pump power.
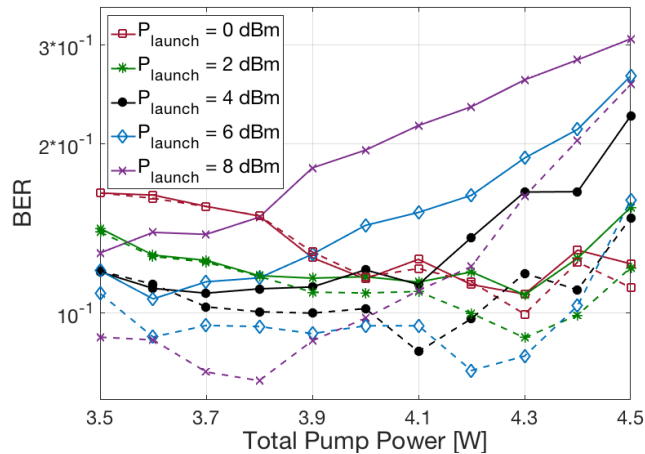
Figure 5.21: Measured BER for the $240\,\mathrm{km}$ bidirectionally pumped link as a function of the pump power for different launch power levels, with (dashed) and without (solid) DBP.

A total of 75 power profiles were generated for 5 different pump power splits and 15 launch power values ranging from $-4\,\mathrm{dBm}$ to $10\,\mathrm{dBm}$. The DBP used these profiles to compute the inverse NLSE calculation and produced 75 results, the best of which was included in Fig. 5.21. Although the simulated pump powers differ considerably from the actual pump

power used in the experiment, a certain impact of the power profile can be seen. As the simulated launch power approaches the experimental power, DBP performance improves. The best BER is achieved for simulated launch powers in between $4\,\mathrm{dBm}$ and $8\,\mathrm{dBm}$. Interestingly, minimum BERs corresponds to different simulated pump splits depending on the simulated input power, which can be attributed to changes in the average power evolution due to pump depletion as the signal power increases. Moreover, optimum BER is about $8.5 \cdot 10^{-2}$ regardless of the power profile, which suggests that a good match between simulated and experimental signal power profiles in a fixed step DBP can provide only that degree of improvement to a system that is inherently limited by other sources of distortion.
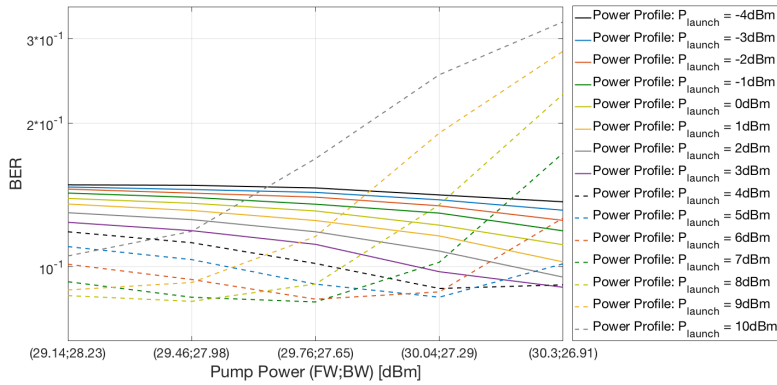
Figure 5.22: BER for a single acquired waveform with $8\,\mathrm{W}$ launch power and $3.8\,\mathrm{W}$ total pump power as a function of the power profile fed to the DBP simulated with launch powers from $-4\,\mathrm{dBm}$ to $10\,\mathrm{dBm}$ and different pump splits.

6

Raman Polarizers

Electromagnetic waves, such as light, exhibit polarization. Polarization is a valuable property of the signals propagating in optical fibers, as it provides an additional degree of freedom in various applications, such as advanced modulation formats in optical fiber communication systems, polarization-assisted fiber sensor applications, sensitivity-enhanced biomedical applications, etc. On the other hand, polarization is difficult to control and it is sometimes associated with signal degradations due to the random and dynamic polarization evolutions along the fiber, mainly caused by PMD. Moreover, polarization has a key role also in the development of Raman amplifiers as they exhibit a high degree of polarization dependent gain (PDG), which causes components of the signal co-polarized with the pump to be more efficiently amplified than others.

Besides being an impairment, PDG can be also exploited to control polarization. The non-linear polarization pulling (NLPP), also referred to as polarization attraction, is an all-optical way to control the state of polarization of signals which has been proposed in recent years [159, 160, 161, 162, 163, 164, 165]. More precisely, the polarization attraction effect enables to align a generic input state of polarization (SOP) towards a fixed one. This type of polarization pulling, which occurs thanks to the strong polarization dependence of the

Raman gain, has the great advantage to completely occur in the optical domain and to be nearly instantaneous.

6.1 Polarization Attraction

In circular fibers, because of the circular symmetry, two perpendicularly polarized waves exhibit the same propagation constant. Therefore, the polarization state of the wave stays constant throughout the propagation. However, despite the advancements in optical fiber manufacturing, real fibers may exhibit considerable variation in the shape of their core along the fiber length. They may also experience nonuniform stress, such that the cylindrical symmetry is broken. As a result the polarization state at the end of propagation is different than the initial state. This is the primary reason why optical communication components typically need to be polarization insensitive.

One parameter used to characterize the circular symmetry of a fiber is called modal birefringence, which is defined as in Eq. (2.30). One way to eliminate the fluctuation in the polarization state is to intentionally increase the birefringence. When the birefringence is large enough (in the order of 10^{-4}), coupling from one polarization to another is difficult. Similarly, by increasing the birefringence small changes in the birefringence do not significantly affect the final polarization state.

In recent years, the nonlinearity of low-birefringence optical fibers has been exploited to achieve control and stabilization of the SOP of a signal through the polarization pulling effect: the nonlinear interaction of the signal with a strong polarized CW pump, causes the signal SOP to be attracted towards the pump SOP.

Nonlinear polarizers have a twofold advantage over conventional linear polarizers as they do not polarize light by discarding the orthogonally polarized component, thus averting the 50% loss of the initial energy, and virtually eliminate the polarization dependent loss due to polarization fluctuations of the signal that result in intensity fluctuations after a linear polarizer.

Two main nonlinear polarization techniques are currently being actively investigated:

i. Techniques based on either cross-polarization modulation or degenerate four wave mixing that consist in injecting into the fiber two intense beams with the same or similar wavelength. First demonstrated by counter-propagating the two beams into short sections of isotropic highly nonlinear fibers [159, 160, 161], polarization attraction has also been observed on a signal co-propagating with a CW control pump in a few km of telecom fiber [162, 163], which has random birefringence due to its anisotropy.

ii. Techniques based on the polarization dependent gain associated with scattering phenomena such as Brillouin [166] and Raman [167], and with the parametric amplification process [168]. These polarizers can concurrently amplify and polarize an initially depolarized signal by means of a polarized CW pump beam at a different wavelength. Polarization attraction, in this case, is far more efficient when low-PMD fibers are used. In fact, when the nonlinear length of the fiber is shorter than the PMD diffusion length $L_D = 3/(D_p\Omega)$, the signal is amplified before the SOPs of the signal and the pump become decorrelated due to the wavelength dependance of the linear birefringence. Since the gain is strongly polarization dependent, the signal SOP is attracted to the pump SOP.

Polarizers based on Raman and Brillouin scattering can produce strong output intensity variations due to the effect of PDG when the input signal SOP fluctuates. However, this RIN contribution, not to be confused with the RIN induced by fluctuations of the pump intensity, can be remarkably mitigated in Raman polarizers operating in the pump depletion regime [169]. On the other hand, polarizers based on PDG are also very efficient distributed amplifiers, with a gain coefficient twice as large as that of conventional DRAs, where depolarized pumps are used to circumvent the PDG issue. Moreover, Raman-based polarizers have a larger amplification bandwidth with respect to Brillouin-based ones, which makes them best suited for optical communications. Therefore, this chapter focuses on polarizers relying on the combined action of Kerr effects and stimulated Raman scattering to achieve simultaneous amplification and polarization control.

Raman polarizers have been broadly studied, theoretically [159, 165, 167, 170, 171, 172, 173] as well as analytically [174] and numerically [165, 167, 171, 172, 173, 175, 176, 177,

178], and the polarization pulling phenomenon repeatedly observed experimentally for co-propagating [167, 176, 179] and counter-propagating [159, 179, 180, 181] signals alike. As the scope of this study is primarily experimental, this section only introduces the main analytical model used to describe the evolution along the fiber of the pump and signal Stokes vectors, **P** and **S** respectively, by means of the following coupled differential vector equations in the Stokes space [170], under the assumption that chromatic dispersion and Raman gain for orthogonally polarized beams can be neglected

$$\xi \frac{d\mathbf{P}}{dz} = -\alpha_p \mathbf{P} - \frac{\omega_p}{2\omega_s} g_R \left(P_0 \mathbf{S} + S_0 \mathbf{P} \right) + \left(\omega_p \boldsymbol{\beta} + \gamma_p \mathbf{W}_p^{NL} \right) \times \mathbf{P} \tag{6.1}$$

$$\frac{d\mathbf{S}}{dz} = -\alpha_s \mathbf{S} + \frac{1}{2} g_R \left(S_0 \mathbf{P} + P_0 \mathbf{S} \right) + \left(\omega_s \boldsymbol{\beta} + \gamma_s \mathbf{W}_s^{NL} \right) \times \mathbf{S} \tag{6.2}$$

where $\xi = +1$ for co-propagating and $\xi = -1$ for counter-propagating waves, α_p and α_s are the fiber losses at the pump and signal frequencies ω_p and ω_s respectively, g_R is the Raman gain coefficient for parallel Stokes vector **P** and **S**, $P_0 = |\mathbf{P}|$ and $S_0 = |\mathbf{S}|$ are the pump and signal powers, respectively, γ_p and γ_s are the pump and signal nonlinear Kerr coefficients, respectively, and the vector $\boldsymbol{\beta}$ is the linear birefringence vector divided by the angular frequency ω and depends stochastically on the propagation distance z. Moreover, the effect of nonlinear polarization rotation caused by cross- and self-phase modulation is accounted for through the vectors

$$\mathbf{W}_p^{NL} = \frac{2}{3} \left(-2S_1, -2S_2, P_3 \right) \tag{6.3}$$

$$\mathbf{W}_s^{NL} = \frac{2}{3} \left(-2P_1, -2P_2, S_3 \right) \tag{6.4}$$

where P_i and S_i, with $i = 1, 2, 3$ are the components of the pump and signal Stokes vector, respectively.

Simply put, the effect of Raman gain, described by the term $(S_0 \mathbf{P} + P_0 \mathbf{S})$ in Eq. (6.2), is to gradually pull the input signal SOP towards the pump SOP, whereas the last term accounts for the SOP scrambling induced by fiber birefringence and nonlinear polarization rotations, that counteract the polarization attraction mechanism.

Numerous variants of this model have been developed over the course of the last years in the attempt to improve its accuracy and computational efficiency in a number of different

conditions ranging from propagation in ideal isotropic fibers [159, 182] and fibers with randomly varying birefringence [171, 183], in the depleted [172] or undepleted regime [165], to propagation and interaction of two [165, 183] or three [173, 184] beams, in co-pumped [165] or counter-pumped [173, 182] configurations. Some of the widely accepted findings, obtained numerically and confirmed experimentally, include:

i. When pump and signal travel along the same propagation direction the output SOP is not predictable, whereas in the counter-propagating configuration the output SOP is locked to the pump input SOP.

ii. In counter-propagating conditions a much higher pump power is required to compensate for fiber birefringence and obtain polarization attraction, as opposed to the co-propagating case, when Raman polarization is much more efficient.

iii. The output DOP increases with the gain G (or equivalently, with the pump power) according to the relations

$$DOP_{co} = 1 - G^{-1} \tag{6.5}$$

$$DOP_{counter} = 1 - \sqrt{\frac{2}{G}} \tag{6.6}$$

respectively for co-propagating and counter-propagating configurations.

iv. Eqs. (6.5)-(6.6) represent an upper bound to the achievable output DOP as they don't take into account the effect of gain saturation, which effectively reduces the maximum achievable DOP. Moreover, after a certain pump power level, the DOP also decreases with pump power due to a sort of self-scrambling effect: if the gain experienced by the signal is high enough, the signal can itself alter the pump SOP through the term $(P_0\mathbf{S} + S_0\mathbf{P})$ in Eq. (6.1).

v. Polarization attraction efficiency is strongly dependent on the PMD: the lower the PMD the more efficient pulling can be obtained and the higher output DOP can be achieved. As a general rule of thumb, PMD parameters below $0.1\,\text{ps}/\sqrt{\text{km}}$ enable full repolarization of the signal ($DOP \sim 100\%$).

The DOP is defined as

$$DOP = \frac{\sqrt{\left\langle S_1^{(s)} \right\rangle^2 + \left\langle S_2^{(s)} \right\rangle^2 + \left\langle S_3^{(s)} \right\rangle^2}}{S_0^{(s)}} \tag{6.7}$$

where $S_i^{(s)}$ is the ith component of the Stokes vector of the signal beam, $S_0^{(s)}$ is its power and $\langle\rangle$ denotes an averaging process over N realizations of the signal input SOP.

The majority of the numerical and experimental analysis conducted to date have dealt with fully open, mirrorless cavity architectures, as the one depicted in Fig. 6.1 for a co-pumping scheme. In the next section, Raman polarizers based on half-open (rDFB-like) and closed (URFL-like) cavities are analyzed for the first time and the polarization properties of the Stokes lasing are recorded for different gain media ranging from low-PMD SPUN to high-PMD DCF fibers.
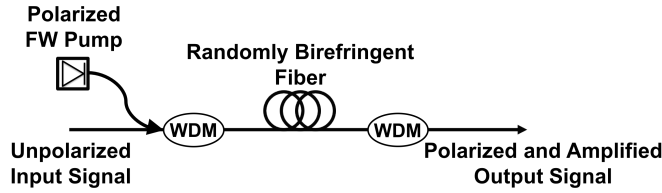
Figure 6.1: Schematic diagram of a mirrorless Raman polarizer in co-propagating configuration.

Table 6.1: Fibers Parameters

Parameter	SMF	SPUN	DCF	DCM	Unit
Length	3	2	2	2.1	km
Attenuation @ 1365 nm	0.62	0.51	1.02	1.59	dB/km
Attenuation @ 1455 nm	0.35	0.29	0.66	1.2	dB/km
Dispersion @ 1365 nm	4.3	4.9	-38.3	-79.5	ps/nm/km
Dispersion @ 1455 nm	10.7	11.1	-33.9	-112.8	ps/nm/km
PMD Coefficient @ 1365 nm	0.05	<0.04	21.8	<0.04	ps/$\sqrt{\text{km}}$
Raman Gain Coefficient @ 1455 nm	0.48	0.29	1.7	1.94	W^{-1} km^{-1}

The investigated fibers were fully characterized and their main features are listed in Table 6.1 for the wavelengths of interest 1365 nm and 1455 nm, where DCM is used to indicate a

dispersion compensation module based on a high negative dispersion DCF. A more detailed characterization as a function of wavelength is presented in Fig. 6.2. The two DCF fibers have the highest Raman gain coefficient, as expected from a reduced core size fiber such as the DCF, but also a very broad water absorption peak and no zero-dispersion wavelength in the inspected wavelength region. On the other hand, the SMF and the SPUN fiber have comparable characteristics in terms of dispersion as well as attenuation and Raman gain.

(a)   **(b)**

(c)
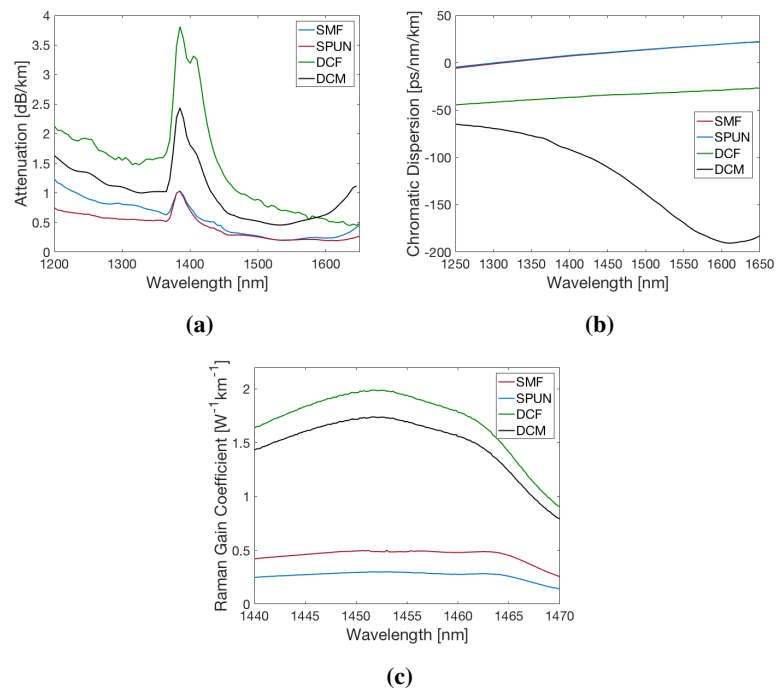
Figure 6.2: Measured attenuation (a), dispersion (b) and Raman gain (c) coefficients for the fibers under test.

6.2 **Half-Open Cavity Raman Polarizers**

In spite of all the advances in random distributed feedback lasers, the study of the polarization properties of rDFBs, and the management of the evolution of the state of polarization of light in these sources still remains as a pending challenge. Effects such as polarization dependent gain and polarization mode dispersion pose important limitations to the performance of

next-generation transparent optical communication systems, which rely on distributed amplification and nonlinearity mitigation. Additionally, PDG also sets important constraints to the design of low-noise fiber lasers, since their PDG significantly contributes to relative intensity noise fluctuations [185, 186]. Polarization control is critical also for applications of these sources in some sensing techniques [187].

As previously stated, thanks to PDG, Raman polarizers are devices capable of producing a highly polarized amplified output. In order to achieve efficient polarization pulling coupled with high gain, Raman polarizers require a highly polarized high-power pump, and a sufficiently long span of low-PMD fiber. One of such fiber is the so-called spun optical fiber, which is produced by quickly rotating (or oscillating) the fiber preform during fiber drawing. This results in the averaging of fiber core non-uniformities, which effectively cancels out the total fiber birefringence. Therefore, the resulting spun fiber exhibits a negligible value of the average PMD [188, 189]. The main advantage of spun low-birefringence fibers is that, unlike traditional polarization-maintaining fibers, they preserve any light SOP, and not only linear polarizations. In particular, spun fibers are able to maintain circular polarization states. Moreover, when fabricated by using standard fiber preforms, spun fibers exhibit similar transmission characteristics (dispersion, attenuation, nonlinearity) to corresponding transmission fibers, and can be potentially produced at a relatively low cost. Thanks to their very low PMD values, spun fibers are particularly suited for implementing devices based on polarization attraction, since they allow for improved polarization alignment between pump and signal, and consequently lead to high Raman gain values.

In this section a novel approach to achieve polarization control coupled with high conversion efficiency in rDFBs is presented. The method is based on the use of highly polarized pumps in an open-cavity (single-grating) rDFB configuration, and the concept of efficient Raman polarization pulling in a low-PMD fiber. The impact of PMD on overall rDFB performance and intra-cavity polarization pulling is evaluated by analyzing the bi-directional output from an active cavity composed of a specially designed low-PMD, SMF-based, rapidly spun fiber and by comparison with other cavities based on SMF or DCF.
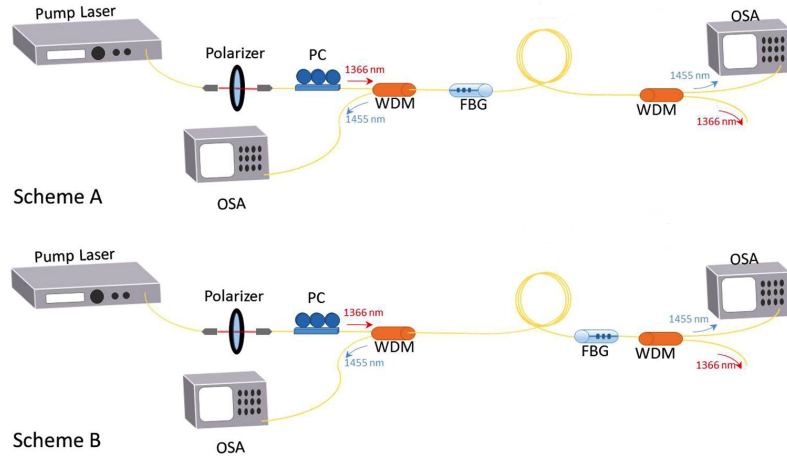
Figure 6.3: Schematic of the experimental setup for a half-open cavity laser. PC: Polarization controller. WDM: Wavelength division multiplexer. FBG: Fiber Bragg grating. OSA: Optical spectrum analyzer. In Scheme A or 1, with a single FBG at the pump input and, in Scheme B or 2 at the output end.

The schematic diagrams of the single-grating open cavity lasers designed for these experiments are depicted in Fig. 6.3. In both cases, the pump source is a CW fiber laser source at $1366\,\text{nm}$, able to emit up to $38\,\text{dBm}$. As it is expected in a fiber laser source, the output is naturally depolarized, exhibiting a low degree of polarization of about 30%. A polarized pump beam (in excess of 99%) is then generated by means of a polarizing prism, after which the polarized output is injected into a fiber polarization controller (PC), which can be used to generate a range of different SOP values. The output pump from the PC is coupled through a WDM into the open-cavity laser, which has a single high reflectivity (close to 90%) fiber Bragg grating, centered at $1454.5\,\text{nm}$, on either the input or the output pumping end, depending on the chosen design. The transmittance and reflectance of this FBG do not display a measurable dependence on the polarization of the incident signal. In Fig. 6.4 the obtained transmittance and reflectance characteristics for two different orthogonal SOPs are shown. As with all similar open-cavity designs, Rayleigh backscattering provides the random distributed feedback mechanism for the open side of the cavity.
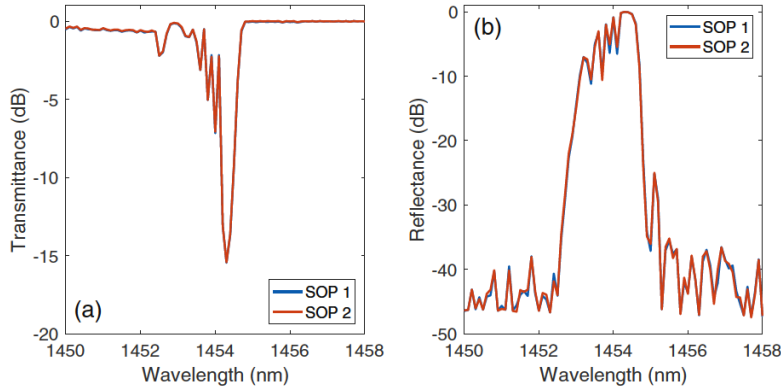
Figure 6.4: FBG transmittance (a) and reflectance (b) for two orthogonal SOPs.

The experimentally observed output spectra for scheme A of Fig. 6.3 based on SPUN fiber are shown in Fig. 6.5a. The spectra are shown between $1360\,\text{nm}$ and $1480\,\text{nm}$, as no features of interest are observed outside this range. The evolution of the co-propagating output laser spectrum with pump power can be divided in two different regimes, as far as the nonlinear effects involved in the laser dynamics are concerned. The first regime is dominated by the presence of XPM and parametric scattering, whereas the second regime is governed by the action of Raman scattering. For relatively low pump powers, one observes the generation of a narrow signal at the $1454.5\,\text{nm}$ FBG wavelength, sitting on a broad supercontinuum with a peak at $1393\,\text{nm}$. The higher the pump power, the higher the signal power level at the FBG frequency. For pump powers higher than $32\,\text{dBm}$, a new spectral peak appears at $1453\,\text{nm}$, which quickly superimposes over the initial $1454.5\,\text{nm}$ peak. The amplitude of the $1453\,\text{nm}$ peak grows larger with pump power, up to pump powers close to $33.5\,\text{dBm}$. Next, the effects of Raman scattering become dominant, until lasing begins at $1453\,\text{nm}$. Subsequently, most power below $1440\,\text{nm}$ is redistributed under the lasing peak. Note that the lasing wavelength is slightly different from the FBG resonant wavelength: it corresponds to the peak of the Raman gain profile. The presence of an FBG has no influence on the generation of the laser emission, where the feedback is provided by distributed Rayleigh backscattering (i.e., it corresponds to the generation of random distributed feedback lasing).
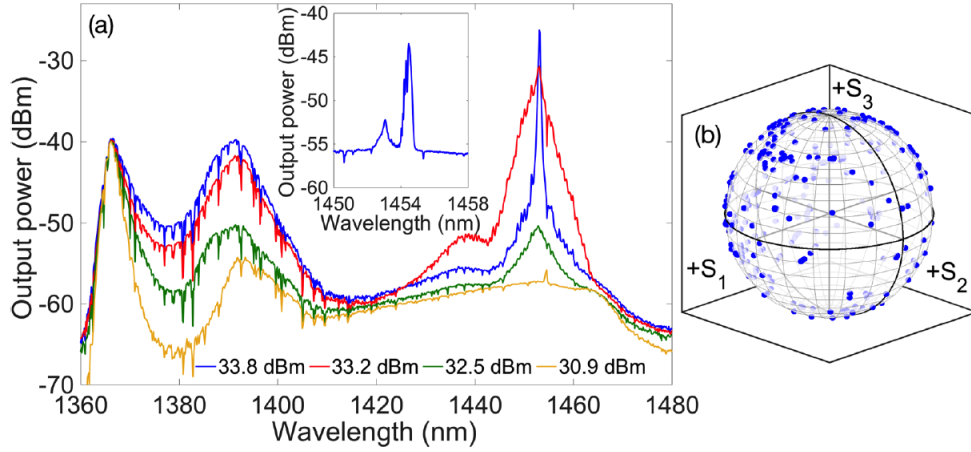
Figure 6.5: Experimental results for scheme A: (a) spectrum of the co-propagating signal output. Inset shows the output spectrum of the counter-propagating signal. (b) Poincaré sphere display of the variation of the SOP of the 1453 nm co-propagating output signal, as the pump SOP is varied.

Whenever the open cavity is pumped with a depolarized pump (i.e., without the polarising prism), Raman gain never reaches a sufficient level to prevent strong supercontinuum generation at 1393 nm. As a result, with the open cavity, lasing at 1453 nm could not be achieved for injected pump powers up to 35.5 dBm. Therefore, polarization alignment between the pump and the generated Stokes is critical to achieve an efficient Raman frequency conversion. This polarization alignment is maintained thanks to the low PMD of the SPUN fiber, which in turn enables the generation of highly polarized random lasing. The measured DOP of the co-propagating laser output is 95% and its SOP widely moves across the entire Poincaré sphere, as shown in Fig. 6.5b. When measuring the output at the pumping end, two spectral peaks at 1453 nm and 1454.5 nm were observed. The first peak corresponds with the Rayleigh backscattering of the lasing signal, whereas the second peak matches the resonant wavelength of the FBG. Due to the position of the FBG, the power of the 1454.5 nm signal was not sufficient for filtering it out, and measuring its polarization characteristics.

The experimental results for scheme B of Fig. 6.3 based on SPUN fiber are shown in Fig. 6.6a. The co-propagating output spectrum remains almost identical to that obtained with the previous configuration (see Fig. 6.5a). In particular, the output laser power remains largely independent of the position of the FBG. However, the DOP of the 1453 nm signal is slightly

higher with scheme B, as it is now close to 100%. Nevertheless, Fig. 6.6b shows that also with scheme B the SOP of the output co-propagating laser Stokes signal is largely dependent on the pump SOP value: its values almost uniformly cover the Poincaré sphere.
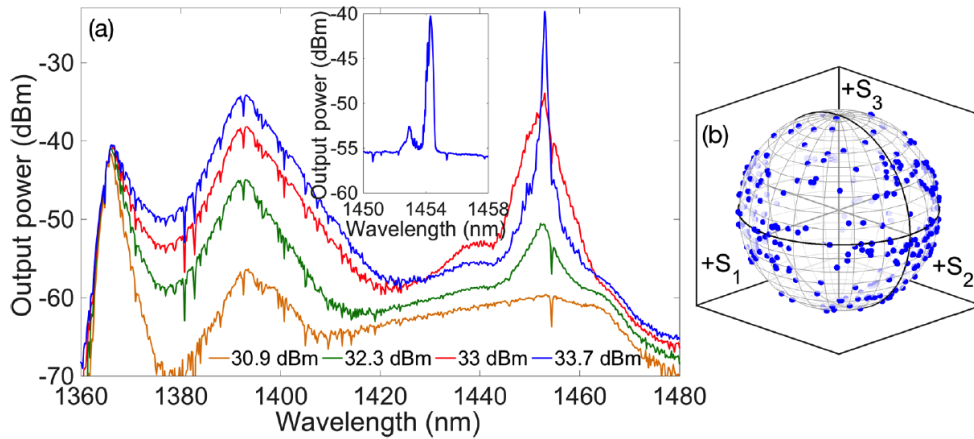
Figure 6.6: Experimental results for scheme B: (a) spectrum of the co-propagating signal output. Inset shows the output spectrum of the counter-propagating signal. (b) Poincaré sphere display of the variation of the SOP of the 1453 nm co-propagating output signal, as the pump SOP is varied.

The most remarkable differences between schemes A and B are observed in the counter-propagating output signal. Firstly, by comparing the insets of Figs. 6.5a and 6.6a, it can be seen that the output power of the 1454.5 nm counter-propagating output Stokes signal is higher with scheme B. This could be expected, given the position of the FBG at the end of the cavity. Next, the output counter-propagating Stokes signal power is slightly dependent on the pump SOP value. The counter-propagating output Stokes signal DOP remains extremely close to 100%. In addition, as shown in Fig. 6.7a, the output signal maintains a well-defined SOP, which is virtually unaffected by the SOP of the pump. These observations suggest the presence of a strong self-attraction of the SOP of the 1454.5 nm nm Stokes signal, as it occurs in the omnipolarizer. The omnipolarization phenomenon refers to the capability of light to self-organize its SOP when it nonlinearly interacts with its counter-propagating replica through four wave mixing. It was first demonstrated by Fatome et al. for a non-zero dispersion shifted fiber with negative dispersion at the wavelengths of interest [190].
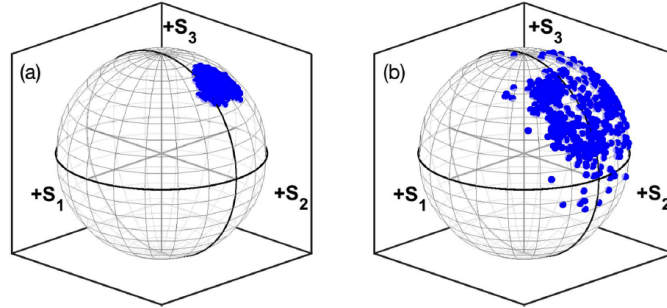
Figure 6.7: Poincaré sphere display of the variation of the SOP of the $1454.5\,\mathrm{nm}$ counter-propagating output signal in configuration B with a SPUN fiber (a) and an SMF fiber (b).
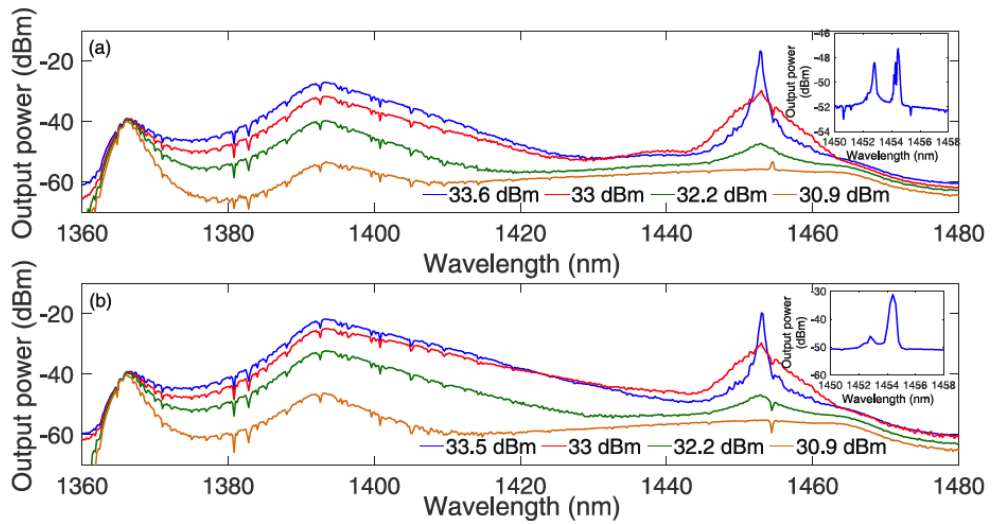
Figure 6.8: Experimental spectrum of the co-propagating output for scheme A using SMF (a). Experimental spectrum of the co-propagating output for scheme B using SMF (b). Insets show the spectrum of the counter-propagating signals.

In order to appreciate the role of the ultra-low PMD SPUN fiber in determining the effectiveness of Raman polarization attraction and random lasing, experiments were repeated by replacing the SPUN fiber with a standard fiber. The experimental spectra are shown in Fig. 6.8. SMF has a lower linear loss and a smaller core area, hence a higher Raman gain coefficient, than the spun fiber. Moreover the used SMF span was also slightly longer than the spun fiber span, which could also be expected to contribute to more efficient amplification

and lasing, in the absence of any polarization effect. In spite of all of these potential advantages, in scheme A with a fully polarized pump and the SMF, lasing at $1453\,\mathrm{nm}$ was easily achievable in the co-propagating direction, with a threshold of only $0.2\,\mathrm{dBm}$ lower than with the SPUN fiber. The output DOP was 100%.

With an FBG at the far end of the pump and using the SMF, the counter-propagating Stokes output power at the pumping end was higher than with the SPUN fiber, as could be expected, given the extra length and higher gain coefficient of the SMF. However, the output DOP is reduced when using an SMF, and the corresponding SOP no longer remains fixed as the pump SOP is varied. The DOP of the output Stokes signal was 85%. As shown in Fig. 6.7b, the signal SOPs are distributed over a broader range on the Poincaré sphere than in the SPUN fiber case, owing to the slightly higher PMD of the SMF.

6.2.1 Extended Analysis for Different Fibers

The results presented in the previous section have been recently extended to include DCF fibers in the analysis of half-open cavities Raman polarizers. The complete, although preliminary, investigation is reported in this section. The experimental setup was refurbished with new components such as WDMs, FBGs and fiber connectors that allowed for improved efficiency and higher lasing power levels. The new FBGs were chosen to match the characteristics of the FBGs used in the previous setup (R>90%, $\sim 0.5\,\mathrm{nm}$ bandwidth).

By way of example, the experimentally observed output spectra for both schemes in Fig. 6.3 are presented in Fig. 6.9 for the co-propagating (FW) and counter-propagating (BW) signals and different pump power values at the fiber input when the open-cavity Raman polarizer is based on SMF. With the exception of the lasing threshold, now much lower thanks to the improved setup, identical spectral features to the ones obtained in the previous experiments can be observed, with two different lasings generated at $1453\,\mathrm{nm}$ in co-propagating direction and at $1454.5\,\mathrm{nm}$ in counter-propagating direction.

Similar considerations can be made for Raman polarizers based on the SPUN, DCF and DCM fibers, whose output spectra are omitted for the sake of readability. All of them have different lasing thresholds depending on the balance between Raman gain coefficient, atten-

uation and PMD. Table 6.2 summarizes the efficiency of the tested open-cavity polarizers, in terms of pump power required to generate the Stokes lasing.
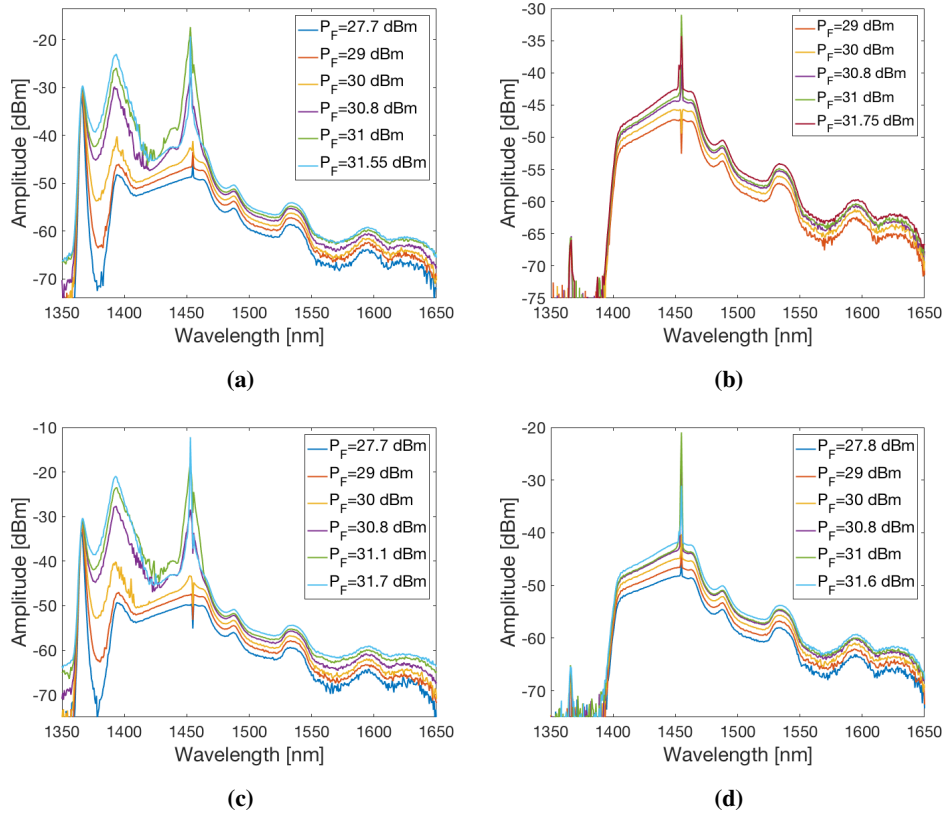
Figure 6.9: Measured output spectrum of the co-propagating (a) and counter-propagating (b) signals in scheme A and of the co-propagating (c) and counter-propagating (d) signals in scheme B, for different pump powers, when SMF is used as gain medium.

Table 6.2: Lasing threshold of the half-open cavity Raman polarizers: pump power (in dBm) required to generate the Stokes lasing.

FBG Location (Scheme)	Propagation Direction	SMF	SPUN	DCF	DCM
Front-end (A)	FW	31.5	32	32.1	27.8
Front-end (A)	BW	30.8	31	32	26.9
Back-end (B)	FW	31.7	32	32	27.4
Back-end (B)	BW	30.8	30.7	31	27

The SMF and SPUN fibers have similar performance as their characteristics are nearly identical. The DCM fiber is by far the best performing as it combines a very high Raman gain with a reasonably moderate attenuation and a remarkably low PMD. The DCF performance, on the other hand, is strongly affected by the extremely high PMD and attenuation, that frustrate the benefit of the highest Raman gain among the tested fibers.

Interestingly enough the thresholds in Table 6.2 do not always correspond to the same lasing in every cavity. Table 6.3 shows that, depending on the cavity configuration and the gain medium, in half-open cavity Raman polarizers lasing can occur either at the FBG central wavelength or as random lasing at the Raman gain profile maximum around 1453 nm.

Table 6.3: Lasing wavelength of the half-open cavity Raman polarizers.

Fiber	Scheme A - FW	Scheme A - BW	Scheme B - FW	Scheme B - BW
SMF	1453 nm	1454.5 nm	1453 nm	1454.5 nm
SPUN	1453 nm	1454.5 nm	1453 nm	1454.5 nm
DCF	1453 nm	1453 nm	1453 nm	1454.5 nm
DCM	1454.5 nm	1454.5 nm	1454.5 nm	1454.5 nm

For each and every cavity setup, the corresponding lasing was optically filtered and its polarization properties measured by means of a Thorlabs IPM5300 polarimeter. Fig. 6.10 displays the co-propagating and counter-propagating output lasing SOP on the Poincaré sphere, for both scheme A and B, as the pump SOP at the fiber input is varied. In some cases, the filtered output intensity was rather low and could not be measured by the polarimeter. As an example, Fig. 6.10b shows the counter-propagating lasing SOP only for the DCM-based half-open cavity as in scheme A, as the DCM is the only efficient enough fiber to produce a measurable signal in these conditions, given the available pump power.

In half-open cavities based on SMF and SPUN fibers, the lasing SOP moves across the entire sphere as the pump input SOP is scrambled, thus showing an output SOP locked to the pump SOP. The sharp contrast between the Poincaré spheres presented in Figs. 6.7 and 6.10 is being currently investigated and may be related to the optical power levels at the polarimeter

input. The new setup, thanks to improved connections between components and reduced WDM insertion loss, is able to supply a stronger signal at the WDMs $1455\,\text{nm}$ output port.
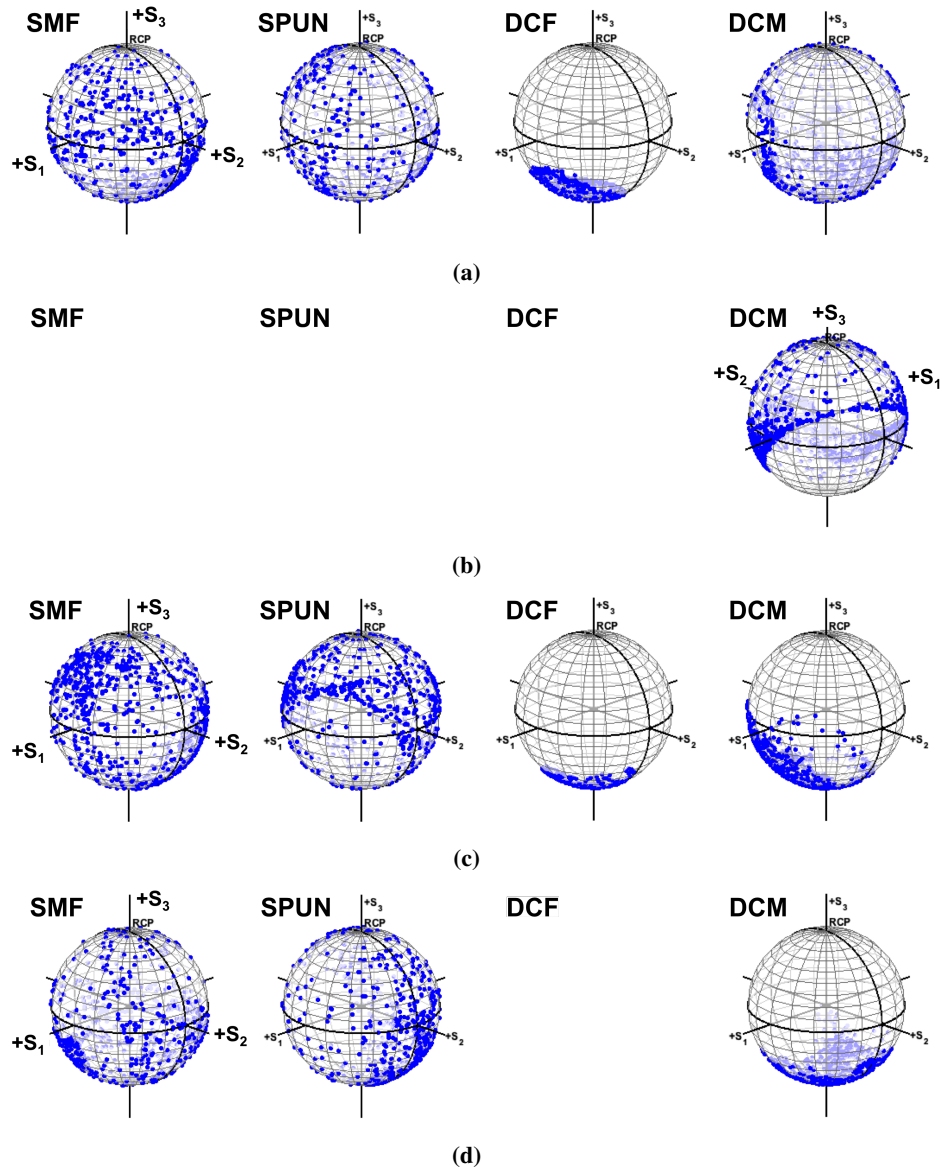
Figure 6.10: Measured SOP of the Stokes lasing for scheme A in co-propagating (a) and counter-propagating (b) conditions and for scheme B in co-propagating (c) and counter-propagating (d) conditions.

Conversely, the two dispersion compensation fibers produce an output with different polarization properties: only a reduced portion of the sphere is covered by the lasing SOP, highlighting the aforementioned omnipolarization effect, that becomes more pronounced with increasing pump power.

Table 6.4: Lasing DOP of the half-open cavity Raman polarizers.

	Scheme A - FW	Scheme A - BW	Scheme B - FW	Scheme B - BW
SMF	95%	-	92%	96%
SPUN	97%	-	91%	90%
DCF	33%	-	32%	-
DCM	97%	98%	90%	99%

The SOP is only one of the polarization properties of the output signal. To achieve proper polarizing operations, the generated Stokes signal needs to exhibit a high DOP. Table 6.4 outlines the output DOP for the four configurations. Not surprisingly, the DCF fiber, which exhibits the highest degree of PMD, also shows the lowest achievable DOP among the fibers under test. A DOP of about 30% in the measurable configurations highlights that low PMD is the key feature for a fiber to be suitable for use in Raman polarizers with a half-open cavity architecture. As a result, the benefit associated with an output SOP fixed around a single state via the omnipolarization effect (see Fig. 6.10) is counteracted by a drastically low generated DOP, which makes this high-PMD high-negative-dispersion DCF fiber ineffectual for these devices. By contrast, a low-PMD high-negative-dispersion fiber, such as the DCM, brings the two advantages together, enabling effective polarizing operations (DOP ranging from 90% to 99%) with reduced output SOP variations. The SMF and SPUN fibers also display remarkable polarizing properties thanks to their low PMD coefficient, yielding DOP in excess of 90% for every cavity configuration.

The output DOP depends on the pump power at the fiber input. As previously stated in section 6.1, the DOP is expected to grow with pump power up to the point where the intense, amplified signal has an impact on the pump SOP, thus causing a self-scrambling effect. This prediction is confirmed by the results presented in Fig. 6.11, where the DOP is shown as

a function of the pump power for the DCM-based polarizer, whose exceptional efficiency allowed for a wide sweep of the pump power at relatively low levels.

The DOP peak is clearly visible in both configurations and for both the FW propagating and the BW propagating lasing. However, the counter-propagating lasing develops at slightly lower pump powers than the co-propagating one, and so does the self-scrambling effect. Interestingly, the DOP drops almost immediately after the lasing threshold of the BW lasing in scheme A, because of the improved pumping efficiency when the FBG is placed at the pump side, whereas the maximum DOP of the FW lasing occurs at the same pump power in both schemes.
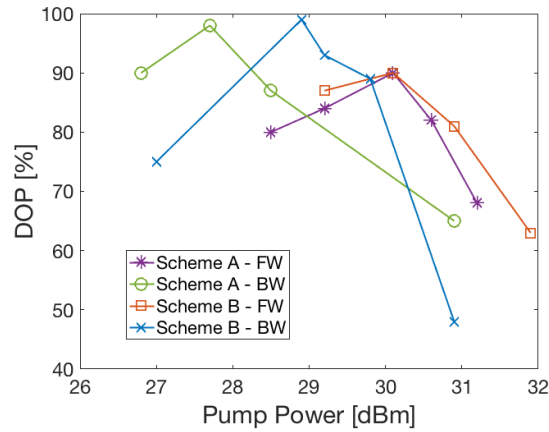
Figure 6.11: Output DOP as a function of the pump power at the fiber input for the DCM-based half-open cavity Raman polarizers.

6.3 **Closed Cavity Raman Polarizers (Preliminary Results)**

As shown in previous chapters, closed cavity Raman amplifiers provide a dramatic improvement of the pumping efficiency when compared to half-open cavity architectures. Although Raman polarizers are structured differently (e.g. polarized pump, short fiber) and are operated in dissimilar conditions (e.g. extremely high pump power, extremely low PMD) than Raman amplifiers, they can potentially bring about the same pros and cons depending on the chosen cavity configuration. Hence, great interest also lies in the study of closed cavity Raman polarizers.
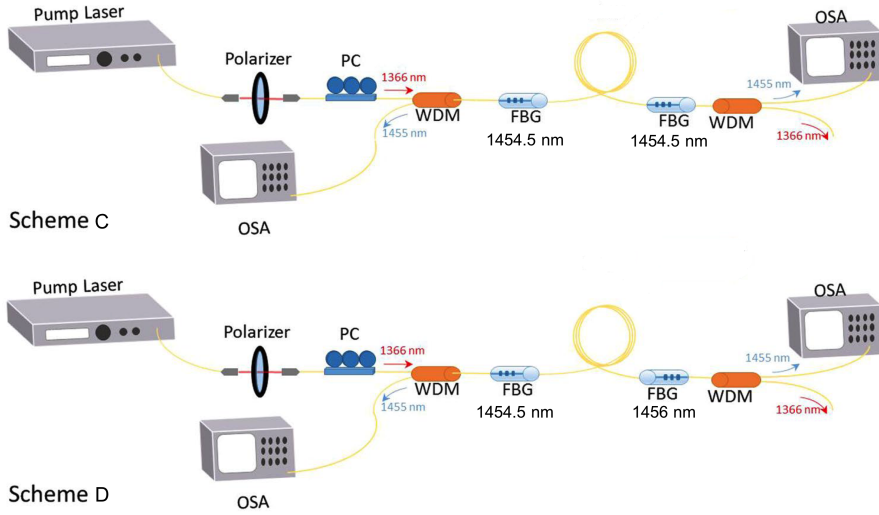
Figure 6.12: Schematic of the experimental setup for a closed cavity laser. PC: Polarization controller. WDM: Wavelength division multiplexer. FBG: Fiber Bragg grating. OSA: Optical spectrum analyzer. In Scheme C, with two FBGs centered at the same wavelength and, in Scheme D with two FBGs at different central wavelengths.
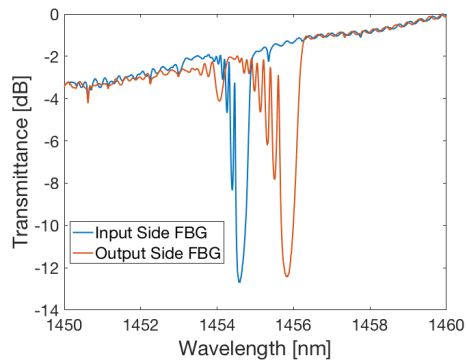
Figure 6.13: Transmittance of the input side FBG and output side FBG of scheme D.

This section presents the same analysis of the output spectrum, SOP and DOP of a Raman polarizer performed in section 6.2, applied to the schemes depicted in Fig. 6.12. Both schemes C and D share the same components as schemes A and B analyzed in the previous section, with the addition of an extra FBG. In scheme C two FBGs with the same central

wavelength (tuned), bandwidth and reflectivity are used to enclose the cavity, whereas in scheme D the two FBGs are slightly detuned by $1.5\,\text{nm}$. The FBGs transmittance profiles are compared in Fig. 6.13.

Figure 6.14: Measured output spectrum of the co-propagating (a) and counter-propagating (b) signals in scheme C and of the co-propagating (c) and counter-propagating (d) signals in scheme D, for different pump powers, when SMF is used as gain medium.

As Fig. 6.14 shows, the lasing threshold for an SMF fiber is noticeably lower for a closed cavity polarizer than for an open cavity one, especially when the two FBGs are tuned at exactly the same wavelength (Figs. 6.14a and 6.14b). Moreover, the OSNR at the lasing wavelength is exceptionally high (in excess of $50\,\text{dB}$) even for relatively low pump power, just above the lasing threshold. Thus, the OSNR exceeds the dynamic range of the optical

spectrum analyzer, resulting in a rise of the noise floor across the whole instrument bandwidth.

The lasing thresholds of all the closed-cavity polarizers are listed in Table 6.5. It can be noticed that, when the FBGs have the same central wavelength, the polarizer efficiency is improved by more than $1.5\,$dB. The most efficient fiber is the DCM, whereas the least efficient is the DCF, as it was the case with half-open cavity polarizers. Surprisingly enough, in closed cavity conditions, the SMF and the SPUN fibers behave differently, with a lasing threshold difference of about $3\,$dB attributable to modified propagation conditions of the backreflected Stokes component in a rapidly spun fiber.

Moreover, the lasing in the two propagation directions occurs at the same pump power thanks to the symmetry of the closed cavity. In addition, it is worth mentioning that in all the configurations, whenever the lasing is generated at the FBG wavelength, the threshold is strongly dependent on the pump SOP at the fiber input, despite the fact that no polarization sensitive components are present on the light path after the polarizing crystal. This property does not apply to the lasing generated at the Raman gain peak outside the FBGs bandwidth (see the FW propagating case for a DCF-based scheme D in Tables 6.5 and 6.6) and, as it will be explained, can give rise to interesting features.

Table 6.5: Lasing thresholds of the closed cavity Raman polarizers: pump power (in dBm) required to generate the Stokes lasing.

FBG (Scheme)	Propagation Direction	SMF	SPUN	DCF	DCM
Tuned (C)	FW	25.7	28.8	29.5	21.2
Tuned (C)	BW	25.8	28.8	29.6	21.2
De-Tuned (D)	FW	27.5	30.4	31.2/31.6	22.9
De-Tuned (D)	BW	27.5	30.4	31.6	22.9

Table 6.6 shows the wavelength of the generated lasing in each configuration. When the cavity is enclosed between two tuned FBGs the lasing appears at their central wavelength ($1454.5\,$nm). On the other hand, when the FBGs wavelengths are offset with respect to each other, the lasing peak is located at an intermediate wavelength ($1455.5\,$nm), as shown in Fig. 6.15a for the co-propagating signal in an SMF.

Table 6.6: Lasing wavelength of the closed cavity Raman polarizers

Fiber	Scheme C - FW	Scheme C - BW	Scheme D - FW	Scheme D - BW
SMF	1454.5 nm	1454.5 nm	1455.5 nm	1455.5 nm
SPUN	1454.5 nm	1454.5 nm	1455.5 nm	1455.5 nm
DCF	1454.5 nm	1454.5 nm	1453 nm/1455.5 nm	1455.5 nm
DCM	1454.5 nm	1454.5 nm	1455.5 nm	1455.5 nm

Furthermore, two different lasings originate within the DCF fiber in FW direction at slightly different pump powers (see Table 6.5): one at the middle wavelength and another at the Raman gain peak, as depicted in Fig. 6.15b. To be precise, the intermediate wavelength is not exactly halfway between the FBGs central wavelengths, but slightly shifted towards the longer wavelength side of the spectrum, as a consequence of the change of the FBGs spectral features due to thermal expansion (see section 4.2).
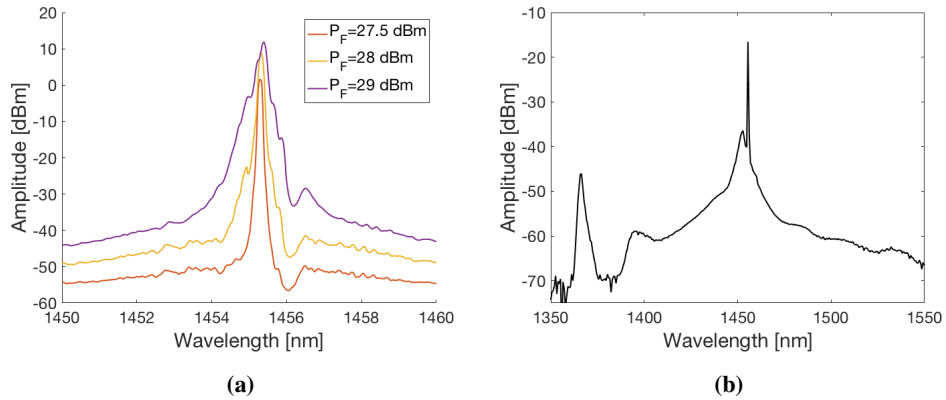
Figure 6.15: Intermediate co-propagating lasing in an SMF-based Raman polarizer with two detuned FBGs (a) and double lasing produced in FW direction in a DCF-based Raman polarizer arranged as in scheme D, with a pump power of $31.6\,\mathrm{dBm}$ (b).

As far as the polarization properties of the lasing are concerned, a proper characterization of SOP and DOP was prevented by the instability of the lasing intensity with the pump SOP. In some cases in fact, different pump SOPs correspond to different lasing regimes, even for pump powers well above the lasing threshold. Fig. 6.16 shows the FW and BW output

spectrum of an SMF-based Raman polarizer in scheme C configuration for three pump SOPs. At the same pump power of $27\,\mathrm{dBm}$ no lasing is generated for a pump polarization state SOP1, a high intensity lasing emerges when the pump state is SOP3, whereas SOP2 results in an intermediate intensity Stokes component.

(a)   **(b)**
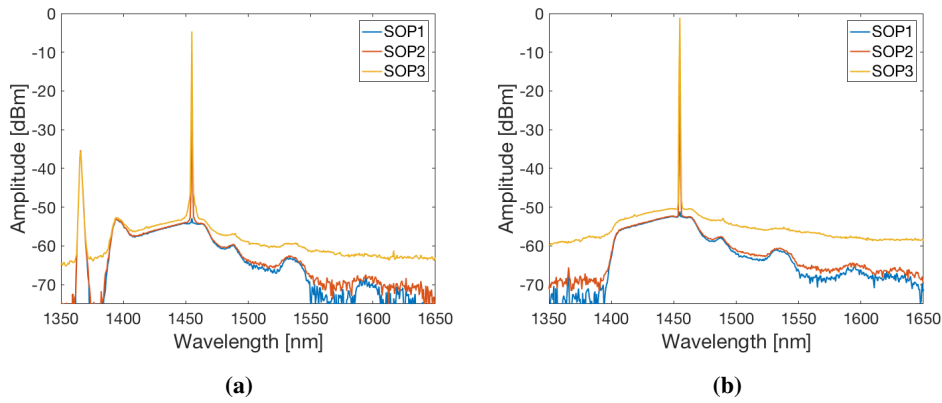
Figure 6.16: FW (a) and BW (b) output spectrum of an SMF-based Raman polarizer in scheme C configuration for three different pump SOPs. Pump power is $27\,\mathrm{dBm}$.
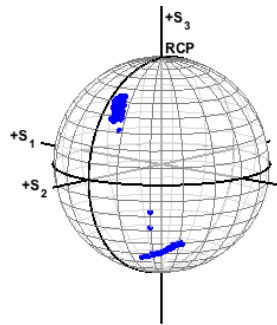
Figure 6.17: Poincaré sphere display of the variation of the SOP of the co-propagating output signal of an SMF-based Raman polarizer in scheme C configuration when the pump power is close to the lasing threshold and the pump input SOP is varied.

When the pump power level is close to the lasing threshold, each pump SOP can either enable or disable the lasing formation, yielding a sort of ON-OFF behavior. Interestingly, the output lasing, when present, is always highly polarized with a 99% DOP.

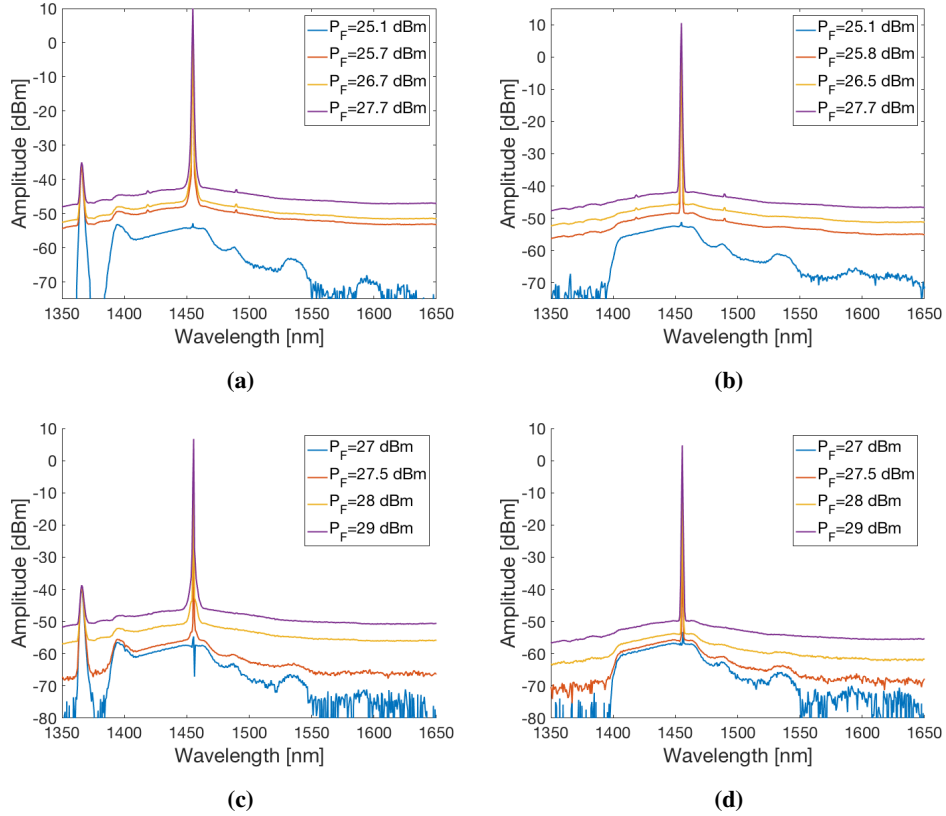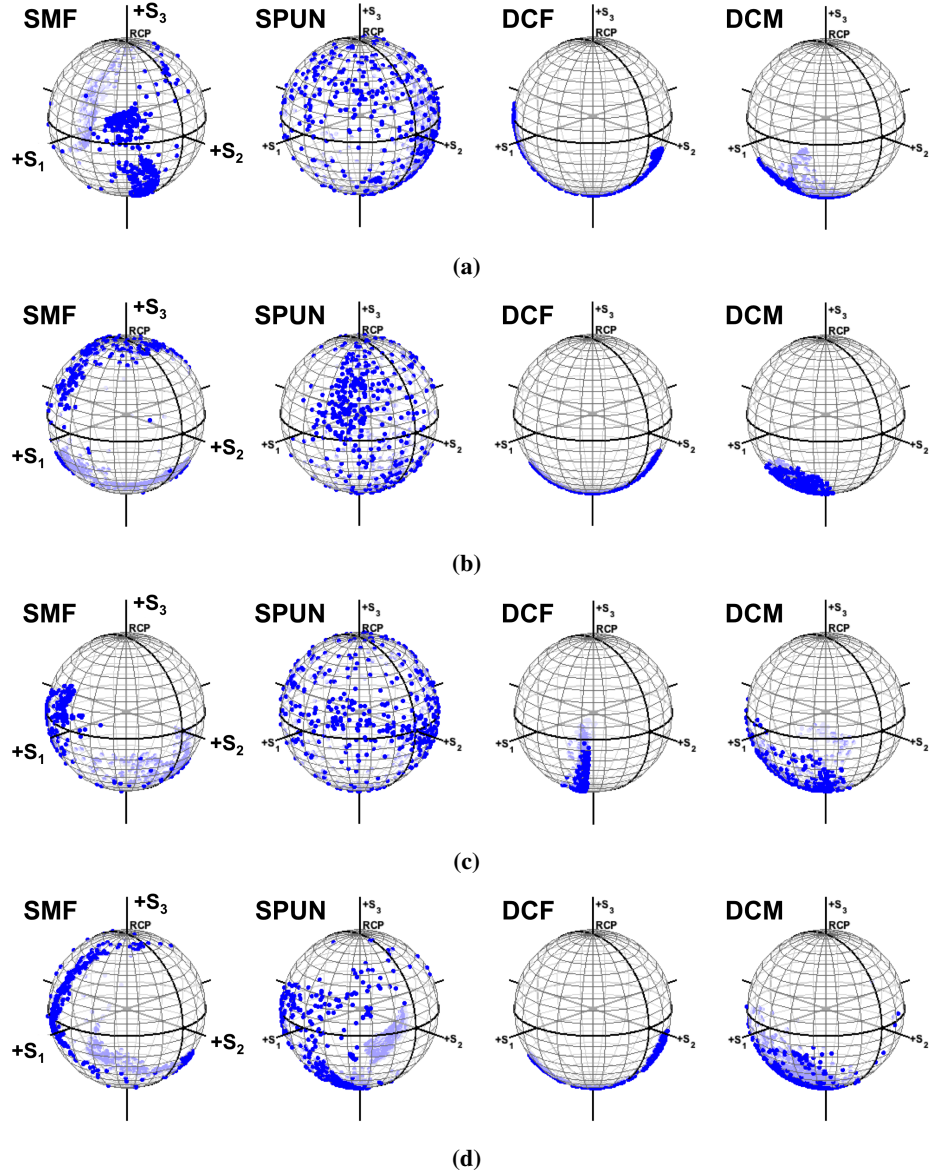**Figure 6.18:** Measured SOP of the co-propagating (a) and counter-propagating (b) lasing in scheme C and of the co-propagating (c) and counter-propagating (d) lasing in scheme D.

The Poincaré sphere measured in these operating conditions for the co-propagating output Stokes is depicted in Fig. 6.17, where the points in the northern hemisphere are by default

drawn by the polarimeter when the input power is too low to perform a measurement and, therefore, correspond to the no-lasing (OFF) mode.

The variation of the output SOP as a function of the pump input SOP was measured for each Raman polarizer and the resulting Poincaré spheres are shown in Fig. 6.18. In each cavity, two intense lasings in the two propagation directions interact differently with each other and with their generated backscattered replicas, resulting in different output SOP evolutions. A strong confinement of the lasing SOP on the sphere is still visible when DCFs are used. The SOP of the lasing generated inside an SMF or SPUN fiber, on the other hand, is scattered over a much broader area of the sphere, which seems to confirm the importance of the amount and the sign of chromatic dispersion on a fiber in the omnipolarization process.

Table 6.7 outlines the output DOP for the four architectures. The polarizing capabilities of Raman polarizers are greatly improved by the closed cavity design, yielding DOPs very close to 100% in the majority of the tested configurations. Even when the high-PMD DCF is used a nearly 50% DOP increase can be obtained in a closed cavity when compared to the half-open cavity scheme.

Table 6.7: Lasing DOP of the closed cavity Raman polarizers.

	Scheme C - FW	Scheme C - BW	Scheme D - FW	Scheme D - BW
SMF	95%	95%	100%	100%
SPUN	100%	95%	100%	100%
DCF	75%	80%	75%	75%
DCM	100%	100%	90%	95%

In conclusion, the lasing process in half-open cavity and closed cavity Raman polarizers and their polarization properties have been investigated. The findings presented in this chapter highlight the improved lasing efficiency of these devices, and especially those based on a closed cavity, with respect to traditional mirrorless designs. Open cavity polarizers based on SMF or SPUN fiber are capable of producing two different lasings in the two propagation directions, whose polarization features include high DOP for low-PMD fibers, strong polarization pulling and omnipolarization effect dependent on the chromatic dispersion of

the constituent fiber. The polarization induced by the pump on the Stokes lasing is greatly improved in closed cavity architectures, where a remarkable increase in the lasing DOP could be achieved in high-PMD fibers such as the tested DCF. In addition, a strong dependence of the lasing threshold on the pump SOP has been observed in closed cavity polarizers, which translates into ON-OFF operations that can lead to interesting applications to polarization sensitive systems.

Conclusions

This thesis was designed with the aim of addressing the continuously growing necessity for capacity of modern digital services, that owe their existence to one of the fastest developing infrastructure on the planet: the optical network. In view of the upcoming "capacity crunch" associated with the rapidly depleting ability of optical fibers to sustain the data rate increase driven by modern technologies, a twofold research approach is being undertaken by the scientific community worldwide: the development of novel, disruptive solutions at the physical level (e.g. spatial division multiplexing), or the improvement of existing concept enabled by recent technological advancements.

Following the second approach, over the course of this study the possibility to rely on a decades old nonlinear effect to improve the current network performance has been investigated. The Raman effect as a means for optical amplification has proved effective ever since its discovery in the 1920s. Nowadays, innovations in the optical as well as digital domain are empowering its ultimate comeback. Nevertheless, some noise-related issues in the amplification process are still to be properly addressed.

In this scenario, this research work has tried to answer some of the most pressing questions about Raman amplification efficiency and reliability, exploring new methods for a full

exploitation of its advantages. The main results issuing from this thesis, in order of appearance within the dissertation, can be described as:

i. A detailed characterization of three Raman amplification schemes has been conducted numerically. A reliable model has been implemented to describe propagation within a mirrorless 1st-order, a closed cavity 2nd-order (URFL) and a half-open cavity 2nd-order (rDFB) Raman laser amplifier. Simulations allowed to extract informations about the performance of each amplifier architecture in quasi-lossless transmission conditions, in terms of average signal power evolution, pumping efficiency, achievable output OSNR and generated nonlinear effects. The URFL configuration offers advantages in relation to a flatter signal power distribution along Raman amplified links up to $250\,\mathrm{km}$, which translates into higher output OSNRs. Nevertheless, for URFL amplifiers lengths above $200\,\mathrm{km}$, the benefit of a higher input power are offset by a stronger ASE noise generation that worsens the achievable OSNR. 1st-order amplifiers only yield a slightly better pumping efficiency, whereas rDFBs advantage lies in a remarkably reduced nonlinear phase shift, at the price of lower efficiency and decreased output OSNR for amplifiers longer than $100\,\mathrm{km}$.

ii. Based on the aforementioned numerical model, a method for the multilevel optimization of Raman amplifiers parameters has been developed for the purpose of eliminating the need for lengthy and computational demanding full NLSE simulations of Raman-based transmission systems. The method has been applied to the analysis of unrepeaterd and long-haul systems, in search for the optimal trajectories that optimize the balance between noise and nonlinearities. Results show the impracticality of fully loaded DP-QPSK and Nyquist-PDM-16QAM systems that would require pump powers in excess of $9\,\mathrm{W}$ and $5\,\mathrm{W}$ in unrepeatered and long-haul transmission respectively. This suggests that purely distributed multi-wavelength Raman pumped amplification solutions for superchannel transmission encompassing the C or the C+L windows might prove to be both unable to deal with low-cost scalability, and unpractical in terms of reliable operation due to the high pump power requirements.

iii. A model for the study of the RIN transfer from the pumps to the signal in Raman amplifiers has been applied to the numerical analysis of the RIN transfer function for 1st-order, URFL and rDFB amplifiers as a function of transmission distance, input power and pump ratio. It is found that in 2nd-order, bidirectionally pumped amplifiers, the high-frequency contribution to the overall RIN transfer function can be neglected, whereas it increases dramatically with increasing amplifier length and forward pump power ratio. In general, the URFL and rDFB amplifiers have similar performance in terms of intensity noise, with maximum RIN transfer function values reaching $26\,\mathrm{dB}$ in a symmetrically pumped $100\,\mathrm{km}$ cavity. However, the URFL cavity produces strong fluctuations in the high frequency regime that enhance the overall amount of RIN that can be transferred to the signal. Contrarily, 1st-order amplifiers exhibit a lower maximum RIN transfer as well as a negligible high frequency contribution. Simulations also show that for high input signal powers, pump depletion translates into a mitigated RIN transfer in the investigated pump modulation frequency range up to $100\,\mathrm{MHz}$, in cavities longer than $50\,\mathrm{km}$.

iv. A thorough experimental characterization of a wide spectrum of 2nd-order amplifier configurations has been performed to evaluate the RIN transfer mechanism dependence on the cavity design, including pumping configuration and front FBG reflectivity. Measurements of the output signal RIN and of the Stokes lasing mode structure expose a tight relationship between the two phenomena. It is indeed the presence of the FW-propagating $1455\,\mathrm{nm}$ seed that mediates in the RIN transfer between the high-order pump and the signal. As a result, a 1.5% front reflectivity allows for a 20% FPR with low-RIN operation, whereas with the same 20% FPR, a high reflectivity in the order of 40%, causes the RIN to get more easily transferred due to the rise of a well structured lasing, and leads to a $7\,\mathrm{dB}$ RIN penalty. Thus, in 2nd-order amplification the maximum admissible forward pump contribution before RIN build-up depends on the amount of backreflected light at the front-end of the cavity.

v. Parameters such as length, FW pump ratio and front-end FBG reflectivity have been experimentally optimized with the aim of finding the best possible 2nd-order ampli-

fier configuration for a specific application, showcasing different optimal operational conditions depending on the preferred span length. The rDFB architecture provides benefits in terms of both OSNR and tolerance to RIN transfer only when the cavity length can be chosen to be shorter than $100\,km$ and paying a non-negligible price in pump power requirements.Therefore, it can only be used in long-haul communications as a repeatered transmission cell, or in very-short-range unrepeatered communication links. In longer unrepeatered transmission links, the Raman-based span configurations that maximize OSNR require increased front-end reflectivity and strong FW pumping that, in turn, produce the highest RIN transfer from the pumps to the signal.

The optimization results have been confirmed by long-haul coherent transmission experiments. In a single-channel $30\,GBaud$ DP-QPSK system, after about $2000\,km$ transmission, the impact of RIN translates into a Q penalty greater than $1\,dB$ for reflectivities above 10% and 40% FPR, resulting in a 7% maximum admissible front-end reflectivity. Likewise, in a 10 channels system the transmission distance is improved by increasing the front FBG reflectivity up to $6479\,km$ for a 10% reflectivity and 20% FW pump ratio, which offers the best trade-off between OSNR and RIN performance.

vi. The in-span asymmetry of the average signal power evolution within 1st-order, URFL and rDFB amplifiers has been numerically optimized and its impact in OPC-based transmission systems demonstrated. The lowest asymmetry values and highest signal OSNRs for all span lengths above $58\,km$ were achieved with random DFB Raman amplification. A "sweet spot" was found at $58\,km$ with a signal power asymmetry just below 3%, for a symmetrical pump power split, that corresponds to a $5\,dB$ Q factor improvement in a 7x15 GBaud 16-QAM Nyquist spaced WDM system. Moreover, the wavelength-dependent in-span asymmetry of a single channel across the $30\,nm$ C-band has been studied. The flattest and lowest overall asymmetry excursion across the simulated band was found again at $58\,km$.

Similarly, the intra-span asymmetry between 20 transmitted and conjugated channels has been optimized. Asymmetries below 4% were found to be achievable for all frequency sections from $193\,THz$ to $195.775\,THz$ for span lengths between $50\,km$ and

$62\,\mathrm{km}$.

vii. A Raman-based, DBP-assisted $30\,\mathrm{GBaud}$ Nyquist-shaped optical 64-QAM unrepeated transmission experiment has been conducted and the impact of simulated signal power profiles on the DBP performance evaluated. Below FEC bit error rates could be achieved in 1st-order purely counter-pumped $160\,\mathrm{km}$ and $200\,\mathrm{km}$ long links, where the DBP impact is negligible due to the low level of generated nonlinear effects and no improvement resulted from the simulated power profile used in the DBP algorithm.

Some beneficial effects of the power profile was observed for a 2nd-order $240\,\mathrm{km}$ amplifier although reliable, below FEC data transmission could not be obtained. Optimum BER was about $8.5 \cdot 10^{-2}$ regardless of the power profile, which suggests that a good match between simulated and experimental signal power profiles in the DBP can provide only marginal improvement to a system that is limited not only by nonlinearities, but also by other sources of distortion, such as RIN.

As light, as opposed to other electromagnetic waves, provide an extra degree of freedom, polarization, that can be exploited to increase the amount of transmitted data, a relatively recent class of devices has been analyzed. The lasing mechanism and the polarization properties of two novel Raman polarizer designs have been experimentally studied for the first time:

viii. The possibility to achieve controllable polarization pulling and simultaneous lasing at different wavelengths with high output DOP in the context of random distributed feedback fiber Raman lasers has been demonstrated.

ix. Improved lasing threshold and polarization pulling efficiency has been obtained for closed-cavity Raman polarizers. Even when a high-PMD DCF fiber was used as the gain medium, output DOPs close to 80% have been obtained, with an approximate 50% DOP improvement with respect to half-open cavity polarizers.

7.1 **Future Work**

A number of further studies are being planned as a follow-up to the work presented in this thesis. Recent advances in the manufacturing of semiconductor pump lasers makes it realistic to envisage a bidirectionally pumped, URFL architecture where the co-propagating pump is represented by a low-RIN semiconductor pump. Although the optical power provided by these compact, relatively low cost lasers at a $1365\,\mathrm{nm}$ wavelength is still rather limited, the coupling of two or more orthogonally polarized high-power semiconductor pumps may produce enough FW gain to be able to effectively operate a reasonably long 2nd-order DRA. This would allow to further increase the FW pump contribution above the 20% limit exposed in this thesis, closer to the desired 50% FPR, with reduced RIN-induced impairments, even for a fully closed cavity with a high reflectivity front FBG.

It would also be interesting to evaluate the RIN transferred from the FW pump to the signal in a 3rd-order Raman amplifier. Due to a further reduced pumping efficiency, this amplification scheme would require the use of traditional fiber pump lasers, as the ones employed in this study. Nevertheless, the presence of two cascaded front FBGs adds an extra degree of freedom to the cavity design that may yield significant improvements in terms of output RIN, in addition to the well-known advantages that higher order Raman amplification generates in terms of OSNR enhancement and reduced nonlinear effects.

As explained in section 3.3.2, the walk-off parameter between the pump and the signal directly affects the RIN transfer function. Simulation results shown in Fig. 7.1 confirm that by increasing the walk-off between the co-propagating pump and the signal, the integrated output RIN can be remarkably attenuated across the whole FPR range. As the use of specialty fibers (e.g. DCF, DSF) is highly undesirable mainly due to cost constraints, another option is represented by the use of chirped FBGs in a closed cavity 2nd-order DRA. Phase jumps induced on the Stokes component whenever it hits the gratings, should help the $1455\,\mathrm{nm}$ lasing "walk away" from the $1365\,\mathrm{nm}$ pump and, thus, limit the time window for the exchange of RIN between the two signals.
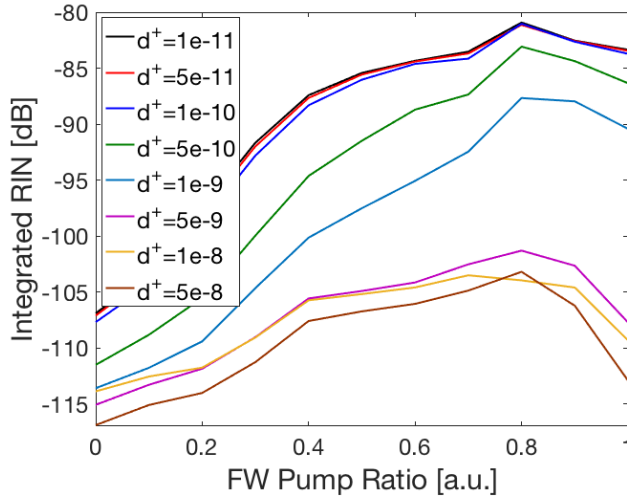
Figure 7.1: Signal RIN integrated over $1\,\mathrm{MHz}$ as a function of the forward pump ratio for different values of the walk-off parameter in a $100\,\mathrm{km}$ long 2nd-order DRA with a 5% front FBG reflectivity.

As far as the Raman polarizers are concerned, much is yet to be done in order to fully understand the combined effect of several different phenomena within these devices. However, the natural evolution of the work discussed in this thesis is associated with the polarization dynamics of a modulated signal propagating through the polarizer. In this work, the polarization properties of the generated lasing in the absence of a seed have been examined. How these properties translate to a realistic WDM signal is a question that will be addressed in the studies following this thesis.

7.2 Publications Issuing From This Work

7.2.1 Journal Contributions

1. P. Rosa, G. Rizzelli, M. Tan, P. Harper and J. D. Ania-Castañón, *Characterisation of random DFB Raman laser amplifier for WDM transmission*, Optics Express **23** (22), pp. 28634-28639 (2015).

2. Pawel Rosa, Son Thai Le, Giuseppe Rizzelli, Mingming Tan, and Juan Diego Ania-

Castañón, *Signal power asymmetry optimisation for optical phase conjugation using Raman amplification*, Optics Express **23** (25), pp. 31772-31778 (2015).

3. Giuseppe Rizzelli, Md Asif Iqbal, Francesca Gallazzi, Pawel Rosa, Mingming Tan, Juan Diego Ania-Castañón, Lukasz Krzczanowicz, Pedro Corredera, Ian Phillips, Wladek Forysiak, and Paul Harper, *Impact of input FBG reflectivity and forward pump power on RIN transfer in ultralong Raman laser amplifiers*, Optics Express **24** (25), pp. 29170-29175 (2016).

4. Pawel Rosa, Giuseppe Rizzelli, and Juan Diego Ania-Castañón, *Link optimization for DWDM transmission with an optical phase conjugation*, Optics Express **24** (15), pp. 16450-16455 (2016).

5. Francesca Gallazzi, Giuseppe Rizzelli, Md Iqbal, Mingming Tan, Paul Harper and Juan Diego Ania-Castañón, *Performance optimization in Ultra-long Raman Laser Amplified 10x30 GBaud DP-QPSK Transmission: Balancing RIN and ASE Noise*, Optics Express **25** (18), pp. 21454-21459 (2017).

6. Javier Nuño, Giuseppe Rizzelli, Francesca Gallazzi, Francisco Prieto, Concepción Pulido, Pedro Corredera, Stefan Wabnitz, and Juan Diego Ania Castañón, *Open-Cavity Spun Fiber Raman Lasers with Dual Polarization Output*, Scientific Reports **7** (1), pp. 13681 (2017).

7. Giuseppe Rizzelli, Pawel Rosa, Pedro Corredera, and Juan Diego Ania-Castañón, *Transmission Span Optimization in Fiber Systems With Cavity and Random Distributed Feedback Ultralong Raman Laser Amplification*, Journal of Lightwave Technology **35** (22), pp. 4967-4972 (2017).

7.2.2 Conference Contributions

1. G. Rizzelli, M. Camarasa-Gómez, D. Hernangómez-Pérez, and J. D. Ania-Castañón, *Multi-level Approach to the Optimization of Unrepeatered WDM Systems with Distributed Amplification*, in European Conference on Lasers and Electro-Optics - European Quantum Electronics Conference (CLEO-EU 2015).

2. Pawel Rosa, Giuseppe Rizzelli and J.D. Ania-Castañón, *Symmetry Optimisation for Optical Phase Conjugation in Raman-Amplified Communication Systems*, in IX Reunión Española de Optoelectrónica (OPTOEL 2015).

3. P. Rosa, G. Rizzelli, and J. D. Ania-Castañón, *Signal Power Symmetry Optimization for Optical Phase Conjugation Using Raman Amplification*, in Nonlinear Optics (NLO 2015).

4. P. Rosa, G. Rizzelli, M. Tan and J. D. Ania-Castañón, *Optimisation of random DFB Raman laser amplifier*, in 17th International Conference on Transparent Optical Networks (ICTON 2015).

5. Rosa, Pawel; Le, Son Thai; Rizzelli, Giuseppe; Tan, Mingming; Ania-Castañón, Juan Diego, *Signal power asymmetry optimisation for optical phase conjugation using random DFB laser Raman amplification*, in Asia Communications and Photonics Conference (ACP 2015).

6. Giuseppe Rizzelli, Md Asif Iqbal, Francesca Gallazzi, Pawel Rosa, Mingming Tan, Pedro Corredera, Juan Diego Ania-Castañón and Paul Harper, *FBG Reflectivity Impact on RIN in Ultralong Laser Amplifiers*, in 42nd European Conference on Optical Communication (ECOC 2016).

7. M. A. Iqbal, G. Rizzelli, F. Gallazzi, Mingming Tan, P. Harper and J. D. Ania-Castañón, *Performance improvement of broadband distributed Raman amplifier using bidirectional pumping with first and dual order forward pumps*, in 18th International Conference on Transparent Optical Networks (ICTON 2016).

8. P. Rosa, G. Rizzelli and J. D. Ania-Castañón, *Link optimisation for DWDM transmission with an optical phase conjugation*, in 18th International Conference on Transparent Optical Networks (ICTON 2016).

9. J. D. Ania-Castañón, P. Rosa, G. Rizzelli, F. Gallazzi, J. Nuño and P. Corredera, *The role of distributed Raman amplification in the times of the"capacity crunch"* (Invited), in 18th International Conference on Transparent Optical Networks (ICTON 2016).

10. G. Rizzelli, M. A. Iqbal, P. Rosa, M. Tan, L. Krzczanowicz, I. Phillips, W. Forysiak, J. D. Ania-Castañón, and P. Harper, *Impact of Front-FBG Reflectivity in Raman Fiber Laser Based Amplification*, in Conference on Lasers and Electro-Optics (CLEO-US 2016).

11. J. Nuño del Campo, G. Rizzelli, F. Gallazzi, F. Prieto, M. C. Pulido-De-Torres, P. Corredera, S. Wabnitz, and J. D. Ania-Castañón, *Open-Cavity Spun Fiber Raman Lasers with a Polarized Output*, in Conference on Lasers and Electro-Optics (CLEO-US 2016).

12. M. A. Iqbal, M. Tan, L. Krzczanowicz, G. Rizzelli, F. Gallazzi, A. El-Taher, W. Forysiak, P. Harper, and J. D. Ania-Castañón, *Noise Performance Improvement of Broadband Distributed Raman Amplifier Using Dual Order Bidirectional Pumping*, in Asia Communications and Photonics Conference (ACP 2016).

13. Juan Diego Ania-Castañón, Pawel Rosa, and Giuseppe Rizzelli, *Raman-amplified DWDM Transmission in Links with Symmetry-optimised Optical Phase Conjugation* (Invited), in Progress in Electromagnetics Research Symposium (PIERS 2017).

14. Francesca Gallazzi, Giuseppe Rizzelli, Md Asif Iqbal, Mingming Tan, Paul Harper, J.D. AniaCastañón, *Optimal Balance of RIN and ASE Impairments in Ultra-long Raman Laser Amplified 10x30 GBaud DP-QPSK Transmission*, in European Conference on Lasers and Electro-Optics - European Quantum Electronics Conference (CLEO-EU 2017).

15. Giuseppe Rizzelli, Pawel Rosa, Pedro Corredera Guillén and Juan Diego Ania-Castañón, *Cell Optimisation for Transmission with Ultralong Laser Amplification*, in European Conference on Lasers and Electro-Optics - European Quantum Electronics Conference (CLEO-EU 2017).

16. Francesca Gallazzi, Giuseppe Rizzelli, Md Asif Iqbal, Mingming Tan, Paul Harper, and Juan Diego Ania-Castañón, *Balancing RIN and ASE Noise in Ultra-long Raman Laser Amplified 10x30 GBaud DP-QPSK Transmission*, in X Reunión Española de Optoelectrónica (OPTOEL 2017).

17. Giuseppe Rizzelli, Pawel Rosa, Pedro Corredera Guillén and Juan Diego Ania-Castañón, *Periodic Cell Optimization in Long-Haul Transmission with Ultralong Cavity and Random Raman Laser Amplification*, in X Reunión Española de Optoelectrónica (OPTOEL 2017).

18. Giuseppe Rizzelli, Francesca Gallazzi, Pawel Rosa, Pedro Corredera Guillén, Juan Diego Ania-Castañón, *Raman Cell Optimisation for Distributed Amplification Based Transmission Systems* (Invited), in 19th International Conference on Transparent Optical Networks (ICTON 2017).

19. Pawel Rosa, Giuseppe Rizzelli, Xiaodan Pang, Oskars Ozolins, Aleksejs Udalcovs, Mingming Tan, Sergey Sergeyev, Richard Schatz, Gunnar Jacobsen, Sergei Popov and Juan Diego Ania-Castañón, *Unrepeatered 64QAM over SMF-28 using Raman Amplification and Digital Backpropagation*, in Asia Communications and Photonics Conference (ACP 2017).

20. Giuseppe Rizzelli, Pawel Rosa, Pedro Corredera Guillén and Juan Diego Ania-Castañón, *Span optimization for transmission based on ultralong Raman fiber laser amplifier*, submitted to SPIE Photonics Europe 2018.

References

[1] I. Hayashi, M. B. Panish, P. W. Foy, and S. Sumski, "Junction lasers which operate continuously at room temperature," *Applied Physics Letters*, vol. 17, p. 109, 1970.

[2] F. Kapron, D. Keck, and R. Maurer, "Radiation losses in glass optical waveguides," *Applied Physics Letters*, vol. 17, no. 10, pp. 423–425, 1970.

[3] R. J. Sanferrare, "Terrestrial lightwave systems," *AT&T Technical Journal*, vol. 66, no. 1, pp. 95–107, 1987.

[4] T. Miya, Y. Terunuma, T. Hosaka, and T. Miyashita, "Ultimate low-loss single-mode fibre at 1.55 μm," *Electronics Letters*, vol. 15, no. 4, pp. 106–108, 1979.

[5] T. Otani, K. Goto, H. Abe, M. Tanaka, H. Yamamoto, and H. Wakabayashi, "5.3 gbit/s 11300 km data transmission using actual submarine cables and repeaters," *Electronics Letters*, vol. 31, no. 5, pp. 380–381, 1995.

[6] N. S. Bergano, "Wavelength division multiplexing in long-haul transoceanic transmission systems," *Journal of Lightwave Technology*, vol. 23, no. 12, pp. 4125–4139, 2005.

[7] G. P. Agrawal, *Fiber-Optic Communication Systems*. Wiley, 2010.

[8] P. Winzer and R. J. Essiambre, "Advanced modulation formats for high-capacity optical transport networks," *Journal of Lightwave Technology*, vol. 24, no. 12, pp. 4711–4728, 2006.

[9] H. A. Fevrier and M. W. Chbat, "Raman amplification technology for bandwidth extension," in *14th Annual Meeting of the IEEE Lasers and Electro-Optics Society*, 2001.

REFERENCES

[10] P. Mitra and J. Stark, "Nonlinear limits to the information capacity of optical fibre communications," *Nature*, vol. 411, pp. 1027–1030, 2001.

[11] R. J. Essiambre, G. Kramer, P. Winzer, G. Foschini, and B. Goebel, "Capacity limits of optical fiber networks," *Journal of Lightwave Technology*, vol. 28, no. 4, pp. 662–701, 2010.

[12] C. E. Shannon, "A mathematical theory of communication," *Bell Labs Technical Journal*, vol. 27, no. 3, pp. 379–423, 1948.

[13] D. Richardson, "New optical fibres for high-capacity optical communications," *Philosophical Transactions of the Royal Society A: Mathematical, Physical and Engineering Sciences*, vol. 374, 2016.

[14] W. Pelouch, "Raman amplification: An enabling technology for long-haul coherent transmission systems," *Journal of Lightwave Technology*, vol. 34, no. 1, pp. 6–19, 2015.

[15] E. Harstedt and P. H. Van Heyningen, "Optical access networks," in *Optical Fiber Telecommunications, IV-B*, pp. 438–513, Academic Press, 2002.

[16] TeleGeography, "Submarine cable map." https://www.submarinecablemap.com/.

[17] K. C. Kao and G. A. Hockham, "Dielectric-fibre surface waveguides for optical frequencies," *Proceedings of the Institution of Electrical Engineers*, vol. 113, no. 7, pp. 1151–1158, 1966.

[18] R. Maurer and P. Schultz, "Fused silica optical waveguide." U.S. Patent No. 3, 659, 915, 1972.

[19] F. Mitschke, *Fiber Optics Physics and Technology*. Springer, 2009.

[20] M. Born and E. Wolf, *Principles of Optics*. Cambridge University Press, 7th ed., 1999.

[21] G. P. Agrawal, *Nonlinear Fiber Optics*. Academic Press, 5th ed., 2013.

[22] L. N. Binh, *Optical Fiber Communication Systems with Matlab and Simulink Models*. CRC Press, 2nd ed., 2015.

[23] K. Nagayama, M. Kakui, M. Matsui, I. Saitoh, and Y. Chigusa, "Ultra-low-loss (0.1484 db/km) pure silica core fibre and extension of transmission distance," *Electronics Letters*, vol. 38, no. 20, pp. 1168–1169, 2002.

[24] G. A. Thomas, B. I. Shraiman, P. F. Glodis, and M. J. Stephen, "Towards the clarity limit in optical fibre," *Nature*, vol. 404, pp. 262–264, 2000.

[25] M. Wilder, "Understanding and measuring chromatic dispersion." https://www.fiberopticsonline.com/doc/understanding-and-measuring-chromatic-dispers-0002.

[26] L. Gruner-Nielsen, M. Wandel, P. Kristensen, C. Jorgensen, L. V. Jorgensen, B. Edvold, B. Palsdottir, and D. Jakobsen, "Dispersion-compensating fibers," *Journal of Lightwave Technology*, vol. 23, no. 11, pp. 2566–2579, 2005.

[27] I. Kaminow, "Polarization in optical fibers," *Journal of Quantum Electronics*, vol. 17, no. 1, pp. 15–22, 1981.

[28] C. D. Poole, J. H. Winters, and J. A. Nagel, "Dynamical equation for polarization dispersion," *Optics Letters*, vol. 16, no. 6, pp. 372–374, 1991.

[29] G. J. Foschini and C. D. Poole, "Statistical theory of polarization dispersion in single mode fibers," *Journal of Lightwave Technology*, vol. 9, no. 11, pp. 1439–1456, 1991.

[30] A. Hasegawa and F. Tappert, "Transmission of stationary nonlinear optical pulses in dispersive dielectric fibers. i. anomalous dispersion," *Applied Physics Letters*, vol. 23, no. 3, pp. 142–144, 1973.

[31] J. A. Armstrong, N. Bloemberg, J. Ducuing, and P. S. Pershan, "Interactions between light waves in a nonlinear dielectric," *Physical Review Journal*, vol. 127, no. 6, pp. 449–470, 1962.

REFERENCES

[32] R. H. Stolen and J. Bjorkholm, "Parametric amplification and frequency conversion in optical fibers," *IEEE Journal of Quantum Electronics*, vol. 18, no. 7, pp. 1062–1072, 1982.

[33] E. Buchoud, V. D. Vrabie, J. I. Mars, G. DÚrso, A. Girard, S. Blairon, and J.-M. Hénault, "Enhancement of an optical fiber sensor: Source separation based on brillouin spectrum," *IEEE Access*, vol. 1, pp. 789–802, 2013.

[34] R. W. Boyd, *Nonlinear Optics*. Academic Press, 3rd ed., 2008.

[35] D. N. Payne and L. Reekie, "Rare-earth-doped fibre lasers and amplifiers," in *European Conference on Optical Communication*, 1988.

[36] R. Paschotta, J. Nilsson, A. C. Tropper, and D. C. Hanna, "Ytterbium-doped fiber amplifiers," *IEEE Journal of Quantum Electronics*, vol. 33, no. 7, pp. 1049–1056, 1997.

[37] M. J. Connely, *Semiconductor Optical Amplifiers*. Kluwer Academic Publisher, 2002.

[38] P. S. Cho and J. B. Khurgin, "Suppression of cross-gain modulation in soa using rz-dpsk modulation format," *IEEE Photonics Technology Letters*, vol. 15, no. 1, pp. 162–164, 2003.

[39] X. Fu, X. Guo, and C. Shu, "Raman-enhanced phase-sensitive fibre optical parametric amplifier," *Scientific Reports*, vol. 6, no. 20180, 2016.

[40] J. Hansryd, P. A. Andrekson, M. Westlund, J. Li, and P. O. Hedekvist, "Fiber-based optical parametric amplifiers and their applications," *IIEEE Journal of Selected Topics in Quantum Electronics*, vol. 8, no. 3, pp. 506–520, 2002.

[41] M. E. Mahric, "Fiber optical parametric amplifiers in optical communication," in *CLEO: Science and Innovations*, 2013.

[42] M. E. Mahric, *Fiber Optical Parametric Amplifiers, Oscillators and Related Devices*. Cambridge University Press, 2010.

[43] A. Yariv, "Signal-to-noise considerations in fiber links with periodic or distributed optical amplification," *Optics Letters*, vol. 15, no. 19, pp. 1064–1066, 1990.

[44] G. P. Agrawal, *Lightwave Technology: Telecommunication Systems*. Wiley, 2005.

[45] H. Kogelnik and A. Yariv, "Considerations of noise and schemes for its reduction in laser amplifiers," *Proceedings of the IEEE*, vol. 52, no. 2, pp. 165–167, 1964.

[46] P. F. Wysocky, N. Park, and D. DiGiovanni, "Dual-stage erbium-doped, erbium/ytterbium-codoped fiber amplifier with up to +26-dbm output power and a 17-nm flat spectrum," *Optics Letters*, vol. 21, no. 21, pp. 1744–1746, 1996.

[47] H. Ono, M. Yamada, T. Kanamori, S. Sudo, and Y. Ohishi, "1.58 /spl mu/m band fluoride-based er/sup 3+/-doped fibre amplifier for wdm transmission systems," *Electronics Letters*, vol. 33, no. 17, pp. 1471–1472, 1997.

[48] V. E. Perlin and H. G. Winful, "On distributed raman amplification for ultrabroad-band long-haul wdm systems," *Journal of Lightwave Technology*, vol. 20, no. 3, pp. 409–416, 2002.

[49] Y. Emori, K. Tanaka, and S. Namiki, "100 nm bandwidth flat-gain raman amplifiers pumped and gain-equalised by 12-wavelength-channel wdm laser diode unit," *Electronics Letters*, vol. 35, no. 16, pp. 1355–1356, 1999.

[50] M. A. Iqbal, M. Tan, L. Krzczanowicz, A. E. El-Taher, W. Forysiak, J. D. Ania Castañón, and P. Harper, "Noise and transmission performance improvement of broadband distributed raman amplifier using bidirectional raman pumping with dual order co-pumps," *Optics Express*, vol. 25, no. 22, pp. 27533–27542, 2017.

[51] A. Klekamp, R. Dischler, and W. Idler, "Impairments of bit-to-bit alternate-polarization on non-linear threshold, cd and dgd tolerance of 43 gb/s ask and dpsk formats," in *Optical Fiber Communication Conference*, 2005.

[52] R. Ludwig, U. Feiste, E. Dietrich, H. G. Weber, D. Breuer, M. Martin, and F. Kuppers, "Experimental comparison of 40 gbit/s rz and nrz transmission over standard single-mode fibre," *Electronics Letters*, vol. 35, no. 25, pp. 2216–2218, 1999.

REFERENCES

[53] M. I. Hayee and A. E. Willner, "Nrz versus rz in 10-40-gb/s dispersion-managed wdm transmission systems," *IEEE Photonics Technology Letters*, vol. 11, no. 8, pp. 991–993, 1999.

[54] G. Jacobsen, *Noise in Digital Optical Transmission Systems*. Artech House Inc, 1994.

[55] P. A. Humblet and M. Azizoglu, "On the bit error rate of lightwave systems with optical amplifiers," *Journal of Lightwave Technology*, vol. 9, no. 11, pp. 1576–1582, 1991.

[56] C. Headley and G. P. Agrawal, *Raman Amplification in Fiber Optical Communication Systems*. Elsevier Academic Press, 2005.

[57] J. D. Ania Castañón, "Quasi-lossless transmission using second-order raman amplification and fibre bragg gratings," *Optics Express*, vol. 12, no. 19, pp. 4372–4377, 2004.

[58] S. Turitsyn, S. A. Babin, A. E. El-Taher, P. Harper, D. V. Churkin, S. I. Kablukov, J. D. Ania Castañón, V. Karalekas, and E. V. Podivilov, "Random distributed feedback fibre laser," *Nature Photonics*, vol. 4, no. 4, pp. 231–235, 2010.

[59] J. D. Ania Castañón, T. Ellingham, R. Ibbotson, X. Chen, L. Zhang, and S. Turitsyn, "Ultralong raman fiber lasers as virtually lossless optical media," *Physical Review Letters*, vol. 96, no. 2, p. 023902, 2006.

[60] J. D. Ania Castañón, V. Karalekas, P. Harper, and S. Turitsyn, "Simultaneous spatial and spectral transparency in ultralong fiber lasers," *Physical Review Letters*, vol. 101, no. 12, p. 123903, 2008.

[61] S. A. Babin, V. Karalekas, E. V. Podivilov, V. K. Mezentsev, P. Harper, J. D. Ania Castañón, and S. Turitsyn, "Characterization of ultra-long raman fibre lasers," in *Proc. of SPIE*, vol. 6873, 2008.

[62] I. Gladwell, L. F. Shampine, and S. Thompson, *Solving ODEs with Matlab*. Cambridge University Press, 2003.

[63] E. Desurvire, *Erbium-Doped Fiber Amplifiers: Principles and Applications*. Wiley, 1994.

[64] P. Wan and J. Conradi, "Impact of double rayleigh backscatter noise on digital and analog fiber systems," *Journal of Lightwave Technology*, vol. 14, no. 3, pp. 288–297, 1996.

[65] P. B. Hansen, L. Eskildsen, J. Stentz, T. A. Strasser, J. Judkins, J. J. DeMarco, R. Pedrazzani, and D. DiGiovanni, "Rayleigh scattering limitations in distributed raman pre-amplifiers," *Photonics Technology Letters*, vol. 10, no. 1, pp. 159–161, 1998.

[66] C. R. S. Fludger, V. Handerek, and R. J. Mears, "Pump to signal rin transfer in raman fiber amplifiers," *Journal of Lightwave Technology*, vol. 19, no. 8, pp. 1140–1148, 2001.

[67] M. D. Mermelstein, C. Headley, and J.-C. Bouteiller, "Rin transfer analysis in pump depletion regime for raman fibre amplifiers," *Electronics Letters*, vol. 38, no. 9, pp. 403–405, 2002.

[68] M. Yan, J. Chen, W. Jiang, J. Li, J. Chen, and X. Li, "Pump depletion induced noise and crosstalk in distributed optical fiber raman amplifiers," *Photonics Technology Letters*, vol. 13, no. 7, pp. 651–653, 2001.

[69] D. Chang, H. de Pedro, P. Perrier, H. A. Fevrier, S. Ten, C. Towery, I. Davis, and S. Makovejs, "150 × 120 gb/s unrepeatered transmission over 333.6 km and 389.6 km (with ropa) g.652 fiber," in *European Conference on Optical Communication*, 2014.

[70] J. D. Ania Castañón, I. Nasieva, N. Kurukitkoson, S. Turitsyn, C. Borsier, and E. Pincemin, "Nonlinearity management in hybrid amplification systems," *Optics Communications*, vol. 233, no. 4-6, pp. 353–357, 2004.

[71] J. D. Ania Castañón, S. Turitsyn, A. Tonello, S. Wabnitz, and E. Pincemin, "Multilevel optimization of a fiber transmission system via nonlinearity management," *Optics Express*, vol. 14, no. 18, pp. 8065–8071, 2006.

[72] S. Chandrasekhar and X. Liu, "Ofdm based superchannel transmission technology," *Journal of Lightwave Technology*, vol. 30, no. 24, pp. 3816–3823, 2012.

REFERENCES

[73] R. Maher, T. Xu, L. Galdino, M. Sato, A. Alvarado, K. Shi, S. Savory, B. C. Thomsen, R. I. Killey, and P. Bayvel, "Spectrally shaped dp-16qam super-channel transmission with multi-channel digital back-propagation," *Scientific Reports*, vol. 5, p. 13990, 2015.

[74] F. Zhang, D. Wang, R. Ding, T. Zhang, Z. Zheng, and Z. Chen, "High spectral efficiency nyquist optical superchannel transmission," in *Wireless and Optical Communication Conference*, 2014.

[75] M. Xiang, S. Fu, M. Tang, H. Tang, P. Shum, and D. Liu, "Nyquist wdm superchannel using offset-16qam and receiver-side digital spectral shaping," *Optics Express*, vol. 22, no. 14, pp. 17448–17457, 2014.

[76] L. Galdino, M. Tan, D. Lavery, P. Rosa, R. Maher, I. Phillips, J. D. Ania Castañón, P. Harper, R. I. Killey, B. C. Thomsen, S. Makovejs, and P. Bayvel, "Unrepeatered nyquist pdm-16qam transmission over 364 km using raman amplification and multi-channel digital back-propagation," *Optics Letters*, vol. 40, no. 13, pp. 3025–3028, 2015.

[77] J. Wang and K. Petermann, "Small signal analysis for dispersive optical fiber communication systems," *Journal of Lightwave Technology*, vol. 10, no. 1, pp. 96–100, 1992.

[78] I. Joindot, "Dispersion map optimization in hybrid raman/erbium-doped fiber amplifier-based 40-gb/s link," *Photonics Technology Letters*, vol. 17, no. 7, pp. 1555–1557, 2005.

[79] R. I. Killey, H. J. Thiele, V. Mikhailov, and P. Bayvel, "Reduction of intrachannel nonlinear distortion in 40-gb/s-based wdm transmission over standard fiber," *Photonics Technology Letters*, vol. 12, no. 12, pp. 1624–1626, 2000.

[80] R. H. Stolen, J. P. Gordon, W. J. Tomlinson, and H. A. Haus, "Raman response function of silica-core fibers," *Journal of the Optical Society of America B*, vol. 6, no. 6, pp. 1159–1166, 1989.

[81] Q. Lin and G. P. Agrawal, "Raman response function for silica fibers," *Optics Letters*, vol. 31, no. 21, pp. 3086–3088, 2006.

[82] P. Rosa, J. D. Ania Castañón, and P. Harper, "Unrepeatered dpsk transmission over 360 km smf-28 fibre using urfl based amplification," *Optics Express*, vol. 22, no. 8, pp. 9687–9692, 2014.

[83] M. Tan, P. Rosa, S. T. Le, I. Phillips, and P. Harper, "Evaluation of 100g dp-qpsk long-haul transmission performance using second order co-pumped raman laser based amplification," *Optics Express*, vol. 23, no. 17, pp. 22181–22189, 2015.

[84] M. Tan, P. Rosa, I. Phillips, and P. Harper, "Extended reach of 116 gb/s dp-qpsk transmission using random dfb fiber laser based raman amplification and bidirectional second-order pumping," in *Optical Fiber Communication Conference*, p. W4E.1, 2015.

[85] I. Phillips, M. Tan, M. F. C. Stephens, M. E. McCarthy, E. Giacoumidis, S. Sygletos, P. Rosa, S. Fabbri, S. T. Le, T. Kanesan, S. Turitsyn, N. J. Doran, P. Harper, and A. D. Ellis, "Exceeding the nonlinear-shannon limit using raman laser based amplification and optical phase conjugation," in *Optical Fiber Communications Conference and Exhibition*, no. M3C.1, 2014.

[86] K. Solis-Trapala, T. Inoue, and S. Namiki, "Signal power asymmetry tolerance of an optical phase conjugation-based nonlinear compensation system," in *European Conference on Optical Communication*, 2014.

[87] B. Bristiel, S. Jiang, P. Gallion, and E. Pincemin, "New model of noise figure and rin transfer in fiber raman amplifiers," *IEEE Photonics Technology Letters*, vol. 18, no. 8, pp. 980–982, 2006.

[88] M. Tan, P. Rosa, M. A. Iqbal, I. Phillips, J. Nuño, J. D. Ania Castañón, and P. Harper, "Rin mitigation in second-order pumped raman fibre laser based amplification," in *Asia Communications and Photonics Conference*, no. AM2E.6, 2015.

REFERENCES

[89] M. Tan, P. Rosa, S. T. Le, M. A. Iqbal, I. Phillips, and P. Harper, "Transmission performance improvement using random dfb laser based raman amplification and bidirectional second-order pumping," *Optics Express*, vol. 24, no. 3, pp. 2215–2221, 2016.

[90] M. Krause, S. Cierullies, H. Renner, and E. Brinkmeyer, "Pump-to-stokes rin transfer in raman fiber lasers and its impact on the performance of co-pumped raman amplifiers," *Optics Communications*, vol. 260, no. 2, pp. 656–661, 2006.

[91] J. Nuño, M. Alcón-Camas, and J. D. Ania Castañón, "Rin transfer in random distributed feedback fiber lasers," *Optics Express*, vol. 20, no. 24, pp. 27376–27381, 2012.

[92] V. Karalekas, J. D. Ania Castañón, P. Harper, S. A. Babin, E. V. Podivilov, and S. Turitsyn, "Impact of nonlinear spectral broadening in ultra-long raman fibre lasers," *Optics Express*, vol. 15, no. 25, pp. 16690–16695, 2007.

[93] S. A. Babin, V. Karalekas, P. Harper, E. V. Podivilov, V. K. Mezentsev, J. D. Ania Castañón, and S. Turitsyn, "Experimental demonstration of mode structure in ultralong raman fiber lasers," *Optics Letters*, vol. 32, no. 9, pp. 1135–1137, 20007.

[94] L. E. Nelson, X. Zhou, B. Zhu, M. F. Yan, P. W. Wisk, and P. D. Magill, "All-raman-amplified, 73 nm seamless band transmission of 9 tb/s over 6000 km of fiber," *IEEE Photonics Technology Letters*, vol. 26, no. 3, pp. 242–245, 2014.

[95] P. Rosa, M. Tan, S. T. Le, I. Phillips, J. D. Ania Castañón, S. Sygletos, and P. Harper, "Unrepeatered dp-qpsk transmission over 352.8 km smf using random dfb fiber laser amplification," *IEEE Photonics Technology Letters*, vol. 27, no. 11, pp. 1189–1192, 2015.

[96] M. Alcón-Camas and J. D. Ania Castañón, "Rin transfer in 2nd-order distributed amplification with ultralong fiber lasers," *Optics Express*, vol. 18, no. 23, pp. 23569–23575, 2010.

[97] L. Galdino, M. Tan, A. Alvarado, D. Lavery, P. Rosa, R. Maher, J. D. Ania Castañón, P. Harper, S. Makovejs, B. C. Thomsen, and P. Bayvel, "Amplification schemes and

multi-channel dbp for unrepeated transmission," *Journal of Lightwave Technology*, vol. 34, no. 9, pp. 2221–2227, 2016.

[98] J. Cheng, M. Tang, S. Fu, P. Shum, and D. Liu, "Characterization and optimization of unrepeatered coherent transmission systems using dra and ropa," *Journal of Lightwave Technology*, vol. 35, no. 10, pp. 1830–1836, 2017.

[99] J.-C. Bouteiller, K. Brar, and C. Headley, "Quasi-constant signal power transmission," in *European Conference on Optical Communication*, 2002.

[100] X. Liu, A. R. Chraplyvy, P. Winzer, R. W. Tkach, and S. Chandrasekhar, "Phase-conjugated twin waves for communication beyond the kerr nonlinearity limit," *Nature Photonics*, vol. 7, pp. 560–568, 2013.

[101] S. Olsson, B. Corcoran, C. Lundström, T. A. Eriksson, M. Karlsson, and P. A. Andrekson, "Phase-sensitive amplified transmission links for improved sensitivity and nonlinearity tolerance," *Journal of Lightwave Technology*, vol. 33, no. 3, pp. 710–721, 2015.

[102] J. P. Gordon and L. F. Mollenauer, "Effects of fiber nonlinearities and amplifier spacing on ultra-long distance transmission," *Journal of Lightwave Technology*, vol. 9, no. 2, pp. 170–173, 1991.

[103] A. Hasegawa, "An historical review of application of optical solitons for high speed communications," *Chaos*, vol. 10, no. 3, pp. 475–485, 2000.

[104] S. Wahls and H. V. Poor, "Introducing the fast nonlinear fourier transform," in *IEEE International Conference on Acoustics, Speech and Signal Processing*, 2013.

[105] M. I. Yousefi and F. R. Kschischang, "Information transmission using the nonlinear fourier transform, part i: Mathematical tools," *IEEE Transactions on Information Theory*, vol. 60, no. 7, pp. 4312–4328, 2014.

[106] S. T. Le, J. E. Prilepsky, and S. Turitsyn, "Nonlinear inverse synthesis technique for optical links with lumped amplification," *Optics Express*, vol. 23, no. 7, pp. 8317–8328, 2015.

[107] S. Hari, M. I. Yousefi, and F. R. Kschischang, "Multieigenvalue communication," *Journal of Lightwave Technology*, vol. 34, no. 13, pp. 3110–3117, 2016.

[108] A. Yariv, D. Fekete, and D. M. Pepper, "Compensation for channel dispersion by nonlinear optical phase conjugation," *Optics Letters*, vol. 4, no. 2, pp. 52–54, 1979.

[109] R. A. Fisher, B. R. Suydam, and D. Yevick, "Optical phase conjugation for time-domain undoing of dispersive self-phase-modulation effects," *Optics Letters*, vol. 8, no. 12, pp. 611–613, 1983.

[110] S. T. Le, M. E. McCarthy, S. Turitsyn, I. Phillips, D. Lavery, T. Xu, P. Bayvel, and A. D. Ellis, "Optical and digital phase conjugation techniques for fiber nonlinearity compensation," in *Opto-Electronics and Communications Conference*, 2015.

[111] J. C. Cartledge, A. D. Ellis, A. Shiner, A. I. Abd El-Rahman, M. E. McCarthy, M. Reimer, A. Borowiec, and A. Kashi, "Signal processing techniques for reducing the impact of fiber nonlinearities on system performance," in *Optical Fiber Communications Conference and Exhibition*, 2016.

[112] A. D. Ellis, S. T. Le, M. E. McCarthy, and S. Turitsyn, "The impact of parametric noise amplification on long haul transmission throughput," in *17th International Conference on Transparent Optical Networks*, 2015.

[113] A. D. Ellis, M. E. McCarthy, M. A. Z. Al-Khateeb, and S. Sygletos, "Capacity limits of systems employing multiple optical phase conjugators," *Optics Express*, vol. 23, no. 16, pp. 20381–20393, 2015.

[114] J. H. Winters and R. D. Gitlin, "Electrical signal processing techniques in long-haul fiber-optic systems," *IEEE Transactions on Communications*, vol. 38, no. 9, pp. 1439–1453, 1990.

[115] G. M. Taylor, "Coherent detection method using dsp for demodulation of signal and subsequent equalization of propagation impairments," *Photonics Technology Letters*, vol. 16, no. 2, pp. 674–676, 2004.

[116] R. I. Killey, P. M. Watts, V. Mikhailov, M. Glick, and P. Bayvel, "Electronic dispersion compensation by signal predistortion using digital processing and a dual-drive mach-zehnder modulator," *Photonics Technology Letters*, vol. 17, no. 3, pp. 714–716, 2005.

[117] R. I. Killey, "Dispersion and nonlinearity compensation using electronic predistortion techniques," in *The IEEE Seminar on Optical Fibre Communications and Electronic Signal Processing*, 2005.

[118] G. Liga, A. Alvarado, E. Agrell, M. Secondini, R. I. Killey, and P. Bayvel, "Optimum detection in presence of nonlinear distortions with memory," in *European Conference on Optical Communication*, 2015.

[119] D. Marselle, M. Secondini, and E. Forestieri, "Maximum likelihood sequence detection for mitigating nonlinear effects," *Journal of Lightwave Technology*, vol. 32, no. 5, pp. 908–916, 2014.

[120] R. Dar and P. Winzer, "On the limits of digital back-propagation in fully loaded wdm systems," *Photonics Technology Letters*, vol. 28, no. 11, pp. 1253–1256, 2016.

[121] D. Rafique, "Fiber nonlinearity compensation: Commercial applications and complexity analysis," *Journal of Lightwave Technology*, vol. 34, no. 2, pp. 544–553, 2016.

[122] F. P. Guiomar and A. Pinto, "Simplified volterra series nonlinear equalizer for polarization-multiplexed coherent optical systems," *Journal of Lightwave Technology*, vol. 31, no. 23, pp. 3879–3891, 2013.

[123] G. Shulkind and M. Nazarathy, "Efficient nonlinear compensator for coherent ofdm based on volterra series transfer function (vstf) factorization," in *Optical Fiber Communication Conference and Exposition and the National Fiber Optic Engineers Conference*, no. OM2B.5, 2013.

[124] K. V. Peddanarappagari and M. Brandt-Pearce, "Volterra series transfer function of single-mode fibers," *Journal of Lightwave Technology*, vol. 15, no. 12, pp. 2232–2241, 1997.

REFERENCES

[125] Y. Cai, D. G. Foursa, C. R. Davidson, J.-X. Cai, O. Sinkin, M. Nissov, and A. Pilipetskii, "Experimental demonstration of coherent map detection for nonlinearity mitigation in long-haul transmissions," in *Conference on Optical Fiber Communication*, 2010.

[126] A. Rezania and J. C. Cartledge, "Transmission performance of 448 gb/s single-carrier and 1.2 tb/s three-carrier superchannel using dual-polarization 16-qam with fixed lut based map detection," *Journal of Lightwave Technology*, vol. 33, no. 23, pp. 4738–4745, 2015.

[127] H. Bulow, F. Buchali, and A. Klekamp, "Electronic dispersion compensation," *Journal of Lightwave Technology*, vol. 26, no. 1, pp. 158–167, 2008.

[128] G. Saavedra, D. Semrau, L. Galdino, R. I. Killey, and P. Bayvel, "Digital back-propagation for nonlinearity mitigation in distributed raman amplified links," *Optics Express*, vol. 25, no. 5, pp. 5431–5439, 2017.

[129] R. Stremler, *Introduction to Communication Systems*. Springer, 1977.

[130] A. H. Gnauck, R. M. Jopson, and R. M. Derosier, "10-gb/s 360-km transmission over dispersive fiber using midsystem spectral inversion," *Photonics Technology Letters*, vol. 5, no. 6, pp. 663–666, 1993.

[131] S. Watanabe, T. Naito, and T. Chikama, "Compensation of chromatic dispersion in a single-mode fiber by optical phase conjugation," *Photonics Technology Letters*, vol. 5, no. 1, pp. 92–95, 1993.

[132] C. Lorattanasane and K. Kikuchi, "Design theory of long-distance optical transmission systems using midway optical phase conjugation," *Journal of Lightwave Technology*, vol. 15, no. 6, pp. 948–955, 1997.

[133] S. Watanabe and M. Shirasaki, "Exact compensation for both chromatic dispersion and kerr effect in a transmission fiber using optical phase conjugation," *Journal of Lightwave Technology*, vol. 14, no. 3, pp. 243–248, 1996.

[134] I. Brener, B. Mikkelsen, K. Rottwitt, W. Burkett, G. Raybon, J. Stark, K. Parameswaran, M. H. Chou, M. M. Fejer, E. E. Chaban, R. Harel, D. L. Philen, and A. Kosinski, "Cancellation of all kerr nonlinearities in long fiber spans using a linbo/sub 3/ phase conjugator and raman amplification," in *Conference on Optical Fiber Communication*, 2000.

[135] X. Shu, K. Chisholm, and K. Sugden, "Design and realization of dispersion slope compensators using distributed gires-tournois etalons," *Photonics Technology Letters*, vol. 16, no. 4, pp. 1092–1094, 2004.

[136] S. L. Jansen, D. van den Borne, P. M. Krummrich, S. Spälter, H. Suche, W. Sohler, G. D. Khoe, and H. de Waardt, "Phase conjugation for increased system robustness," in *Optical Fiber Communication Conference and Exposition and the National Fiber Optic Engineers Conference*, no. OTuK3, 2006.

[137] M. D. Pelusi and B. J. Eggleton, "Optically tunable compensation of nonlinear signal distortion in optical fiber by end-span optical phase conjugation," *Optics Express*, vol. 20, no. 7, pp. 8015–8023, 2012.

[138] R. J. Essiambre and P. Winzer, "Fibre nonlinearities in electronically pre-distorted transmission," in *Conference on Optical Fiber Communication*, 2005.

[139] E. Ip and J. M. Kahn, "Compensation of dispersion and nonlinear impairments using digital backpropagation," *Journal of Lightwave Technology*, vol. 26, no. 20, pp. 3416–3425, 2008.

[140] D. Lavery, D. Ives, G. Liga, A. Alvarado, S. Savory, and P. Bayvel, "The benefit of split nonlinearity compensation for single-channel optical fiber communications," *Photonics Technology Letters*, vol. 28, no. 17, pp. 1803–1806, 2016.

[141] O. Sinkin, R. Holzlohner, J. Zweck, and C. R. Menyuk, "Optimization of the split-step fourier method in modeling optical-fiber communications systems," *Journal of Lightwave Technology*, vol. 21, no. 1, pp. 61–68, 2003.

REFERENCES

[142] Q. Zhang and M. I. Hayee, "Symmetrized split-step fourier scheme to control global simulation accuracy in fiber-optic communication systems," *Journal of Lightwave Technology*, vol. 26, no. 2, pp. 302–316, 2008.

[143] E. Ip and J. M. Kahn, "Fiber impairment compensation using coherent detection and digital signal processing," *Journal of Lightwave Technology*, vol. 28, no. 4, pp. 502–519, 2010.

[144] X. Li, X. Chen, G. Goldfarb, E. Mateo, I. Kim, F. Yaman, and G. Li, "Electronic post-compensation of wdm transmission impairments using coherent detection and digital signal processing," *Optics Express*, vol. 16, no. 2, pp. 880–888, 2008.

[145] E. Ip, E. Mateo, and T. Wang, "Reduced-complexity nonlinear compensation based on equivalent-span digital backpropagation," in *International Conference on Optical Internet*, 2012.

[146] P. Serena, "Nonlinear signal–noise interaction in optical links with nonlinear equalization," *Journal of Lightwave Technology*, vol. 34, no. 6, pp. 1476–1483, 2016.

[147] D. Rafique, M. Mussolin, M. Forzati, J. Mårtensson, M. N. Chugtai, and A. D. Ellis, "Modified split-step fourier method for compensation of nonlinear fibre impairments," in *International Conference on Transparent Optical Networks*, 2011.

[148] L. Li, Z. Tao, L. Dou, W. Yan, S. Oda, T. Tanimura, T. Hoshida, and J. C. Rasmussen, "Implementation efficient nonlinear equalizer based on correlated digital backpropagation," in *Optical Fiber Communication Conference and Exposition and the National Fiber Optic Engineers Conference*, 2011.

[149] P. Rosa, P. Harper, N. Murray, and J. D. Ania Castañón, "Unrepeatered 8 x 40gb/s transmission over 320km smf-28 using ultra-long raman fibre based amplification," in *European Conference on Optical Communication*, 2012.

[150] L. Galdino, G. Liga, D. Lavery, R. Maher, T. Xu, M. Sato, R. I. Killey, S. Savory, B. C. Thomsen, and P. Bayvel, "Unrepeated transmission over 253.4 km ultra low loss fiber

achieving 6.95 b/s/hz se using edfa-only pre-amplification," in *European Conference on Optical Communication*, 2014.

[151] H. Bissessur, C. Bastide, S. Dubost, S. Etienne, and D. Mongardien, "8 tb/s unrepeatered transmission of real-time processed 200 gb/s pdm 16-qam over 363 km," in *European Conference on Optical Communication*, 2014.

[152] H. Bissessur, C. Bastide, S. Dubost, and S. Etienne, "80×200 gb/s 16-qam unrepeatered transmission over 321km with third order raman amplification," in *Optical Fiber Communication Conference*, no. W4E.2, 2015.

[153] J. C. S. S. Januario, S. M. Rossi, S. M. Ranzini, V. E. Parahyba, V. N. Rozental, A. L. Nunes de Souza, A. C. Bordonalli, J. R. Fernandes de Oliveira, and J. Dias Reis, "Unrepeatered transmission of 10×400g over 370 km via amplification map optimization," *Photonics Technology Letters*, vol. 28, no. 20, pp. 2289–2292, 2016.

[154] X. Lv, D. Wang, Y. Zhu, K. Zou, Z. Zheng, F. Zhang, L. Zhu, and Z. Chen, "Unrepeatered 447gb/s nyquist pdm-64qam transmission over 160km ssmf with backward raman amplification," in *European Conference on Optical Communication*, 2015.

[155] D. Wang, X. Lv, Y. Zhu, K. Zou, F. Zhang, L. Zhu, and Z. Chen, "Unrepeatered 515gb/s nyquist pdm-128qam transmission over 120km ssmf with backward raman amplification," in *Opto-Electronics and Communications Conference*, 2015.

[156] H. Bissessur, C. Bastide, S. Etienne, and S. Dupont, "24 tb/s unrepeatered c-band transmission of real-time processed 200 gb/s pdm-16-qam over 349 km," in *Optical Fiber Communication Conference*, 2017.

[157] J. C. S. S. Januario, S. M. Rossi, J. H. C. Junior, A. Chiuchiarelli, A. L. N. Souza, A. Felipe, A. C. Bordonalli, S. Makovejs, J. R. Fernandes de Oliveira, and J. D. Reis, "Unrepeatered wdm transmission of singlecarrier 400g (66-gbd pdm-16qam) over 403 km," in *Optical Fiber Communication Conference*, 2017.

[158] J. R. Navarro, A. Kakkar, R. Schatz, X. Pang, O. Ozolins, F. Nordwall, H. Louchet, S. Popov, and G. Jacobsen, "High performance and low complexity carrier phase recovery schemes for 64-qam coherent optical systems," in *Optical Fiber Communications Conference and Exhibition*, 2017.

[159] S. Pitois, A. Sauter, and G. Millot, "Simultaneous achievement of polarization attraction and raman amplification in isotropic optical fibers," *Optics Letters*, vol. 29, no. 6, pp. 599–601, 2004.

[160] S. Pitois, A. Picozzi, G. Millot, H. R. Jauslin, and M. Haelterman, "Polarization and modal attractors in conservative counterpropagating four-wave interaction," *Europhysics Letters*, vol. 70, no. 1, pp. 88–94, 2005.

[161] S. Pitois, J. Fatome, and G. Millot, "Polarization attraction using counter-propagating waves in optical fiber at telecommunication wavelengths," *Optics Express*, vol. 16, no. 9, pp. 6646–6651, 2008.

[162] J. Fatome, S. Pitois, P. Morin, and G. Millot, "Observation of light-by-light polarization control and stabilization in optical fibre for telecommunication applications," *Optics Express*, vol. 18, no. 15, pp. 15311–15317, 2010.

[163] J. Fatome, S. Pitois, P. Morin, C. Finot, and G. Millot, "Light-by-light polarization control for telecommunication applications," in *International Conference on Transparent Optical Networks*, 2010.

[164] V. Kozlov, J. Nuño, and S. Wabnitz, "Theory of lossless polarization attraction in telecommunication fibers," *Journal of the Optical Society of America B*, vol. 28, no. 1, pp. 100–108, 2011.

[165] V. Kozlov, J. Nuño, J. D. Ania Castañón, and S. Wabnitz, "Theory of fiber optic raman polarizers," *Optics Letters*, vol. 35, no. 23, pp. 3970–3972, 2010.

[166] J. Fatome, S. Pitois, and G. Millot, "Experimental evidence of brillouin-induced polarization wheeling in highly birefringent optical fibers," *Optics Express*, vol. 17, no. 15, pp. 12612–12618, 2009.

[167] M. Martinelli, M. Cirigliano, M. Ferrario, L. Marazzi, and P. Martelli, "Evidence of raman-induced polarization pulling," *Optics Express*, vol. 17, no. 2, pp. 947–955, 2009.

[168] B. Stiller, P. Morin, D. M. Nguyen, J. Fatome, H. Maillotte, S. Pitois, and T. Sylvestre, "Demonstration of polarization pulling in a fiber-optical parametric amplifier," in *Advanced Photonics Congress*, 2012.

[169] V. Kozlov and S. Wabnitz, "Suppression of relative intensity noise in fiber-optic raman polarizers," *Photonics Technology Letters*, vol. 23, no. 15, pp. 1088–1090, 2011.

[170] Q. Lin and G. P. Agrawal, "Statistics of polarization-dependent gain in fiber-based raman amplifiers," *Optics Letters*, vol. 28, no. 4, pp. 227–229, 2003.

[171] A. Galtarossa, L. Palmieri, M. Santagiustina, and L. Ursini, "Polarized backward raman amplification in randomly birefringent fibers," *Journal of Lightwave Technology*, vol. 24, no. 11, pp. 4055–4063, 2006.

[172] L. Ursini, M. Santagiustina, and L. Palmieri, "Raman nonlinear polarization pulling in the pump depleted regime in randomly birefringent fibers," *Photonics Technology Letters*, vol. 23, no. 4, pp. 254–256, 2011.

[173] V. Kozlov, J. Nuño, J. D. Ania Castañón, and S. Wabnitz, "Theoretical study of optical fiber raman polarizers with counterpropagating beams," *Journal of Lightwave Technology*, vol. 29, no. 3, pp. 341–347, 2011.

[174] V. Kozlov, J. Nuño, J. D. Ania Castañón, and S. Wabnitz, "Analytic theory of fiber-optic raman polarizers," *Optics Express*, vol. 20, no. 24, pp. 27242–27247, 2012.

[175] K. Perlicki, "Raman polarization pulling and amplification for polarization multiplexing transmission systems," *International Journal of Electronics and Telecommunications*, vol. 57, no. 4, pp. 519–522, 2011.

[176] M. Ferrario, V. Gilardone, P. Martelli, L. Marazzi, and M. Martinelli, "Effective all-optical polarization control induced by raman nonlinear amplification," in *European Conference on Optical Communication*, 2010.

REFERENCES

[177] F. Chiarello, L. Ursini, L. Palmieri, and M. Santagiustina, "Polarization attraction in counterpropagating fiber raman amplifiers," *Photonics Technology Letters*, vol. 23, no. 20, pp. 1457–1459, 2011.

[178] N. J. Muga, M. F. S. Ferreira, and A. N. Pinto, "Broadband polarization pulling using raman amplification," *Optics Express*, vol. 19, no. 19, pp. 18707–18712, 2011.

[179] H. Wu, Z. N. Wang, D. V. Churkin, I. D. Vatnik, M. Q. Fan, and Y. J. Rao, "Random distributed feedback raman fiber laser with polarized pumping," *Laser Physics Letters*, vol. 12, no. 1, p. 015101, 2014.

[180] P. Morin, S. Pitois, and J. Fatome, "Simultaneous polarization attraction and raman amplification of a light beam in optical fibers," *Journal of the Optical Society of America B*, vol. 29, no. 8, pp. 2046–2052, 2012.

[181] F. Chiarello, L. Palmieri, M. Santagiustina, R. Gamathan, and A. Galtarossa, "Experimental characterization of the counter-propagating raman polarization attraction," *Optics Express*, vol. 20, no. 23, pp. 26050–26055, 2012.

[182] S. Pitois, G. Millot, and S. Wabnitz, "Nonlinear polarization dynamics of counterpropagating waves in an isotropic optical fiber: theory and experiments," *Journal of the Optical Society of America B*, vol. 18, no. 4, pp. 432–443, 2001.

[183] S. Sergeyev, S. Popov, and A. T. Friberg, "Modeling polarization-dependent gain in fiber raman amplifiers with randomly varying birefringence," *Optics Communications*, vol. 262, no. 1, pp. 114–119, 2006.

[184] J. Nuño, G. Rizzelli, F. Gallazzi, F. Prieto, C. Pulido, P. Corredera, S. Wabnitz, and J. D. Ania Castañón, "Open-cavity spun fiber raman lasers with dual polarization output," *Scientific Reports*, vol. 7, no. 1, p. 13681, 2017.

[185] P. K. A. Wai and C. R. Menyak, "Polarization mode dispersion, decorrelation, and diffusion in optical fibers with randomly varying birefringence," *Journal of Lightwave Technology*, vol. 14, no. 2, pp. 148–157, 1996.

[186] Q. Lin and G. P. Agrawal, "Polarization mode dispersion–induced fluctuations during raman amplifications in optical fibers.," *Optics Letters*, vol. 27, no. 24, pp. 2194–2196, 2002.

[187] X. Bao and L. Chen, "Recent progress in brillouin scattering based fiber sensors," *Sensors*, vol. 11, no. 4, pp. 4152–4187, 2011.

[188] X. Chen, M. J. Li, and D. A. Nolan, "Polarization mode dispersion of spun fibers an analytical solution," *Optics Letters*, vol. 27, no. 5, pp. 294–296, 2002.

[189] A. Galtarossa, P. Griggio, L. Palmieri, and A. Pizzinat, "Low-pmd spun fibers," *Journal of Optical and Fiber Communications Reports*, vol. 1, no. 1, pp. 32–62, 2004.

[190] J. Fatome, S. Pitois, P. Morin, E. Assémat, D. Sugny, A. Picozzi, H. R. Jauslin, G. Millot, V. Kozlov, and S. Wabnitz, "A universal optical all-fiber omnipolarizer," *Scientific Reports*, vol. 2, no. 938, 2012.

Declaration

I herewith declare that I have produced this work without the prohibited assistance of third parties and without making use of aids other than those specified; notions taken over directly or indirectly from other sources have been identified as such. This work has not previously been presented in identical or similar form to any examination board. Part of this work has been included in preceding scientific contributions in the form of journal articles or conference proceedings.

The dissertation work was conducted from 2015 to 2018 under the supervision of Dr. Juan Diego Ania-Castañón and Dr. Miguel González Herráez at the Instituto de Óptica of the Consejo Superior de Investigaciones Científicas and at the Universidad de Alcalá.

Madrid,

This dissertation was finished writing in Madrid on 20 de enero de 2018

This page is intentionally left blank